**The scramble for new drugs to stop the coronavirus** p. 1092

**Market design to expand vaccine capacity** p. 1107

**Making and remodeling the lung's gas-exchange unit** p. 1124

# Science

$15
12 MARCH 2021
sciencemag.org

AAAS

## STABLE SHEETS

Borophane attains stability from reversible hydrogenation p. 1143

## Apply for our exciting research Prize!

SCIENCE-PINS PRIZE FOR NEUROMODULATION

SCIENCE-PINS

# $25, 000 Grand Prize!
# Get published in *Science*!

The *Science*-PINS Prize is a highly competitive international prize that honors scientists for their excellent contributions to neuromodulation research. For purposes of the Prize, neuromodulation is any form of alteration of nerve activity through the delivery of physical (electrical, magnetic, or optical) stimulation to targeted sites of the nervous system with impications for translational medicine.

For full details, judging criteria and eligibility requirements, visit:

**www.sciencemag.org/prizes/pins**

# Submission Deadline: 15 March 2021

Science AAAS

PINS 品驰

Science Translational Medicine AAAS

# German mathematician braves COVID-19 to advance his research in Tokyo

Felix Scholz, a junior researcher at Waseda University in Tokyo, researches the integration of computational geometry and computer engineering. More precisely, he develops geometry representations suitable for computer-aided design (CAD), computer-aided engineering (CAE), and computer-aided manufacturing.

"Classically, these areas have used different geometry representations, for example, smooth spline surfaces for CAD and finite element meshes for CAE, and a lot of effort was needed to translate one to the other in practical applications," he says.

To solve the puzzle, Scholz has been using a newly developed method known as isogeometric analysis (IGA). IGA reduces the time needed for scientists and engineers to produce computer models or simulations of complex and diverse events such as hurricanes and car crash tests. "Currently, I am working on piece-wise developable surfaces—surfaces that can be manufactured by bending flat materials such as sheet metal without stretching them," says Scholz. For example, this method can be applied to architecture, where buildings are designed using such surfaces for their ease of construction as well as their aesthetic properties.

[1] www.tafsm.org.

## Japan beckons but...

Scholz made his way to Japan in November 2020 on the advice of his postdoctoral advisor at the Johann Radon Institute for Computational and Applied Mathematics in Austria, who told him about a position at Waseda. He successfully applied for the job and was fortunate to be offered a place in Kenji Takizawa's laboratory at Waseda.

Takizawa is affiliated with the Multiscale Analysis, Modelling and Simulation (MAMAS) Model Unit at Waseda (see sidebar), and his laboratory is also a member of the Team for Advanced Flow Simulation and Modeling (TAFSM[1]). TAFSM is focused on computational engineering analysis using a space–time computer modeling method developed by the team. By combining their method with IGA, they were able to more precisely model and analyze interactions between fluids and moving structures. This enabled them to solve modeling problems as varied and challenging as designing the parachute system for NASA's returning Orion spacecraft and illustrating the effects of an aneurysm on blood flow to help clinicians.

Scholz was supposed to arrive in Japan on June 1, 2020, but that came undone with the rise of COVID-19.

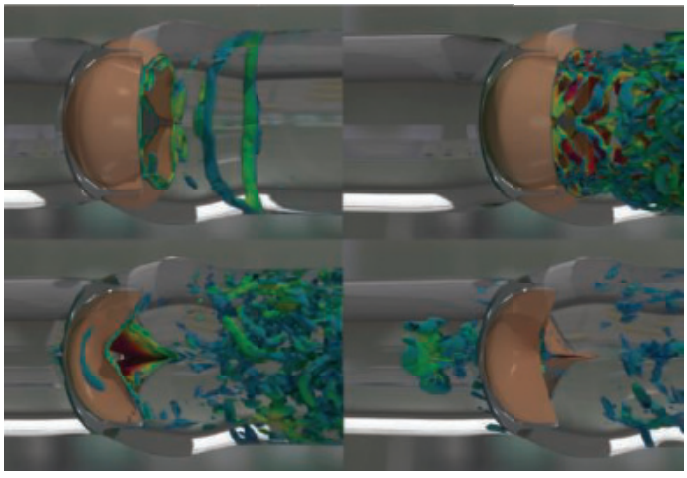

Computational fluid–structure interaction analysis of a bioprosthetic heart valve

IMAGE: PROVIDED BY WASEDA UNIVERSITY

## Waseda University's Multiscale Analysis, Modelling and Simulation (MAMAS) Model Unit

The aim of MAMAS is to develop joint education and research opportunities in physics and mathematics—two disciplines for which Waseda is renowned. MAMAS is one of the seven model research units comprising the Waseda Goes Global plan, an ambitious, 10-year project started in 2014 and part of the Japanese government's multibillion-dollar Top Global University scheme to internationalize the country's leading universities. The other model research units are in the fields of global Japanese studies, health promotion, information and communications technology and robotics, energy and nanomaterials, empirical research in political economics, and global Asia studies.

MAMAS has collaborated with several universities worldwide to create a global doctoral program that has students apply interdisciplinary studies such as nonlinear partial differential equations, geometry, and quantum mechanics to practical applications such as fluidics and the flow of gases and liquids. Research topics include mathematical modeling based on imaging the interaction of molten metals with concrete, analyzing cloud formations to better understand climate change, and observing blood flow in humans for early diagnosis of cardiovascular disease.

To prevent the disease from spreading, the Japanese government restricted overseas travelers from entering the country. Fortunately, Waseda was able to arrange for him to work remotely.

When the entry of foreigners was permitted again in October 2020, Scholz made new preparations and finally arrived in Japan in November. "But I had to stay indoors because the government had imposed a fourteen-day quarantine on people coming into the country," says Scholz.

He was impressed with the care Waseda's administrative staff took to help him settle in during those difficult early weeks. "For instance, I wasn't able to use public transport on arriving in Japan because of the quarantine restrictions. So Waseda arranged private transport for me, and they set me up in an apartment in the university's guest housing."

### Unique solutions to real-world problems

When he was finally able to visit the main Waseda campus in Tokyo, Scholz was delighted to find it larger than expected: "The area around the campus is very attractive; it's very enjoyable living here." He was also happy with his work location in the Institute for Frontier Fluid Structure Interaction Analysis, which is housed in the Green Computing Systems Research Organization. At the institute, Scholz and his colleagues tackle a wide range of real-world problems that few research groups are equipped to address. The classes of applications targeted include fluid machinery, ground vehicles, aerospace technologies, home appliances, and medical applications. "We have a large, active group that includes experienced researchers as well as bachelor's, Master's, and doctoral degree students."

The plan is for Scholz to spend up to 3 years doing research at Waseda, which he believes will give him ample time to develop the skills and form the professional relationships necessary to advance his career. "I want to formulate efficient and powerful methods for numerical simulations on complicated geometries. Using new methods, we can increase the efficiency of the overall design process. I'd like to produce results that can be generalized and used to tackle a large class of applications stemming from real-world problems."

# CONTENTS

12 MARCH 2021 • VOLUME 371 • ISSUE 6534

1092

## NEWS

### IN BRIEF



### IN DEPTH



### FEATURES



## INSIGHTS

### PERSPECTIVES



### POLICY FORUM



### BOOKS *ET AL.*



ILLUSTRATION: STEPHAN SCHMITZ/FOLIO ART


PHOTO: MICHAEL P. GADOMSKI/SCIENCE SOURCE

## ON THE COVER

Atomically thin boron, or borophene, has attracted attention because of its distinctive electronic properties. However, borophene is highly reactive, which makes it difficult to study outside of idealized vacuum conditions. Reversible hydrogenation of borophene (right), which exists as a flat sheet, enables synthesis of borophane (left), a puckered sheet with atomic hydrogen (individual white circles). Borophane's chemical stability may facilitate potential applications in electronics, batteries, sensors, and quantum technologies. See page 1143. *Illustration: V. Altounian/* Science





**SCIENCE (ISSN 0036-8075) is published weekly on Friday, except last week in December, by the American Association for the Advancement of Science, 1200 New York Avenue, NW, Washington, DC 20005.** Periodicals mail postage (publication No. 484460) paid at Washington, DC, and additional mailing offices.



Domestic individual membership, including subscription (12 months): $165 ($74 allocated to subscription). Domestic institutional subscription (51 issues): $2148; Foreign postage extra: Air assist delivery: $98. First class, airmail, student, and emeritus rates on request. Canadian rates with GST available upon request, GST #125488122. Publications Mail Agreement Number 1069624. **Printed in the U.S.A.**
**Change of address:** Allow 4 weeks, giving old and new addresses and 8-digit account number. **Postmaster:** Send change of address to AAAS, P.O. Box 96178, Washington, DC 20090–6178. **Single-copy sales:** $15 each plus shipping and handling available from backissues.sciencemag.org; bulk rate on request. **Authorization to reproduce** material for internal or personal use under circumstances not falling within the fair use provisions of the Copyright Act can be obtained through the Copyright Clearance Center (CCC), www.copyright.com. The identification code for *Science* is 0036-8075. *Science* is indexed in the *Reader's Guide to Periodical Literature* and in several specialized indexes.

# Science AAAS

**Editor-in-Chief** Holden Thorp, hthorp@aaas.org

**Executive Editor** Monica M. Bradford

**Editors, Research** Valda Vinson, Jake S. Yeston **Editor, Insights** Lisa D. Chong

**DEPUTY EDITORS** Julia Fahrenkamp-Uppenbrink (UK), Stella M. Hurtley (UK), Phillip D. Szuromi, Sacha Vignieri **SR. EDITORIAL FELLOW** Andrew M. Sugden (UK) **SR. EDITORS** Gemma Alderton (UK), Caroline Ash (UK), Brent Grocholski, Pamela J. Hines, Di Jiang, Marc S. Lavine (Canada), Yevgeniya Nusinovich, Ian S. Osborne (UK), Beverly A. Purnell, L. Bryan Ray, H. Jesse Smith, Keith T. Smith (UK), Jelena Stajic, Peter Stern (UK), Valerie B. Thompson, Brad Wible, Laura M. Zahn **ASSOCIATE EDITORS** Michael A. Funk, Priscilla N. Kelly, Tage S. Rai, Seth Thomas Scanlon (UK), Yury V. Suleymanov **LETTERS EDITOR** Jennifer Sills **LEAD CONTENT PRODUCTION EDITORS** Harry Jach, Lauren Kmec **CONTENT PRODUCTION EDITORS** Amelia Beyna, Jeffrey E. Cook, Chris Filiatreau, Julia Katris, Nida Masiulis, Suzanne M. White **SR. EDITORIAL COORDINATORS** Carolyn Kyle, Beverly Shields **EDITORIAL COORDINATORS** Aneera Dobbins, Joi S. Granger, Jeffrey Hearn, Lisa Johnson, Maryrose Madrid, Ope Martins, Shannon McMahon, Jerry Richardson, Hilary Stewart (UK), Alana Warnke, Alice Whaley (UK), Anita Wynn **PUBLICATIONS ASSISTANTS** Jeremy Dow, Alexander Kief, Ronmel Navas, Brian White **EXECUTIVE ASSISTANT** Jessica Slater **ASI DIRECTOR, OPERATIONS** Janet Clements (UK) **ASI SR. OFFICE ADMINISTRATOR** Jessica Waldock (UK)

**News Editor** Tim Appenzeller

**NEWS MANAGING EDITOR** John Travis **INTERNATIONAL EDITOR** Martin Enserink **DEPUTY NEWS EDITORS** Elizabeth Culotta, Lila Guterman, David Grimm, Eric Hand (Europe), David Malakoff **SR. CORRESPONDENTS** Daniel Clery (UK), Jon Cohen, Jeffrey Mervis, Elizabeth Pennisi **ASSOCIATE EDITORS** Jeffrey Brainard, Catherine Matacic **NEWS REPORTERS** Adrian Cho, Jennifer Couzin-Frankel, Jocelyn Kaiser, Kelly Servick, Robert F. Service, Erik Stokstad, Paul Voosen, Meredith Wadman **INTERNS** Lucy Hicks, Cathleen O'Grady **CONTRIBUTING CORRESPONDENTS** Warren Cornwall, Andrew Curry (Berlin), Ann Gibbons, Sam Kean, Eli Kintisch, Kai Kupferschmidt (Berlin), Andrew Lawler, Mitch Leslie, Eliot Marshall, Virginia Morell, Dennis Normile (Shanghai), Elisabeth Pain (Careers), Charles Piller, Michael Price, Tania Rabesandratana (Barcelona), Joshua Sokol, Emily Underwood, Gretchen Vogel (Berlin), Lizzie Wade (Mexico City) **CAREERS** Donisha Adams, Rachel Bernstein (Editor), Katie Langin (Associate Editor) **COPY EDITORS** Julia Cole (Senior Copy Editor), Cyra Master (Copy Chief) **ADMINISTRATIVE SUPPORT** Meagan Weiland

**Creative Director** Beth Rakouskas

**DESIGN MANAGING EDITOR** Marcy Atarod **GRAPHICS MANAGING EDITOR** Alberto Cuadra **PHOTOGRAPHY MANAGING EDITOR** William Douthitt **WEB CONTENT STRATEGY MANAGER** Kara Estelle-Powers **DESIGN EDITOR** Chrystal Smith **DESIGNER** Christina Aycock **GRAPHICS EDITOR** Nirja Desai **INTERACTIVE GRAPHICS EDITOR** Kelly Franklin **SENIOR SCIENTIFIC ILLUSTRATORS** Valerie Altounian, Chris Bickel **SCIENTIFIC ILLUSTRATOR** Alice Kitterman **SENIOR GRAPHICS SPECIALISTS** Holly Bishop, Nathalie Cary **SENIOR PHOTO EDITOR** Emily Petersen **PHOTO EDITOR** Kaitlyn Dolan **WEB DESIGNER** Jennie Pajerowski

**Chief Executive Officer and Executive Publisher** Sudip Parikh

**Publisher, Science Family of Journals** Bill Moran

**DIRECTOR, BUSINESS SYSTEMS AND FINANCIAL ANALYSIS** Randy Yi **DIRECTOR, BUSINESS OPERATIONS & ANALYSIS** Eric Knott **DIRECTOR OF ANALYTICS** Enrique Gonzales **MANAGER, BUSINESS OPERATIONS** Jessica Tierney **SENIOR BUSINESS ANALYST** Cory Lipman, Meron Kebede **FINANCIAL ANALYST** Alexander Lee **ADVERTISING SYSTEM ADMINISTRATOR** Tina Burks **SENIOR SALES COORDINATOR** Shirley Young **DIGITAL/PRINT STRATEGY MANAGER** Jason Hillman **QUALITY TECHNICAL MANAGER** Marcus Spiegler **ASSISTANT MANAGER DIGITAL/PRINT** Rebecca Doshi **SENIOR CONTENT SPECIALISTS** Steve Forrester, Jacob Hedrick, Antoinette Hodal, Lori Murphy **PRODUCTION SPECIALIST** Kristin Wowk **DIGITAL PRODUCTION MANAGER** Lisa Stanford **CONTENT SPECIALIST** Kimberley Oster **ADVERTISING PRODUCTION OPERATIONS MANAGER** Deborah Tompkins **DESIGNER, CUSTOM PUBLISHING** Jeremy Huntsinger **SR. TRAFFIC ASSOCIATE** Christine Hall **SPECIAL PROJECTS ASSOCIATE** Sarah Dhere

**ASSOCIATE DIRECTOR, BUSINESS DEVELOPMENT** Justin Sawyers **GLOBAL MARKETING MANAGER** Allison Pritchard **DIGITAL MARKETING MANAGER** Aimee Aponte **JOURNALS MARKETING MANAGER** Shawana Arnold **MARKETING ASSOCIATES** Tori Velasquez, Mike Romano, Ashley Hylton **DIGITAL MARKETING SPECIALIST** Asleigh Rojanavongse **SENIOR DESIGNER** Kim Huynh

**DIRECTOR AND SENIOR EDITOR, CUSTOM PUBLISHING** Sean Sanders **ASSISTANT EDITOR, CUSTOM PUBLISHING** Jackie Oberst

**DIRECTOR, PRODUCT & PUBLISHING DEVELOPMENT** Chris Reid **DIRECTOR, BUSINESS STRATEGY AND PORTFOLIO MANAGEMENT** Sarah Whalen **ASSOCIATE DIRECTOR, PRODUCT MANAGMENT** Kris Bishop **PRODUCT DEVELOPMENT MANAGER** Scott Chernoff **PUBLISHING TECHNOLOGY MANAGER** Michael Di Natale **SR. PRODUCT ASSOCIATE** Robert Koepke **SPJ ASSOCIATE** Samantha Bruno Fuller

**DIRECTOR, INSTITUTIONAL LICENSING** Iquo Edim **ASSOCIATE DIRECTOR, RESEARCH & DEVELOPMENT** Elisabeth Leonard **MARKETING MANAGER** Kess Knight **SENIOR INSTITUTIONAL LICENSING MANAGER** Ryan Rexroth **INSTITUTIONAL LICENSING MANAGER** Marco Castellan **MANAGER, AGENT RELATIONS & CUSTOMER SUCCESS** Judy Lillibridge **SENIOR OPERATIONS ANALYST** Lana Guz **FULFILLMENT COORDINATOR** Melody Stringer **SALES COORDINATOR** Josh Haverlock

**DIRECTOR, GLOBAL SALES** Tracy Holmes **US EAST COAST AND MID WEST SALES** Stephanie O'Connor **US WEST COAST SALES** Lynne Stickrod **US SALES MANAGER, SCIENCE CAREERS** Claudia Paulsen-Young **US SALES REP, SCIENCE CAREERS** Tracy Anderson **ASSOCIATE DIRECTOR, ROW** Roger Goncalves **SALES REP, ROW** Sarah Lelarge **SALES ADMIN ASSISTANT, ROW** Bryony Cousins **DIRECTOR OF GLOBAL COLLABORATION AND ACADEMIC PUBLISHING RELATIONS, ASIA** Xiaoying Chu **ASSOCIATE DIRECTOR, INTERNATIONAL COLLABORATION** Grace Yao **SALES MANAGER** Danny Zhao **MARKETING MANAGER** Kilo Lan **ASCA CORPORATION, JAPAN** Kaoru Sasaki (Tokyo), Miyuki Tani (Osaka) **COLLABORATION/ CUSTOM PUBLICATIONS/JAPAN** Adarsh Sandhu

**DIRECTOR, COPYRIGHT, LICENSING AND SPECIAL PROJECTS** Emilie David **RIGHTS AND LICENSING COORDINATOR** Jessica Adams **RIGHTS AND PERMISSIONS ASSOCIATE** Elizabeth Sandler **CONTRACTS AND LICENSING ASSOCIATE** Lili Catlett

---

**MAIN HEADQUARTERS**
Science/AAAS
1200 New York Ave. NW
Washington, DC 20005

**SCIENCE INTERNATIONAL**
Clarendon House
Clarendon Road
Cambridge, CB2 8FH, UK

**SCIENCE CHINA**
Room 1004, Culture Square
No. 59 Zhongguancun St.
Haidian District, Beijing, 100872

**SCIENCE JAPAN**
ASCA Corporation
Sibaura TY Bldg. 4F, 1-14-5
Shibaura Minato-ku
Tokyo, 108-0073 Japan

**EDITORIAL**
science_editors@aaas.org

**NEWS**
science_news@aaas.org

**INFORMATION FOR AUTHORS**
sciencemag.org/authors/science-information-authors

**REPRINTS AND PERMISSIONS**
sciencemag.org/help/reprints-and-permissions

**MEDIA CONTACTS**
scipak@aaas.org

**MULTIMEDIA CONTACTS**
SciencePodcast@aaas.org
ScienceVideo@aaas.org

**INSTITUTIONAL SALES AND SITE LICENSES**
sciencemag.org/librarian

**PRODUCT ADVERTISING & CUSTOM PUBLISHING**
advertising.sciencemag.org/products-services
science_advertising@aaas.org

**CLASSIFIED ADVERTISING**
advertising.sciencemag.org/science-careers
advertise@sciencecareers.org

**JOB POSTING CUSTOMER SERVICE**
employers.sciencecareers.org
support@sciencecareers.org

**MEMBERSHIP AND INDIVIDUAL SUBSCRIPTIONS**
sciencemag.org/subscriptions

**MEMBER BENEFITS**
aaas.org/membercentral

**AAAS BOARD OF DIRECTORS**
**CHAIR** Steven Chu
**PRESIDENT** Claire M. Fraser
**PRESIDENT-ELECT** Susan G. Amara
**TREASURER** Carolyn N. Ainslie
**CHIEF EXECUTIVE OFFICER**
Sudip Parikh
**BOARD** Cynthia M. Beall
Rosina M. Bierbaum
Ann Bostrom
Stephen P.A. Fodor
S. James Gates, Jr.
Laura H. Greene
Kaye Husbands Fealing
Maria M. Klawe
Robert B. Millard
Alondra Nelson
William D. Provine




*Science* serves as a forum for discussion of important issues related to the advancement of science by publishing material on which a consensus has been reached as well as including the presentation of minority or conflicting points of view. Accordingly, all articles published in *Science*—including editorials, news and comment, and book reviews—are signed and reflect the individual views of the authors and not official points of view adopted by AAAS or the institutions with which the authors are affiliated.

EDITORIAL

# COVID-19 lessons for research

As we mark the 1-year anniversary of the declaration by the World Health Organization (WHO) of COVID-19 as a global pandemic, the world has suffered a staggering and tragic human toll. During this dark time, the scientific community has been called to rise to the occasion in unprecedented ways. The intensity of the work and the sense of urgency have been unremitting and exhausting. As we sort out the triumphs and frustrations, we can begin to reflect on what we have learned.

The rapid development of vaccines has been breathtaking. Moving at least five times faster than ever before, the design, development, rigorous testing, and manufacture of multiple vaccines using different platforms have been astoundingly successful. This was only possible because of decades of investment in the long arc of technology development—working out the details of a messenger RNA strategy, for instance, was a 25-year journey. To prepare for future pandemics, we must extrapolate this lesson to the most likely pathogens lurking in the future. We should also learn from the experience of vaccine trial recruitment, where special efforts like the U.S. National Institutes of Health (NIH) Community Engagement Alliance (CEAL) were needed to reach out to communities of color, where the disease has taken its highest toll in the United States. Diversity in clinical trial enrollment is not just a nice idea—it is essential if the results are going to be meaningful to all groups.

> "...we must extrapolate... to the most likely pathogens lurking in the future."

Therapeutics that have proven beneficial for COVID-19 include an antiviral (remdesivir), immunosuppressives (dexamethasone, baracitinib), several outpatient monoclonal antibodies, and anticoagulants. Important contributions were made by the Randomised Evaluation of COVID-19 Therapy (RECOVERY) trial in the United Kingdom and the Solidarity Trial sponsored by WHO. In the United States, a public-private partnership, Accelerating COVID-19 Therapeutic Interventions and Vaccines (ACTIV), brought together government agencies, academics, and 20 pharmaceutical companies, ably managed by the Foundation for the NIH. With a priority on therapeutic agents, ACTIV designed master protocols and coordinated rigorous, well-powered randomized controlled trials. Operation Warp Speed, a public-private partnership initiated by the U.S. government, provided billions of dollars for trial operation and at-risk manufacturing. One lesson learned, however, was that many clinical trials in the United States were not initially well suited to a public health emergency. Far too many small and poorly designed trials (many focused on hydroxychloroquine, which turned out to be a dead end) were initiated in the early days of the pandemic—all with good intentions but contributing relatively little in terms of new knowledge. Another lesson is that the necessary short-term dependence on repurposing existing drugs will not often produce true successful outcomes. For the future, we should begin to work on potent oral antivirals against all major classes of potential pathogens, with the goal of having drugs ready for phase 2/3 efficacy trials when the next threat emerges.

Another major challenge was the need for fast, widely accessible, and highly accurate virus testing. For all their merits, the first-arriving nucleic acid tests, which generally had to be conducted in central labs, took too long to produce the rapid results urgently needed to prevent spread. This inspired an innovative response—the NIH Rapid Acceleration of Diagnostics (RADx) program in which test developers drew on a "shark tank" of engineering, business, and manufacturing experts. From over 700 applications, 137 went through an intense evaluation, and those judged most promising were provided with additional resources. As a result, today there are 28 novel diagnostic platforms collectively contributing an additional 2.5 million tests daily. An analysis of the potential benefits of widespread home testing is about to get under way. This approach, whereby NIH took on the role of venture capitalist, should be considered in the future when rapid development of new technologies is the goal.

In the past, the world has rallied to confront new pandemics, only to lapse into complacency as the risk faded. Having now experienced the worst pandemic in 103 years, we must not make that mistake again.

**–Francis S. Collins**

PHOTO: NIH

**Francis S. Collins** is the director of the National Institutes of Health, Bethesda, MD, USA. francis.collins@nih.gov

10.1126/science.abh3996

# NEWS

> “Neanderthals … are resilient, resourceful. I think Joe Biden needs to rethink what he is saying.”
>
> **U.S. Senator Marsha Blackburn (R–TN),** on *Fox Business*, after the president invoked the extinct hominins to criticize two Republican governors for rescinding mask requirements during the pandemic.

## IN BRIEF

*Edited by* **Jeffrey Brainard**

**DISPATCHES FROM THE PANDEMIC**

### A racial divide in COVID-19 vaccination

Black people make up a disproportionately small percentage of those vaccinated in every state that has broken out these data by race, the Kaiser Family Foundation reports. It says data gaps make comparing states difficult.

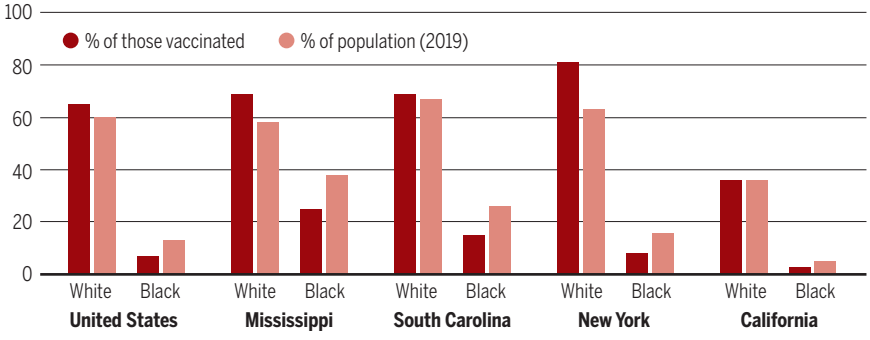


### U.S. support for shots grows

PUBLIC HEALTH | A large majority of Americans—now 69%—say they want to receive a COVID-19 vaccine or have gotten at least one dose, according to a Pew Research Center survey of 10,121 people released last week. Pew had reported that in November 2020, before vaccine became available, only 60% wanted it. The most growth came among Black people, 61% of whom wanted or had received the vaccine, up from 42%. The numbers challenge the idea that a disproportionate number of Black people are refusing a vaccine. Instead, other factors, such as work schedules and geography, may help explain stark differences in vaccination by race: In all 41 states that report such data, the percentage of Black people inoculated is less than their share of the overall population, the Kaiser Family Foundation said last week in a separate report (see chart, above). The Pew survey also found a large and growing partisan divide in attitudes—83% of those who lean Democratic want or have received the vaccine, versus 56% of Republicans.

### India’s home-grown vaccine works

INFECTIOUS DISEASES | A COVID-19 vaccine developed in India has an efficacy of 81%, its manufacturer, Bharat Biotech, reported on 3 March, based on the first interim analysis of a clinical trial in 25,800 volunteers. The result is expected to encourage Indians to receive the COVAXIN vaccine and may help plans to export it. India’s government drew criticism in January for authorizing the vaccine’s emergency use before a phase 3 study had produced results. The newly announced data have yet to be peer reviewed, but according to a press release from Bharat, the ongoing study has recorded 36 cases of mild, moderate, or severe cases of COVID-19 in volunteers who received a placebo and seven in those given COVAXIN. The two-dose vaccine uses an inactivated whole virus. India, which has recorded the fourth most deaths from the disease of any country, plans to vaccinate 300 million of its more than 1.3 billion people by August. Prime Minister Narendra Modi received the vaccine on 28 February.

### A push to sequence virus genomes

VIROLOGY | Immunologist Rick Bright, a former U.S. official removed by the Trump administration after he resisted an effort to prioritize an unproven COVID-19 treatment, was named this week to lead a new project by the Rockefeller Foundation to quickly ramp up surveillance of the pandemic coronavirus’ genome in the United States. The country is now sequencing the virus in fewer than 1% of patients reported infected, which makes it difficult to identify fast-spreading versions such as the B.1.1.7 variant that originated in the United Kingdom. In an 8 March action plan, Rockefeller calls for creating U.S. “sentinel sites” to detect variants and developing data standards and software tools. The plan is part of the foundation’s October 2020 commitment to spend $1 billion to develop a pandemic prevention system, which it says will require cooperation with the government, academe, and industry.

### Pandemic bill funds virus science

FUNDING | Congress and the White House this week are expected to finalize a $1.9 trillion pandemic relief spending bill that includes money for research. Efforts to sequence and track variants of the pandemic coronavirus will get $1.75 billion—a boost over the $200 million already allotted. The Fish and Wildlife Service will get $45 million to study and track wildlife diseases that could jump to humans and cause a future pandemic. To help mitigate COVID-19’s impact on research, the National Science Foundation receives $600 million; the National Institute of Standards and Technology, $150 million. Research about the pandemic’s effects on student achievement gets $100 million.

### Risk rises with countries’ obesity

BIOMEDICINE | Countries with higher rates of obesity have many more deaths from COVID-19, according to a 3 March report from the World Obesity Federation that is one of the first comprehensive studies of this risk factor’s toll. In countries where more than half the adult population is classified as overweight, the likelihood of death from COVID-19 is about 10 times higher than in countries where fewer than half of adults are overweight or obese. The report calls for prioritizing people who are overweight for testing and vaccination.

**SCIENCEMAG.ORG/TAGS/CORONAVIRUS**

Read *Science*’s online coverage of the pandemic.

CREDITS: (GRAPHIC) N. DESAI/*SCIENCE*; (DATA) KAISER FAMILY FOUNDATION

A large marsh restoration project would divert sediment from the Mississippi River (right) into Barataria Bay, to its left.

PHOTO: NASA EARTH OBSERVATORY

CONSERVATION

# Gulf marsh rebuild moves forward

An ambitious plan to rebuild part of Louisiana's coastline by diverting a portion of the Mississippi River has earned a pivotal endorsement from the U.S. Army Corps of Engineers. The Corps last week issued a draft environmental impact statement concluding the project would build as much as 7000 hectares of marshland in Barataria Bay, south of New Orleans, by filling it with gravel and mud now flushed into the Gulf of Mexico at the river's mouth. The project would punch a hole in a levee that now constricts the river, using enormous gates to control the flow of sediment-laden water into the bay. The Corps, which may give final approval next year, concluded the land-building benefits outweigh harms from resulting changes in salinity to oysters, brown shrimp, and dolphins in parts of the bay. The project is a linchpin of a 50-year, $50 billion initiative to reverse the demise of wetlands critical to protecting southern Louisiana from hurricanes and flooding. The initiative is among the world's largest and most costly ecological restoration projects.

## China pledges 5-year R&D push

FUNDING | China would increase R&D spending by 7% or more in each of the next 5 years under a new Five-Year Plan that the National People's Congress is expected to ratify this week. By one estimate, that pace could bring the spending to 2.8% of gross domestic product by 2025—a share almost that of the United States. The central government would increase spending on basic research by more than 10% this year. Details of China's 5-year plans, whose targets are often met, are fleshed out by ministries and agencies after adoption. But the plan disappointed environmentalists, who hoped it would provide more details on how the country will start to reduce greenhouse gas emissions by 2030 and reach carbon neutrality by 2060, goals set by President Xi Jinping in September 2020.

## NSF calls for Arecibo probe

ASTRONOMY | Outside experts should investigate the causes of cable breaks that led the Arecibo telescope in Puerto Rico to collapse, the U.S. National Science Foundation (NSF) said last week. Heavy instruments suspended high above the radio telescope crashed into the dish on 1 December 2020 following failures of support cables in August and November (*Science*, 15 January, p. 225). The University of Central Florida, which manages the facility, has hired engineers to investigate the causes, but NSF says it has also asked the National Academies of Sciences, Engineering, and Medicine to study what went wrong. Also last week, NSF estimated the cost of removing the debris at between $30 million and $50 million. Meanwhile, a draft plan for a successor, the Next Generation Arecibo Telescope, is gathering endorsements from researchers around the world. It would be nearly twice as sensitive as the original and provide a field of view 500 times larger. NSF says the scientific community must vet and prioritize any new telescope proposal before it would consider funding.

## Ireland pivots back to basics

FUNDING | Science Foundation Ireland, the nation's biggest science funder, is planning a major boost to its budget to support a renewed focus on fundamental research. For the past decade, the agency has spent most of its funding on industry-aligned research centers, a response to a recession that followed the 2008 financial crisis. The new strategy, published last week and the first since 2012, plans for 15% annual rises

BIOMEDICINE

## Psychedelics no better than placebos for mood boost

People who took tiny amounts of psychedelic substances in a study improved in psychological well-being—but so did participants who took placebos. Such trials have been tricky to pull off because psychedelics are tightly regulated and incorporating placebos is challenging. Researchers came up with a creative study design that relied on 246 volunteers to supply their own microdoses, typically less than 10% of the amount that causes a true psychedelic experience. They followed instructions for mixing up coded capsules containing psychedelics and placebos so that they were blinded to which they were ingesting, but the research team knew. The researchers tracked whether participants correctly guessed which was which. Overall, volunteers who thought they had taken psychedelics reported greater well-being and lower anxiety than those who thought they had taken a placebo, regardless of which they actually took, the researchers at Imperial College London reported last week in *eLife*. Follow-up studies are planned.

that will lift grant spending—most of the agency's budget—from €200 million in 2020 to €376 million by 2025. Annual principal investigator awards would more than double, to 140. The agency says the budget rises will help boost the nation's overall public and private R&D spending from a meager 1.1% of gross domestic product, well below the European average of 2.2%, to a goal of 2.5% by 2025. Research advocates applauded the move but said its success will require Ireland to also hike spending on higher education broadly.

## Nuclear test fallout tainted Tahiti

NUCLEAR SAFETY | Ninety percent of French Polynesia's population may have been exposed to fallout during above-ground tests of nuclear weapons that France conducted there from 1966 to 1974—10 times more than the French government had estimated—according to an independent analysis of declassified documents. Low but potentially dangerous doses rained down on many as 110,000 people, according to an investigation led by Sébastien Philippe, a physicist at Princeton University, and Tomas Statius of Disclose, a French investigative journalism nonprofit, which released the findings last week. Almost everyone living in the region at the time should be eligible for compensation under a 2010 French law if they develop certain cancers such as thyroid cancer, the authors suggest. Most of the exposures came from a single test in 1974, which released radiation that drifted directly over Tahiti, the most populous island in French Polynesia.

## Pacific hosts half-trillion corals

MARINE BIOLOGY | The Pacific Ocean contains more than 500 billion colonies of corals—on par with the number of birds in the world and trees in the Amazon, a study has estimated. The work, based on counts and satellite data in a 10,000-kilometer swath from Indonesia to French Polynesia, is the first such comprehensive look; previous studies have looked at a single species or coral populations in a small area. Corals have suffered tremendous damage from warming seas and other human-driven impacts. But the findings raise questions about existing conservation priorities: Eighty of 318 species identified in the study are listed as either vulnerable, endangered, or critically endangered by the International Union for Conservation of Nature. But 12 of those 80 have estimated populations exceeding 1 billion each, say the authors of the 1 March study in *Nature Ecology & Evolution*. They suggest rethinking the list, measuring populations carefully, and studying causes that can shrink even abundant species.

## Group elevates climate scientist

LEADERSHIP | The Nature Conservancy last week named Katharine Hayhoe of Texas Tech University, a specialist in climate change, as its chief scientist. The advocacy group, which specializes in buying land for conservation, said Hayhoe would help it apply climate science to its efforts to protect biodiversity. Hayhoe was a lead author of multiple U.S. National Climate Assessments, scientific syntheses that identify how climate change affects different U.S. regions and help policy planners and local governments prepare for future conditions. She is also known for drawing on her evangelical Christianity to persuade fellow believers that climate change is a serious problem society needs to address.

PHOTO: JAHI CHIKWENDIU/*THE WASHINGTON POST*/GETTY IMAGES

eppendorf & Science

# PRIZE FOR NEURO BIOLOGY

2020 Winner
Christopher Zimmerman, Ph.D.
Princeton Neuroscience Institute
For research on thirst and drinking behavior

**Application Deadline**
June 15, 2021

# Now It's Your Turn!

**Eppendorf & Science Prize for Neurobiology**
The annual Eppendorf & Science Prize for Neurobiology is an international prize which honors young scientists for their outstanding contributions to neurobiological research based on methods of molecular and cell biology. The winner and finalists are selected by a committee of independent scientists, chaired by *Science*'s Senior Editor, Dr. Peter Stern. If you are 35 years of age or younger and doing great research, now is the time to apply for this prize.

**As the Grand Prize Winner, you could be next to receive**
> Prize money of US$25,000
> Publication of your work in *Science*
> Full support to attend the Prize Ceremony held in conjunction with the Annual Meeting of the Society for Neuroscience in the USA
> 10-year AAAS membership and online subscription to *Science*
> Complimentary products worth US$1,000 from Eppendorf
> An invitation to visit Eppendorf in Hamburg, Germany

It's easy to apply! Write a 1,000-word essay and tell the world about your work. Learn more at:

eppendorf.com/prize

eppendorf Science AAAS

IN DEPTH

SCIENTIFIC COMMUNITY

# Coronavirus sequence trove sparks frustration

## Users of GISAID complain of opaque decisions and onerous restrictions

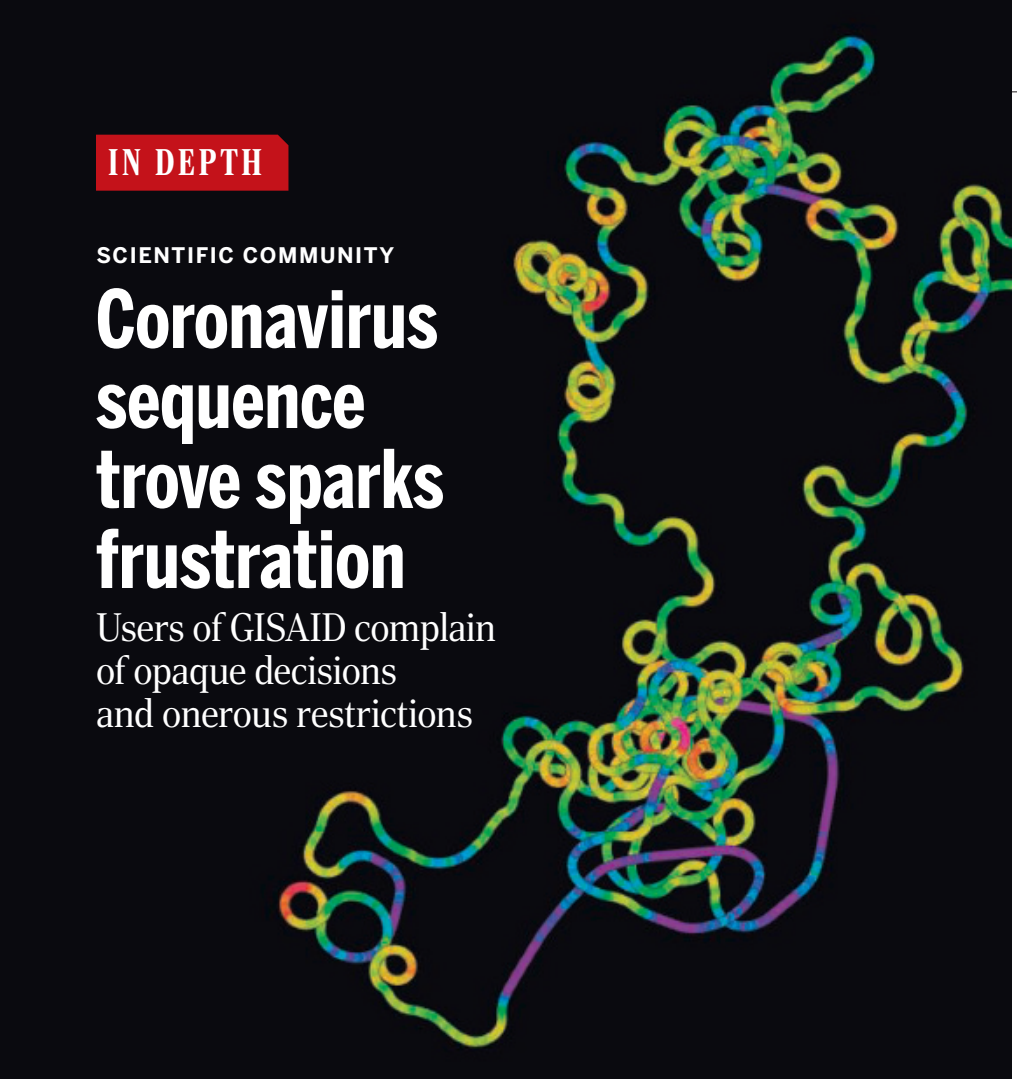

GISAID data can help scientists build visualizations such as this one of the coronavirus genome.

PHOTO: MARTIN KRZYWINSKI/SCIENCE SOURCE

*By* **Meredith Wadman**

In December 2020, software developer Angie Hinrichs at the University of California, Santa Cruz (UCSC), applied for access to a labor-saving data feed from GISAID, a nonprofit database of viral sequences including those of the pandemic coronavirus, SARS-CoV-2. She wanted GISAID's data so she could display mutations on UCSC's coronavirus Genome Browser. That tool ties any position in the virus' nearly 30,000-letter genome to other scientific information, much as Google Maps shows gas stations and restaurants near addresses.

With more than 700,000 genomes from more than 160 countries, GISAID is by far the world's largest database of SARS-CoV-2 sequences. Access to the free, nonprofit repository has become vital to Hinrichs and thousands of other scientists and public health agencies tracking the virus' alarmingly rapid evolution.

But instead of getting a direct data feed, Hinrichs lost her existing access to two conveniently packaged GISAID files that are the next best thing. She emailed GISAID repeatedly pleading for restored access, but hasn't gotten it. Since December, she has had to download GISAID's sequences 10,000 at a time, with no access to most of the metadata unless she looks at each of the 10,000 sequences individually. As a result, she says, "My [phylogenetic] trees that use GISAID data are falling behind."

Hinrichs's experience is not unique. A dozen scientists spoke with *Science* raising complaints about their interactions with GISAID. They reported an opaque process of gaining access, unexplained interruptions once access was won, and phone harangues or threatening legal letters when they got on the wrong side of GISAID's strict rules against resharing data. Many scientists who voiced criticisms declined to be identified for fear of losing GISAID access. They say that even as they race to study coronavirus evolution, they are walking on eggshells around their chief data supplier.

"I am so tired of being scared all the time, of being terrified that if I take a step wrong I will lose access to the data that I base my research on," says one scientist who declines to be identified. "[GISAID] has that sword hanging over any scientist that works on SARS-CoV-2."

In a statement, GISAID said, "Any individual who registers with GISAID and agrees to the GISAID terms of use will be granted access credentials. … On rare occasions, GISAID has found it necessary to temporarily suspend access credentials to protect the GISAID sharing mechanism."

Both fans and critics emphasize that GISAID has provided an invaluable service during the pandemic, gathering many more coronavirus sequences than open-access databases like the United States's GenBank (see graphic, p. 1087). Even critics note that data are much easier to upload to GISAID than to open-access repositories, and that GISAID speedily curates sequences.

"GISAID has done an amazing job. They really have revolutionized access to all these data," says David Haussler, a computational biologist at UCSC who is Hinrichs's boss. "We really, really want give them credit for what they have accomplished."

Many scientists trace what they view as a secretive, controlling organizational culture to GISAID's co-creator and head, former Time Warner studio executive Peter Bogner. GISAID "has a personality behind it that is fiercely protective of the organization [and] very insulted if somebody else … is praised for SARS-CoV-2 data," Hinrichs says.

Bogner has said he invested several million dollars to launch GISAID in 2008. Its goal was to open up access to then-restricted avian flu sequences, and to protect scientists in non-Western countries against having their data scooped for publication or profit by requiring users to credit and try to collaborate with depositors (*Science*, 25 August 2006, p. 1026 and 16 February 2007, p. 923).

GISAID, which stands for the Global Initiative on Sharing All Influenza Data, is today supported by private donors, governments, and nonprofits and is based in Germany; it says it remains "*independent* of government and corporate interests."

In its statement to *Science*, GISAID said scientists deposit to its database because they "are confident that their rights will be protected." Without GISAID, "We would now be in real trouble, because it's been successful in building confidence in SARS-CoV-2 genomic data sharing in countries around the world," says GISAID co-founder Nancy Cox, now retired from the U.S. Centers for Disease Control and Prevention.

*Science*'s COVID-19 reporting is supported by the Heising-Simons Foundation.

But critics complain about GISAID's constraints on access, chief among them its prohibition on resharing of its data. Its agreement for access to the direct data feed also requires applicants to use only GISAID data in their websites and tools, as well as only GISAID-approved strain names.

Other scientists say the access process itself is opaque. Brooks Miner, an evolutionary ecologist at Ithaca College, contacted GISAID on 2 February hoping to get a data feed for a lay-friendly website mapping the frequency of coronavirus variants. He got a phone call with instructions from a man who refused to identify himself except as "a GISAID representative" and whose identity he still does not know. "I started calling him Mr. GISAID," Miner says. (GISAID said it does not have a policy of not identifying its representatives.)

Puzzled, Miner contacted other GISAID users and found they lived in fear of losing access. "I realized people doing phenomenal cutting-edge science carry this fear that their career could be ruined on a whim by this faceless organization," Miner says.

Miner was granted GISAID access last week but says he fears losing it because of his criticisms. "I'm speaking out anyway because I believe the way GISAID operates is flawed," he says.

Other scientists say they have received threatening letters from GISAID lawyers. Early in the pandemic, Hinrichs pulled GISAID data from another organization, Nextstrain, and mistakenly failed to credit GISAID, prompting what she calls an "ominous" missive from a law firm directed to Haussler. "This was a new experience for us," Hinrichs says. "We are used to speaking with scientists, not hearing from lawyers." She added GISAID credits to the browser.

## Data dominance

By 4 March, GISAID had amassed nearly 700,000 sequences of the pandemic coronavirus from 160 countries—far more than any other database.

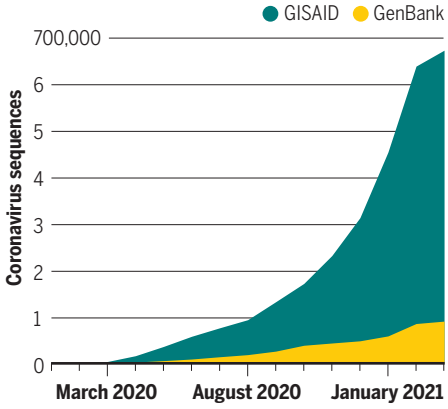


CREDITS: (GRAPHIC) K. FRANKLIN/*SCIENCE*; (DATA) GISAID; NATIONAL LIBRARY OF MEDICINE/GENBANK

In its statement, GISAID said, "GISAID has never found it necessary to commence a legal action against a participant. … We typically are able to come to a speedy and amicable resolution of any issues." GISAID says it has revoked access for only one user in the past year, because they "would not abide by GISAID's terms of use."

Some scientists say they have gotten phone calls lecturing them on the virtues of GISAID and the flaws of public-access databases. "GISAID sees every sequence submitted to GenBank as a battle lost," another scientist says.

Kelly Oakeson, chief sequencing scientist at the Utah Public Health Laboratory, which relies on GISAID data to track coronavirus variants in his state, recalls Bogner phoning him last year for a technical matter and then urging him not to deposit sequences in GenBank. He "really wanted to know … 'What possible good could come of that? You've got it in one place, why do you need it in both?'"

GISAID denies disparaging GenBank or discouraging users from depositing in it or other open-access databases.

In January, scientists pushed back in an open letter urging scientists to deposit sequences in GenBank, the European Nucleotide Archive (ENA), and Japan's DDBJ, open-access databases that allow users to access sequences anonymously and share data freely. "The ideal setup is completely open access," to speed research, says signatory Guy Cochrane, head of the ENA. "Having a limited group controlling [access] would never be a good thing."

GISAID countered in its statement that the letter "effectively calls for data to be shared anonymously and without any protection for the data contributors."

Some users say they have only had good experiences with GISAID. "I've gotten much more support from GISAID than from any government agency," says Jeremy Kamil, a virologist at Louisiana State University Health, Shreveport, and senior author on a recent preprint that identified seven new SARS-CoV-2 variants in the United States. He says he finds GISAID's global, 24/7 staff responsive and helpful.

But others see much room for improvement. They want a right of appeal if they lose GISAID access and a transparent view of how GISAID is governed. They would like to open a conversation about ways GISAID might relax its data-sharing requirements during the pandemic, without risking their access by raising the subject.

Miner would also like to see a less territorial approach: "Aren't we just trying to do good work that's helpful in the pandemic?" ■

COVID-19

# As vaccine surpluses loom, donation plans urged

## Rich countries have ordered billions of doses more than needed for their populations

*By* **Jon Cohen** *and* **Kai Kupferschmidt**

Last week, U.S. President Joe Biden shaved 2 months off earlier projections and promised COVID-19 vaccine doses would be available for all U.S. adults by the end of May. That's welcome news for the United States, which has had more COVID-19 cases and deaths than any other country. It could also be good news for nations that may benefit from the more than 1 billion extra doses the federal government has ordered.

Like three dozen other countries, the United States contracted with multiple vaccine companies for several times the number of doses needed to cover its population. No one knew at the time which, if any, of the candidate vaccines would work or when they might prove safe and effective. But by now, most of the prepurchased vaccines appear to offer solid protection—which means many countries will receive far more vaccine than they need. The excess doses the United States alone may have by July would vaccinate at least 200 million people. Over the next year or two, U.S. surplus doses and those from other countries could add up to enough to immunize everyone in the many poorer nations that lack any secured COVID-19 vaccine (see table, p. 1088).

No country yet has warehouses filled with unneeded COVID-19 vaccines—many hard-hit European nations may not have surpluses until the end of the year. But global health leaders stress that the time has come to figure out how to share those committed but extra doses. "It would be hugely beneficial to lay out a road map of 2021," says Jeremy Farrar, who heads the Wellcome Trust biomedical research charity. "Planning is critical."

Last summer, the World Health Organization (WHO) and other groups created the COVID-19 Vaccines Global Access (COVAX) Facility to address expected vaccine inequi-

ties, in part by soliciting money to buy doses for poorer countries. COVAX has raised $6.3 billion, but to date it has been at the back of the vaccine supply line. "You can't buy something that's already legally obliged to be allocated elsewhere," notes Lawrence Gostin, a global health law specialist at Georgetown University. By the end of May, COVAX plans to ship just 237 million doses of a COVID-19 vaccine developed by AstraZeneca and the University of Oxford.

The coming surpluses could provide a major boost to COVAX's supply, but transferring vaccine already committed to a particular country is challenging. "It's not as simple as just saying to COVAX, here are some doses," explains Nicole Lurie of the Coalition for Epidemic Preparedness Innovations, which helps WHO run COVAX. "There are a whole set of issues that one needs to work through with regulators, and indemnification and liability on the contracts between manufacturers and countries that say how the doses can be used."

## Vaccines to spare—and share

These 11 countries alone have enough COVID-19 vaccine doses secured or optioned to immunize about 2.9 billion people beyond their own populations.

| COUNTRY | POPULATION (MILLIONS) | POPULATION COVERAGE (%)* | EXTRA PEOPLE COVERED (MILLIONS) |
|---|---|---|---|
| Canada | 37 | 609 | 188 |
| United States | 329 | 553 | 1490 |
| Italy | 60 | 422 | 193 |
| United Kingdom | 68 | 421 | 218 |
| Germany | 84 | 394 | 247 |
| Poland | 38 | 364 | 100 |
| Spain | 47 | 364 | 124 |
| France | 65 | 364 | 172 |
| Australia | 25 | 345 | 61 |
| Mexico | 128 | 158 | 74 |
| Japan | 127 | 124 | 31 |

*Based on secured and optioned vaccines, some still unauthorized for use, and whether they require one or two doses

Lurie was a top U.S. government health official during the 2009 influenza pandemic and recalls that it took the United States months to donate flu vaccine. "There were a gazillion steps that nobody knew about, including my favorite, a fumigation certificate of a wood pallet to ship doses to the Philippines—that took an extra 2 weeks," she says.

The process can be vastly simplified if vaccine is donated before leaving the factory gate, says Gian Gandhi, COVAX coordinator at UNICEF. "We get into problems if it's a dose that's sitting in a central storage facility in Berlin or Paris or London," he says. Lurie would like the countries with the largest potential surpluses to hold a "tabletop exercise" soon to iron out donation details. "What's it going to take to do this?" she asks. "Let's not get caught off guard by fumigation certificates."

In December 2020, countries anticipating a vaccine surplus had begun to discuss donation plans with COVAX. But after variants of SARS-CoV-2 appeared that spread faster or evaded some immune responses, those conversations stopped, Gandhi says. Nations suddenly didn't know which of their secured vaccines would be most effective against the variants, he says. Additional booster shots might also be needed to extend immunity or fortify it against variants.

Politics has also held up donations. In many countries that have secured large vaccine supplies but are struggling to deliver the shots, politicians cannot openly discuss the topic, Farrar says. "Fierce vaccine nationalism" will prevail for several more months, Gostin says. "It becomes politically tenable to share a vaccine when we're at the point where vaccines are chasing the people rather than the people chasing the vaccine."

COVAX has chosen not to accept donations directed to specific populations or regions of the world. But China and India already have donated more than 12 million doses of COVID-19 vaccines to particular countries, in what many see as "vaccine diplomacy." It's a strategy the United States could employ through COVAX, according to Cornell University's Jason Rao, a biosecurity specialist who worked in former President Barack Obama's White House. Vaccine donations, he says, could "rebuild those diplomatic ties that we know have been unplugged from the last administration."

France has already pledged to share 5% of its secured vaccine, but it has only administered 5.8 million doses within its own country as of 7 March. Norway has also committed to donating doses in parallel with vaccinating citizens, but it would only have enough surplus to vaccinate 14 million people beyond its own 5.4 million people. WHO advocates that more countries donate doses now, in parallel with their own vaccination campaigns, in order to protect frontline health care workers elsewhere.

At a press conference last week, Soumya Swaminathan, chief scientist at WHO, stressed that for wealthy nations, vaccine equity is a matter of self-interest. Vaccinating the world will slow emergence and spread of mutants—and has financial benefits, too. "It's clear that unless everyone is protected around the world that global economic recovery cannot start," she says. ■

EARTH SCIENCE

# Ancient Earth was a water world

## Life and plate tectonics may have emerged on a planet drowned in water that was rejected by the mantle

*By* **Paul Voosen**

Across the ages, sea levels have risen and fallen with temperatures—but Earth's total surface water was always assumed to be constant. Now, evidence is mounting that some 3 billion to 4 billion years ago, the planet's oceans held nearly twice as much water—enough to submerge today's continents above the peak of Mount Everest. The flood could have primed the engine of plate tectonics and made it more difficult for life to start on land.

Rocks in today's mantle, the thick layer beneath the crust, are thought to sequester an ocean's worth of water or more in their mineral structures. But early in Earth's history, the mantle, warmed by radioactivity, was four times hotter. Now, experiments in hydraulic presses have shown that many minerals would not hold as much hydrogen and oxygen at those mantle temperatures. "That suggests the water must have been somewhere else," says Junjie Dong, a graduate student in mineral physics at Harvard University who led a model, based on those lab experiments, that was published this week in *AGU Advances*. "And the most likely reservoir is the surface."

The paper makes intuitive sense, says Michael Walter, an experimental petrologist at the Carnegie Institution for Science. "It's a simple idea that could have important implications."

Two mantle minerals store much of its water today: wadsleyite and ringwoodite, high-pressure variants of the volcanic mineral olivine. Rocks rich in them make up 7% of the planet's mass, and although only 2% of their weight is water today, "a little bit adds up to a lot," says Steven Jacobsen, an experimental mineralogist at Northwestern University.

CREDITS: (DATA) UNICEF; (IMAGE) ALEC BRENNER/HARVARD UNIVERSITY

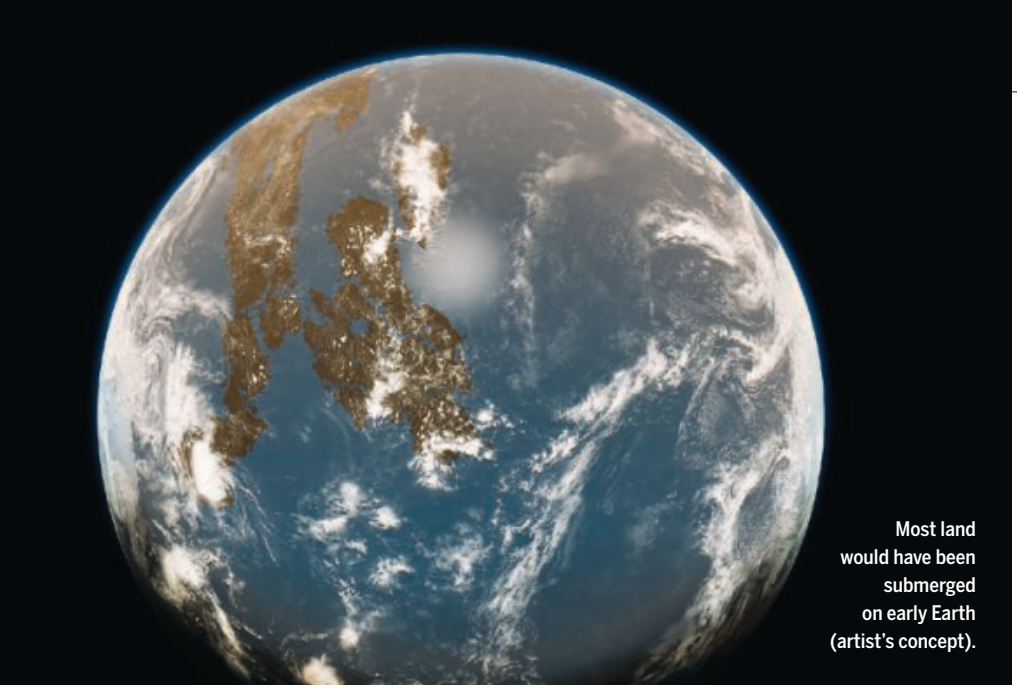

Most land would have been submerged on early Earth (artist's concept).

Jacobsen and others have created the minerals by squeezing rock powders to tens of thousands of atmospheres and heating them to 1600°C or more. Dong's team stitched together the results to show wadsleyite and ringwoodite hold fractionally less water at higher temperatures. Moreover, the team found that the minerals would be scarcer in the ancient, hotter mantle than today, further limiting their ability to store water.

The experiments aren't alone in suggesting a water-bound planet. "There's pretty clear geological evidence," too, says Benjamin Johnson, a geochemist at Iowa State University. Titanium concentrations in 4-billion-year-old zircon crystals from Western Australia suggest they formed underwater. And some of the oldest known rocks on Earth, 3-billion-year-old formations in Australia and Greenland, are pillow basalts, bulbous rocks that form as magma cools underwater.

Work by Johnson and Boswell Wing, a geobiologist at the University of Colorado, Boulder, offers more evidence. Samples from a 3.24-billion-year-old chunk of oceanic crust left on Australia's mainland were far richer in a heavy oxygen isotope than the present-day oceans. Water loses this heavy oxygen when rain reacts with continental rocks to form clays, so its abundance in the ancient ocean suggests the continents had barely emerged by that point, Johnson and Wing conclude in a 2020 *Nature Geoscience* study. The finding doesn't prove oceans were larger, Johnson says, but, "It is easier to have submerged continents if the oceans are bigger."

Although the larger ocean would have made it harder for the continents to stick their necks out, it could explain why they appear to have been on the move early in Earth's history, says Rebecca Fischer, an experimental petrologist at Harvard and coauthor on the *AGU Advances* study. Larger oceans could have helped kick off plate tectonics as water penetrated fractures and weakened the crust, creating subduction zones where one slab of crust slipped below another. And once a subducting slab began its dive, the dryer, inherently stronger mantle would have helped bend the slab, ensuring its plunge would continue, says Jun Korenaga, a geophysicist at Yale University. "If you cannot bend plates, you cannot have plate tectonics."

The evidence for larger oceans challenges scenarios for how life began on Earth, says Thomas Carell, a biochemist at Ludwig Maximilian University of Munich. Some researchers believe it began at nutrient-rich hydrothermal vents in the ocean, whereas others favor shallow ponds on dry land, which would have frequently evaporated, creating a concentrated bath of chemicals.

A larger ocean exacerbates a problem with the underwater scenario: The ocean itself might have diluted any nascent biomolecules to insignificance. But by drowning most land, it also complicates the shallow pond scenario. Carell, a pond advocate, says in light of the new paper, he is now considering a different birthplace for life: sheltered, watery pockets within oceanic rocks that broke the surface in volcanic seamounts. "Maybe we had little caves in which it all happened," he says.

The ancient water world is also a reminder of how conditional Earth's evolution is. The planet was likely parched until water-rich asteroids bombarded it shortly after its birth. If the asteroids had deposited twice as much water, or if the present-day mantle had less appetite for water, then the continents, so essential for the planet's life and climate, would never have emerged. "It's a very delicate system, the Earth," Dong says. "Too much water, or too little, and it wouldn't work." ■

GRAVITATIONAL WAVES

# Giant detectors could hear murmurs from across universe

## Rival designs pit Yankee brawn versus continental sophistication

*By* **Adrian Cho**

Just 5 years ago, physicists opened a new window on the universe when they first detected gravitational waves, ripples in space itself set off when massive black holes or neutron stars collide. Even as discoveries pour in, researchers are already planning bigger, more sensitive detectors. And a Ford versus Ferrari kind of rivalry has emerged, with scientists in the United States simply proposing bigger detectors, and researchers in Europe pursuing a more radical design.

"Right now, we're only catching the rarest, loudest events, but there's a whole lot more, murmuring through the universe," says Jocelyn Read, an astrophysicist at California State University, Fullerton, who's working on the U.S. effort. Physicists hope to have the new detectors running in the 2030s, which means they have to start planning now, says David Reitze, a physicist at the California Institute of Technology (Caltech). "Gravitational wave discoveries have captivated the world, so now is a great time to be thinking about what comes next."

Current detectors are all L-shaped instruments called interferometers (see diagram, p. 1090). Laser light bounces between mirrors suspended at either end of each arm, and some of it leaks through to meet at the crook of the L. There, the light interferes in a way that depends on the arms' relative lengths. By monitoring that interference, physicists can spot a passing gravitational wave, which will generally make the lengths of the arms waver by different amounts.

To tamp down other vibrations, the interferometer must be housed in a vacuum chamber and the weighty mirrors hung from sophisticated suspension systems. And to detect the tiny stretching of space, the interferometer arms must be long. In the Laser Interferometer Gravitational-Wave

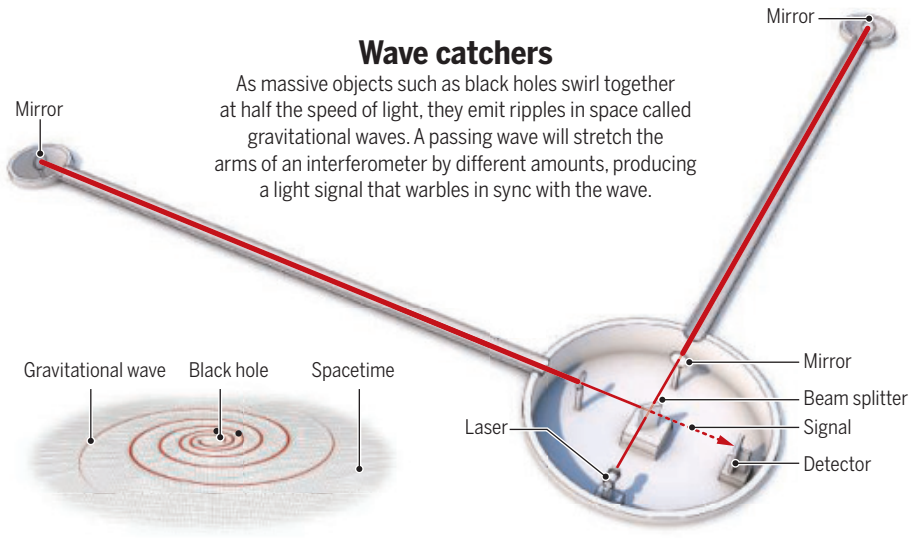


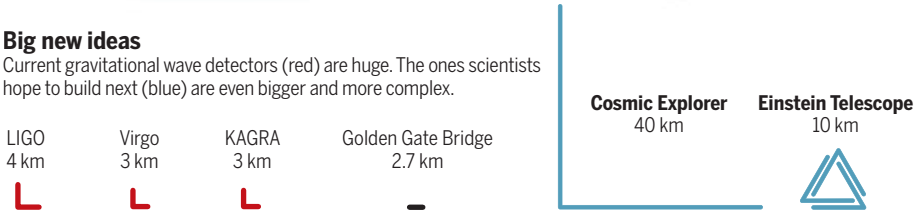


Observatory (LIGO), twin instruments in Louisiana and Washington state that spotted the first gravitational wave from two black holes whirling into each other, the arms are 4 kilometers long. Europe's Virgo detector in Italy has 3-kilometer-long arms. In spite of the detectors' sizes, a gravitational wave changes the relative lengths of their arms by less than the width of a proton.

The dozens of black hole mergers that LIGO and Virgo have spotted have shown that stellar-mass black holes, created when massive stars collapse to points, are more varied in mass than theorists expected (*Science*, 6 November 2020, p. 648). In 2017, LIGO and Virgo delivered another revelation, detecting two neutron stars spiraling together and alerting astronomers to the merger's location on the sky. Within hours telescopes of all types had studied the aftermath of the resulting "kilonova," observing how the explosion forged copious heavy elements (*Science*, 20 October 2017, p. 282).

Researchers now want a detector 10 times more sensitive, which they say would have mind-boggling potential. It could spot all black hole mergers within the observable universe and even peer back to the time before the first stars to search for primordial black holes that formed in the big bang. It should also spot hundreds of kilonovae, laying bare the nature of the ultra-dense matter in neutron stars.

The U.S. vision for such a dream machine is simple. "We're just going to make it really, really big," says Read, who is helping design Cosmic Explorer, an interferometer with arms 40 kilometers long—essentially, a LIGO detector scaled up 10-fold. The "cookie cutter design" might enable the United States to afford multiple, widely separated detectors, which would help pinpoint sources on the sky as LIGO and Virgo do now, says Barry Barish, a physicist at Caltech who directed the construction of LIGO.

Siting such mammoth wave catchers may be tricky. The 40-kilometer arms have to be straight, but Earth is round. If the crook of the L sits on the ground, then the ends of the interferometers might have to rest on berms 30 meters high. So U.S. researchers hope to find bowl-like areas that might accommodate the structure more naturally.

In contrast, European physicists envision a single subterranean gravitational wave observatory, called the Einstein Telescope (ET), that would do it all. "We want to realize an infrastructure that is able to host all the evolutions [of detectors] for 50 years," says Michele Punturo, a physicist with Italy's National Institute for Nuclear Physics in Perugia and cochair of the ET steering committee.

The ET would comprise multiple V-shaped interferometers with arms 10 kilometers long, arranged in an equilateral triangle deep underground to help shield out vibrations. With interferometers pointed in three directions, the ET could determine the polarization of gravitational waves—the direction in which they stretch space—to help locate sources on the sky and probe the fundamental nature of the waves.

The tunnels would actually house two sets of interferometers. The signals detected by LIGO and Virgo hum at frequencies that range from about 10 to 2000 cycles per second and rise as a pair of objects spirals together. But picking up lower frequencies of just a few cycles per second would open new realms. To detect them, a second interferometer that uses a lower power laser and mirrors cooled to near absolute zero would nestle in each corner of the ET. (Such mirrors are already in use at Japan's Kamioka Gravitational Wave Detector (KAGRA) which has 3-kilometer arms and is striving to catch up with LIGO and Virgo.)

By going to lower frequencies, the ET could detect the merger of black holes hundreds of times as massive as the Sun. It could also catch neutron-star pairs hours before they actually merge, giving astronomers advance warning of kilonova explosions, says Marica Branchesi, an astronomer at Italy's Gran Sasso Science Institute. "The early emission [of light] is extremely important, because there is a lot of physics there," she says.

The ET should cost €1.7 billion, including €900 million for the tunneling and basic infrastructure, Punturo says. Researchers are considering two sites, one near where Belgium, Germany, and the Netherlands meet and another on the island of Sardinia. The plan is under review by the European Strategy Forum on Research Infrastructures, which could put the ET on its to-do list this summer. "This is an important political step," Punturo says, but not final approval for construction.

The U.S. proposal is less mature. Researchers want the National Science Foundation to provide $65 million for design work so a decision on the billion-dollar machine can be made in the mid-2020s, Barish says. Physicists hope to have both Cosmic Explorer and the ET running in the mid-2030s, at the same time as the planned Laser Interferometer Space Antenna, a constellation of three spacecraft millions of kilometers apart that will sense gravitational waves of far lower frequencies from supermassive black holes in the centers of galaxies.

The push for new gravitational wave detectors isn't necessarily a competition. "What we really want is to have ET and Cosmic Explorer and, ideally, even a third detector of similar sensitivity," says Stefan Hild, a physicist at Maastricht University who works on the ET. Reitze notes, however, that timing and cost could "push towards convergence and simplicity in designs." Instead of a Ford and a Ferrari, perhaps physicists will end up building a few Audis. ■

GRAPHIC: C. BICKEL/*SCIENCE*

FUSION

# Magnet tests kick off bid for net fusion energy

## High-temperature superconductors are key to companies' planned compact reactors

*By* **Daniel Clery**

A startup chasing the dream of plentiful, safe, carbon-free electricity from fusion, the energy source of the Sun, has settled on a site for its compact reactor. Flush with more than $200 million from investors, including Bill Gates's Breakthrough Energy, 3-year-old Commonwealth Fusion Systems announced last week that later this year it will start to build its first test reactor, dubbed SPARC, in Devens, Massachusetts. The company says the reactor, which would be the first in the world to produce more energy than is needed to run the reaction, could fire up as soon as 2025.

Commonwealth and a rival U.K. company have also chosen the technology they think will let them leap ahead of the giant, publicly funded ITER reactor under construction in France and a U.S. pilot plant being considered by the Department of Energy: small but powerful magnets, made from high-temperature superconductors. Commonwealth is assembling its first nearly full-scale magnet and hopes to test it in June. "It's a big deal," CEO Bob Mumgaard says. "It's beyond what everyone else aspires to."

Fusion reactors burn an ionized gas of hydrogen isotopes at more than 100 million degrees Celsius—so hot that the plasma must be contained by a mesh of magnetic fields to keep it from melting the reactor walls. At ITER, sufficiently powerful fields are achieved with magnetic coils made of niobium alloy superconducting wires that can carry huge currents without resistance. But such superconductors must be chilled to 4° above absolute zero, which requires bulky and expensive liquid helium cooling. And there's a limit to the amount of current niobium wires can carry, forcing ITER to adopt large magnets with many wire turns. ITER's largest magnets are 24 meters across, adding to its $20 billion price tag.

Newer high-temperature superconductors—so called because some can superconduct at relatively balmy liquid nitrogen temperatures above 77 K—were not around when ITER was designed. They can carry much more current, tantalizing fusion designers with the prospect of smaller, cheaper reactors. Yet they are brittle, persnickety materials, so "a lot of people had given up on them," says Rod Bateman of Tokamak Energy, the U.K. startup that is also betting on the technology. "They were just too unreliable."

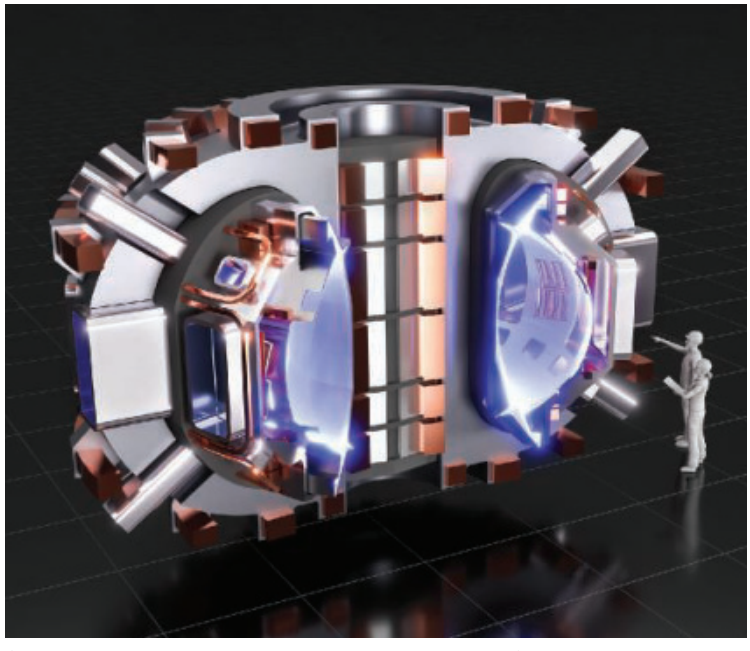

Commonwealth's compact reactor aims to produce net energy 10 years before ITER.

IMAGE: CFS/MIT, T. HENDERSON

In the past decade, researchers have developed ways to deposit thin layers of superconducting rare-earth barium copper oxide (ReBCO) on metal tape. The tapes can be manufactured reliably in long lengths, and perform best at about 10 K. But in terms of low-temperature engineering, "10 K is a lot easier than 4 K," says magnet engineer John Smith of General Atomics in San Diego.

The ReBCO tapes can be bent but, being flat, are challenging to wind into coils, Mumgaard says. "You have to stop treating it like a wire and asking it to do the things that wire does." Commonwealth has developed a cable with stacked layers of tape twisting like candy cane stripes. Tokamak Energy takes a simpler, more compact approach: winding coils with the tape flat, one layer on top of another like a roll of Scotch tape. "It makes winding so much simpler," Bateman says.

Another challenge for both companies is supply. Together, manufacturers of ReBCO tape were only producing a few hundred kilometers per year, and Commonwealth needs 500 kilometers just to build its first test magnet. "Manufacturers are scaling up like crazy now," Bateman says. "Fusion is the market high-temperature superconductors have been waiting for."

The next few months are critical for the two companies. Following years of modeling and experiments, they are both constructing test magnets to demonstrate 20-tesla fields—1.5 times stronger than ITER's—in coils just a few meters across. Commonwealth is winding a single 2.5-meter-tall, D-shaped magnet, slightly smaller than what's planned for SPARC. Still, Mumgaard says, when completed in June it will be the largest high-temperature superconducting magnet ever built.

Tokamak Energy is planning to test a full set of 16 coils, sized for a test reactor about 1 meter across. Bateman says the company will start to wind its magnets in the next few weeks and hopes to test them by the end of the year. If successful, the company plans to embark on building a demo reactor, ST-F1, in 2027.

Smith says successful demonstrations of the coils will be "a phenomenal statement on the technology." But Hartmut Zohm, of the Max Planck Institute for Plasma Physics, says Commonwealth's goal of operating in 2025 is overly ambitious. Simultaneously developing a technology, building a reactor, and satisfying regulators about using radioactive fusion fuel will take more than 4 years, he says. "This will take more time," he says. "But I'm happy to be proven wrong." ■

# A CALL TO ARMS

## Researchers are testing an arsenal of weapons against the pandemic coronavirus

By **Robert F. Service**

In March 2020, as the scope of the COVID-19 pandemic was coming into view, Jen Nwankwo and colleagues turned a pair of artificial intelligence (AI) tools against SARS-CoV-2. One newly developed AI program, called SUEDE, digitally screens all known druglike compounds for likely activity against biomolecules thought to be involved in disease. The other, BAGEL, predicts how to build inhibitors to known targets. The two programs searched for compounds able to block human enzymes that play essential roles in enabling the virus to infect our cells.

While SUEDE sifted through 14 billion compounds in just hours and spit out a hit, BAGEL made equally fast work of designing a lead. Nwankwo, CEO of a Massachusetts biotech startup called 1910 Genetics, asked a chemical company partner to synthesize the compounds. A week or so later, her team received the orders, added each compound in turn to human cells, and learned that each blocked its target and prevented viral entry into cells. 1910 Genetics is now looking to partner with antiviral drug developers to pursue animal and human trials. "It shows that AI can massively accelerate drug design," Nwankwo says.

ILLUSTRATION: STEPHAN SCHMITZ/FOLIO ART

Designing and developing a medicine is almost always painfully slow, regularly taking at least a decade. Many steps—such as animal studies, tweaking molecules to avoid side effects, and clinical trials—can't be accelerated. But the race toward new treatments against COVID-19 is off to a blistering start as researchers accelerate other parts of the search, deploying supercomputers, robots, synchrotrons, and every other tool they have to find and lab test possible medicines at speed. According to a biotech industry drug tracker, some 239 antiviral molecules against COVID-19 are under development, targeting multiple parts of the viral life cycle.

Antivirals have proved critical in fighting other infections such as HIV and hepatitis C. Such drugs will be vital in the struggle against the pandemic coronavirus, too, despite the ongoing rollout of COVID-19 vaccines. "We know not everyone will be able to take the vaccine or respond to it," says Mark Denison, a virologist at Vanderbilt University. Vaccines may also lose effectiveness as immune protection wanes or viral variants emerge. "So, continuing development of antivirals is critical," Denison says.

To date, most of that search has centered on "repurposed" compounds, antivirals originally developed to combat other diseases. (Other repurposed drugs, such as the steroid dexamethasone, target the body's reaction to infection rather than the virus itself.) "Drug repurposing made sense as the first thing to try," Nwankwo says. Many repurposed antivirals have shown promise against SARS-CoV-2 in cell and animal studies and are now in clinical trials. One, remdesivir, has already proved to speed recovery by a few days in very ill people. But several other repurposed antivirals have failed to prove effective.

*Science*'s COVID-19 reporting is supported by the Heising-Simons Foundation.

As a result, says Francis Collins, director of the National Institutes of Health (NIH), "We really, really need a bunch more [antivirals]." Buoyed by almost daily advances in understanding SARS-CoV-2, the rapidly growing list of new compounds that might block it, and ongoing clinical trials—some of them late stage—Denison and others hope to deliver effective drugs this year. Says Andrew Mesecar, a structural biologist from Purdue University: "I am confident we will have more treatments for coronavirus."

**AS VIRUSES GO**, SARS-CoV-2 is a behemoth, with some 30,000 letters of RNA in its genetic code. Those letters encode 29 viral proteins that enable the virus to infect cells, reproduce, escape, and spread. "We're fortunate this virus has provided us with so many targets, so many opportunities for intervention," says Sandra Weller, a molecular biologist at UConn Health.

The 29 proteins come in three main categories: structural proteins that make up the outer coat; nonstructural proteins (NSPs), most of which help the virus replicate; and accessory proteins, several of which appear to subdue the host's immune response. Thus far, drug hunters have taken aim mainly at the structural and replication proteins, concentrating on molecules similar to those that have paid off in fighting other viruses.

SARS-CoV-2 has just four structural proteins. The envelope and membrane proteins make up the virus' spherical shell, and the nucleocapsid protein shields its genome. The fourth protein, spike, protrudes from the shell, creating the crown of thorns that gives the virus its name and enables it to bind to angiotensin-converting enzyme 2 (ACE2) receptors, its main entry point into cells.

Spike is the primary target of many vaccines and antivirals. However, small molecules, the typical focus for drug discovery programs, won't work because they aren't bulky enough to prevent spike from binding to the ACE2 receptor.

David Baker, a computational biologist at the University of Washington, Seattle, and colleagues turned instead to miniproteins, each with about 60 amino acids, customized to block protein-protein interactions. In late 2020, Baker's team described miniproteins tailormade to bind tightly to the virus' spike protein and block it from attaching to the ACE2 receptor (*Science*, 23 October 2020, p. 426). The tiny proteins kept the virus from infecting human cells in a test tube, and Baker says miniproteins could make ideal drugs because they are far more stable than conventional protein therapeutics, such as antibodies, which must be refrigerated. Baker is in discussions with drug companies to pursue his leads.

Other researchers have a different strategy for interfering with viral binding. They are designing ACE2 look-alikes to serve as decoys, drawing SARS-CoV-2 away from cells. Researchers at Neoleukin Therapeutics and their partners, for example, reported creating a miniprotein, CTC-445.2d, that mimics ACE2, binding tenaciously to spike (*Science*, 4 December 2020, p. 1208). The compound protected human cells from infection in vitro. When given to hamsters in a nasal spray, the decoy also prevented them from getting severe disease after they received a normally lethal dose of the virus. Another "receptor trap" molecule, described in November 2020 in the *Proceedings of the National Academy of Sciences*, also diverted SARS-CoV-2, keeping it from infecting cells in the test tube.

**AFTER ENTERING A CELL**, a virus transforms its host into a virus factory. That's where SARS-CoV-2's NSPs come in. The viral proteins are made by the host cell's own protein factories, the ribosomes, which translate the viral RNA into two long "polyprotein" chains. The chains spin off two smaller proteins, NSP3 and NSP5, protein-cutting protease enzymes that then chop up the rest of the polyproteins into independent, functioning proteins.

"These are absolutely critical functions that are highly conserved and should be very, very vulnerable" to antivirals, Denison says.

Drugs that block proteases have successfully fought HIV and hepatitis C and have been among the most popular candidate antivirals for SARS-CoV-2. Two repurposed protease inhibitors for treating HIV, lopinavir and ritonavir, showed promise in vitro against SARS-CoV-2, but in October 2020, the United Kingdom's large Recovery clinical trial reported they offered no benefit.

Researchers at the drug giant Pfizer are pursuing an inhibitor that may work better

because it is designed to target NSP5, a protease that is specific to SARS-CoV-2 and its coronavirus relatives. Pfizer scientists developed the drug in 2003 to block the molecule, also known as main protease (Mpro), in severe acute respiratory syndrome (SARS), the deadly coronavirus that emerged the previous year. That work was set aside when the SARS epidemic died out. Now, Pfizer has pulled the compound off the shelf and found that it stops SARS-CoV-2 from reproducing inside human cells. Pfizer researchers tweaked the structure to make a more soluble version, known as PF-07304814. They showed that it sharply reduced viral load in mice; in other animals, high concentrations of the drug could reach tissues.

"It's a promising lead," says Celia Schiffer, a molecular biologist with the University of Massachusetts Medical School. In September 2020, Pfizer launched a small clinical trial to test the safety of PF-07304814, delivered intravenously. But Annaliesa Anderson, who leads Pfizer's antiviral program, says recruiting volunteers has been difficult. "Patients are either very sick, and it might be too late [to inhibit viral replication], or they might not feel that bad," making an intravenous therapy less appealing. Given the slow recruitment, she expects results toward the end of this year.

Other researchers are also working on Mpro inhibitors. In *Nature Communications* in September 2020, researchers in China reported on two repurposed drugs, boceprevir and GC376. Boceprevir is a hepatitis C drug, whereas GC376 was designed to target a feline coronavirus. Both compounds slowed SARS-CoV-2 replication in cells. On 5 February, U.S. researchers reported in a bioRxiv preprint that most mice given GC376 after receiving a lethal dose of the pandemic virus survived. And in August 2020 in *Science Translational Medicine*, U.S. researchers described a GC376 analog that dramatically boosted survival rates in mice infected with Middle East respiratory syndrome and showed potent antiviral effects against SARS-CoV-2 in cells.

Other molecules designed specifically to inhibit SARS-CoV-2's Mpro remain at an earlier testing stage. In November 2020, for example, Charlotte Lanteri, a research microbiologist at the Walter Reed Army Institute of Research, reported discovering 807 Mpro inhibitors through an AI screen of 41 million compounds. Her team has identified seven as particularly promising, but turning one or more of those into drugs remains at least a couple of years away, says Lanteri, who reported the findings at an antiviral drug summit at NIH. She and colleagues are also looking for antiviral drugs effective against all coronaviruses. "We want to be prepared as much as possible for the next emerging threat," she says.

## Antivirals take aim

As it infects cells, reproduces itself, and spreads, the pandemic coronavirus relies on dozens of viral and host proteins. They offer an array of targets for candidate drugs (blue boxes) that aim to block proteins key to different stages in SARS-CoV-2's life cycle.

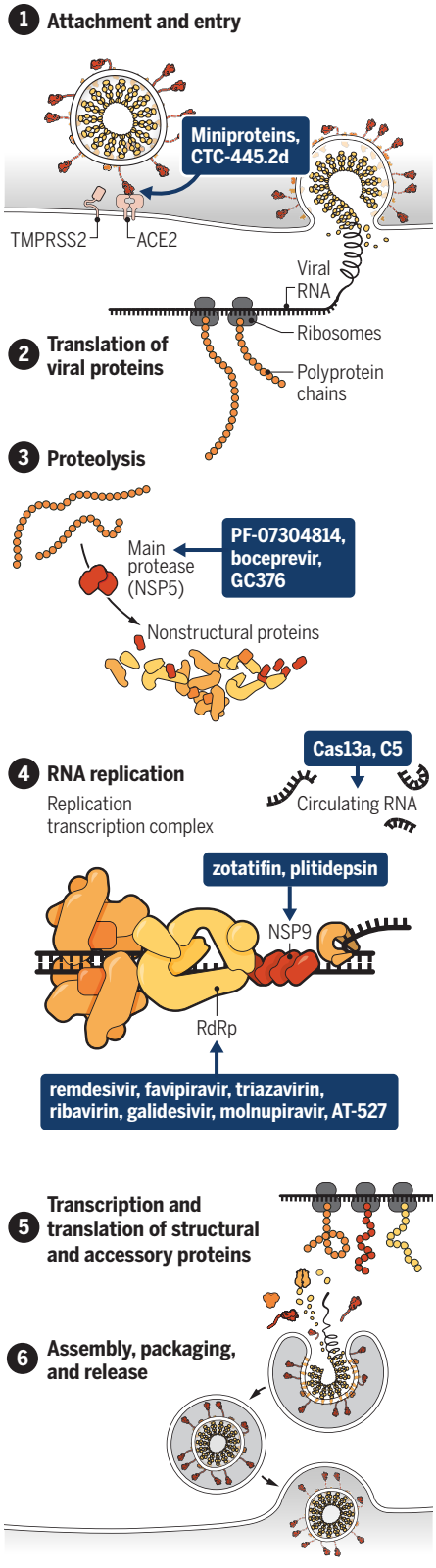


GRAPHIC: V. ALTOUNIAN/*SCIENCE*

**AFTER SARS-COV-2'S** proteases have freed coronavirus proteins from the original chains, 15 of them come together to form the replication transcription complex (RTC), which copies the virus' RNA genome to make new viruses (see graphic, left). Central to that machinery are NSP9, which locks onto the virus' RNA strand, and the RNA-dependent RNA polymerase (RdRp) that copies the RNA.

The RTC's critical role has made it, and RdRp in particular, the most popular treatment bull's-eye of all. It's where remdesivir does its work. The drug is a nucleoside analog, a sort of imitation RNA building block that resembles adenosine (A), one of the four letters that make up RNA. The imposter tricks the RdRp into inserting remdesivir molecules instead of A's into growing RNA strands, jamming RdRp and stopping viral replication.

Researchers hope other repurposed nucleoside and nucleotide analogs will be better at fooling the coronavirus' RdRp. (Nucleotides are nucleosides with one or more phosphate groups added.) The candidates include favipiravir and triazavirin, both originally designed to combat flu viruses; ribavirin, a treatment for respiratory syncytial virus and hepatitis C; and galidesivir, which can block replication of Ebola, Zika, and yellow fever viruses.

Researchers are guardedly optimistic about molnupiravir, a nucleoside analog that can be taken as a pill and was originally developed to combat influenza. Last year, concerns swirled around the drug after a whistleblower alleged that political cronyism led to expedited federal backing for it (*Science*, 13 May 2020). But positive results have kept progress on track.

Early work showed molnupiravir inserts itself into RNA in place of the nucleoside cytidine, prompting errors in the copying process and causing a lethal buildup of mutations in the virus. That mechanism has raised worries that the drug might cause similar mutations in host cells. But Richard Plemper, a cell biologist at Georgia State University, says such problems have not been seen in animal studies.

In April 2020 in *Science Translational Medicine*, Denison and colleagues reported that in mice, molnupiravir sharply reduced replication of multiple coronaviruses, including SARS-CoV-2; the drug also cut SARS-CoV-2 replication in human airway epithelial cells. A *Nature* paper added to the encouraging data in February, showing the compound decreased viral replication 100,000-fold in mice engineered to have human lung tissue.

In December 2020, Plemper and colleagues reported in *Nature Microbiology* that molnupiravir might do more than just prevent symptoms. The researchers gave the drug to ferrets, which readily spread the coronavirus,

and transmission fell to zero within 24 hours. "This is the first demonstration of an orally available drug to rapidly block SARS-CoV-2 transmission," Plemper says. That's crucial to slowing the spread of disease. Because it is a pill, molnupiravir can be given early in the disease cycle, just when SARS-CoV-2 replication typically peaks, in contrast to injectable drugs such as remdesivir. "We want to start treatment early and prevent people from ever showing up in a hospital," Plemper says.

The same month, a medRxiv preprint reported that a small safety trial showed the drug was well tolerated, with no serious side effects in healthy volunteers. Molnupiravir is now in phase 2/3 clinical trials run by Merck and Ridgeback Biotherapeutics; in March, scientists reported at a meeting that molnupiravir reduced patients' viral levels.

AT-527, another oral nucleoside analog developed to treat hepatitis C by Atea Pharmaceuticals and Roche, is also in a phase 2 clinical trial against COVID-19.

Pharmaceutical researchers use high-speed robotics and other tools to speed the search for antivirals.

Scientists are trying to shut down other RTC proteins, too. In recent results, two compounds—zotatifin and plitidepsin—appear to block viral replication by interfering with NSP9, the RNA-grabbing enzyme. Plitidepsin is in a phase 2/3 trial by the Spanish drug company PharmaMar. At least three other NSPs are considered good targets, says Tomáš Cihlář, a virologist with Gilead Sciences, maker of remdesivir.

Eventually, drugs could target the coronavirus' RNA, not just its proteins. In *Nature Biotechnology* in February, Emmeline Blanchard, a biomedical engineer at the Georgia Institute of Technology, and colleagues reported creating a polymer-encased formulation of a gene-editing enzyme called Cas13a that seeks out and chops up snippets of SARS-CoV-2 RNA. The team's Cas13a enzyme targets highly conserved regions of two viral genes encoding the RdRp enzyme and the nucleocapsid protein. When hamsters infected with SARS-CoV-2 inhaled a vaporized formulation of the drug, it reduced viral replication and disease symptoms.

And in September 2020 in *ACS Central Science*, Matthew Disney, a chemist at the Scripps Research Institute, and colleagues reported discovering a compound called C5 that blocks a short, hairpin-shaped segment of RNA involved in SARS-CoV-2 replication. "We have other segments of the viral genome we think we can target as well," he says.

**BECAUSE SARS-COV-2** relies on a host cell's proteins to reproduce, disrupting those proteins could be another avenue to treatments—with the advantage that not targeting the virus directly could lower its odds of becoming resistant to the drugs. Their targets include host cell proteases TMPRSS2 and furin, which the candidate drugs from Nwankwo's team block. Last month, NIH announced it was launching a phase 2/3 trial for camostat mesilate, another TMPRSS2 inhibitor.

Another target is a protein called dihydroorotate dehydrogenase (DHODH). It's the linchpin in a pathway that cells use to make two of RNA's four bases when they need extra RNA—for example, when proliferating. Viruses hijack that pathway to replicate. In cell studies, blocking DHODH has halted cancer and viral diseases, such as influenza and cytomegalovirus. And DHODH blockers have thus far proved safe when tested in hundreds of patients.

Two biotech companies, PTC Therapeutics and Immunic Therapeutics, are trying the same strategy against SARS-CoV-2. Rapidly reproducing viruses "have a great need for RNA," says Marla Weetall, vice president of pharmacology with PTC Therapeutics. The company's compound, PTC299, was originally designed as an oral drug to halt cell proliferation in acute myeloid leukemia. In an August 2020 preprint on bioRxiv, Weetall and colleagues reported that PTC299 sharply inhibited SARS-CoV-2 replication in cells. The compound also blocked the production of immune molecules that cells build using RNA bases, hinting that PTC299 might help tame the immune overreaction seen in severe COVID-19.

Daniel Vitt, CEO of Immunic Therapeutics, says his company has also seen promising results in human trials of its oral compound, IMU-838, developed to treat inflammatory and autoimmune diseases. In February, the company reported preliminary results suggesting hospitalized patients on the drug had less need for ventilators. Trials continue for both companies.

**ULTIMATELY**, no one compound is likely to deliver a knockout punch to the pandemic coronavirus, in part because drug-resistant viruses are likely to emerge. Collins and others argue that the best strategy takes a page from the treatment for HIV and hepatitis C: mixing and matching antivirals aimed at several proteins, making it harder for the virus to evolve multiple workarounds at once. "We really need an arsenal," says Lillian Chiang, CEO of Evrys Bio, which is working on antivirals against host-cell proteins.

"This is going to take time," says Michael Sofia, a chief scientific officer with Arbutus Biopharma, a Canadian antiviral company. And money. According to recent estimates, bringing a new drug to market costs between $985 million and $2.8 billion. Anderson says Pfizer, for one, is committing company resources to defeating the pandemic without expectation of profit. Other companies say the same. But during previous lulls in infectious disease outbreaks, many drug companies abandoned work on antivirals. "As soon as this stops being a hot area, people will move on," Nwankwo says.

In another disincentive, antiviral treatments for SARS-CoV-2 might be given for only a week or two, giving drugmakers a narrow window to reap returns. As a result, Denison and others argue that more government support is needed to keep stocking the antiviral arsenal. Any lull in the battle against SARS-CoV-2 and its kin is likely to be temporary, they say.

"We are going to have another coronavirus," Mesecar says. "We just don't know what it will look like." ■

PHOTO: SCRIPPS RESEARCH



CLIMATE CHANGE

# Who is stirring the waters?

## Emerging pathways could improve attribution of changes in river flow across the globe

By **Julia Hall**[1] *and* **Rui A. P. Perdigão**[1,2,3]

Climate change, water, and land management affect the terrestrial water cycle and river flow. They do so through changes in precipitation and evaporation, aside from a multitude of other land surface processes. Earth system models are routinely used to simulate and detect globally observed changes and attribute these changes to climate change. Attribution is based on an assessment of the consistency or inconsistency of change signatures by including or excluding hypothesized drivers of change in process-based models (*1*). On page 1159 of this issue, Gudmundsson *et al.* (*2*) compare the consistency that globally observed trend-patterns in mean river flow and hydrological extremes exhibit with regard to a set of model simulations.

Gudmundsson *et al.* conclude, on the basis of the ESM output, that the simulated effects of water and land management cannot reproduce the observed change pattern in river flow. Rather, the modeled changes in river flow are only consistent with the observed changes in climatic variables if historical radiative forcing that accounts for climate change is used.

This finding is distinct and important, although Gudmundsson *et al.*'s attribution of changing river flow patterns to anthropogenic climate change is made by a simple

[1]Meteoceanics Institute for Complex System Science, Vienna, Austria. [2]cE3c, Faculdade de Ciências, Universidade de Lisboa, Lisbon, Portugal. [3]Instituto de Telecomunicações, Instituto Superior Técnico, Universidade de Lisboa, Lisbon, Portugal. Email: hall@meteoceanics.pt; perdigao@meteoceanics.pt

PHOTO: MICHAEL P. GADOMSKI/SCIENCE SOURCE

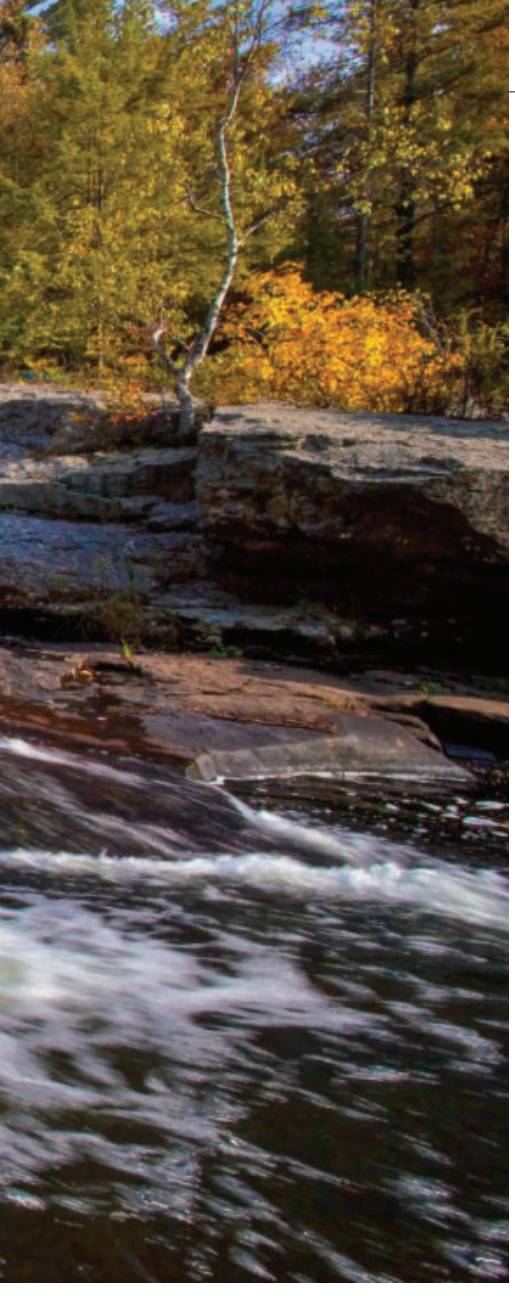

Several factors could cause changes in river discharge at Tobyhanna Falls (shown). The principles of information physics could help to better understand and attribute underlying causal mechanisms such as climate change.

quantitative line of arguments. For instance, if the model is driven by observational atmospheric forcing and it reproduces the observed global change pattern, the authors concluded that the observed trends are related to changes in the radiative forcing. If the observed changes are only consistent with model output driven with historical atmospheric forcing, then these trends are attributed to that driver.

Although the attribution statement in Gudmundsson *et al.* is logical and likely in terms of process understanding of climate dynamics, technically that evidence is still circumstantial. Indeed, different causal pathways could still lead to a similar outcome, that is, the same trend observed in the data could have emerged from a different process, even though not accounted for in the models. Additionally, owing to the presence of internal variability, such attribution will always have some degree of uncertainty (even with complete consistency between models and data) (*1*).

To improve the explanatory power of such important studies and to generate more confidence in such attribution statements, we need to move beyond these first-order assessments that involve simple proof of consistency and inconsistency when investigating the effects of climatic change.

The key for a more robust way to elicit the most likely driving mechanisms resides in characterizing the information transfer between potential drivers and the process of interest (e.g., between climatic change and river flows). Those providing strongest information transfer can be attributed as dominant drivers. Additionally, these information transfer metrics are probabilistic, hence internal variability and uncertainties are natively incorporated. This strengthens the process of attribution and makes it more realistic and reliable.

To achieve robust attribution, several measures of information transfer are already used elsewhere, including transfer entropy (*3*), traditional Bayesian approaches (*4*), and network connectivity metrics with time directionality (*5*, *6*).

Attribution procedures by information transfer and Bayesian approaches are traditionally perceived as indicators of causality. However, they only allow quantifying the ability to infer the state of a process given the knowledge of another. Whether or not there is a cause-effect relation remains elusive, because no physical causation mechanism can be retrieved from these inferential statistics alone.

More recently, dynamical system metrics have been proposed with the aim to assess causal codependencies between drivers and processes (*7*) by evaluating whether there is a deterministic link between them (connection in phase space). This brings the added value of dynamic connectivity and allows for seamless integration with modeling approaches. However, even with these more advanced measures, a true cause-effect diagnostic is still elusive because the phase spatial diagnostics are basically correlative. The connected variables can simply be dynamically correlated effects of a common third-party cause.

The way forward is therefore to combine information transfer and dynamical system approaches, with fundamental principles and methodological understanding in mind. Such a combined approach allows bridging the best of both worlds while overcoming the respective caveats.

This brings us to the emerging pathways of information physics (*8*), reconciling and generalizing statistical, geometric, and mechanistic information metrics (*9*). The use of information physics enables the retrieval of physically consistent information attributes and dependencies in coevolutionary systems such as in hydrology and Earth system dynamics in a changing climate. Information physics can pave the way for bringing physical meaning to inferential metrics, and a dynamic coevolving flexibility to the statistical metrics of information transfer, bringing new pathways for causal discovery and attribution.

Exploring such pathways may thus provide further validation to the findings presented by Gudmundsson *et al.* and might also bring out unknown unknowns to add to the discussion of drivers of change in the hydrological system. This may thus complement any measure of causality that entails the development of multiple working hypotheses based on a thorough process-based understanding to avoid overlooking potential drivers of change that might cause the same signature (*10*).

The findings by Gudmundsson *et al.* allow one to infer that climate change has affected low, mean, and high flows at the global scale. Whether the retrieved drivers are the real causes or just predictors requires further investigation, and the development and application of causal discovery methods grounded on information physics offer encouraging pathways to further that quest for attribution. ■

## REFERENCES AND NOTES


1. N. L. Bindoff *et al.*, in *Climate Change 2013: The Physical Science Basis. Working Group I Contribution to the Fifth Assessment Report of the Intergovernmental Panel on Climate Change*, T. F. Stocker *et al.*, Eds. (Cambridge Univ. Press, 2013), p. 872.
2. L. Gudmundsson *et al.*, *Science* **371**, 1159 (2021).
3. T. Schreiber, *Phys. Rev. Lett.* **85**, 461 (2000).
4. N. Najibi, *et al.*, *NPJ Clim. Atmos. Sci* **2**, 19 (2019).
5. J. Runge *et al.*, *Nat. Commun.* **6**, 8502 (2015).
6. A. E. Goodwell *et al.*, *Proc. Natl. Acad. Sci. U.S.A.* **115**, E8604 (2018).
7. S. Vannitsem, P. Ekelmans, *Earth Syst. Dynam* **9**, 1063 (2018).
8. R. A. P. Perdigão *et al.*, *Water Resour. Res.* **56**, e2019WR025270 (2020).
9. R. A. P. Perdigão, *Entropy* **20**, 26 (2018).
10. S. Harrigan, C. Murphy, J. Hall, R. L. Wilby, J. Sweeney, *Hydrol. Earth Syst. Sci.* **18**, 1935 (2014).


## ACKNOWLEDGMENTS


We acknowledge the Meteoceanics research programs MR-220617 "Mathematical Physics and Predictability of Complex Coevolutionary Systems" and MR-010319 "Synergistic Dynamics of Complex Socio-Natural Systems." R.A.P.P. also acknowledges the "Fundação para a Ciência e Tecnologia" through projects UIDB/00329/2020, UIDP/00329/2020, and UID/EEA/50008/2019. Both authors contributed equally to this work.

10.1126/science.abg6514

SUPERCONDUCTIVITY

# Magic, symmetry, and twisted matter

## Alternating magic-angle twist induces unconventional superconductivity

*By* **Ali Yazdani**

The discovery in 2018 of superconductivity when two layers of graphene are stacked on top of each other at a "magic angle" has opened a new paradigm for studying electronic phenomena (*1*). Now, a pair of studies, one on page 1133 of this issue by Hao *et al.* (*2*) and the other by Park *et al.* (*3*), take the twisting magic trick one step further. More robust and tunable superconductivity was realized in three-layer stacks of graphene arranged at an alternating magic twist angle that is a factor of $\sqrt{2}$ greater than the magic angle for twisted layers of graphene, at a magic angle of ~1°, creates electronic bands with vanishing bandwidths (*4*, *5*). The quenched kinetic energy of electrons occupying such flat bands creates strong interactions and would make magic angle–twisted bilayer graphene (TBG) a spectacular platform for collective phenomena. for sighting new quantum phases (*6*) including unexpected interaction-driven topological insulators (*7*).

Although steady progress is being made in understanding TBG, the mechanism and nature of its superconducting phase remains a mystery. It is tempting to think in terms of a simple weak-coupling BCS scenario in which bands coexist with dispersing Dirac bands, and a perpendicular displacement field can be used to tune its band structure (see the figure). The two experimental studies fabricated trilayer near the predicted greater alternating magic angle and explored trilayer properties as a function of carrier density and perpendicular displacement field.

The presence of the Dirac bands circumvents the formation of correlated insulating states, which also slightly screens the interaction between electrons in the flat band of the trilayer. However, the interactions within the trilayer flat bands give rise to cascades of transitions at several of the integer filling ($\nu$) of carriers per moiré unit cell of its flat bands, similar to those observed in TBG (*10*, *11*). These transitions signal the propensity for flavor (spin or valley isospin) symmetry–breaking, near-integer fillings, including at $\nu = \pm 2$, from which superconductivity emerges upon doping. The trilayer appears at a superconducting transition temperature ($T_c$) of 2 K (twice that of the bilayer) system. The cause of this enhancement is unclear, but the moiré superlattice constant is smaller in the trilayer, which would increase the Coulomb-interaction scale at the same electron density

Several experimental findings in the magic trilayer signal unconventional superconductivity. The superconducting coherence length is about the same as the interparticle distance, and $T_c$ increases almost linearly with doping. The ratio of $T_c$ to the Fermi temperature is also large (0.1). The superconducting state appears to be in the strong-coupling regime and likely driven by Bose condensation of tightly bound Cooper pairs and limited by their density. Pairing might occur at temperatures much higher than when the zero-resistance state is detected.

Tuning the trilayer's band structure allows experimental determination of the role of enhanced density of states at the van Hove singularity (vHS) of the flat bands in superconductivity. The new studies monitored the Hall conductivity as a function of doping and displacement field. When the vHS

## Alternating twists

Superconductivity in twisted graphene layers arises from flat-band structures near zero energy.

**Magic angles**
The structures of graphene bilayer, alternating trilayer, and quadrilayers constructed at a hierarchy of respective magic angles $\Theta_{BM}$, $\Theta_{TM}$, and $\Theta_{QM}$.

**Flat bands**
The theoretical energy-momentum bands are very flat near the Fermi level. Electrons in such flat bands experience strong interactions. Near half filling, bilayers and trilayers superconduct at below their transition temperature $T_c$. Calculations also predict flat bands in the alternating quadrilayers. K, K′, and Γ are symmetry points.

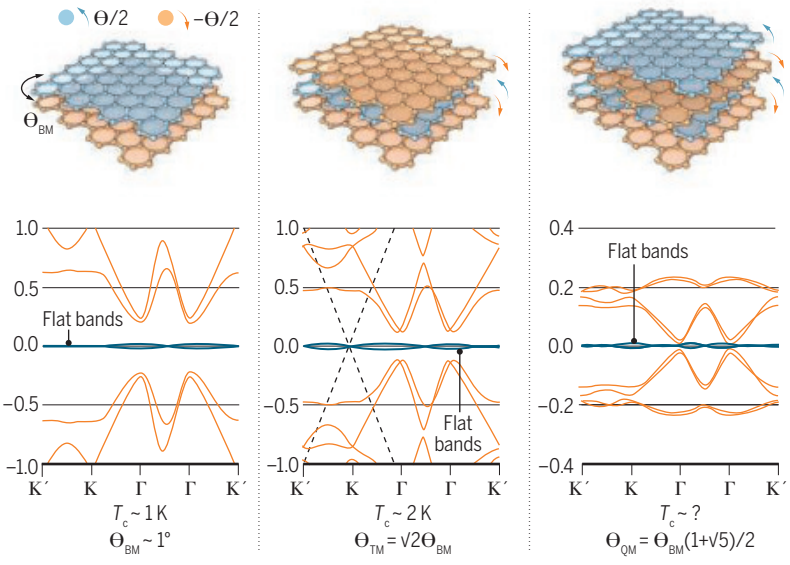


bilayers. The authors also present evidence that superconductivity in twisted graphene is not caused by the conventional weak-coupling Bardeen-Cooper-Schrieffer (BCS) electron-pairing mechanism. The mechanism of pairing remains unknown, but the experiments suggest that the electrons form tightly bound pairs at temperatures above those at which superconductivity is macroscopically detected.

Early theoretical work predicted that the moiré superlattice created by stacking two a large density of states of a nearly flat band can enhance superconductivity. However, superconductivity occurs in the presence of strong Coulomb interactions that are comparable with or larger than the bandwidth of TBG in the noninteracting limit (*8*), and other flat-band moiré systems do not show reliable signs of superconductivity, despite exhibiting other strongly correlated behavior.

Twisting three-layer graphene was predicted to possess flat bands if it was constructed with a curious alternating magic twist angle $\sqrt{2}$ greater than that of the bilayer system (*9*). This trilayer differs from the bilayer in several respects. For example, its flat

Department of Physics, Princeton University, Princeton, NJ, USA. Email: yazdani@princeton.edu

GRAPHIC: C. BICKEL/*SCIENCE*

is tuned to the chemical potential, $T_c$ in the trilayer is suppressed, opposite of what is expected from the simple BCS weak-coupling mechanism. Superconductivity appears to be strongly tied to flavor-polarized states, which are beginning to be understood in the bilayer [for example, (*12*)]. Topological excitations of these states may be responsible for the pairing mechanism (*13*), but the breakdown of weak coupling does not mean phonons are not involved. Some calculations show that in a fully flat band, electrons cannot pair on their own (*14*).

The presence of superconductivity in bilayer and alternating trilayer systems, and its absence in the other flat band system, suggests the importance of spatial-time $C_{2z}T$ symmetry for the emergence of superconductivity. The discovery of superconductivity in this trilayer raises the possibility that the stacking of multilayers of graphene respecting certain symmetry at other magic angles will uncover more and hopefully greater-$T_c$ twisted superconductors. The theory that predicted the $\sqrt{2}$ ratio for trilayer also identified a hierarchy of magic angles for multilayers with alternating layers (*8*). The prediction for quadrilayers with alternating magic angle larger than the bilayer by the golden ratio is that they would have flat bands without dispersing Dirac bands because they have an even number of layers (see the figure).

An unspoken rule in the hunt for new superconductors attributed to early Bell Lab pioneer Bernd Matthias (*15*) is to "never listen to the theorists." However, maybe the signs of symmetry and the elegance of special ratios need to be heeded. Finding superconductivity in twisted matter with a prescribed symmetry related by the golden ratio of twist angles would be pure magic. ■

## REFERENCES AND NOTES


1. Y. Cao *et al.*, *Nature* **556**, 43 (2018).
2. Z. Hao *et al.*, *Science* **371**, 1133 (2021).
3. J. M. Park *et al.*, *Nature* **590**, 249 (2021).
4. R. Bistritzer, A. H. MacDonald, *Proc. Natl. Acad. Sci. U.S.A.* **108**, 12233 (2011).
5. E. Suárez Morell *et al.*, *Phys. Rev. B Condens. Matter Mater. Phys.* **82**, 121407 (2010).
6. E. Y. Andrei *et al.*, *Nat. Rev. Mater.* 10.1038/s41578-021-00284-1 (2020).
7. K. P. Nuckolls *et al.*, *Nature* **588**, 610 (2020).
8. Y. Xie *et al.*, *Nature* **572**, 101 (2019).
9. E. Khalaf *et al.*, *Phys. Rev. B* **100**, 085109 (2019).
10. D. Wong *et al.*, *Nature* **582**, 198 (2020).
11. U. Zondiner *et al.*, *Nature* **582**, 203 (2020).
12. B. Lian *et al.*, arXiv:1811.11786 [cond-mat.str-el] (2020).
13. E. Khalaf *et al.*, arXiv:2004.00638 [cond-mat.str-el] (2020).
14. B. A. Bernevig *et al.*, arXiv:2009.14200 [cond-mat.str-el] (2020).
15. T. H. Geballe, J. K. Hulm, in *Biographical Memoirs* (National Academies Press, 1996), vol. 70, pp. 240–259.


## ACKNOWLEDGMENTS


I acknowledge discussions with X. Li and funding from the Gordon and Betty Moore Foundation, the U.S. Department of Energy, and the U.S. National Science Foundation.

10.1126/science.abg5641


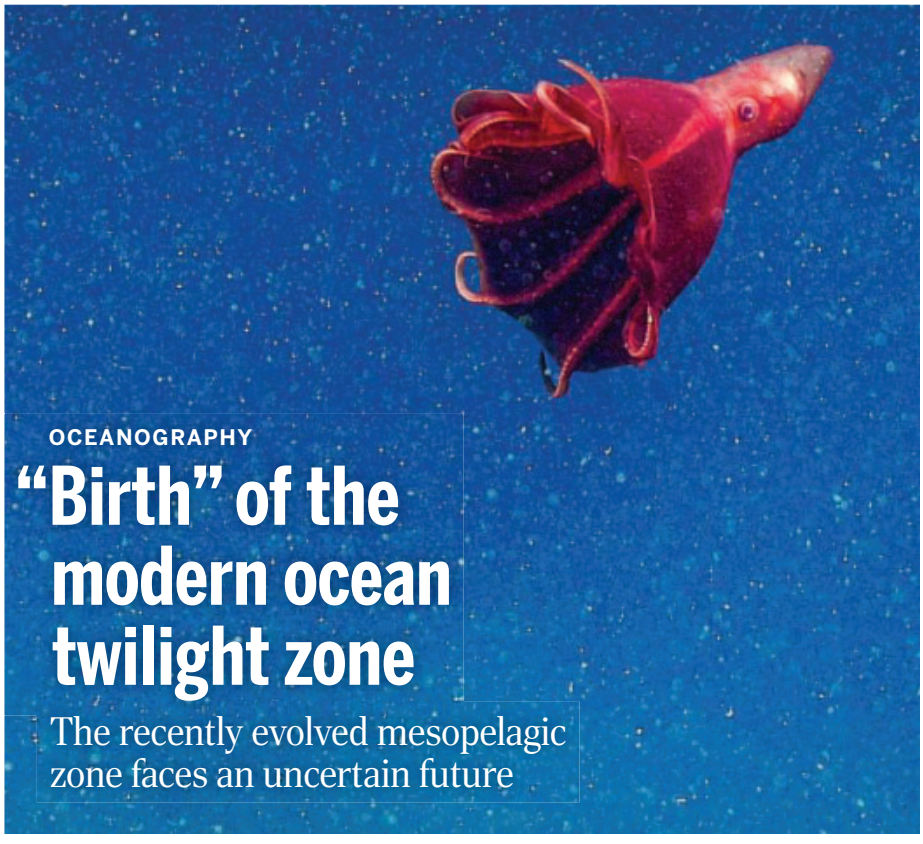

PHOTO: NOAA OFFICE OF OCEAN EXPLORATION AND RESEARCH

OCEANOGRAPHY

# "Birth" of the modern ocean twilight zone

## The recently evolved mesopelagic zone faces an uncertain future

An octopus moves through the "marine snow" of organic matter at 400-m depth in the North Atlantic Ocean.

*By* **Laurent Bopp**

The ocean "twilight zone," where sunlight hardly penetrates, is located at depths of 200 to 1000 m from the sea surface. Inhabited by iconic species such as lantern fish and giant squid, it has stimulated our collective imagination for generations. To this day it remains largely unexplored and has revealed few of its secrets. Also known as the mesopelagic, this zone occupies 20% of the volume of the world's oceans. It plays a key role in the global carbon cycle (*1*, *2*) and may contain both biomass and biodiversity that have been largely underestimated (*3*, *4*). On page 1148 of this issue, Boscolo-Gallazzo *et al.* (*5*) provide evidence that the establishment of the modern twilight zone is, on planetary time scales, a relatively recent phenomenon that has taken place gradually over the past 15 million years.

Using an approach that couples ocean biogeochemical simulations and a compilation of sedimentary isotopic data, Boscolo-Gallazzo *et al.* show the role of the gradual cooling of the climate system (by 4° to 6°C for the global surface ocean) in establishing the modern twilight zone. This global decrease in temperature has reduced the decomposition of organic matter that is formed by upper-ocean ecosystems and then sinks to depth. As such, the export of organic carbon to the deeper ocean has become more efficient and has increased the amount of food available to mesopelagic ecosystems. These long-term paleoclimatic changes are likely responsible for the establishment of relatively new deep ecological niches and the modern twilight zone.

The role of the twilight zone in the ocean carbon cycle has been recognized for more than 30 years, with the identification of the importance of the biological carbon pump in transporting carbon out of the ocean's surface layers (*1*). Indeed, it is in the twilight zone that most of the organic carbon that is exported from the surface ocean is remineralized back to carbon dioxide through a series of biological, physical, and chemical processes that are not yet well understood. However, what is known is that this input of organic matter is critical to the survival of most organisms living at these depths and to the ecosystems they inhabit. Hence, although a few billion tons of carbon leave the surface ocean every


Laboratoire de Météorologie Dynamique/Institut Pierre Simon Laplace, CNRS, Ecole Normale Superieure/PSL University, Sorbonne Université, Ecole Polytechnique, Paris, France. Email: bopp@lmd.ens.fr

year in the form of particulate organic carbon, only a tiny fraction reaches the bottom of the twilight zone at 1000 m. This fraction nevertheless represents a long-term carbon sink, with this deep carbon remaining isolated from the atmosphere for centuries to millennia.

The mean depth at which organic carbon is converted back to $CO_2$, known as the remineralization depth, has a substantial impact on atmospheric $CO_2$. Kwon *et al.* (*6*) have shown that a deepening or shoaling of the mean remineralization depth by just a few tens of meters could decrease or increase atmospheric $CO_2$ by a few tens of parts per million over long time scales. It is therefore crucial to determine as accurately as possible the mechanisms by which organic matter is used by biota in the twilight zone, so as to better project the response of these mechanisms under changing ocean conditions and their role in altering the capacity of the ocean to hold carbon in the coming decades and centuries.

Some of the growing interest in the twilight zone stems from the recognition that it could harbor considerably more fish biomass than previously estimated (*3*)—potentially 20 times as much as in the surface ocean. This discovery has led to new prospects for industrial fisheries, which hope to overcome the limitations posed by depleted or overfished surface fish stocks (*7*). Increasing interest in commercial exploitation of mesopelagic stocks for human consumption, fishmeal, and nutraceuticals is exemplified by the recent European Union Blue Growth Strategy position paper (*8*, *9*), which is open to the exploration and exploitation of mesopelagic fish resources. However, there are large uncertainties about the extent of these stocks, which are estimated at 1000 to 20,000 million tons (*3*, *10*), and little is known about their vulnerability to fishing and other human pressures.

Taking advantage of several oceanographic campaigns and many innovative technological developments (autonomous floats, video profilers), several large-scale scientific projects grouped within the JETZON consortium (*10*) aim to explore the ocean twilight zone and unravel some of its mysteries. The questions are numerous: For example, it is not known what species are present at these depths and what the biomass of these organisms is. Also unclear is the role of processes in the mesopelagic zone in the transfer of carbon from the surface ocean to the deep ocean where it is sequestered for long periods. Another question concerns the sensitivity of these mesopelagic ecosystems to the input of matter from the surface, and to variations in local environmental conditions, in particular temperature, oxygenation, and acidification.

The work of Boscolo-Gallazzo *et al.* on the "birth" of the current twilight zone is particularly timely and relevant to these questions. Indeed, it shows how mesopelagic ecosystems may be vulnerable to future ocean warming through its impact on the delivery of organic matter from surface waters. Other ocean conditions, such as oxygen concentrations and ocean acidity, may also alter the viability of these specific ecosystems. The climate projections carried out in the framework of the recent Coupled Model Intercomparison Project Phase 6 (CMIP6) confirm that future warming, deoxygenation, and acidification may concurrently alter the deep-ocean environment, with unknown consequences for mesopelagic ecosystems (*11*).

In *Twenty Thousand Leagues Under the Sea* (*12*), Jules Verne used his legendary intuition to describe the depths of the ocean, evoking their mysteries and the fascination they exert on humankind: "The sea is the vast reservoir of Nature. The globe began with sea, so to speak; and who knows if it will not end with it? In it is supreme tranquility. The sea does not belong to despots. Upon its surface men can still exercise unjust laws, fight, tear one another to pieces, and be carried away with terrestrial horrors. But at thirty feet below its level, their reign ceases, their influence is quenched, and their power disappears."

Even the prescient Jules Verne had not foreseen how far-reaching human influence may become. More than 150 years after the publication of his classic novel, we are confronted with the realization that the ocean twilight zone now faces several human threats. ■

## REFERENCES AND NOTES


1. T. Volk, M. I. Hoffert, in *The Carbon Cycle and Atmospheric $CO_2$: Natural Variations, Archean to Present*, E. T. Sundquist, W. S. Broecker, Eds. (American Geophysical Union, 1985), pp. 99–110.
2. C. M. Marsay *et al.*, *Proc. Natl. Acad. Sci. U.S.A.* **112**, 1089 (2015).
3. X. Irigoien *et al.*, *Nat. Commun.* **5**, 3271 (2014).
4. C. Robinson *et al.*, *Deep Sea Res. II* **57**, 1504 (2010).
5. F. Boscolo-Galazzo *et al.*, *Science* **371**, 1148 (2021).
6. E. Y. Kwon, F. Primeau, J. L. Sarmiento, *Nat. Geosci.* **2**, 630 (2009).
7. Food and Agriculture Organization of the United Nations, *The State of World Fisheries and Aquaculture 2020: Sustainability in Action* (2020).
8. European Union Directorate-General for Maritime Affairs and Fisheries, *Blue Bioeconomy Situation Report and Perspectives* (2018); www.eumofa.eu/documents/20178/84590/Blue+bioeconomy_Final.pdf.
9. European Commission, *Blue Growth* (2020); https://ec.europa.eu/maritimeaffairs/policy/blue_growth_en.
10. A. Martin *et al.*, *Nature* **580**, 26 (2020).
11. L. Kwiatkowski *et al.*, *Biogeosciences* **17**, 3439 (2020).
12. J. Verne, *Vingt mille lieues sous les mers* (Hetzel, 1869–1870).


10.1126/science.abg5994

IMMUNOLOGY

# Linking clotting and autoimmunity

## A receptor for phospholipid antibodies drives clotting and inflammation

*By* **Mariana J. Kaplan**

Antiphospholipid syndrome (APS) is a systemic autoimmune disorder characterized by increased risk for arterial, venous and/or microvascular thrombosis and various obstetric complications, including recurrent miscarriages, premature births, and preeclampsia, in association with the persistent presence of autoantibodies targeting phospholipids (aPLs). The clinical spectrum of APS ranges from mild clinical manifestations to the development of a catastrophic event involving multiorgan failure and high mortality due to disseminated thrombosis. APS diagnosis requires the detection of serum aPLs targeting cardiolipins and/or the plasma protein $\beta_2$ glycoprotein I ($\beta_2$GPI). However, the full spectrum of specific autoantigens primarily recognized by aPLs remains unknown, which has hampered therapeutic development. On page 1121 of this issue, Müller-Calleja *et al.* (*1*) report the identification of a cell surface antigenic complex composed of endosomal lysobiphosphatidic acid (LBPA) presented by the endothelial protein C receptor (EPCR), which is specifically recognized by aPLs and promotes immune dysregulation and thrombosis in mice.

The pathogenic mechanisms leading to the generation of aPLs and to the various vascular and organ complications characteristic of APS are incompletely characterized and pleiotropic, involving events such as endothelial, platelet, and myeloid cell activation, as well as dysregulation and crosstalk of the complement and coagulation cascades (*2*). aPLs characteristically display reactivity toward various anionic phospholipids (cardiolipins) in cell membranes and plasma proteins. $\beta_2$GPI has high avidity for phospholipid surfaces and is considered a major target of aPLs (*2*).

Systemic Autoimmunity Branch, National Institute of Arthritis and Musculoskeletal and Skin Diseases (NIAMS), National Institutes of Health, Bethesda, MD 20892, USA. Email: mariana.kaplan@nih.gov

Less is understood about the antigen specificity and pathogenicity of aPLs that primarily target phospholipids. In addition to activating the extrinsic pathway of coagulation (*3*), phospholipid-reactive aPLs induce translocation of endosomal Toll-like receptor 7 (TLR7) and TLR8 from the endoplasmic reticulum to the endosomes in myeloid cells, thereby sensitizing them to proinflammatory signaling and interferon (IFN) responses driven by danger signals (*4*). APS can occur in isolation (primary) or in association with other systemic autoimmune diseases such as systemic lupus erythematosus (SLE). Both SLE and primary APS have been associated with dysregulation of the type I IFN pathway, which has several putative pathogenic roles (*5, 6*).

EPCR is expressed by endothelial and myeloid cells, placental trophoblasts, and various differentiated and progenitor cells that may be targeted by aPLs. It is a CD1d-like transmembrane glycoprotein with a tightly bound phospholipid in its antigen-presenting groove. Phospholipid-bound EPCR promotes anticoagulant protein C activation, with downstream antithrombotic effects (*7*). However, EPCR can bind other ligands besides protein C, and this may determine pro- or anti-inflammatory effects (*8*). Furthermore, EPCR activation of proteinase-activated receptor 2 (PAR-2) triggers TLR4-mediated type I IFN responses in mouse myeloid cells, independent of coagulation (*9*). Therefore, EPCR may be pro- or anti-thrombotic and trigger innate immune responses that are relevant to autoimmunity in a context-dependent manner.

Previous reports identified in vitro reactivity of aPLs against LBPA, a phospholipid that is mostly expressed in late endosomes (*10*). Building on these observations, Müller-Calleja *et al.* report that phospholipid-reactive human monoclonal aPLs induce inflammatory gene responses in myeloid, endothelial, and embryonic cells in an EPCR-dependent manner, and that EPCR can serve as a receptor for aPL endosomal trafficking. The ability of EPCR to bind aPLs requires LBPA in the antigen-presenting groove.

To assess whether this pathway was pathogenic in vivo, Müller-Calleja *et al.* used mouse models of aPL-induced fetal loss and thrombosis and found that EPCR-deficient mice were protected from these complications. Additionally, in a mouse model of SLE, aPLs were also prothrombotic and induced IFN responses in myeloid cells in an EPCR-LBPA–dependent manner (see the figure). Furthermore, immunization of non-autoimmune–prone mice with aPLs induced the appearance of cardiolipin-reactive antibodies and expansion of EPCR-LBPA–reactive B1 cells, a subset of B cells that has been linked to innate immune responses and autoimmunity. Supporting that engagement of the EPCR-LBPA complex promotes inflammation, administration of an antibody blocking EPCR-LBPA to a mouse model of SLE inhibited the synthesis of aPLs and other SLE-associated autoantibodies and mitigated renal inflammation and damage.

Although Müller-Calleja *et al.* used only one SLE mouse model, these results suggest that the EPCR-LBPA pathway may play a broader role in immune dysregulation driven not only by aPLs but, potentially, also by other pathways associated with SLE-like autoimmunity, including the type I IFN pathway. It remains unclear how EPCR-LBPA leads to the thrombotic phenotype observed in mice and whether the type I IFN pathway is also involved in this complication, given previous studies linking IFN-mediated transcriptional modulation to platelet activation (*11*). It also remains to be determined what makes EPCR preferentially bind LBPA over other phospholipids, to allow preferential attachment to aPLs.

The study of Müller-Calleja *et al.* expands the repertoire of antigens potentially involved in the pathogenesis of APS. Validating these findings in large clinical cohorts will be important to assess if testing EPCR-LBPA autoantibody specificity will improve the diagnosis of primary and SLE-associated APS, and its association with various organ complications and clinical manifestations. In addition, identifying genetic drivers of abnormalities in the pathways found in the study that are associated with APS or other autoimmune conditions may allow subgroups of patients to be distinguished in whom this pathway could be particularly relevant.

Notably, aPLs can be generated during various acute infections, including that of severe acute respiratory syndrome coronavirus 2 (SARS-CoV-2) (*12*), as well as in cancers and with the use of certain medications. In contrast to APS, the presence of aPLs in these conditions is not necessarily linked to enhanced risk for clotting, although they may have proinflammatory effects. It remains to be confirmed whether phospholipid-reactive aPLs generated during infections signal through the EPCR-LBPA pathway. Even if this pathway is confirmed to be important in human APS, targeting EPCR may prove a double-edged sword, given its well-described anti-thrombotic and anti-inflammatory effects. In this case, it will be important to determine if inhibiting downstream pathways, such as endosomal TLRs and/or type I IFN signaling, could result in abrogation of prothrombotic or inflammatory cascades that are triggered by this complex. ■

## Autoantibody-induced cell signaling

In homeostasis, EPCR is bound to phospholipids in cell membranes, such as phosphatidylcholine. This activates protein C and downstream anti-thrombotic and anti-inflammatory effects. In antiphospholipid syndrome, aPLs, a type of autoantibody, bind to EPCR that is bound to LBPA. Subsequent endocytosis activates TLR7-TLR8 and type I IFN signaling. This leads to further synthesis of autoantibodies, inflammation, and clinical features of antiphospholipid syndrome in mice.

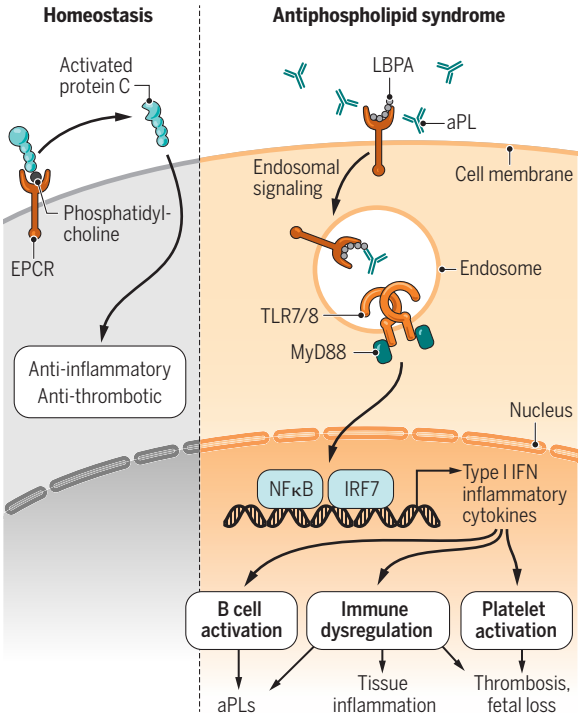


aPL, phospholipid antibody; EPCR, endothelial protein C receptor; IFN, interferon; IRF7, interferon regulatory factor 7; LBPA, lysobiphosphatidic acid; MyD88, myeloid differentiation primary response protein 88; NFκB, nuclear factor κB; TLR 7/8, Toll-like receptor 7 and 8.

GRAPHIC: KELLIE HOLOSKI/*SCIENCE*

### REFERENCES AND NOTES


1. N. Müller-Calleja *et al.*, *Science* **371**, eabc0956 (2021).
2. D. Garcia, D. Erkan, *N. Engl. J. Med.* **378**, 2010 (2018).
3. N. Müller-Calleja *et al.*, *Blood* **134**, 1119 (2019).
4. N. Prinz *et al.*, *Blood* **118**, 2322 (2011).
5. S. Gupta, M. J. Kaplan, *J. Clin. Invest.* **131**, e144918 (2021).
6. R. C. Grenn *et al.*, *Ann. Rheum. Dis.* **76**, 450 (2017).
7. B. Dahlbäck, B. O. Villoutreix, *Arterioscler. Thromb. Vasc. Biol.* **25**, 1311 (2005).
8. V. Kondreddy *et al.*, *Blood* **131**, 2379 (2018).
9. H. P. Liang *et al.*, *Blood* **125**, 2845 (2015).
10. B. Galve-de Rochemonteix *et al.*, *Arterioscler. Thromb. Vasc. Biol.* **20**, 563 (2000).
11. C. Lood *et al.*, *Blood* **116**, 1951 (2010).
12. A. Martirosyan *et al.*, *Front. Immunol.* **10**, 1609 (2019).


### ACKNOWLEDGMENTS


M.J.K. is supported by NIAMS (ZIAAR041199).

10.1126/science.abg6449

MICROBIOLOGY

# Fungi prevent intestinal healing

## Antibiotics open niches for fungi with detrimental consequences to wound healing

By **Tyson Chiaro**[1] and **June L. Round**[1,2]

Chronic intestinal diseases, such as inflammatory bowel disease (IBD), are associated with continual tissue damage that must be repaired. Mucosal restoration is a coordinated process that can be influenced by extrinsic factors, including the commensal bacterial community (*1*–*3*). However, individuals with intestinal disease often receive antibiotics during their care, disrupting these beneficial bacteria. Although fungi comprise a relatively small proportion of the microbial community, they can take over mucosal niches because they are not targeted by antibiotics (*4*). On page 1154 of this issue, Jain *et al.* (*5*) find that the yeast *Debaryomyces hansenii*, which is commonly used in the food industry, can colonize wounds in antibiotic-treated mice and is present in the inflamed tissue of individuals with IBD. This colonization enhances inflammation by blocking the signaling required for wound healing. Thus, disruption of commensal bacteria can open niches for fungi that exacerbate disease.

The intestinal microbiota is a consortium of microorganisms, including bacteria, archaea, fungi, and viruses. Many investigations have identified a role for bacterial members of the microbiota in IBD (*6*). Clinical evidence suggests that fungi may also influence IBD, including the presence of serum antibodies to fungal cell surface moieties in patients with certain types of IBD. Additionally, mutations in the gene that encodes the pattern recognition receptor DECTIN-1 (dendritic cell–associated C-type lectin 1), which recognizes fungal cell walls, or the downstream inflammatory signaling molecule CARD9 (caspase recruitment domain–containing protein 9) are commonly found in IBD patients (*7*). Furthermore, investigations in animal models have demonstrated that common gut fungi, such as *Saccharomyces cerevisiae* or *Candida tropicalis*, can influence IBD severity (*8*–*10*). However, a role for fungi during intestinal epithelial healing has never been evaluated.

IBD is characterized by chronic intestinal inflammation, loss of intestinal barrier integrity, and epithelial damage, requiring constant repair of the mucosa. To study the injury process, Jain *et al.* used forceps to remove areas of the colonic mucosa during endoscopy in mice. As opposed to chemical or infectious models of intestinal injury, this method allows for spatial and temporal control of the wound. Mucosal healing occurs in three discrete and coordinated stages: barrier reestablishment involving neutrophil infiltration, extensive proliferation, and then tissue remodeling. Preventing any of these stages leads to chronic inflammation and a failure to reform the epithelium.

Studies have identified a beneficial role for commensal bacteria during mucosal healing (*1*–*3*). In a healthy gut, shortly after tissue injury, neutrophils are recruited to the injured tissue, creating an anaerobic environment that allows specific bacterial members to seed the wound bed. In particular, *Akkermansia muciniphila* colonizes the injured tissue and influences signaling in epithelial cells to enhance proliferation and wound closure (*1*). Additionally, bacterial metabolites, such as deoxycholate, affect epithelial signaling to coordinate tissue remodeling (*3*). Thus, mucosal wound healing requires signaling from specific commensal bacteria to occur properly.

During inflammatory flares associated with IBD, antibiotics are often used to prevent potentially harmful bacteria accessing the bloodstream. Jain *et al.* found that antibiotic treatment during the biopsy injury model prevented tissue repair. However, known microbiota-dependent pathways were not involved in this phenotype, leading the authors to test other hypotheses. Fungal outgrowth is a frequent side effect of antibiotic use (*4*), and Jain *et al.* observed *D. hansenii* colonization of the injured tissue in antibiotic-treated mice. Treatment with the antifungal agent amphotericin B improved tissue regeneration. Introduction of *D. hansenii*, but not *S. cerevisiae*, by oral gavage into non–antibiotic-treated, conventionally raised animals was sufficient to impair the wound healing process. The same species of yeast was also detected in inflamed colonic tissue from two geographically distinct populations of patients with Crohn's disease, a type of IBD. Therefore, *D. hansenii* can specifically infect intestinal wounds in mice and humans with IBD and restrict the wound healing process in mice.

Jain *et al.* found that macrophages were increased within the wound bed of animals infected with *D. hansenii*. Moreover, expression of the chemokine CCL5 (C-C

### The yeast *Debaryomyces hansenii* prevents intestinal wound healing

During homeostasis, anaerobic organisms, such as *Akkermansia muciniphila*, seed the wound bed and, together with bacterial metabolites, such as deoxycholate, promote wound healing. Antibiotic therapy or loss of bacteria owing to chronic inflammation in inflammatory bowel disease can lead to the colonization of wounds in the epithelial lining with environmental organisms such as the yeast *Debaryomyces hansenii*. This stimulates a type I interferon (IFN) response in macrophages, which leads to production of C-C motif chemokine 5 (CCL5) and chronic inflammation that prevents wound healing.

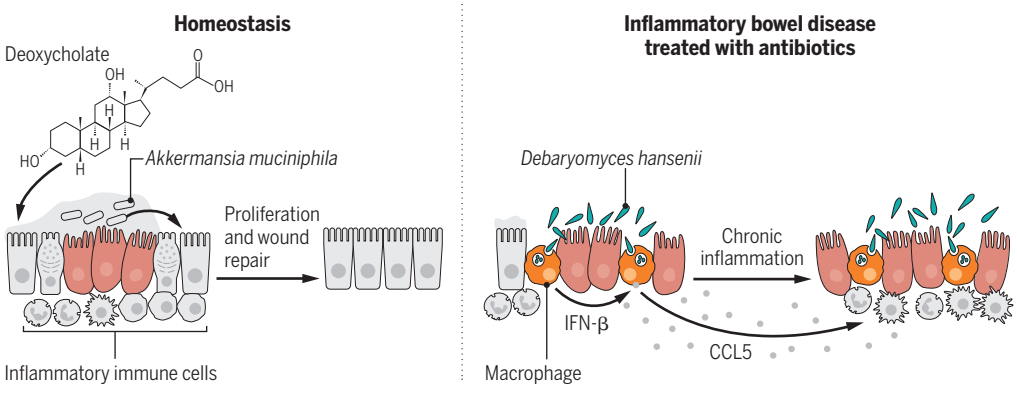


GRAPHIC: MELISSA THOMAS BAUM/*SCIENCE*

[1]Department of Pathology, Division of Microbiology and Immunology, University of Utah School of Medicine, Salt Lake City, UT, USA. [2]Huntsman Cancer Institute, University of Utah, Circle of Hope Drive, Salt Lake City, UT, USA. Email: june.round@path.utah.edu

motif chemokine 5) was enriched in macrophages isolated from the wound bed. CCL5 promotes inflammation by recruiting other immune cells to the tissue, and its expression is increased in individuals with IBD (*11*, *12*). Wound healing was not impaired by *D. hansenii* colonization in mice in which *Ccl5* was deleted. Culture of macrophages with *D. hansenii* followed by RNA sequencing revealed that activation of the type I interferon–CCL5 pathway in macrophages prevents wound healing (see the figure).

*D. hansenii* is likely not a common resident of the gut, because it was isolated from all samples obtained from individuals with IBD but from only 1 of 10 healthy donors. *D. hansenii* is an environmental yeast that is distinctive in its ability to tolerate high-salt and pH conditions and is often used in cheese and meat production (*13*). It is possible that the ability of *D. hansenii* to persist in extreme environments also allows it to survive within inflamed tissue. This suggests that certain dietary recommendations could be made for patients with IBD to prevent colonization with *D. hansenii*, but this would need to be established with clinical trials. Additionally, use of antibiotics in individuals with chronic intestinal disease should be evaluated more carefully. The study of Jain *et al.* demonstrates that the loss of commensal microbes can open up niches for potentially harmful opportunistic organisms. Although CCL5 represents an attractive drug target that is currently being explored in IBD patients (*14*), it is one of many factors that is dysregulated during disease. Because commensal microbes can influence multiple host pathways that include preventing inflammation (*15*), colonization of pathogens, and promoting wound healing, specific cocktails of commensal bacteria might prove to be better therapeutic agents that act on several levels to protect from disease. ■

## REFERENCES AND NOTES


1. A. Alam *et al.*, *Nat. Microbiol.* **1**, 15021 (2016).
2. A. Alam *et al.*, *Mucosal Immunol.* **7**, 645 (2014).
3. U. Jain *et al.*, *Cell Host Microbe* **24**, 353 (2018).
4. M. C. Noverr, R. M. Noggle, G. B. Toews, G. B. Huffnagle, *Infect. Immun.* **72**, 4996 (2004).
5. U. Jain *et al.*, *Science* **371**, 1154 (2021).
6. R. Caruso, B. C. Lo, G. Núñez, *Nat. Rev. Immunol.* **20**, 411 (2020).
7. J. J. Limon, J. H. Skalski, D. M. Underhill, *Cell Host Microbe* **22**, 156 (2017).
8. T. R. Chiaro *et al.*, *Sci. Transl. Med.* **9**, eaaf9044 (2017).
9. I. D. Iliev *et al.*, *Science* **336**, 1314 (2012).
10. T. T. Jiang *et al.*, *Cell Host Microbe* **22**, 809 (2017).
11. A. Mencarelli *et al.*, *Sci. Rep.* **6**, 30802 (2016).
12. X. Ye *et al.*, *Scand. J. Gastroenterol.* **52**, 551 (2017).
13. U. Breuer, H. Harms, *Yeast* **23**, 415 (2006).
14. L. Vangelista, S. Vento, *Front. Immunol.* **8**, 1981 (2018).
15. K. S. Ost, J. L. Round, *Annu. Rev. Microbiol.* **72**, 399 (2018).


10.1126/science.abg6017

CORONAVIRUS

# Immunity to SARS-CoV-2 variants of concern

## Variants show variable escape from vaccine immunity, but residual protection may suffice

*By* **Daniel M. Altmann[1], Rosemary J. Boyton[2,3], Rupert Beale[4,5]**

Vaccine candidates based on spike, the glycoprotein that is essential for host cell entry by severe acute respiratory syndrome coronavirus 2 (SARS-CoV-2), were being designed within days of its reported sequence in January 2020. All the vaccines aim to prevent disease primarily (but not exclusively) by eliciting neutralizing antibodies that block spike and therefore prevent the ability of SARS-CoV-2 to infect cells. The 95% efficacy of the BNT162b2 messenger RNA (mRNA) vaccine (from Pfizer/BioNTech) heralded a series of results showing that eliciting neutralizing antibodies to spike strongly correlated with protection from disease in clinical trials of various vaccines. Currently, there is concern about reduced vaccine-induced immune protection to emerging variants that have mutations in the spike protein. On page 1152 of this issue, Muik *et al.* (*1*) found reduced induction of neutralizing antibodies from BNT62b2. However, there is likely sufficient efficacy remaining to confer protection from symptomatic disease.

Coronaviruses are very large and complex compared with other RNA viruses (around four times the size of the hepatitis A virus genome), and their replication fidelity must therefore be higher. Despite this, once a pathogen has been allowed to infect more than 100 million people, it is not a surprise that sequence variants with a selective advantage emerge. Toward the latter part of 2020, just as regulators were granting approvals to a series of vaccines based largely on the wild-type "Wuhan" sequence spike antigen, several SARS-CoV-2 "variants of concern" were detected. These variants have potentially enhanced transmission, pathogenicity, immune escape, or a combination of all three.

The first sequences of a variant of concern that emerged in the UK, B.1.1.7 (also called 501Y.V1), emerged in September 2020. It includes eight amino acid changes within spike. One of these, N501Y ($Asn^{501}$→Tyr), increases the affinity of spike for its cellular target angiotensin-converting enzyme 2 (ACE2) and, together with other less well characterized mutations, has resulted in enhanced transmission (recognized since December) and possibly enhanced pathogenicity. Might this variant also escape antibody-mediated immunity? Muick *et al.* examined the ability of immune sera from 40 older or younger two-dose BNT162b2 vaccine recipients for neutralization of a pseudotype virus (a safe, surrogate virus engineered to express spike) carrying wild-type sequence spike or all of the B.1.1.7 spike mutations. The sera had a wide range of neutralizing antibody titers measured against the wild-type spike, from around 1/50 to around 1/1200. Although there was a significant reduction in geometric mean titers for the younger (though not the older) cohort against the B.1.1.7 variant, the authors argue that on the basis of our understanding of other respiratory viruses such as influenza virus, an overall reduced titer of some 20% would not be predicted to meaningfully reduce vaccine efficacy. However, such findings confirm that the B.1.1.7 spike mutations affect not only transmission but also immune recognition.

Another study looked in considerable detail at potential vaccine escape by B.1.1.7 (*2*). They considered immune sera from 23 vaccinees with a mean age of 82, analyzed 3 weeks after a single dose of BNT162b2. Using a pseudotype virus carrying spike with all eight mutations led to a sixfold reduction of neutralization for the majority of sera. In this older cohort, the ablation of functional neutralization was more apparent in those starting with lower antibody titers to the wild-type sequence spike. A parallel dataset for pseudotype neutralization of wild-type sequence or B.1.1.7 spike by mRNA-1273 (Moderna) or NVX-CoV2373 (Novavax) vaccinee sera detects a more marginal reduction in activity against the variant (*3*).

When population variation can mean that people develop diverse neutralizing antibody titers after vaccination, the extent to which a small drop in neutralization endangers

[1]Department of Immunology and Inflammation, Imperial College London, UK. [2]Department of Infectious Disease, Imperial College London, UK. [3]Lung Division, Royal Brompton and Harefield Hospitals, London, UK. [4]The Francis Crick Institute, London, UK. [5]Division of Medicine, University College London, London, UK. Email: d.altmann@imperial.ac.uk

protection from symptomatic disease depends to some extent on the immunogenicity of the vaccine and how much margin it leaves for protection. This issue is starting to be addressed through analyses of ChAdOx1 nCoV-19 (University of Oxford/AstraZeneca) vaccinees in the UK (*4*). Although neutralizing antibody titer against B.1.1.7 was reduced approximately ninefold (from a mean of about 1/500 neutralizing antibody titer against wild-type virus), this did not affect vaccine efficacy because there was no enhanced susceptibility to infection [as determined with polymerase chain reaction (PCR) testing] attributable to the variant among the 499 participants who became infected.

Although the B.1.1.7 variant has had massive impact in exacerbating caseload and severity across many countries, there is even greater concern about variants that carry additional immune evasion mutations, notably the E484K (Glu$^{484}$→Lys) mutation found in the B.1.351 (501Y.V2) variant that emerged in South Africa, the P.1 variant found in Brazil, and sporadic examples from UK sequencing that show E484K on the B.1.1.7 background (*5*). That the immune evasion mutations—K417N (Lys$^{417}$→Asn), E484K, and N501Y—can arise in evolution experiments in vitro involving culture of SARS-CoV-2 in the presence of immune sera offers caution against suboptimal vaccination regimens (*6*).

Concern about the B.1.351 variant derives from analyses of its effects on neutralization activity. The variant shows substantial ablation of any virus-neutralizing activity of therapeutic monoclonal antibodies (mAbs) (*7*). Preliminary data suggest a reduced neutralizing response in sera from ChAdOx1 nCoV-19 vaccinees and reduced efficacy in preventing mild to moderate COVID-19 (*8*). This supports the view that neutralizing antibody titer is the key correlate of protection (CoP). Although analysis based on loss of in vitro neutralizing activity by individual mAbs representing the three dominant classes of epitopes on spike offers strong evidence for immune evasion by the variants, the effect is less pronounced at the level of polyclonal immune serum after convalescence or vaccination. This suggests that the neutralizing repertoire is broader and more resilient than so far documented.

Findings from studies with mAbs offer caution for using these therapeutically, given their vulnerability to loss of individual epitopes and also their ability to drive selection of variants that can evade immune recognition. Of course, the flip side of this argument is that detailed mapping of the neutralizing antibody epitopes in spike can facilitate the design of broadly neutralizing vaccines and mAbs that can target numerous spike mutants (*9*). It has been posited that SARS-CoV-2 may continue to accumulate mutations that evade immune responses (*10*). But as previously explored for other viruses, such as HIV, immune evasion often comes at a biological fitness cost to the virus, tending to impose an upper limit to the number of mutations that can be afforded when faced with a broad, neutralizing antibody repertoire (*11*).

Additionally, given that similar mutations arise recurrently in spike, presumably through convergent evolution in geographically distinct isolates, it is possible that the spike variants offering a survival advantage to the virus will be constrained and finite. Furthermore, a spike protein that mutates residues A, B, and C to evade antibody recognition runs the structural risk of generating a new neutralizing epitope, D. Therefore, a finite number of iterative vaccines could target key variants, but this would not necessarily have to be reappraised annually as with influenza virus vaccines. Seasonal "common cold" human coronaviruses tend to appear with 2-year cycles, and recent data for one of these suggest that antigenic drift (mutations that undermine immune recognition) may underlie escape from acquired immunity (*12*).

T cell immunity is likely to feature as an additional CoP against COVID-19 (*13*). The CD4$^+$ and CD8$^+$ T cell response encompasses specificity to several hundred epitopes across the entire SARS-CoV-2 proteome, the majority of which are unimpaired in the variants (*14*, *15*). Even those T cell epitopes that are altered in the SARS-CoV-2 variants will in most cases bind to the different human leukocyte antigen (HLA) molecules that present antigenic peptides to T cells, although binding affinities may be altered. It would be helpful to investigate whether T cell immunity is modified by the SARS-CoV-2 variants.

The assessment of variants on neutralization are complicated by the variability of pseudotype assays used in these studies. It would be helpful to have standardized live-virus in vitro neutralization assays as internationally comparable reference points. As ever, these are discussions that must be tethered to some sense of CoP values. Although much debated, many researchers have the sense that people with a neutralizing antibody IC$_{50}$ (half maximal inhibitory concentration) greater than ~1/100 serum dilution would likely be safe from infection, or at least from symptomatic infection. Given that these are highly potent vaccines that often induce neutralizing antibody responses with IC$_{50}$ of at least 1/1000, there is hopefully a reasonable safety margin before reduced recognition of variants means that effective protection is lost (see the figure). Ultimately, the best defense against emergence of further variants of concern is a rapid, global, vaccination campaign—in concert with other public health measures to block transmission. A virus that cannot transmit and infect others has no chance to mutate. ■

## Vaccine-induced protection

Loss of neutralizing epitopes in the spike protein in severe acute respiratory syndrome coronavirus 2 (SARS-CoV-2) variants could reduce protection induced by vaccination based on wild-type spike. Most vaccinated people develop neutralizing antibody (Ab) with an IC$_{50}$ (half maximal inhibitory concentration) within the protective margin, although precise correlates of protection (CoP) are unknown. Variants with E484K mutations and future escape mutants may bring protection below this margin, prompting the need for new vaccines.

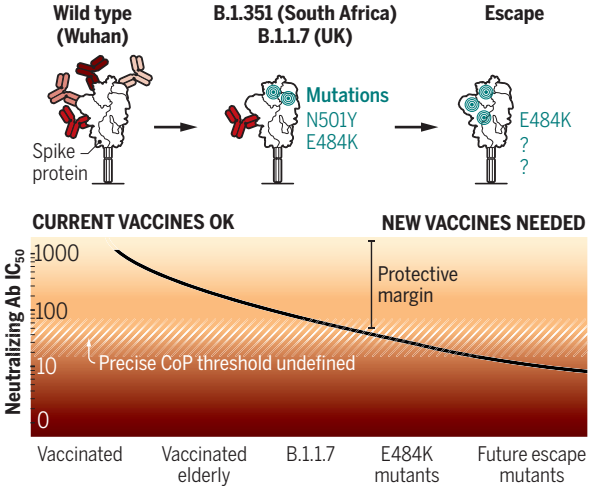


GRAPHIC: V. ALTOUNIAN/*SCIENCE*

### REFERENCES AND NOTES


1. A. Muik *et al.*, *Science* **371**, 1152 (2021).
2. D. A. Collier *et al.*, *medRxiv* 10.1101/2021.01.19.21249840v3 (2021).
3. X. Shen *et al.*, *bioRxiv* 10.1101/2021.01.27.428516v2 (2021).
4. K. R. W. Emary *et al.*, *Lancet* 10.2139/ssrn.3779160 (2021).
5. A. J. Greaney *et al.*, *bioRxiv* 10.1101/2020.12.31.425021v1 (2020).
6. Z. Wang *et al.*, *Nature* 10.1038/s41586-021-03324-6 (2021).
7. C. K. Wibmer *et al.*, *bioRxiv* 10.1101/2021.01.18.427166v1 (2021).
8. S. A. Madhi *et al.*, *medRxiv* 10.1101/2021.02.10.21251247 (2021).
9. D. R. Burton, E. J. Topol, *Nature* **590**, 386 (2021).
10. P. Wang *et al.*, *bioRxiv* 10.1101/2021.01.25.428137 (2020).
11. H. Dreja, C. Pade, L. Chen, A. McKnight, *J. Gen. Virol.* **98**, 1899 (2015).
12. R. Eguia *et al.*, *bioRxiv* 10.1101/2020.12.17.423313v1 (2020).
13. A. Bertoletti, A. Tan, N. le Bert, *Oxford Open Immunol.* 10.1093/oxfimm/iqab006 (2021).
14. D. M. Altmann, R. J. Boyton, *Sci. Immunol.* **5**, eabd6160 (2020).
15. A. Tarke *et al.*, *bioRxiv* 10.1101/2020.12.08.416750v1 (2020).


10.1126/science.abg7404

INFECTIOUS DISEASE

# Using digital twins in viral infection

## Personalized computer simulations of infection could allow more effective treatments

*By* **Reinhard Laubenbacher[1], James P. Sluka[2], James A. Glazier[2]**

When the severe acute respiratory syndrome coronavirus 2 (SARS-CoV-2) pandemic emerged in 2019, researchers rapidly recalibrated epidemiological computer models originally developed for other pandemics to serve as decision support tools for policy-makers and health care professionals planning public health responses. However, no current tools can predict the course of disease and help a doctor decide on the most appropriate treatment for an individual COVID-19 patient. "Digital twins" are software replicas of the dynamic function and failure of engineered products and processes. The medical analog, patient-specific digital twins, could integrate known human physiology and immunology with real-time patient-specific clinical data to produce predictive computer simulations of viral infection and immune response. Such medical digital twins could be a powerful addition to our arsenal of tools to fight future pandemics, combining mechanistic knowledge, observational data, medical histories, and the power of artificial intelligence (AI).

An industrial digital twin of a device, such as a specific jet engine, combines a predictive template computational model calibrated using historical data aggregated from many devices with regularly collected operational data for the particular device. Digital twins allow continual forecasting, and small-scale interventions to prevent problems before they become serious. This greatly reduces the frequency of critical failures. The most sophisticated engineering digital twins are also self-improving—they continuously monitor divergence between predictions and observations and use these divergences to improve their own accuracy.

Although medical digital twins are much more difficult to develop than those for engineered devices, they have begun to find applications in improving human health. Examples include the "artificial pancreas" for type 1 diabetes patients (*1*, *2*). In the artificial pancreas model, a template mathematical model of human glucose metabolism and a closed-loop control algorithm modeling insulin delivery and data from an implanted glucose sensor are customized into a patient-specific digital twin that continuously calculates insulin needs and drives an implanted pump that adjusts blood insulin concentrations. Additionally, pediatric cardiac digital twins combine template models of the heart with patient-derived clinical measurements to optimize some heart surgeries (*3*) and assess the risk of thrombosis (*4*). These examples illustrate how current digital twins can operate in real time to maintain health continuously, or they can be used off-line to design personalized medical interventions. The ARCHIMEDES diabetes model expands these technologies by including models not only of the progression of diabetes within individual patients but also of medical diagnosis, treatments, and the functioning of the health care system that is providing the treatment (*5*). These examples provide a vision of the potential of medical digital twins.

Medical digital twins that combine mechanistic understanding of physiology and viral replication with AI-based models derived from population and individual clinical data are promising as tools for optimizing the treatment of patients infected with a virus. As clinical outcomes of SARS treatment revealed, therapies such as steroidal anti-inflammatories can be lifesaving but also ineffective or even lethal if they are not adjusted carefully to suit individual patient responses (*6*). Thus, more complex therapies combining antivirals and multiple immune-stimulating and anti-inflammatory drugs would need to be personalized for time of application and dose of each component to be both effective and safe. Validated digital twins could greatly reduce the cost and complexity of such combinatorial clinical applications. Even primitive digital twins could improve diagnosis, prognosis, and treatment by providing a framework to combine patient-specific population data in a consistent framework. Their deployment would enable rapid refinement and improvement, especially if they were designed in a modular fashion to permit the parallel development and optimization of their component submodels.

However, a digital twin that can continuously replicate the complexity of an infection and immune responses sufficiently well to guide individual treatment is currently out of reach. To realize the potential of digital twins in the treatment of viral diseases, there are a number of issues that need to be addressed. The spread of infection within the body and the immune response to viral pathogens are still poorly understood, as are the factors determining if and when specific components of the immune response are beneficial (viral clearance) or harmful (hyperinflammation). Viral infections can be complex, with pathologies developing in organs beyond the sites of primary infection, requiring an understanding of the responses of multiple organs. Therapies are also complex, with combinations integrating phased doses of antivirals, anti-inflammatory drugs, antibodies, and immune-stimulating drugs such as interferon (IFN) or interleukin-7 (IL-7).

Where to start in building viral-infection digital twins? When considering how to build mechanistic model components for a viral-infection digital twin, many of the necessary submodels of relevant pathways and processes already exist (*7*) or could be developed using existing experimental methodologies (see the figure). For example, at the subcellular scale, transcriptomics data analysis of human macrophages can be used to construct dynamic network models of the interactions of highly expressed genes for each macrophage subtype (*8*), forming the basis for dynamic models of gene regulatory networks. At the multicellular scale, imaging technology reveals spatial aspects of the immune response (*9*). At the tissue scale, a simulation of an alveolar sac can capture the spatiotemporal variability of the immune response. At the organ scale, computational fluid dynamics models can simulate airflow in the lungs (*10*). And at the whole-body scale, computational models calibrated with simultaneous data from different organs, such as respiratory contractions and cerebral blood flow, can be used to integrate different organ systems (*11*). Physiologically based kinetic models (*12*) are widely used in the development and regulation of pharmaceuticals. Virologists have developed template models that capture aspects of viral spread, immune response, viral replication in individual cells, physiology, and dysfunction of specific organ systems, transport in the blood and lymph, airway transport of viruses, and aerosol therapies (*13*).

[1]Department of Medicine, University of Florida, Gainesville, FL, USA. [2]Department of Intelligent Systems Engineering and Biocomplexity Institute, Indiana University, Bloomington, IN, USA. Email: reinhard.laubenbacher@medicine.ufl.edu; jsluka@iu.edu; jaglazier@gmail.com

Digital twins describing infection and treatment require the development, validation, and integration of numerous component submodels in the context of a rapidly developing scientific understanding of biological behaviors and continual generation of new experimental and clinical data. Although individual laboratories may construct submodels, the development of comprehensive digital twins will require laboratories and research groups around the world to integrate and validate submodels independently, with only limited central coordination. Enabling such parallel development requires a flexible simulation architecture that uses a multiscale map of all the relevant components of a patient's response to viral infection, as well as responses to available treatments. Community efforts such as the COVID-19 Disease Map Project and Computational Modeling in Biology Network (COMBINE) are working to build such infrastructure, although much work needs to be done to adapt those for use in digital-twin technology.

Another substantial challenge is the generation of the heterogeneous data required to both calibrate template models to known human biology and physiology and to personalize template models into digital twins. Data from clinical trials are an important resource for model validation and discovery, as are high-resolution time-series data characterizing the immune response in a variety of individuals and settings. Model construction and validation require collection of synchronous measurements at different physiological scales: 'omics data from tissues and single cells, from diverse experimental systems, including two-dimensional (2D) and 3D cell cultures, in vivo and ex vivo animal models, and patients; at the tissue level, data characterizing immune cell trafficking and patterns of damage and recovery; and biophysical and structural data from tissues and organs, combined with data characterizing transport throughout the body. To personalize a digital twin, the model template must integrate with clinical records and time courses, such as vital signs, immune cell counts, computed tomography scans of infected organs, measured viral loads, and treatment responses. Given the likely complexity of the underlying models, even the abundance of such data will leave considerable challenges in model validation and uncertainty quantification.

Data-driven AI digital twins for prognosis and treatment optimization are often viewed as alternatives to mechanistic modeling. However, AI and mechanistic approaches are most valuable when used together. Mechanistic modeling can provide important constraints for training AI algorithms (*14*). Conversely, AI can assist mechanistic modeling in a host of ways, including parameter identification, model structure evaluation, simulation acceleration, and continuous model refinement through comparison of model predictions with observations.

Building a useful digital twin requires improved communication between clinicians, experimentalists, and modelers. Relatively few clinical and biological insights are currently translated into computational models that could serve as building blocks for medical digital twins. In many cases, data collected as part of experimental studies are not usable for this purpose in part because simulation was not an explicit aim of these studies.

The many challenges that have arisen as health systems have sought to respond to the current global health crisis highlight the urgent need for a viral-infection digital twin that can serve as an integration platform for heterogeneous high-dimensional data that serve to inform data collection and guide evidence-based approaches to personalized treatment. They could result in a core technology that enables a rapid medical response to future emerging viral pathogens. In addition, they can form the basis for digital twins for other diseases. Initially, repurposing the immune response portion of the viral digital twin to other diseases where the immune system is key, such as cancer, could rapidly leverage the viral models. Longer term, digital twins could be coupled to other disease-specific twins already being developed, resulting in much more comprehensive models. Ultimately, these larger-scale digital twins could increase the resilience of the entire health care system. ■

## Building a personalized digital twin

Data from multiple scales are needed to build computational representations of biological processes and body systems that are affected by viral infection. These submodels are integrated and personalized with clinical data from individual patients. The digital twin can then be used to derive predictions about diagnosis, prognosis, and efficacy and optimization of therapeutic interventions.

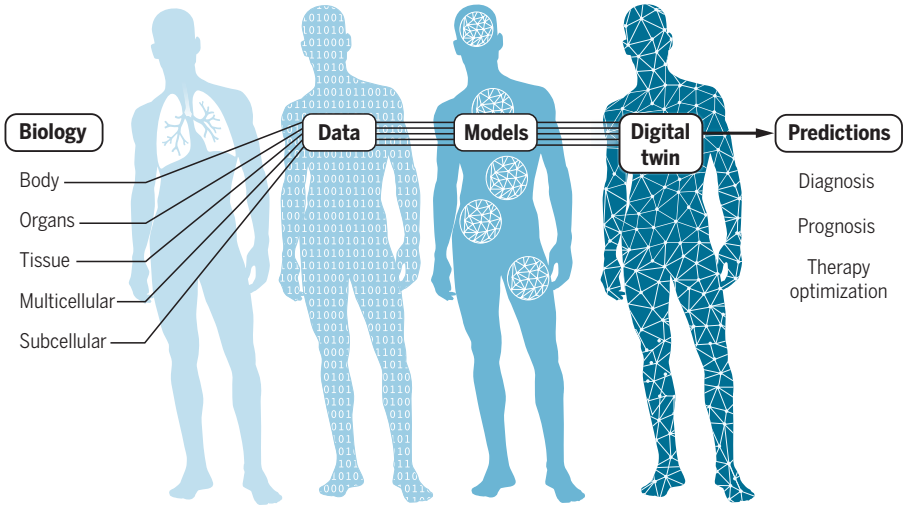


GRAPHIC: N. CARY/*SCIENCE*


### REFERENCES AND NOTES

1. B. Kovatchev, *Trends Endocrinol. Metab.* **30**, 432 (2019).
2. S. A. Brown *et al.*, *N. Engl. J. Med.* **381**, 1707 (2019).
3. J. K. Shang *et al.*, *Ann. Thorac. Surg.* **107**, 1232 (2019).
4. N. Grande Gutierrez *et al.*, *Int. J. Cardiol.* **281**, 15 (2019).
5. D. M. Eddy, L. Schlessinger, *Diabetes Care* **26**, 3102 (2003).
6. L. J. Stockman, R. Bellamy, P. Garner, *PLOS Med.* **3**, e343 (2006).
7. A. S. Perelson, R. Ke, *Clin. Pharmacol. Ther.* 10.1002/cpt.2160 (2021).
8. M. Beyer *et al.*, *PLOS ONE* **7**, e45466 (2012).
9. R. B. Martines *et al.*, *U.S. Emerg. Infect. Dis.* **26**, 2005 (2020).
10. A. V. Kolanjiyil, C. Kleinstreuer, *Comput. Biol. Med.* **79**, 193 (2016).
11. T. J. Cross *et al.*, *PLOS ONE* **8**, e66950 (2013).
12. A. Goyal, E. F. Cardozo-Ojeda, J. T. Schiffer, *Sci. Adv.* **6**, eabc7112 (2020).
13. T. J. Sego *et al.*, *PLOS Comput. Biol.* **16**, e1008451 (2020).
14. M. Alber *et al.*, *NPJ Digit. Med.* **2**, 115 (2019).



### ACKNOWLEDGMENTS

We thank the members of the NIH Working Group on Multiscale Modeling and Viral Pandemics for many helpful discussions. We thank B. Shapiro and L. Sordo Vieira for help with the figure. R.L. is partially supported by the NIH (NIHR011AI135128, NIHU01EB024501, and NIHR01GM127909). J.P.S. and J.A.G are supported by the NIH (NIHU24EB028887, NIHR01GM122424, and NSF1720625). J.A.G. holds shares in Gilead Pharmaceuticals and is a partner in Apoptocys LLC. He is the sole proprietor of Virtual Tissues for Health LLC. He has a patent pending on the application of virtual tissues to improve therapy for diabetic retinopathy.

10.1126/science.abf3370

POLICY FORUM

COVID-19: ECONOMICS

# Market design to accelerate COVID-19 vaccine supply

## Build more capacity, and stretch what we already have

*By* **Juan Camilo Castillo[1], Amrita Ahuja[2], Susan Athey[3,4], Arthur Baker[5], Eric Budish[4,6], Tasneem Chipty[7], Rachel Glennerster[8], Scott Duke Kominers[4,9,10], Michael Kremer[4,5], Greg Larson[11], Jean Lee[12], Canice Prendergast[6], Christopher M. Snyder[4,13], Alex Tabarrok[14], Brandon Joel Tan[10], Witold Więcek[15]**

Each month, COVID-19 kills hundreds of thousands of people, reduces global gross domestic product (GDP) by hundreds of billions of dollars, and generates large, accumulating losses to human capital by harming education and health (*1*–*4*). Achieving widespread immunization 1 month faster would thus save many lives and mitigate short- and long-run economic harm. Although the value of vaccines may seem obvious, government action and investment in vaccines have not been commensurate with the enormous scale of benefits, with many countries not likely to achieve widespread immunization until the end of 2022.

We estimate below that installed capacity for 3 billion annual vaccine courses has a global benefit of $17.4 trillion, over $5800 per course. Investing now in expanding capacity for an additional annual 1 billion courses could accelerate completion of widespread immunization by over 4 months, providing additional global benefits of $576 to $989 per course. This dwarfs prices of $6 to $40 per course seen in deals with vaccine producers, indicating the wide gap between social and commercial incentives. We urge governments and international organizations to contract with vaccine producers to further expand capacity and encourage measures described below to "stretch" existing capacity (such as lower-dose regimens) and efficiently allocate courses (such as a cross-country vaccine exchange).

Our analysis involves two exercises, first estimating the global benefits from vaccine capacity already in place, then estimating the benefits of undertaking additional capacity investment starting now (see supplementary materials for all data and methods). The enormous estimates from both exercises provide a wake-up call relevant for the current pandemic—that it is not too late to invest in more capacity—and future pandemics—that preparations to shorten delays in rolling out vaccines, treatments, and other countermeasures at global scale could prevent enormous harm.

### Global value of vaccine capacity

| GLOBAL CAPACITY (BILLION COURSES) | GLOBAL BENEFIT (TRILLION $) | | TIME TO 70% VACCINATION (MONTHS) | |
|---|---|---|---|---|
| | GDP ALONE | COMPREHENSIVE | HIGH-INCOME COUNTRIES | WORLD |
| 1 | 5.3 | 10.5 | 31.5 | 66.0 |
| 2 | 7.5 | 15.0 | 16.5 | 33.7 |
| 3 | 8.7 | 17.4 | 11.5 | 23.0 |
| 4 | 9.4 | 18.8 | 9.0 | 17.6 |
| 5 | 9.8 | 19.7 | 7.5 | 14.4 |

Vaccine capacity assumes ramp-up such that half of the indicated capacity is available starting January 2021 and the remainder starting April 2021. First two columns estimate global benefit in monetary terms from specified capacity over a 24-month period. Last two columns estimate time until 70% of high-income countries or world population is vaccinated using available capacity. Allocation of capacity to countries of different income levels is based on reported bilateral deals and assumes that global capacity is fully utilized until the target of 70% of world population is vaccinated. Calculations are based on the model outlined in the text and detailed further in the supplementary materials.

Vaccine capacity equals speed, which has enormous value in a pandemic. Vials of the COVID-19 vaccine developed by AstraZeneca move along the production line at the Serum Institute of India plant in Pune, India.

### VALUE OF CAPACITY IN PLACE

In our model, a unit of capacity is defined as the fixed investment needed for one course per year of a regulatory-approved COVID-19 vaccine, including production lines as well as complementary investments necessary to get shots into arms (e.g., input-supply chains, transportation logistics, and medical staff at administration sites). Our discussion focuses on production capacity because it involves the most economic risk and lead time, so may be the rate-limiting step.

Capacity already in place, some of which was installed "at risk" before clinical trials were completed, is more valuable than capacity that comes online later because it can produce vaccine courses without delay. Some credit for the extent of capacity in place can be ascribed to advance contracts that many countries signed with firms. Typically, firms only install capacity at commercial scale once a vaccine is proven safe and effective, creating a delay of at least 6 months between clinical approval and large-scale vaccination. By signing contracts in advance of clinical approval, governments shoulder some of this risk and incentivize firms to install capacity earlier.

It is difficult to pin down the level of capacity currently in place precisely. We take 3 billion courses of annual capacity as our baseline, with half coming online in January and half in April. This baseline is high relative to current production but low relative to best-case production plans for 2021 announced by firms succeeding in phase 3 clinical trials (table S1). We trace out global benefits for a range of capacities around this baseline, from 1 billion to 5 billion annual courses.

The International Monetary Fund (IMF) estimates global GDP losses from COVID-19 of $12 trillion during 2020–2021 (*2*), an average monthly GDP loss of $500 billion. More comprehensive harm estimates—including education and health losses—are multiples larger. For example, comprehensive harm in the United States has been estimated (*3*) to be over five times the projected GDP loss. We use $1 trillion (double the IMF estimate of GDP losses) as a conservative measure of comprehensive global monthly harm.

PHOTO: DHIRAJ SINGH/BLOOMBERG/GETTY IMAGES

We estimate that having 3 billion courses of annual capacity provides a global benefit of $8.7 trillion in GDP alone and $17.4 trillion in comprehensive benefits (see the first table), an average of over $5800 per course. More capacity provides more value and reduces the time to complete widespread vaccination, but at a decreasing rate, the next billion courses of capacity contributing about half as much as the billion before.

Projecting allocations of vaccine courses across countries on the basis of reported bilateral deals with vaccine manufacturers, given that high-income countries (HICs) have signed a disproportionate share of the deals, we estimate that completing widespread vaccination in the world will take about twice as long as in HICs. A mathematical consequence is that an increase in capacity generates a larger absolute reduction in time to vaccination for the world than for HICs. For example, an increase from 3 billion to 5 billion courses of capacity would speed up vaccination by 4 months for HICs but by nearly 9 months for the world.

The value of capacity comes not just from large scale but also from early availability. If all 3 billion courses of annual capacity were available in January instead of half not ramping up until April, comprehensive benefits in the first table would be $1.3 trillion higher. The huge estimates of monthly harm cited above mean that our finding that capacity in place has huge value is not very sensitive to our modeling assumptions.

## VALUE OF ADDITIONAL CAPACITY

The case for additional investments may be less clear than it was for initial investments given that we are a year into the pandemic and investing now generates additional capacity only with a lag. Even assuming a lag of several months, we find that additional investment can still be extremely valuable. Adding capacity for 1 billion annual courses to the baseline 3 billion would avert $576 billion in comprehensive losses if the capacity comes online in July and $989 billion if the capacity comes online in April (see the second table) and would speed up completion of widespread vaccination by over 4 months. Although April or July may be ambitious targets for new capacity, they might be achieved by creative "stretching" measures described below or repurposing of existing vaccine capacity, if not a well-resourced effort to build new capacity.

The substantial value of investing in additional capacity is driven by two key factors. First, although a large fraction of health benefits may be obtained by vaccinating a small proportion of the population (e.g., health care workers and the elderly), obtaining full economic benefits may require reaching the broader population. Second, it is far from certain that current capacity is sufficient to fulfill best-case production plans. The less baseline capacity that materializes, the more valuable is adding to that capacity. If baseline capacity is just 2 billion courses, the economic benefits of 1 billion additional courses grow to $1.3 trillion to $1.9 trillion, and widespread vaccination is sped up by over 9 months.

Our estimates may understate the need for additional vaccine capacity if boosters prove necessary, some existing capacity is nullified by vaccine-resistant strains, or some existing production lines are hampered by technical glitches. Even if there is only a small chance that new capacity will be needed for these or other reasons, additional capacity is valuable in expectation because it provides insurance against the worst pandemic outcomes.

The IMF estimates that governments are spending around $1.5 trillion a month on fiscal support during the pandemic (*5*), which may lead some to feel that their budgets are too strained to pay for vaccine capacity. Even now, only a small amount of vaccine capacity has been installed to serve low- and middle-income countries. Investing in accelerating vaccines can pay for itself many times over from reduced fiscal costs alone. Even if governments' savings on fiscal expenditures is a fraction of the GDP benefit from additional vaccines, this exceeds any estimate of the cost of capacity inferred from COVID-19 deals. The World Bank has made $12 billion of financing available to fund vaccination (among other priorities), but most has not been taken up. Using these funds to expand vaccine capacity would have high net benefits for developing countries and their donors.

## Global value of additional 1 billion annual courses of capacity

| SCENARIO | | ADDITIONAL GLOBAL BENEFIT ($ BILLION) | | SPEED-UP TO 70% VACCINATION (MONTHS) | |
|---|---|---|---|---|---|
| ADDITIONAL CAPACITY ONLINE | BASELINE CAPACITY (BILLION COURSES) | GDP ALONE | COMPREHENSIVE | HIGH-INCOME COUNTRIES | WORLD |
| April 2021 | 2 | 970 | 1940 | 4.5 | 10.2 |
| | 3 | 495 | 989 | 2.1 | 5.0 |
| | 4 | 270 | 540 | 1.2 | 2.9 |
| July 2021 | 2 | 636 | 1273 | 3.5 | 9.2 |
| | 3 | 288 | 576 | 1.4 | 4.3 |
| | 4 | 129 | 257 | 0.6 | 2.3 |

First two columns estimate global benefit in monetary terms from 1 billion courses of capacity, coming online April or July 2021, added to specified baseline capacity. In all scenarios, baseline capacity ramps up such that half is available starting January 2021 and the remainder starting April 2021. Additional global benefits (which can be added to baseline from the previous table to compute total benefits) are computed over a 24-month period. Last two columns estimate the speed-up of vaccination of 70% of high-income countries or world population relative to baseline time from the previous table. See the previous table for additional notes.

## MARKET-DESIGN PRINCIPLES

The enormous global benefits of additional vaccine capacity ($576 to $989 per annual course by our estimate) compared to prices of $6 to $40 obtained by vaccine producers in deals to date suggest a wide gap between social and commercial incentives for vaccine capacity. Economic principles of market and contract design can help bridge the gap, allowing society to realize the large potential gains at reasonable cost.

### Contract on capacity versus output

Contracts should include provisions for installing new capacity dedicated to the buyer rather than only specifying a quantity of vaccine courses. An advance contract for the delivery of a set number of courses for a set price may provide too little incentive for speed if not structured thoughtfully (*6*). Unless bound by an explicit capacity commitment or delivery date, the firm's commercial incentives are to save costs by investing in smaller capacity, fulfilling the order over a longer period but generating the same revenue from the contract. Although buyers could try to eliminate delays by specifying deadlines for delivery, these may slip (as many existing contracts have) unless backed by late penalties. However, firms are unlikely to accept contracts with substantial penalties that reflect the full social cost of delay.

The danger of signing a contract on courses is that the country may find itself at the end of a queue with a long wait for life-saving vaccines. Provisions to shorten this wait may harm other countries that are pushed back in the queue. Contracts that

[1]University of Pennsylvania, Philadelphia, PA, USA. [2]Douglas B. Marshall, Jr. Family Foundation, Houston, TX, USA. [3]Stanford Graduate School of Business, Stanford, CA, USA. [4]National Bureau of Economic Research, Cambridge, MA, USA. [5]University of Chicago, Chicago, IL, USA. [6]University of Chicago Booth School of Business, Chicago, IL, USA. [7]AlixPartners, Boston, MA, USA. [8]Foreign Commonwealth and Development Office (FCDO), London, UK. [9]Harvard Business School, Boston, MA, USA. [10]Harvard University, Cambridge, MA, USA. [11]Independent researcher, Washington, DC, USA. [12]World Bank, Washington, DC, USA. [13]Dartmouth College, Hanover, NH, USA. [14]George Mason University, Fairfax, VA, USA. [15]Independent researcher, London, UK. Email: kremermr@uchicago.edu

expand capacity can benefit both the signer and other countries by increasing the rate at which the queue is served.

Paying up front for capacity may end up being cheaper for governments. Imagine a future pandemic in which firms are again striving to develop vaccines with no assurance of success. By paying up front for capacity for vaccines still at risk of failure, governments can bear most of the risk. Paying for courses conditional on success can end up inflating government expenditures owing to the private information firms have on their costs (*7*) or probabilities of success (*8*).

### Relax supply-chain constraints

Governments should invest in supply-chain capacity for intermediate goods needed to make vaccines. Rapid expansion of vaccine manufacturing capacity creates a spike in demand for inputs like glass vials, lipid particles, and bioreactors. Meeting this demand requires an expansion of input capacity. The spike in demand may be temporary, however, after which the added input capacity may be left idle. To justify an expansion of input capacity commercially, a short-term price surge may be needed. Social constraints on pricing during a pandemic may preclude surges (*9*), however, resulting in shortages of intermediate goods. Public agencies may need to intervene in the input market, building input stockpiles in anticipation of manufacturing scale-up or signing contracts for the installation of new input capacity.

### Solicit bids

Some commentators contend that all feasible capacity is being brought to bear on COVID-19 vaccines; further expansion will be prohibitively expensive, if not impossible, in a reasonable time frame. The need for additional capacity is too urgent to take these contentions for granted. By soliciting bids from firms for capacity expansion (whether by installing new factories, repurposing existing ones, or finding ways to increase yield), governments could discover potential opportunities and their costs, allowing them to make informed investment decisions. Our analysis suggests that governments should aim to install substantial capacity even if they must pay a higher price for marginal units of capacity than in deals to date.

## USING CAPACITY EFFICIENTLY

The COVID-19 pandemic is far from "business as usual" in the vaccine market, calling for creative ideas to stretch capacity.

### Dosing regimens

Proposals to stretch existing capacity by delaying the second of two doses in a course, by using lower-dose regimens, or by giving only one dose to those previously infected with the virus have a similar effect on supply as a direct increase in capacity. These proposals could have large potential benefits; thus, investigating their medical appropriateness is worthwhile.

### Vaccine trials

Some vaccines may be more effective than others against new strains of COVID-19. New vaccine trials could help determine the best matches, enabling vaccines to be distributed to the appropriate regions where new strains are spreading. New vaccine trials could also be used to test which dosing regimen is most efficient in the effort to stretch vaccine capacity. Phase 3 trials for efficacy could be conducted head-to-head with no need for an unvaccinated control group, allowing trials to be conducted at large scale—even embedded in national vaccine rollouts—leading to faster results.

### Utilizing lower-efficacy vaccines

Given the value of speed in a pandemic, using a less effective vaccine available now can be better than waiting for the later arrival of a more effective one (fig. S2). Similar logic suggests that lower-dose regimens can have large benefits to a country by getting more vaccine to citizens more quickly even if the regimens reduce the efficacy of individual vaccinations somewhat.

### Cross-country vaccine exchange

As more vaccines are approved, given the scramble to secure bilateral deals, the nature of the fair allocation protocol adopted by COVAX (a global initiative to promote access to COVID-19 vaccines), and rapidly changing circumstances, some countries may end up with vaccine allocations that are not optimally matched to their needs. For example, some countries may have difficulty handling vaccines requiring ultracold storage or may be willing to trade off a small reduction in efficacy for a large increase in quantity. Countries allocated several vaccines may prefer to simplify logistics by consolidating on one or two.

To facilitate efficient allocation across countries, a vaccine exchange mechanism is under consideration by COVAX. The mechanism would enable countries to engage in mutually beneficial trades of vaccine courses. Centralized market clearing will help aggregate the willingness of all countries to trade, thus maximizing gains from trade and minimizing waste of scarce vaccine courses.

Similar mechanisms have been used successfully in other contexts where gains from trade are substantial, yet traditional cash markets are inappropriate and fairness concerns are paramount (*10*, *11*). This setting, however, offers specific challenges. Allowable trades must satisfy regulatory approval, indemnification at the country level, and COVAX goals for population coverage. By incorporating such safeguards, an exchange can maximize efficiency, minimize waste, and ensure an equitable allocation.

## UNPRECEDENTED CAPACITY

Even though unprecedented vaccine capacity has been put in place for COVID-19, expanding capacity yet further would generate substantial global benefits. Standing manufacturing capacity that can be repurposed quickly to produce vaccines and complementary inputs has a very high social value, in the current pandemic and in expectation of outbreaks to come. Capacity can even be an antidote to conflicts over distribution—which countries get scarce vaccines first and which people—by speeding up widespread vaccination. But markets will not deliver this capacity on their own. ■


### REFERENCES AND NOTES

1. L. Boone, "Coronavirus: Living with uncertainty," ECOSCOPE, 16 September 2020, https://oecdecoscope.blog/2020/09/16/coronavirus-living-with-uncertainty/.
2. G. Gopinath, "Reopening from the great lockdown: Uneven and uncertain recovery, IMF Blog, 24 June 2020, https://blogs.imf.org/2020/06/24/reopening-from-the-great-lockdown-uneven-and-uncertain-recovery/.
3. D. M. Cutler, L. H. Summers, *JAMA* **324**, 1495 (2020).
4. E. A. Hanushek, L. Woessmann, "The economic impacts of learning losses," OECD Education Working Paper 225 (2020).
5. IMF, Database of Fiscal Policy Responses to COVID-19, January 2021; www.imf.org/en/Topics/imf-and-covid19/Fiscal-Policies-Database-in-Response-to-COVID-19.
6. M. Kremer, J. Levin, C. M. Snyder, "Designing advance market commitments for new vaccines," NBER Working Paper w28168 (2020).
7. C. M. Snyder, K. Hoyt, D. Gouglas, T. Johnston, J. Robinson, *Health Aff.* (Millwood) **39**, 1633 (2020).
8. A. Ahuja *et al.*, "Preparing for a pandemic: Accelerating vaccine availability," NBER Working Paper w28492 (2021).
9. E. Budish, G. Cachon, J. Kessler, A. Othman, *J. Econ. Perspect.* **21**, 37 (2007).
10. E. Budish *et al.*, *Oper. Res.* **65**, 314 (2017).
11. C. Prendergast, *J. Econ. Perspect.* **31**, 145 (2017).



### ACKNOWLEDGMENTS

We thank H. Kettler and N. Lurie for helpful discussions on vaccine exchange; J. Pickett for review and comments; and E. Chaudhuri, J. Chen, A. Simoes Gomes Junior, and Z. Xia for research assistance. We thank Emergent Ventures, the Golub Capital Social Impact Lab, the Inter-American Development Bank, Schmidt Futures, the Washington Center for Equitable Growth, and the Wellspring Philanthropic Fund for funding. M.K. is a senior advisor to the World Bank on vaccines. J.L. is a senior economist at the World Bank and has some involvement in vaccine financing. S.A., M.K., and C.M.S. served on a pro-bono advisory group on the design of COVAX. E.B., S.D.K., and C.P. serve on a pro-bono expert group advising on the design of the COVAX exchange mechanism. W.W. provides consultancy for Certara, a drug development company, and 1 Day Sooner, a human challenge trial advocacy group. This article does not necessarily reflect FCDO policy.


### SUPPLEMENTARY MATERIALS

science.sciencemag.org/content/371/6534/1107/suppl/DC1


Published online 25 February 2021

10.1126/science.abg0889

## CALL FOR NOMINATIONS FOR THE 2022 HFSP NAKASONE AWARD

The HFSP Nakasone Award is awarded to scientists in recognition of pioneering work that has moved the frontier of the life sciences. This may encompass conceptual, experimental, or technological breakthroughs. The award recognizes the vision of former Prime Minister Nakasone of Japan in the creation of the Organization.

The competition is open; it is not limited to HFSP awardees and there is no age limit for candidates. In selecting the awardee, the Council of Scientists will pay particular attention to recent breakthroughs by younger scientists. The awardee will receive an unrestricted research grant of 10,000 USD, a commemorative medal, and an invitation to deliver the HFSP Nakasone Lecture at the 2022 HFSP Awardees Meeting.

Previous winners of the HFSP Nakasone Award are listed on the HFSP website (see the link below).

Nominations must be received before 23 April 2021 and include the HFSPO nomination form and the nominee's CV. For more information see:

http://www.hfsp.org/awardees/hfsp-nakasone-award

International Human Frontier Science Program Organization

### PREVIOUS WINNERS

Anthony Hyman &
Clifford Brangwynne (2021)
Angelika Amon (2020)
Michael Hall (2019)
Svante Pääbo (2018)
David Julius (2017)
Emmanuelle Charpentier &
Jennifer Doudna (2016)
James Collins (2015)
Uri Alon (2014)
Stephen Quake (2013)
Gina Turrigiano (2012)
Michael Elowitz (2011)
Karl Deisseroth (2010)

Surgeon Mark Hall (James Olsen) removes his protective suit in a scene from *The Andromeda Strain*.

PHOTO: MICHAEL OCHS ARCHIVES/UNIVERSAL PICTURES/GETTY IMAGES

BOOKS *et al.*

FILM

# Pandora's pandemic

## *The Andromeda Strain's* oft-invoked fictional outbreak continues to offer context for considering possible futures

By **Luis A. Campos**

Fifty years ago, the blockbuster du jour was *The Andromeda Strain*, a film based on a new kind of biomedical thriller that depicted a plague of putatively extraterrestrial origins. The film—directed, perhaps incongruously, by Robert Wise of *The Sound of Music* fame—would in time be hailed by the Infectious Diseases Society of America as the "most significant, scientifically accurate, and prototypic of all films of this genre."

The genre itself had effectively been invented 2 years earlier by a young medical school student, Michael Crichton, whose first novel, *The Andromeda Strain* (1969), served as the film's source material and told the story of a military satellite descending to Earth carrying a bug from space that, according to a full-page ad in the *New York Times*, caused "the world's first space-age biological emergency." Selling more than two million copies when it was first released, *The Andromeda Strain* drew the American public's attention from the imminent prospect of atomic apocalypse to a new realm of potential biological catastrophe. (Crichton credited the idea for the novel to a comment made by the paleontologist G. G. Simpson about airborne microorganisms high in Earth's atmosphere.)

**The Andromeda Strain**
*Robert Wise, director*
Universal Pictures, 1971. 131 minutes.

Crichton's distinctive narrative style depended on verisimilitude and on what Joanna Radin has called "authenticating detail ripped from leading academic scholarship," providing reports from the near-future of technology that often "blurred the line between fiction and reality," even as they blurred the line between exobiological concerns and the engineering of biology (*1*).

Speculations about containment, contamination, and colonization were widespread in the 1960s and 1970s in scientific circles concerned with exobiology, evolutionary biology, and the new prospects for the molecular engineering of biology, as these fields invoked a shared language of breaching "barriers"—evolutionary barriers, species barriers, safety barriers, and containment barriers. While exobiologists raised the prospect of interplanetary quarantines, biologists concerned with more terrestrial patterns of invasion biology and the genetics of colonizing species gathered at Asilomar in 1965, a decade before the famous "Pandora's Box Congress" meeting on recombinant DNA, to discuss what they called the "'alien' habitats of invading species," the dominance of "hypervirulent" strains, and whether such "infections" would take (*2, 3*). The concern was clear: how to forestall "biological missteps," whether intentional or unintentional.

*The Andromeda Strain* entered into this dynamic ecosystem, weaving together concerns over planetary protection and earthly decisions about laboratory biocontainment strategies. Although entirely fictional, the narrative described in the book and subsequent film would come to play a central role in the construction of new and contested futures for molecular biology.

As Crichton's story began to infect discussions of the potential biohazards of recombinant DNA, journalists struggled to describe the possibilities and the risks of newly available engineering techniques and often turned to the fictional microbe to capture the issues at stake. The day after the famous 1975 Asilomar conference on recombinant DNA concluded, the *Boston Globe* trumpeted: "Scientists to resume risky work on genes: Danger of 'Andromeda strain' posed."

Many biologists, including Asilomar coorganizers Norton Zinder, Paul Berg, Maxine Singer, and Sydney Brenner and, later, others on the National Institutes of Health Recombinant DNA Advisory Committee, sought to counter such sensationalist coverage as "molecular politics," distracting from actual engineerable futures for biology and conflating sober assessments of risk with speculative science fiction scenarios (*4*). *Andromeda*-inspired fears about genetic engineering were themselves the emerging disease of concern in many scientists' opinion.

Within a few years, as debates over appropriate laboratory biocontainment strategies for newly engineered organisms proceeded, the Andromeda strain would be repeatedly invoked, intruding even into conversations on Capitol Hill. At one Senate hearing on proposed regulation of recombinant DNA research, Oliver Smithies, a former president of the Genetics Society of America, began his remarks by noting: "I think we are here because of a very popular modern science fiction novel by Michael Crichton—*The Andromeda Strain*" (*5*). After pointedly correcting Smithies's testimony, which had referred to an outbreak of plague in New Mexico, Harrison "Jack" Schmitt, a senator from New Mexico and former astronaut, invoked his own literary interpretation of Crichton's tale about a pathogen from space landing in the American Southwest to suggest the lessons of fiction and the likely outcome of a real-world Andromeda strain scenario. At another hearing, the secretary of the U.S. Department of Health, Education, and Welfare referenced the possible emergence of Andromeda-like pathogens as the appropriate context for considering "strict guidelines in the conduct of recombinant DNA research" (*6*).

From the very beginning, the exploration of risk scenarios involving recombinant DNA was an act of both science and science fiction. And the tension was clear: The risk of

The reviewer is secretary of the History of Science Society and regents' lecturer in the Department of History, University of New Mexico, Albuquerque, NM 87131, USA. Email: luiscampos@unm.edu

biological escape and the potential biohazard of newly engineered forms of life were scientifically grounded possibilities worth considering, but it was still useful to distinguish such speculations from sensationalism. Even as *The Andromeda Strain* became fully enfolded into public representations of genetic engineering, its blurry continuum between fact and fiction—the stylistic move at the heart of Crichton's success—made it difficult to classify concerns about the potential hazard of recombinant DNA as either serious or a source of unsubstantiated fears, infuriating many molecular biologists.

As Andromedan echoes persisted in debates about overly complicated biomedical laboratory design (so-called Andromeda design syndrome), the story even came to infect liability discussions at top-ranking research universities. One internal memo from Stanford University's Office of Technology Licensing, titled "The Technology and the Threat," described the appropriate use of licensing to "inhibit scientists from conducting research that might result in an Andromeda Strain being unleashed upon the world" (*7*). Science fiction possibilities and scientific futures (not to mention legal and reputational liabilities) were difficult to disentangle when it came to the engineering of life at the molecular level.

In a retrospective published in 1995, Berg and Singer concluded that "after 20 years of research and risk assessment, most recombinant DNA experiments are, today, unregulated…The fear of 'Andromeda strains' has disappeared" (*8*). And according to *Science*, in 2000, "The technology that seemed like science fiction in 1975 is now commonplace" (*9*). Andromeda-inspired fears had clearly receded by the dawn of the new millennium, replaced, perhaps, for the next generation by new visions of biological possibility à la Crichton's *Jurassic Park*.

Still, for some virologists, *The Andromeda Strain* highlighted important concerns. Virologist Cedric Mims, for example, noted in 1995 that a hypothetical Andromeda strain causing a virulent human pandemic "would depend on its transmissibility, and transmissibility is a neglected subject in microbiology" (*10*). A virulent human pandemic would not always be hypothetical, however.

"What could be more bone-chilling than a seemingly out-of-control virus leaping from region to region around the globe, without a known vaccine to prevent it or slow it down, causing death and economic mayhem along the way?" wrote William Cohan in the *New York Times* at the start of the COVID-19 pandemic in March 2020. "The coronavirus narrative," Cohan continued, "has the texture and feel of 'The Andromeda Strain'… come to life" (*11*).

In mid-May, as American deaths due to COVID-19 neared 100,000, *New Yorker* film critic Anthony Lane offered contemporary audiences a fresh perspective on *The Andromeda Strain*, which contained what Lane called "the most alarming thing I've come across, in this trade-off between the real and the imagined." In an eerie presage of our present pandemical predicament, he described an exchange in the film when the experts' concerns are relayed to the White House:

Mark Hall (James Olsen) and Jeremy Stone (Arthur Hill) examine the satellite on which the extraterrestrial microbe is believed to have arrived.

"By then, the disease could spread into a worldwide epidemic."

"It's because of rash statements like that the President doesn't trust scientists."

"That's a little *too* close to the bone, I reckon," Lane remarked, but he felt that the film presciently captured "how harshly politics and medicine can scrape against each other, whenever peril impends"—just as science and science fiction can (*12*).

Critiques of Andromedan fantasies at the time of Asilomar were attempts to address the ways in which fictional narratives were seen by some scientists as sensationalism in the service of fearmongering. The concern then was hype; ours today, arguably, is hoax. But the divisive and difficult dynamics are familiar: When narratives can have life-or-death consequences, which speculative futures come to be authorized as scientific, as appropriately cautious, and which are rendered fictional, or fake? In a moment when the interpretation of evidence has been compromised, such that large numbers of Americans deny the severity or even the very existence of the pandemic, the stakes are all too real.

Over the past year, we have become familiar with the challenge of ensuring a shared collective understanding and response to a rampaging microbe and the hard social work required to sustain mutually agreed upon futures in the midst of a pandemic. Contemporary "debates" over what is permissible or impermissible, a theory or a conspiracy theory, and the contested terrain of speculative futures and their long afterlives suggest that the ways in which even fictions circulate can reveal important truths. As Operation Warp Speed hastens us into a vaccinated future—our most amazing, cutting-edge science of vaccine development is both wrapped up with legacies of science fiction and also blessedly very real—a better understanding of the intertwined histories of scientific models and science fiction novels makes time a telling tincture.

*Editor's note:* This essay is derived from the George Sarton Memorial Lecture "Pandora's Pandemic: Infectious Futures at the Dawn of Genetic Engineering" delivered by Luis Campos at the 2021 American Association for the Advancement of Science Annual Meeting. A more detailed account, with references, is available in the "Strains of Andromeda: The Cosmic Potential Hazards of Genetic Engineering" chapter of *Nature Remade: Engineering Life, Envisioning Worlds* (University of Chicago Press, 2021). ■

## REFERENCES AND NOTES


1. J. Radin, *Osiris* **34**, 297 (2019).
2. H. G. Baker, G. Ledyard Stebbins, Eds., *The Genetics of Colonizing Species* (Academic Press, 1965).
3. M. Rogers, "The Pandora's Box Congress," *Rolling Stone*, 19 June 1975.
4. S. Wright, *Molecular Politics: Developing American and British Regulatory Policy for Genetic Engineering, 1972–1982* (Univ. of Chicago Press, 1994).
5. Regulation of Recombinant DNA Research: Hearings before the Subcommittee on Science, Technology, and Space, U.S. Senate, 95th Congress, 10 November 1977, Serial No. 95–52.
6. Recombinant DNA Regulation Act, 1977: Hearing before the Subcommittee on Health and Scientific Research, U.S. Senate, 95th Congress, First Session on S. 1217, 6 April 1977.
7. Stanford University Office of Technology Licensing, S74–035, Memo to File, 13 July 1976.
8. P. Berg, M. F. Singer, *Proc. Natl. Acad. Sci. U.S.A.* **92**, 9011 (1995).
9. M. Barinaga, *Science* **287**, 1584 (2000).
10. C. A. Mims, *Epidemiol. Infect.* **115**, 377 (1995).
11. W. D. Cohan, "Coronavirus gives investors an excuse to cut and run," *New York Times*, 2 March 2020.
12. A. Lane, "Our fever for plague movies," *New Yorker*, 15 May 2020.


10.1126/science.abg0479

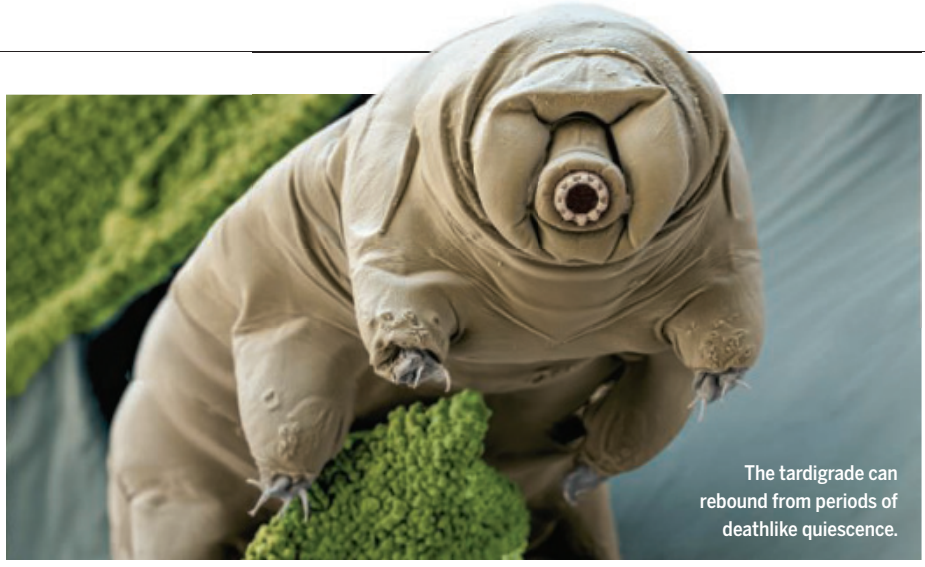

The tardigrade can rebound from periods of deathlike quiescence.

PHOTO: EYE OF SCIENCE/SCIENCE SOURCE

BIOLOGY

# Dispatches from life's blurry boundaries

## How we think about what it means to be alive will always depend on what questions we ask

By **Rob Dunn**

Carl Zimmer's *Life's Edge* is a departure from his previous work in that it is a book that is as much about what scientists have so far failed to understand as what they have come to understand. As its subtitle suggests, this book is about how life is defined, how life arose, and how we tell life from nonlife. These topics seem as though they would be of great concern to the field of biology—biology being, after all, the study of ("ology") life ("bio")—but they have rarely received much formal attention, occupying the scientific margins for hundreds of years and appearing on center stage every so often only to quickly retreat.

Zimmer begins with a story from the early 1900s in which a physicist named John Butler Burke synthesized "highly organized bodies" that resembled microbial colonies using radium and sterilized beef broth. Newspapers buzzed with exciting headlines, proclaiming that Burke had discovered the "secret of life." But the scientist's fame and success were short-lived, his discovery a false start. The book is full of such false starts, including the notable period during which the biologist Thomas Huxley became convinced that life evolved from a kind of primal slime that coats the bottom of the sea. (Spoiler alert: It did not.)

Superficially, the question "What is life?" seems resolvable. After all, as Zimmer points out in the book's first chapter, "experiments on animals," including chickens, "have revealed they can make some of the same distinctions between the living and the nonliving that we do." If poultry can make sense of the boundary between the living and the nonliving, how difficult could it be? Very difficult, it turns out.

At every boundary, life is blurry. When does the life of one generation begin and that of the previous generation end? Is a bacterial spore that is not metabolizing alive or dead or something else? If a human body is partially human cells and partially bacterial cells, and the bacterial cells go on living after the human cells have died, has the organism died? If some of the human cells go on living and dividing, has the human died? Zimmer shows that the more one searches for answers to these questions, the more such answers retreat.

Throughout the book, Zimmer illustrates how our behavior and our conceptions of birth, death, and organismal boundaries are very human-centric. For each species, these criteria are different, sometimes substantially so. The "bodies" of slime molds, for instance, can break apart, dry out, and drift in the wind when times are tough, only to reunite again under better circumstances.

One has the feeling, while reading this book, of fumbling through the unknown. In a section called "The Quickening," for example, Zimmer transitions from a careful discussion of the biological details of fertilization, to studies of species such as tardigrades that can enter life stages in which they are quiescent and neither dead nor fully alive, to research on when early human ancestors began to afford the dead special status by burying them. Meanwhile, the poems of Erasmus Darwin are set alongside Mary Shelley's *Frankenstein* and the chemistry of urea, to fascinating effect.

I found myself feeling very grateful that Zimmer had drawn connections among these disparate themes. We biologists are often necessarily narrow in our perspective. "To become an expert on just one kind of life can demand an entire career," Zimmer acknowledges. His breadth reveals more of the whole, however blurry, than would otherwise be available to the specialist.

There were also plenty of sections that made me wish that we were living in a time when dinner parties were possible, so that some of Zimmer's observations might be readily shared: details about the sex lives and intelligence of slime molds, the possibility that tardigrades are currently living on the Moon, and his descriptions of the expandable hearts of some snakes, for example.

By the end of this book, I felt challenged as a biologist to pull together my colleagues to talk about the big issues related to the limits of life, the origins of life, and the margins of life. We do not have these conversations often, probably partly because we are all so specialized, but also likely because the beginnings of life and the origins of life have become politicized.

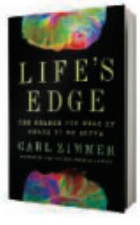


**Life's Edge: The Search for What It Means to Be Alive**
*Carl Zimmer*
Dutton, 2021. 368 pp.

To this latter point, Zimmer reminds readers that how we think about the boundaries of life will always depend on what questions we ask. Quoting the biologist Joshua Lederberg, he writes, "The question of when life begins is answered according to the purposes for which we ask it." By the end of the book, Zimmer had fully convinced me that the question of what it means to be alive is also best answered according to the purposes for which we ask—and that such inquiries will yield different outcomes depending on how we ask them. ■

10.1126/science.abg4672

The reviewer is at the Department of Applied Ecology, North Carolina State University, Raleigh, NC, USA, and the Center for Evolutionary Hologenomics, University of Copenhagen, Copenhagen, Denmark, and is the coauthor of *Delicious: The Evolution of Flavor and How It Made Us Human* (Princeton University Press, 2021). Email: rrdunn@ncsu.edu

CALL FOR PAPERS

SPJ
SCIENCE PARTNER JOURNALS

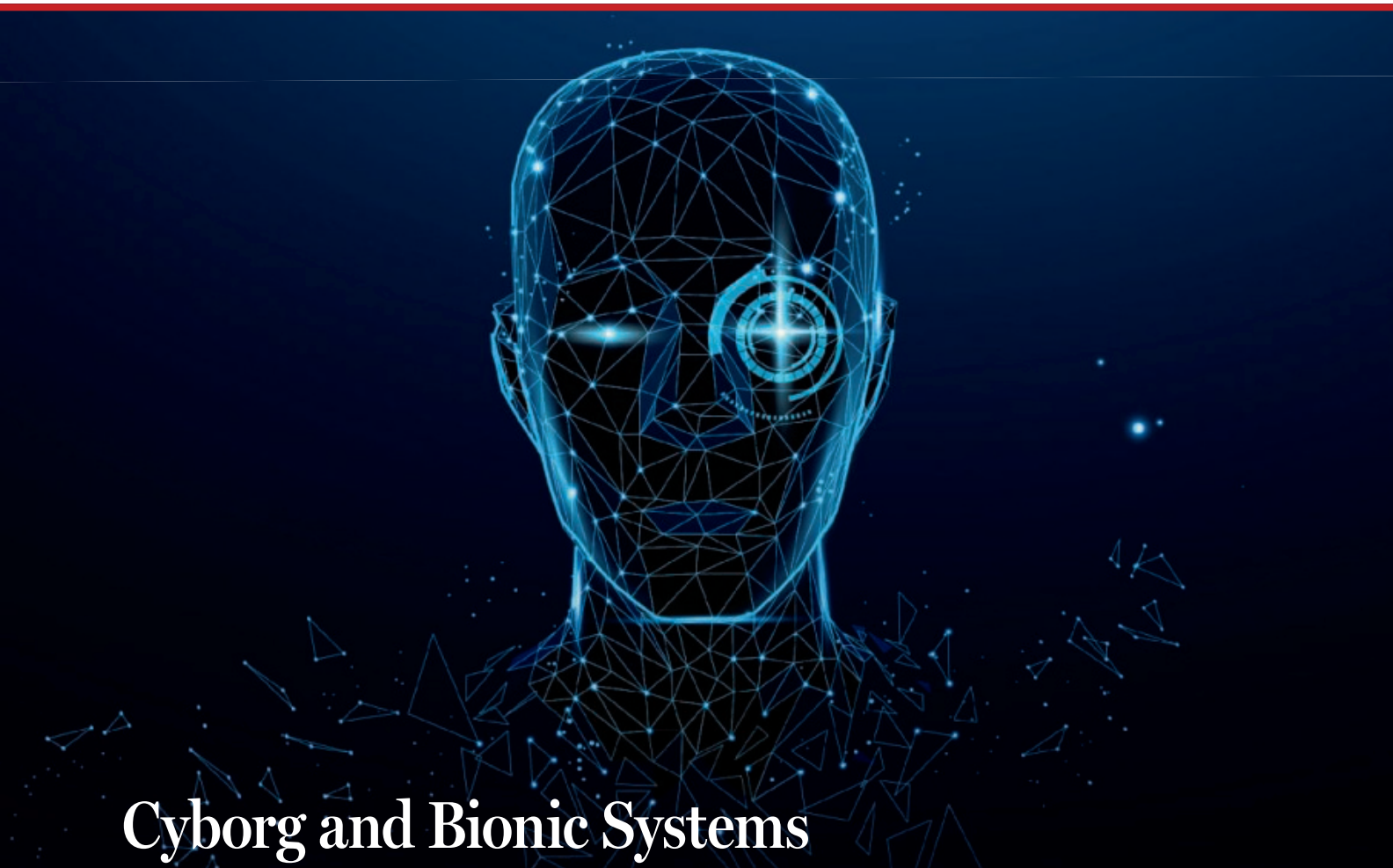

# Cyborg and Bionic Systems

*Cyborg and Bionic Systems* is an online-only, Open Access journal published in affiliation with the **Beijing Institute of Technology (BIT)** and distributed by the **American Association for the Advancement of Science (AAAS).** The journal publishes original, peer-reviewed articles based on fundamental, applied science, or their interaction. *Cyborg and Bionic Systems* promotes the knowledge interchange and hybrid system codesign between living beings and robotic systems. The journal also covers a wide range of fields related to cybernetic organisms (cyborg) and bionic systems (CBS), mainly including robotics, biomedical engineering and neuro-engineering.

**Submit your research to *Cyborg and Bionic System* today!**

Learn more at **spj.sciencemag.org/cbsystems**

The Science Partner Journal (SPJ) program was established by the American Association for the Advancement of Science (AAAS), the nonprofit publisher of the *Science* family of journals. The SPJ program features high-quality, online-only, Open Access publications produced in collaboration with international research institutions, foundations, funders and societies. Through these collaborations, AAAS furthers its mission to communicate science broadly and for the benefit of all people by providing top-tier international research organizations with the technology, visibility, and publishing expertise that AAAS is uniquely positioned to offer as the world's largest general science membership society.

Visit us at **spj.sciencemag.org**

**@SPJournals** **@SPJournals**

OPEN ACCESS

ARTICLE PROCESSING CHARGES WAIVED UNTIL JULY 2023

LETTERS

Australia's iconic koala is threatened with extinction, in part as a result of habitat loss.

PHOTO: BRIANO/WWF-AUS

*Edited by* **Jennifer Sills**

# Australia faces environmental crisis

A decade ago, an Australian report outlined changes the country must make to halt the decline and loss of species (*1*), but the reforms were never implemented. In the years since, most threatened species have continued to decline, and at least three have gone extinct (*2*, *3*). Since the year 2000, more than 7.7 million hectares of threatened species habitat have been destroyed (*4*). Last month, the Australian government released a report that examined Australia's ongoing failure to tackle the species extinction crisis and offered recommendations (*5*). Australia's minister for the environment has committed to work through the full detail of the recommendations (*6*), but there are already worrying signs that they will be ignored. The Federal Government of Australia must protect and preserve nature as required by international agreements (*7*). Without fundamental policy reforms, Australia—a megadiverse country home to about 600,000 species (*8*)—risks mass species extinction.

The most urgent action Australia must take is to establish legally binding National Environmental Standards that are rigorously enforced and underpinned by Indigenous engagement and participation. An Environment Assurance Commissioner should be appointed, one that is responsible for overseeing and auditing government decision-making in accordance with the Standards (*5*). This would improve accountability, transparency, and trust in government. In addition, an independent body should be created to be responsible for monitoring and enforcing compliance with the environmental legislation, a suggestion that has already been dismissed (*9*). Levels of government funding for appropriate environmental management and restoration are insufficient to address Australia's extinction crisis (*10*). Adequate resources must urgently target threatened species recovery. Alongside more funding, existing environmental laws need to be reviewed to close loopholes, such as the one in the current law that effectively grants an exemption to all native forest logging (*5*), threatening hundreds of species (*2*, *3*).

Assessments of the state of Australia's imperiled species show that the government is running out of time (*11*). At least 1807 species are now listed as threatened with extinction, with 290 considered on the very brink, listed as Critically Endangered and on the fast track to extinction (*2*, *3*). The Australian scientific community has been increasingly vocal about the ineffectiveness of Australian environmental legislation for achieving its objectives (*4*, *10*, *12*) and preventing the likelihood of an extinction crisis (*10*), but these calls have been ignored. It is time for Australia's government to heed the calls of scientists and implement urgent, wide-ranging, and reformative policies before it is too late.

**Michelle Ward[1,2,3]*, Shayan Barmand[4], James Watson[1,2], Brooke Williams[1,2]**

[1]Centre for Biodiversity and Conservation Science, The University of Queensland, St. Lucia, QLD 4072, Australia. [2]School of Earth and Environmental Sciences, The University of Queensland, Brisbane, QLD 4072, Australia. [3]World Wildlife Fund–Australia, Brisbane, QLD 4000, Australia. [4]African Climate and Development Initiative, University of Cape Town, Rondebosch, 7700, South Africa.
*Corresponding author. Email: m.ward@uq.edu.au

## REFERENCES AND NOTES

1. A. Hawke, "The Australian Environment Act—Report of the independent review of the Environment Protection and Biodiversity Conservation Act 1999" (Australian Government Department of the Environment, Water, Heritage and the Arts, Canberra, 2009).
2. Commonwealth of Australia, EPBC Act List of Threatened Fauna (2019); www.environment.gov.au/cgi-bin/sprat/public/publicthreatenedlist.pl?wanted=fauna.
3. Commonwealth of Australia, EPBC Act List of Threatened Flora (2019); www.environment.gov.au/cgi-bin/sprat/public/publicthreatenedlist.pl?wanted=flora.
4. M. Ward *et al.*, *Conserv. Sci. Pract.* **1**, e117 (2019).
5. G. Samuel, "Independent review of the EPBC Act – Final report" (Canberra, Australia, 2020).
6. Commonwealth of Australia, "Review supports reform for environmental laws" (2021); https://minister.awe.gov.au/ley/media-releases/review-supports-reform-environmental-laws.

7. Secretariat of the Convention on Biological Diversity, "Preparations for the Post-2020 Biodiversity Framework" (2020).
8. A. D. Chapman, "Number of living species in Australia and the World" (Department of the Environment, Water, Heritage, the Arts, 2009).
9. Commonwealth of Australia, "Reform for Australia's environment laws" (2020); https://minister.awe.gov.au/ley/media-releases/reform-australias-environment-laws.
10. B. Wintle *et al.*, *Conserv. Lett.* **12**, e12682 (2019).
11. I. D. Cresswell, H. T. Murphy, "Australia state of the environment 2016: Biodiversity (Independent report to the Australian Government Minister for the Environment and Energy)" (Canberra, Australia, 2016).
12. Australian Academy of Science, "Academy Fellows say it's time to establish an independent biodiversity agency" (2020); www.science.org.au/news-and-events/news-and-media-releases/academy-fellows-time-establish-independent-biodiversity-agency.

10.1126/science.abg9225

# Vaccine efficacy probable against COVID-19 variants

The U.S. Food and Drug Administration (FDA) emergency use authorization of three vaccines, all of which have shown greater than 85% effectiveness against severe acute respiratory syndrome coronavirus 2 (SARS-CoV-2) (*1*–*3*), has provided the public with the hope of ending the global COVID-19 pandemic. However, recent outbreaks of more transmissible variant SARS-CoV-2 strains that harbor mutations in the spike protein—the critical viral target of immune responses produced by the vaccines (*1*–*3*)—has invited a dour outlook on the vaccines' continued efficacy (*4*). The trepidation is based on the prompt compilation of in vitro data that demonstrate as much as 10-fold reduction in neutralization antibody (NAb) activity in vaccinated samples against mutant spike protein pseudovirus (*5*, *6*), which is thought to be an important metric of acquired immunity (*7*). Although reports of NAb reduction are alarming in magnitude, the proof of vaccine effectiveness can only be measured definitively by challenging vaccinated subjects with infection.

Vaccine efficacy measured by infection challenge experiments using non-human primates is often prerequisite to clinical trials, but these data are seldom articulated in lay reports. For example, in the Moderna-1273 vaccine trial (*8*), nonhuman primates received a 10-microgram dose [10% of the dose recommended for humans by the FDA (*9*)] or a 100-microgram dose (100% of the FDA dose), and researchers found a mean NAb titer of about 300 or about 3500, respectively. Despite the difference in NAb levels, both doses conferred substantial protection from infection, as measured by viral particle titers and prevention of respiratory pathology. Similar data were obtained using the Pfizer (*10*) and Johnson & Johnson (*11*) vaccines. Importantly, vaccinated samples have been tested using pseudoviral particles that express each of the SARS-CoV-2 variant spike proteins, and in each case, the samples appear to exhibit NAb titers greater than 300 in vitro (*12*), suggesting that vaccines will be effective against mutant strains.

These studies show that what appears to be magnitudes of difference in NAb activity may not necessarily correlate with clinical immunity. As variant strains emerge, we will need to reevaluate vaccine efficacy by testing the inhibition of viral infection in vivo rather than by quantifying the antibodies produced after in vitro exposure. Reliable proof of immunity through vaccination may only come through reinfection challenge experiments or through longitudinal studies of post-vaccination subjects.

**Larry L. Luchsinger* and Christopher D. Hillyer**
Lindsley F. Kimball Research Institute, New York Blood Center, New York, NY 10065, USA.
*Corresponding author.
Email: lluchsinger@nybc.org

### REFERENCES AND NOTES

1. F. P. Polack *et al.*, *N. Engl. J. Med.* **383**, 2603 (2020).
2. L. R. Baden *et al.*, *N. Engl. J. Med.* **384**, 403 (2021).
3. J. Sadoff *et al.*, *N. Engl. J. Med.* 10.1056/NEJMoa2034201 (2021).
4. A. S. Lauring, E. B. Hodcroft, *JAMA* **325**, 529 (2021).
5. M. S. Graham *et al.*, *medRxiv*, 10.1101/2021.01.28.21250680 (2021).
6. P. Wang *et al.*, *bioRxiv*, 10.1101/2021.01.25.428137 (2021).
7. L. A. VanBlargan, L. Goo, T. C. Pierson, *Microbiol. Mol. Biol. Rev.* **80**, 989 (2016).
8. K. S. Corbett *et al.*, *N. Engl. J. Med.* **383**, 1544 (2020).
9. ModernaTX, Inc., "Fact sheet for healthcare providers administering vaccine (vaccination providers)" (2020); www.modernatx.com/covid19vaccine-eua/eua-fact-sheet-providers.pdf.
10. A. B. Vogel *et al.*, *bioRxiv*, 10.1101/2020.09.08.280818 (2020).
11. N. B. Mercado, *Nature* **586**, 583 (2020).
12. K. Wu *et al.*, *bioRxiv*, 10.1101/2021.01.25.427948 (2021).

10.1126/science.abg9461

# China needs better postdoctoral policy

In December 2020, the Ministry of Human Resources and Social Security of China and the National Postdoctoral Management Committee met to emphasize the importance of training postdoctoral fellows to maintain international competitiveness in science and technology (*1*). To this end, major cities and well-known universities and institutes in China are increasing recruiting efforts, offering high wages to attract more domestic and international postdocs (*2*, *3*). However, before increasing the number of postdocs in China, the country should formulate more effective policies to protect the interests of postdoctoral fellows.

In addition to adequate salaries, postdocs need a stable scientific research environment and fair promotion channels. In many Chinese colleges and universities, postdoc training is focused only on generating publishable papers that can quickly improve the university's academic rankings (*4*). In addition, for most colleges and universities in China, overseas education is a prerequisite for permanent positions, making it difficult or impossible for their own postdocs to obtain tenure-track positions (*5*). Industry and government departments also hesitate to pay well-trained postdoctoral scientists the salaries they deserve (*6*), even if hiring them would improve the level of scientific research and policy-making.

Without effective training and job prospects, Chinese postdocs are not likely to become the main force of scientific research and innovation, despite their dedication and long work hours. China must take steps to improve the mentorship postdocs receive, and universities, industry, and government must reassess hiring practices to place more value on domestic postdoctoral experience. In addition, China should facilitate better communication between postdoctoral fellows in China and researchers in the United States and Europe to broaden the global vision of local scientists.

**Guo-Qian Yang**
School of Agriculture and Biology, Shanghai Jiao Tong University, Shanghai 200240, China. Email: guoqian.yang@sjtu.edu.cn

### REFERENCES AND NOTES

1. "The 35th anniversary symposium on the implementation of China's postdoctoral system was held in Beijing" (2020); www.chinapostdoctor.org.cn/website/showinfo_zcwj.html?infoid=f4da097e-cfe6-4f8e-87d6-1a1cc985ab58 [in Chinese].
2. "2021 Shenzhen high-level professional talent recognition rewards and subsidies, national and local-level leading talents, and reserve-level talent certification standards" (2021); www.gaoxinbutie.com/rending/#opennewwindow [in Chinese].
3. Qingta Products, "With a million-yuan salary for postdoctoral fellows, there is a 'big money'; is there a bright future?" (2021); www.cingta.com/detail/19354 [in Chinese].
4. Zhang Duanhong, "Stop making postdocs a tool for universities to improve short-term research performance" (*Science China Press*, 2020); http://news.sciencenet.cn/htmlnews/2020/3/437712.shtm [in Chinese].
5. J. Zeng *et al.*, *Modern Educ. Manag.* **10**, 73 (2016) [in Chinese].
6. W. Zhang, *Chin. Youth Stud.* **000**, 21 (2014) [in Chinese].

10.1126/science.abg6881

# RESEARCH

## IN *SCIENCE* JOURNALS

*Edited by* **Michael Funk**

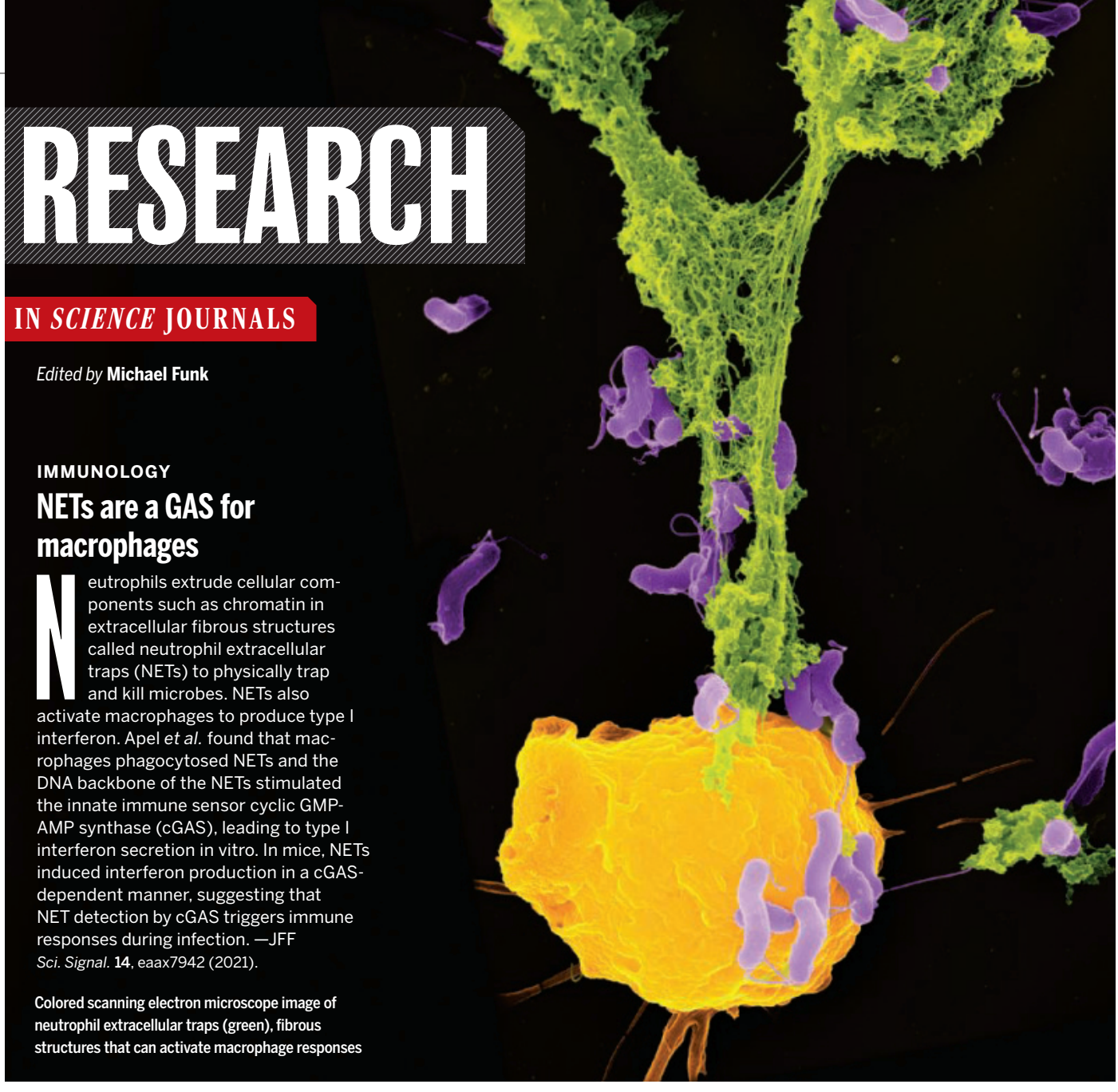

CREDIT: VOLKER BRINKMANN/ MAX PLANCK INSTITUTE FOR INFECTION BIOLOGY

**Colored scanning electron microscope image of neutrophil extracellular traps (green), fibrous structures that can activate macrophage responses**

IMMUNOLOGY

### NETs are a GAS for macrophages

Neutrophils extrude cellular components such as chromatin in extracellular fibrous structures called neutrophil extracellular traps (NETs) to physically trap and kill microbes. NETs also activate macrophages to produce type I interferon. Apel *et al.* found that macrophages phagocytosed NETs and the DNA backbone of the NETs stimulated the innate immune sensor cyclic GMP-AMP synthase (cGAS), leading to type I interferon secretion in vitro. In mice, NETs induced interferon production in a cGAS-dependent manner, suggesting that NET detection by cGAS triggers immune responses during infection. —JFF

*Sci. Signal.* **14**, eaax7942 (2021).

OPTOELECTRONICS

### Spin injection sans magnetism

Light-emitting diodes (LEDs) that emit circularly polarized light (spin-LEDs) have potential applications in in three-dimensional displays, bioencoding, and tomography. The requisite spin polarization of the charge carriers is usually achieved with ferromagnetic contacts and applied magnetic fields, but Kim *et al*. report on a room-temperature spin-LED that relies instead on a chiral-induced spin selectivity organic layer. This layer selectively injected spin-polarized holes into metal halide perovskite nanocrystals, where they radiatively recombined with unpolarized electrons with an efficiency of 2.6%. —PDS

*Science*, this issue p. 1129

QUANTUM GASES

### A supersolid rotation

When a bucket of water is rotated, the water rotates with the vessel, contributing to the total moment of inertia. If such an experiment were done with a superfluid, it would decouple from the vessel and would not contribute to rotation. Tanzi *et al*. studied an intermediate case, a supersolid, which is predicted to only partially decouple, resulting in a moment of inertia smaller than the classical value. Whereas previous such experiments were done with helium, the authors used a gas of highly magnetic dysprosium atoms in an optical trapping potential that was suddenly changed, causing the gas to oscillate. Measuring the frequency of these oscillations provides evidence for a reduced moment of inertia. —JS

*Science*, this issue p. 1162

CORONAVIRUS

### Eluding detection

Influenza viruses evade immunity initiated by previous infection, which explains recurrent influenza pandemics. Unlike the error-prone RNA-dependent RNA polymerase of influenza, severe acute respiratory syndrome coronavirus 2 (SARS-CoV-2) and related viruses contain polymerases with proofreading activity. However, proofreading cannot correct deletions, which during a long-term persistent infection could result in the generation of viruses showing alteration of

entire stretches of amino acids and the structures they form. McCarthy *et al*. identified an evolutionary signature defined by prevalent and recurrent deletions in the spike protein of SARS-CoV-2 at four antigenic sites. Deletion variants show human-to-human transmission of viruses with altered antigenicity. —CA

*Science*, this issue p. 1139

IMMUNOTHERAPY

## Diabodies see the unseeable

*RAS* oncogene mutations are common in various cancers, controlling their growth and survival. Targeting mutant RAS proteins with antibodies has been unsuccessful because of low surface expression, even when targeting mutant RAS peptides presented by human leukocyte antigen (HLA) on the surface of cancer cells. Douglass *et al.* used phage display to generate single-chain variable fragments (scFvs) specific for mutant RAS peptide-HLA complexes. The authors tested various bispecific, T cell–engaging antibody formulations, finding that single-chain diabodies (scDbs) combining the aforementioned scFv with an anti-CD3 scFv were able to induce T cell activation and subsequent killing of tumor cells expressing mutant RAS peptide-HLA complexes. This scDb approach opens the door for antibody-based therapies against mutant neoantigens expressed at very low levels on the surface of cancer cells. —DAE

*Sci. Immunol.* **6**, eabd5515 (2021).

SYNTHETIC BIOLOGY

## Designing smarter anticancer T cells

Biological signaling systems can exhibit a large, nonlinear—or "ultrasensitive"—response, which would be useful to engineer into therapeutic T cells to allow for better discrimination between cancer cells and normal tissues. Hernandez-Lopez *et al*. modified human T cells using a two-step mechanism that allowed them to kill cells expressing large amounts of cancer marker protein but not cells expressing a small amount of the same protein. A first synthetic receptor recognized the antigen with low affinity. That receptor signaled to increase expression of a chimeric antigen receptor (CAR) with high affinity for the same antigen. The circuit proved effective in cell culture and mouse cancer models, offering hope of extending the CAR T cell strategy against solid tumors. —LBR

*Science*, this issue p. 1166

NANOMATERIALS

## Hydrogenating borophene

The two-dimensional material borophene, which is formed on silver surfaces, has a diverse polymorphism and is predicted to have unusual materials and electronic properties. However, it is highly unstable outside of ultrahigh vacuum conditions and oxidizes readily, which hampers exploration of its properties. Li *et al*. hydrogenated these materials with atomic hydrogen and showed that borophane has a lower local work function. This material is stable for days in air, and borophene can be recovered simply by thermally driving off the hydrogen. —PDS

*Science*, this issue p. 1143

INORGANIC CHEMISTRY

## Calcium catches dinitrogen

Although lithium reduces dinitrogen, the other alkali and alkaline Earth metals have proven largely inert to the gas under ambient conditions. Rösch *et al*. report that with just the right β-diketiminate ligand and an assist from potassium as terminal reductant, calcium can mediate dinitrogen reduction. Crystallography and spectroscopic characterization revealed a product in which doubly reduced dinitrogen adopted a side-on bridging motif between two calcium centers. A subsequent reaction with coordinated tetrahydrofuran appeared to release diazene. —JSY

*Science*, this issue p. 1125

# IN OTHER JOURNALS

*Edited by* **Caroline Ash** *and* **Jesse Smith**

SOCIAL COMMUNICATION

## Rays of communication

Sociality requires communication among individuals and is common across species. Identifying modes of communication in some systems and species, however, is much less straightforward than in others. Aquatic environments present challenges for communication, especially for species that are nonvocal, such as many fishes. Elasmobranchs are increasingly being shown to have a complex social structure, and manta rays (*Mobula* spp.) exhibit many different social behaviors. Perryman *et al.* characterized the associations between the cephalic lobes in reef mantas, organs known to assist feeding, and various social and behavioral conditions. The authors found clear relationships between specific lobe positions and interactions with other rays, cleaning fishes, and even human divers. These patterns suggest that they may be used in communication, although whether this communication is positional or chemical remains to be seen. —SNV

*Behav. Ecol. Sociobiol.* **75**, 51 (2021).

TOPOLOGICAL MATERIALS

## Photonic crystals with a touch of topology

Manmade photonic crystals offer a flexible platform for controlling the propagation and flow of light. Such control can be extended across the electromagnetic spectrum by correctly engineering the bandgap. Limitations in the fabrication process, however, can result in structural imperfections that allow the light or energy to leak out. Wang *et al.* add magnetism to the mix to form heterostructures of magnetic photonic crystals. They demonstrate that, for microwaves, this magnetic addition provides a topological aspect to the band structure, resulting in the propagation of the microwaves in one direction that is robust to defects. The ability to controllably route and collimate electromagnetic waves also could be applied to electronic and phononic waveguide systems. —ISO

*Phys. Rev. Lett.* **126**, 067401 (2021).

CELL BIOLOGY

## A tight squeeze?

HIV-1 remains a clinically important challenge. The cell biology of HIV-1 is now quite well understood. The viral RNA is packaged within capsids consisting of 120-nanometer–by–60-nanometer cone-shaped particles, which make their way to the nucleus to allow viral replication. The nuclear envelope is studded with nuclear pores with an internal diameter of only about 40 nanometers. Zila *et al.* used correlative light and electron microscopy and subtomogram averaging to study viral capsids en route to the nucleus. Working with infected T cells, the authors unexpectedly found that the nuclear pore complex was able to dilate sufficiently to allow the

PHOTO: TUI DE ROY/MINDEN PICTURES

Reef manta rays appear to use the lobes on either side of their mouths to signal to other rays.

intact viral capsid to translocate into the nucleus. After translocation, rather than disassembling in an orderly fashion, the capsids ruptured, releasing the viral RNA into the nuclear interior. This detailed view of a key step in productive infection illustrates the power of recent advances in three-dimensional correlative fluorescence light and electron microscopy with cryo–electron tomography for increasing mechanistic understanding of intracellular events. —SMH

*Cell* **184**, 1032 (2021).

CELL BIOLOGY

## Catching the action on the cell

For many proteins, specific proteolysis events are key to their function. This extends to the cell surface, where proteolysis of cell surface proteins can regulate communication between cells. There are several methods to isolate N-terminal peptides derived from proteolytic cleavage, but existing methods do not efficiently detect cleavage of cell surface proteins. Weeks *et al.* started with an enzyme called subtiligase, a tool developed to modify N termini, and fused it to a transmembrane domain to target it to the cell surface (subtiligase-TM). The subtiligase biotinylates the N termini, which can then be isolated and sequenced by mass spectrometry. This method can be used for identifying therapeutic targets and biomarkers. —VV

*Proc. Natl. Acad. Sci. U.S.A.* **118**, e2018809118 (2021).

FERROELECTRICS

## A way to shrink RAM

External electric fields can change the polarization of ferroelectric materials. One application of this effect involves random access memory. Du *et al.* discovered multiple polarization orders in hafnium oxide colloidal nanocrystals. Crystallographic twinning creates an interesting polarization structure at the twin boundary with nanometer-sized ferroelectric and antiferroelectric phases, potentially allowing for a much higher information storage density. The structure occurs without symmetry changes and may not be restricted to oxides. —BG

*Matter* 10.1016/j.matt.2020.12.008 (2021).

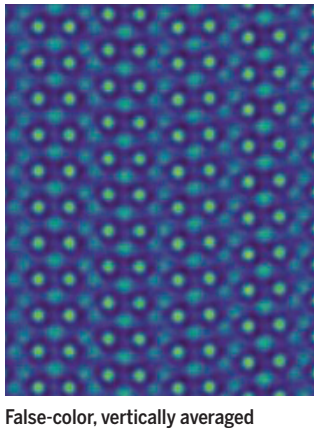

False-color, vertically averaged atomic-resolution transmission electron microscopy image of $HfO_2$

IMAGE: DU *ET AL.*, *MATTER* 10.1016/J.MATT.2020.12.008 (2021)

IMMUNE SIGNALING

## Shedding light on TCR activation

In mammals, T cells recognize fragments of pathogen and other alien peptide antigens using T cell receptors (TCRs). Loaded TCRs then interact with the polymorphic cell surface proteins of the major histocompatibility complexes of antigen-presenting cells, activating killing processes. O'Donoghue *et al.* engineered $CD4^+$ T cells with an optogenetic chimeric antigen receptor stimulated by blue light. This technique provides an experimental on–off switch with which to precisely control the TCR-signaling machinery. The authors could distinguish between the signals induced by self and foreign antigens, the latter inducing CD69, a marker of T cell activation. —STS

*Proc. Natl. Acad. Sci. U.S.A.* **118**, e2019285118 (2021).

WEATHER FORECASTING

## Better predictions with water isotopes

Knowing the water isotopic makeup of the mid-troposphere can substantially improve weather forecasts. Toride *et al.* show that the incorporation of mid-tropospheric water isotope data collected by the Infrared Atmospheric Sounding Interferometer (IASI) into a weather model can improve its representation of parameters such as wind, humidity, and temperature. This allows the heating structure and large-scale circulation of the atmosphere to be better determined, leading to more accurate weather predictions. —HJS

*Geophys. Res. Lett.* **48**, e2020GL091698 (2021).

REVIEW SUMMARY

NATURAL HAZARDS

# Investigating a tsunamigenic megathrust earthquake in the Japan Trench

Shuichi Kodaira*, Takeshi Iinuma, Kentaro Imai

**BACKGROUND:** Ten years have passed since the 2011 Tohoku-oki earthquake occurred in the Japan Trench, where the Pacific plate subducts beneath the continental plate. The earthquake and tsunami caused enormous damage along the coast of northeast Japan in the Tohoku region, and local communities are still recovering. Tsunami traces more than 10 m above sea level were observed along 530 km of coastline in central and northeast Japan, and runups higher than 20 m were observed over about 200 km of the Tohoku coast. The tsunami inundated an area of 561 $km^2$, and its runup reached a maximum of 40 m in northern Tohoku. These statistics made it one of the largest tsunamis ever recorded in historical literature as well as in geological records.

The earthquake occurred in the vicinity of the world's most densely instrumented seismic, geodetic, and tsunami observation networks, which clearly recorded the dramatic geodynamic effects of the earthquake. In addition, geophysical and geological data were acquired offshore, in the rupture zone, before and after the earthquake. These marine observations are decisive ground-truth data showing that coseismic slip exceeded 50 m in places and that the rupture reached the shallowest parts of the megathrust fault in the subduction zone.

**ADVANCES:** Geodetic data from the seafloor before and after the earthquake, from the Global Navigation Satellite System–Acoustic combination technique, show that the seafloor near the epicenter underwent coseismic displacement of 31 m toward the southeast and had an uplift of 3 m. Differential bathymetric mapping, comparing the seafloor before and after the earthquake, inferred a coseismic seafloor displacement of more than 50 m at the trench axis. A rapid-response deep-sea drilling project successfully collected material from the earthquake's rupture zone on the plate boundary fault near the trench and measured the thermal anomaly due to frictional heating of the fault during coseismic slip. This showed that the plate boundary fault is rich in weak layers of clay and suggested that thermal pressurization within the clay layers promoted the exceptionally large coseismic fault slip. These ground-truth data provided evidence to constrain a slip behavior in a shallow part of the subduction zone. Crucial progress in determining the coseismic slip character is represented by the evidence showing lateral variations of coseismic slip near the trench and possible structural factors to control the lateral variation. For example, no resolvable coseismic seafloor displacement from differential bathymetry was observed at the north and south of the main rupture zone, and seismic images showed lateral discontinuity of a pelagic clay layer due to subduction of petite-spots at the north of the main rupture zone.

**OUTLOOK:** Crustal deformation, including afterslip and viscoelastic relaxation of the mantle, continues in the Japan Trench 10 years after the earthquake. Viscoelastic relaxation is predominant in the central part of the trench, where the large coseismic slip extended to the trench. The relaxation displaces this seafloor westward, whereas afterslip displaces it eastward around the main rupture zone. These observations, along with aftershock activity from normal fault earthquakes in the incoming oceanic plate, indicate that trench-normal extension remains in the oceanic plate and seaward of the main rupture zone. The recurrance probability of a great earthquake (magnitude = ~9) in the Japan Trench in the near future is very low, but even 10 years after the Tohoku-oki earthquake, seismic activities in east Japan, including the trench outer-slope and surrounding areas of the main rupture zone, are still higher than those before the earthquake. Because past observations show that large normal fault earthquakes in the incoming oceanic plate can occur after great plate-boundary earthquakes, further investigations into the temporal changes in the stress state around the Japan Trench are necessary to evaluate the possibility of such a "follow-up" earthquake in the incoming Pacific plate. ■

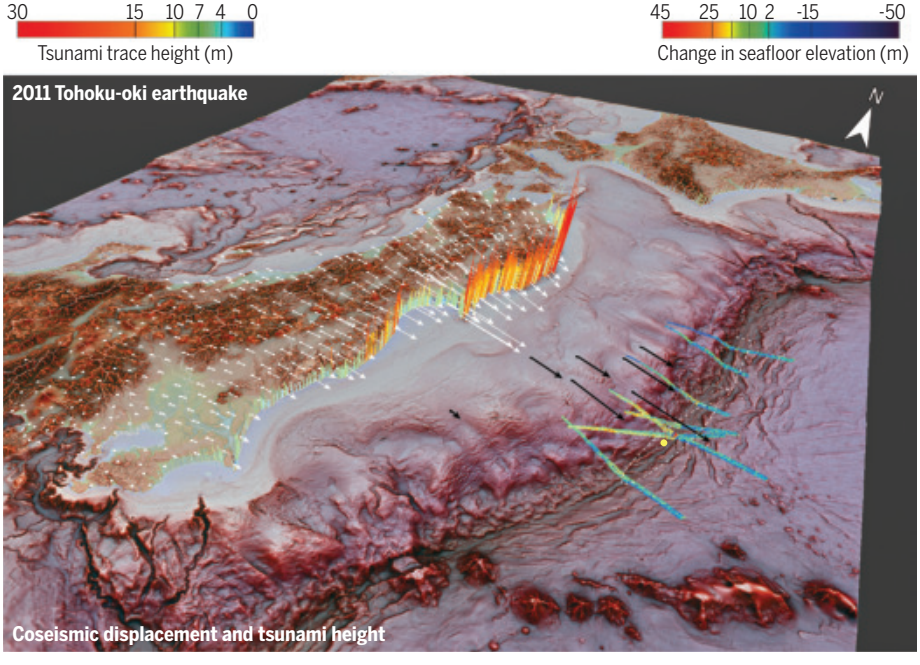


**Coseismic displacement and tsunami height of the 2011 Tohoku-oki earthquake.** Oblique view of northern Japan and the Japan Trench showing coseismic displacements (black and white arrows), tsunami heights (colored bars), and differential bathymetry profiles across the trench (multicolored lines). The scale of the onland displacements is five times as large as those of the seafloor displacements. Dashed areas indicate approximate areas where a set of three turbidite layers attributed to the Tohoku-oki earthquake and past large events are observed (ellipse) and where a deformed and altered pelagic clay layer by a petit-spot volcanism is inferred from seismic images (half-rectangle), respectively. A yellow circle indicates the location of the Japan Trench Fast Drilling Project (JFAST) site.

Japan Agency for Marine-Earth Science and Technology (JAMSTEC), Yokohama, Japan
*Corresponding author. Email: kodaira@jamstec.go.jp
Cite this article as S. Kodaira *et al.*, *Science* **371**, eabe1169 (2021). DOI: 10.1126/science.abe1169

RESEARCH ARTICLE SUMMARY

IMMUNOLOGY

# Lipid presentation by the protein C receptor links coagulation with autoimmunity

**Nadine Müller-Calleja, Anne Hollerbach, Jennifer Royce, Svenja Ritter, Denise Pedrosa, Thati Madhusudhan, Sina Teifel, Myriam Meineck, Friederike Häuser, Antje Canisius, T. Son Nguyen, Johannes Braun, Kai Bruns, Anna Etzold, Ulrich Zechner, Susanne Strand, Markus Radsak, Dennis Strand, Jian-Ming Gu, Julia Weinmann-Menke, Charles T. Esmon, Luc Teyton, Karl J. Lackner*, Wolfram Ruf***

**INTRODUCTION:** Antiphospholipid antibodies (aPLs) transiently appear in infectious diseases but can persist in primary antiphospholipid syndrome (APS) or in association with other autoimmune diseases, including lupus erythematosus. Clinical manifestations of APS range from venous thrombosis and stroke to severe microangiopathic organ damage and pregnancy complications. The activation of coagulation and complement cascades is crucial for the pathogenic effects of aPLs as well as for their proinflammatory cell signaling in innate immune, vascular endothelial, and embryonic trophoblast cells. However, the diverse reactivity of aPLs with negatively charged lipids and with blood proteins has hampered the identification of the central mechanism(s) underlying aPL pathogenic signaling.

**RATIONALE:** Lipid-reactive aPLs sensitize innate immune cells to toll-like receptor 7 (TLR7) agonists and up-regulate the coagulation initiator tissue factor (TF). TF-dependent signaling by protease-activated receptor 2 (PAR2) involves the endothelial protein C receptor (EPCR, encoded by *PROCR*), and this signaling complex specifically participates in interferon (IFN) responses downstream of TLR4. Because aPLs are potent inducers of IFN-α production by dendritic cells, we tested the hypothesis that EPCR contributes to APS pathologies and the development of aPL autoimmunity.

**RESULTS:** We found that EPCR serves as the cell surface receptor for aPLs and mediates aPL internalization following a previously delineated TF–integrin trafficking route in monocytes. Knock-in mutagenesis of the EPCR intracellular cysteine residue in *Procr*$^{C/S}$ mice abolishes aPL endosomal trafficking and aPL proinflammatory and IFN signaling in innate immune cells. We show that these mutant mice have a defect in the ability to exchange phosphatidylcholine structurally bound to EPCR with a late endosomal lipid, lysobisphosphatidic acid (LBPA). This exchange requires ALG-2-interacting protein X (ALIX)–dependent endolysosomal sorting. aPL binding specifically to cell surface EPCR-LBPA disrupts an inhibited TF complex and thereby induces coagulation activation that elicits autocrine PAR signaling in monocytes. This initial aPL effect translocates acid sphingomyelinase (ASM) to the cell surface, where it is activated by EPCR-LBPA to alter the procoagulant membrane properties of monocytes. Stereoselective LBPA loading of EPCR is also required for aPL signaling in embryonic trophoblast cells. *Procr*$^{C/S}$ mice or mice treated with a specific function-blocking antibody to EPCR-LBPA are protected from aPL-induced thrombosis and fetal loss. Notably, EPCR-LBPA engagement not only promotes the detrimental pathological consequences of aPLs but also drives dendritic cell IFN-α production for expansion of aPL-producing B1a cells. In an experimental model of APS, *Tlr7*$^{-/-}$ and *Procr*$^{C/S}$ mice cannot expand B1a cells responsible for production of lipid-reactive aPLs. Blockade of EPCR-LBPA signaling is sufficient to prevent the development of aPLs in mice with a TLR7-dependent systemic lupus erythematosus–like syndrome. Moreover, lupus-associated kidney pathology is markedly attenuated by the inhibition of EPCR-LBPA signaling.

**CONCLUSION:** Pathogenic aPLs recognize a single cell-surface lipid–protein receptor complex that is positioned at the intersections of coagulation and innate immune signaling and involved in the regulation of antimicrobial host defense. Specific blockade of this target not only prevents the pathological consequences of aPLs in vivo but also impairs a self-amplifying autoimmune signaling loop contributing to the development of APS autoimmunity. ■

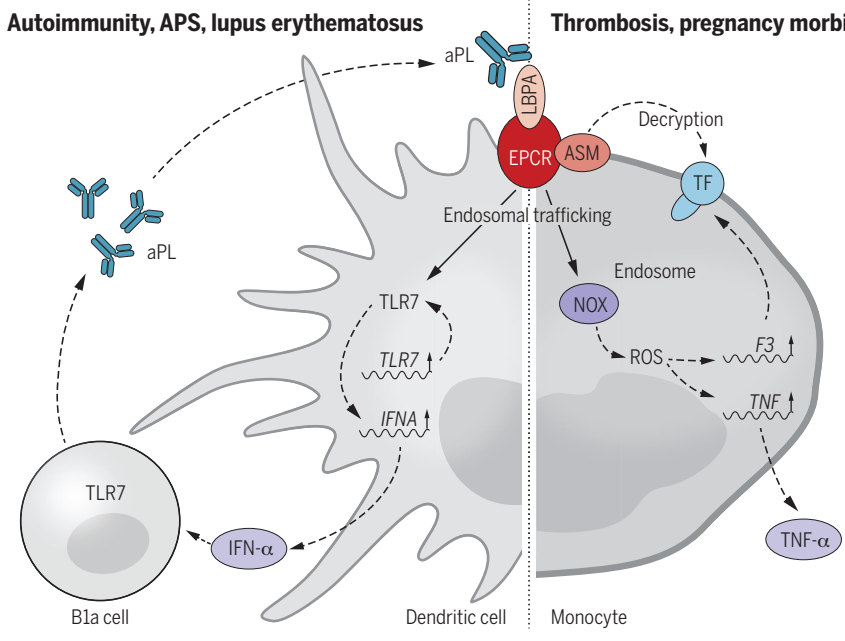


**The recognition of EPCR-LBPA by aPLs promotes autoimmunity.** The interaction of aPLs with EPCR-LBPA promotes activation of embryonic trophoblast cells, monocytes, and dendritic cells. (Right) On monocytes, disruption of the inhibitory control of the coagulation initiator TF induces cellular activation through PAR signaling, which is responsible for recruiting ASM to the cell surface. EPCR-LBPA activation of ASM then causes procoagulant lipid exposure and aPL endosomal trafficking. The subsequent up-regulation of tumor necrosis factor (TNF) and TF is central to thrombosis and pregnancy complications. (Left) In addition, aPL induction of IFN-α in dendritic cells sustains a TLR7-dependent expansion of aPL-producing B1a cells and thereby promotes autoimmunity. NOX, nicotinamide adenine dinucleotide phosphate oxidase; ROS, reactive oxygen species.

The list of author affiliations is available in the full article online.
*Corresponding author. Email: karl.lackner@unimedizin-mainz.de (K.J.L.); ruf@uni-mainz.de (W.R.)
Cite this article as N. Müller-Calleja *et al.*, *Science* **371**, eabc0956 (2021). DOI: 10.1126/science.abc0956

READ THE FULL ARTICLE AT
https://doi.org/10.1126/science.abc0956

RESEARCH ARTICLE SUMMARY

MICROBIOLOGY

# Type III secretion system effectors form robust and flexible intracellular virulence networks

David Ruano-Gallego*, Julia Sanchez-Garrido*, Zuzanna Kozik, Elena Núñez-Berrueco, Massiel Cepeda-Molero, Caroline Mullineaux-Sanders, Jasmine Naemi-Baghshomali Clark, Sabrina L. Slater, Naama Wagner, Izabela Glegola-Madejska, Theodoros I. Roumeliotis, Tal Pupko, Luis Ángel Fernández, Alfonso Rodríguez-Patón, Jyoti S. Choudhary†, Gad Frankel†

**INTRODUCTION:** Infections with many Gram-negative pathogens, including *Escherichia coli*, *Salmonella*, *Shigella*, and *Yersinia*, rely on the injection of effectors via type III secretion systems (T3SSs). The effectors hijack cellular processes through multiple mechanisms, including molecular mimicry and diverse enzymatic activities. Although in vitro analyses have shown that individual effectors can exhibit complementary, interdependent, or antagonistic relationships, most in vivo studies have focused on the contribution of single effectors to pathogenesis.

*Citrobacter rodentium* is a natural mouse pathogen that shares infection strategies and virulence factors with the human pathogens enteropathogenic and enterohemorrhagic *E. coli* (EPEC and EHEC). The ability of these pathogens to colonize the gastrointestinal tract is mediated by the injection of effectors via a T3SS. Although *C. rodentium* infects 31 effectors, the prototype EPEC strain E2348/69 translocates 21 effectors.

**RATIONALE:** The aim of this study was to test the hypotheses that, rather than operating individually, the T3SS effectors form robust intracellular networks that can sustain large contractions and that expanded effector repertoires play a role in distinct disease phenotypes and host adaption.

**RESULTS:** We tested the effector-network paradigm by infecting mice with >100 *C. rodentium* effector mutant combinations. First, using machine learning prediction algorithms, we discovered additional effectors, NleN and NleO. We then sequentially deleted effector genes from two distinct starting points to reach sustainable endpoints, which resulted in strains missing 19 unrelated effectors (CR14) or 10 effectors involved in the modulation of innate immune responses in intestinal epithelial cells (IECs) (CRi9). Moreover, we deleted Map and EspF, which target the mitochondria and disrupt tight junctions. Unexpectedly, all strains colonized the colon and activated conserved metabolic and antimicrobial processes in the IECs while eliciting distinct cytokine and immune cell infiltration responses. In particular, although infection with *C. rodentium* Δ*map*/Δ*espF* failed to induce secretion of interleukin-22 (IL-22), CR14 and CRi9 triggered heightened secretion of IL-6 and granulocyte-macrophage colony-stimulating factor (GM-CSF) and of IL-22, interferon-γ (IFN-γ), and IL-17 from colonic explants, respectively. Nonetheless, infection with CR14 or CRi9 induced protective immunity against secondary infections.

Although Tir, EspZ, and NleA are essential, other effectors exhibit context-dependent essentiality in vivo. Moreover, *C. rodentium* expressing the effector repertoire of EPEC E2348/69 failed to efficiently colonize mice. We used curated functional information and our in vivo data to train a machine learning model that predicted values for colonization efficiency of previously uncharacterized mutant combinations. Notably, a mutant with a low predicted value, lacking only *nleF*, *nleG8*, *nleG1*, *nleB*, and *espL*, failed to colonize.

**CONCLUSION:** Our analysis revealed that T3SS effectors form robust networks, which can sustain substantial contractions while maintaining virulence, and that the composition of the effector network contributes to host adaptation. Alternative effector networks within a single pathogen triggered markedly different immune responses yet induced protective immunity. CR14 did not tolerate any further contraction, which suggests that this network reached its robustness limit with only 12 effectors. As the robustness limits of other effector networks depend on the contraction starting point and the order of the deletions, machine learning models could transform our ability to predict alternative network functions. Together, this study demonstrates the robustness of T3SS effector networks and the ability of IECs to withstand drastic perturbations while maintaining antibacterial functions. ■

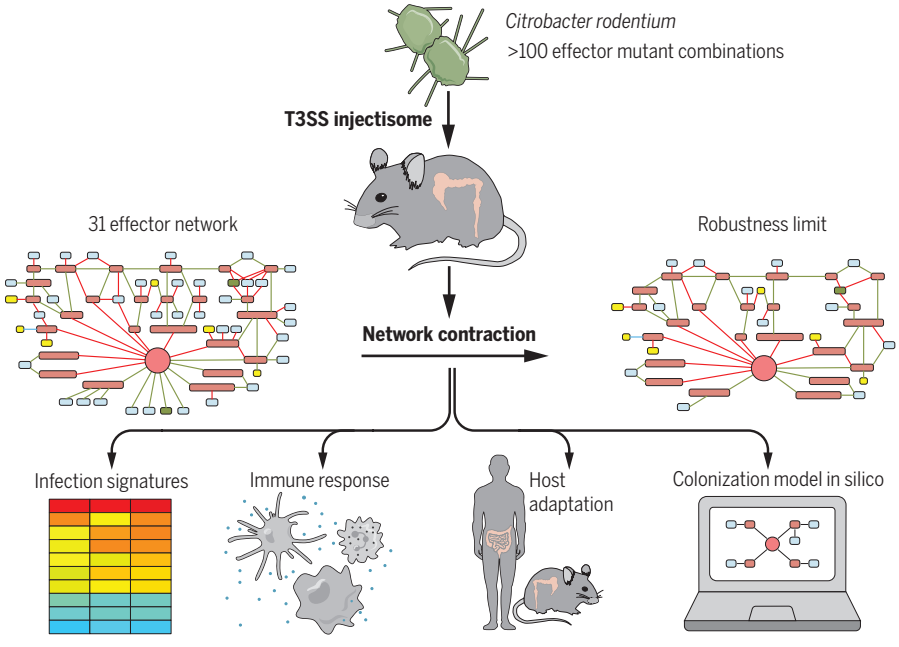


**T3SS effectors form robust intracellular networks.** T3SS effector networks can sustain substantial contractions while maintaining virulence. Using *C. rodentium* as a model showed that although triggering the conserved infection signatures in IECs, distinct networks induce divergent immune responses and affect host adaption. Because the robustness limit depends on the contraction sequence, machine learning models could transform our ability to predict the virulence potential of alternative networks.

The list of author affiliations is available in the full article online.
*These authors contributed equally to this work.
†Corresponding author. Email: g.frankel@imperial.ac.uk (G.F.); jyoti.choudhary@icr.ac.uk (J.S.C.)
Cite this article as D. Ruano-Gallego *et al.*, *Science* **371**, eabc9531 (2021). DOI: 10.1126/science.abc9531

READ THE FULL ARTICLE AT
https://doi.org/10.1126/science.abc9531

RESEARCH ARTICLE SUMMARY

SIGNAL TRANSDUCTION

# Noncanonical scaffolding of $G_{\alpha i}$ and β-arrestin by G protein–coupled receptors

**Jeffrey S. Smith*, Thomas F. Pack*, Asuka Inoue, Claudia Lee, Kevin Zheng, Issac Choi, Dylan S. Eiger, Anmol Warman, Xinyu Xiong, Zhiyuan Ma, Gayathri Viswanathan, Ian M. Levitan, Lauren K. Rochelle, Dean P. Staus, Joshua C. Snyder, Alem W. Kahsai, Marc G. Caron, Sudarshan Rajagopal†**

**INTRODUCTION:** G protein–coupled receptors (GPCRs) are a superfamily of seven transmembrane-spanning receptors and are the target of 30% of all U.S. Food and Drug Administration–approved medications. GPCRs are involved in nearly every human physiological process by serving as receptors for a wide array of ligands, including proteins, peptides, fatty acids, small molecules, and ions. The canonical signaling mechanisms of GPCRs involve coupling to specific G protein subtypes (e.g., $G_{\alpha s}$, $G_{\alpha i}$, $G_{\alpha q}$, and $G_{\alpha 12}$) as well as β-arrestin adaptor proteins. Each G protein subtype regulates specific intracellular second messengers, such as cyclic adenosine 3′,5′-monophosphate (cAMP) responses or calcium mobilization. β-arrestins inhibit, or "arrest," this canonical G protein–mediated signaling while also promoting their own intracellular signaling events such as extracellular signal–regulated kinase (ERK) activity. Because G proteins and β-arrestins can differentially regulate signaling pathways, often with distinct cellular effects, efforts are under way to design drugs that preferentially target either G protein or β-arrestin signaling to generate more selective GPCR-targeted drugs, i.e., biased ligands. In theory, biased ligands can improve the desired pharmacological properties of drugs while also minimizing their on-target side effects. However, potential coordination between G protein and β-arrestin signaling could have a significant impact on our fundamental understanding of GPCR signaling and the development of biased ligands.

**RATIONALE:** G protein and β-arrestin signaling have broadly been considered separable intracellular pathways with distinct signal transduction mechanisms. However, several lines of evidence have also suggested the potential for coordination between G protein and β-arrestin signaling. For example, some GPCRs can simultaneously bind a G protein and a β-arrestin. Furthermore, when GPCRs were activated in cells lacking functional G proteins, some β-arrestin–mediated effects of GPCR activation were also absent. This could be interpreted as a role for G proteins in what had previously been considered solely β-arrestin–mediated cellular responses. To gain further insight into these experimental findings, we investigated whether there is a GPCR-signaling pathway that involves direct interactions between G proteins and β-arrestins.

**RESULTS:** We first developed a bioluminescent resonance energy transfer (BRET) approach to monitor tripartite protein interactions among GPCRs, G proteins, and β-arrestin. After confirming that we could monitor such interactions, we found that GPCRs can catalyze a direct interaction between the $G_{\alpha i}$ protein subtype and β-arrestins at the plasma membrane, and confirmed the interaction using a variety of biochemical and biophysical techniques. This interaction was only observed between β-arrestin and the $G_{\alpha i}$ protein family, not other $G_{\alpha}$ protein subtypes. These $G_{\alpha i}$:β-arrestin complexes were formed downstream of all receptors tested, even with receptors that do not canonically signal through $G_{\alpha i}$, such as the $G_{\alpha s}$-coupled $\beta_2$-adrenergic and vasopressin type 2 receptors. We found that $G_{\alpha i}$:β-arrestin complexes formed scaffolds with the signaling kinase ERK downstream of certain receptors. Stimulation of the angiotensin type II receptor with a β-arrestin–biased agonist promoted the formation of the $G_{\alpha i}$:β-arrestin complex despite not activating canonical G protein signaling. Cellular migration promoted by this β-arrestin–biased agonist was sensitive to inhibition of both β-arrestins and $G_{\alpha i}$, which is consistent with $G_{\alpha i}$:β-arrestin complexes regulating cellular migration.

**CONCLUSION:** Our results reveal a GPCR-signaling paradigm in which GPCRs promote the formation of $G_{\alpha i}$:β-arrestin signaling complexes that are distinct from other canonical forms of GPCR signaling. These $G_{\alpha i}$:β-arrestin complexes have the ability to scaffold important cellular effectors such as ERK, and can play a functional role in cellular responses such as cell migration. Demonstration of Noncanonical coordination of $G_{\alpha i}$ and β-arrestins by GPCRs adds to our understanding of the fundamental mechanisms underlying GPCR signaling, and the potential effects of this complex should be considered when designing and evaluating GPCR ligands. ■

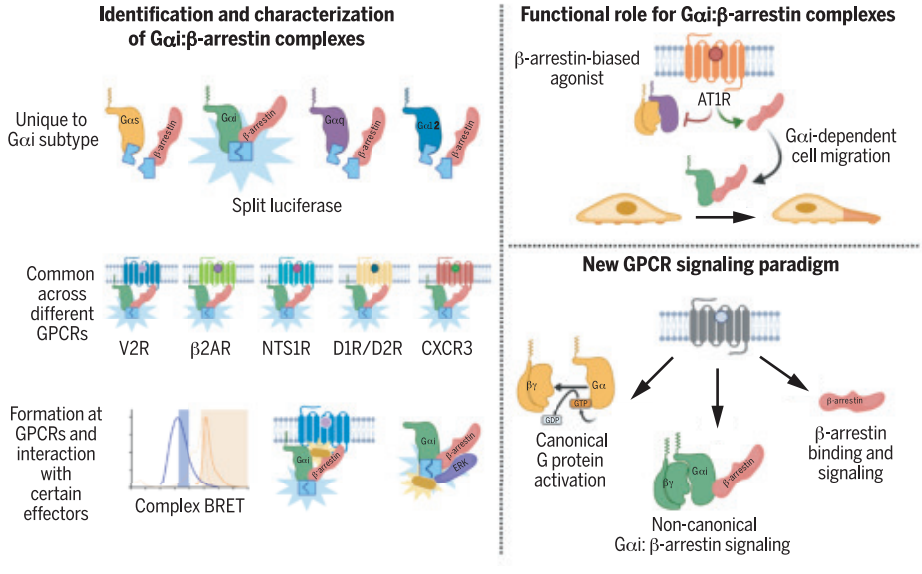


**GPCR signaling by $G_{\alpha i}$:β-arrestin complexes.** Complementation and proximity assays identified a complex between $G_{\alpha i}$ protein family members, but not other $G_{\alpha}$ protein subtypes, and β-arrestin. This was observed across multiple receptors, including those that do not canonically couple to $G_{\alpha i}$. This complex was associated with functional effects, including cell migration. These findings demonstrate GPCR signaling by $G_{\alpha i}$:β-arrestin complexes.

*These authors contributed equally to this work.
†Corresponding author. Email: sudarshan.rajagopal@duke.edu
The list of author affiliations is available in the full article online.
Cite this article as: J. S. Smith *et al.*, *Science* 371, eaay1833 (2021). DOI: 10.1126/science.aay1833

READ THE FULL ARTICLE AT
https://doi.org/10.1126/science.aay1833

RESEARCH ARTICLE SUMMARY

LUNG DEVELOPMENT

# Genomic, epigenomic, and biophysical cues controlling the emergence of the lung alveolus

Jarod A. Zepp*, Michael P. Morley, Claudia Loebel, Madison M. Kremp, Fatima N. Chaudhry, Maria C. Basil, John P. Leach, Derek C. Liberti, Terren K. Niethamer, Yun Ying, Sowmya Jayachandran, Apoorva Babu, Su Zhou, David B. Frank, Jason A. Burdick, Edward E. Morrisey*

**INTRODUCTION:** The alveolar region of the lung develops in a period that spans the late embryonic and early postnatal stages of life. An intricate series of events—including cellular proliferation, surfactant production, and morphogenesis of the alveolar structure—occurs during the transition to air breathing, a process known as alveologenesis. This critical period establishes the spatial arrangement of alveolar epithelium, capillary endothelium, and fibroblasts to generate the gas-exchange niche.

**RATIONALE:** The temporal and spatial alignment of cell compartments and the intercellular signaling that coordinates the development and maturation of the lung alveolus remain poorly characterized. Because of the extensive morphological changes that shape the alveolar niche, it is unclear which subsets of mesenchyme exert mechanical force to remodel alveolar architecture during early postnatal development. Single-cell sequencing and new genetic lineage–tracing tools have helped elucidate the cellular heterogeneity in all three cellular compartments in the lung, with extensive heterogeneity in the lung mesenchyme being of particular note. We sought to integrate these new technologies and tools to assess the cell-cell communication that drives alveolar generation.

**RESULTS:** We generated a single-cell RNA-sequencing (scRNA-seq) atlas of the developing mouse lung that included epithelial, endothelial, and mesenchymal compartments from time points that span embryonic and postnatal stages. We then analyzed ligand and receptor interactions and identified the alveolar type 1 (AT1) epithelial cell as a hub of ligand expression. The cognate receptors for these ligands were restricted to subsets of developing mesenchymal cells. Mesenchymal progenitors are spatially and transcriptionally segregated into *Acta2*-, *Pdgfrb*-, or *Wnt2*-expressing subsets and are committed to generating distinct fibroblasts in the postnatal lung by embryonic day 15.5 (E15.5). We show with scRNA-seq and lineage tracing that the progenitors for the transient secondary crest myofibroblast (SCMF), which exists only during the early postnatal alveolarization period of lung development, are spatially and transcriptionally aligned with AT1 cell progenitors. In comparison with other alveolar fibroblasts, SCMFs exert significantly more traction force ex vivo, indicating that they are a functionally specialized lineage that can remodel the alveolus. To identify intercellular signaling pathways that regulate cell lineage identity, we examined the single-cell chromatin accessibility and pathway expression (SCAPE) of AT1s and SCMFs. We identified Foxa and Tead transcription factors as upstream regulators of several AT1-derived ligands, including Shh and Wnt ligands. Conversely, SCMFs exhibit open chromatin with predicted Gli1 and Tcf target genes, implicating Shh and Wnt pathways in their development and function. To test these pathways, we generated AT1 cell–specific conditional deletions for Wnt-ligand secretion (Wls) and Shh. Conditional ablation of Shh from AT1 cells results in a loss of SCMF cells and subsequent alveolar simplification in the postnatal lung.

**CONCLUSION:** Integrating single-cell genomics and lineage tracing, we identified the spatial and temporal patterning of intercellular signaling pathways that are active during the development and maturation of the distal lung. The AT1 epithelial cell, previously thought to primarily provide gas exchange with capillary endothelium, is also a crucial ligand-expressing node that is required for proper lung development. These observations show that the viability of the AT1 cell is paramount to establish tissue homeostasis during lung development. Our imaging and single-cell biophysical measurement assays show that AT1-adjacent mesenchymal progenitors occupy anatomically discrete regions and are functionally specialized to mold the intricate architecture of the alveolus. These findings underscore the transcriptional and functional heterogeneity in distinct lung fibroblast lineages. ■

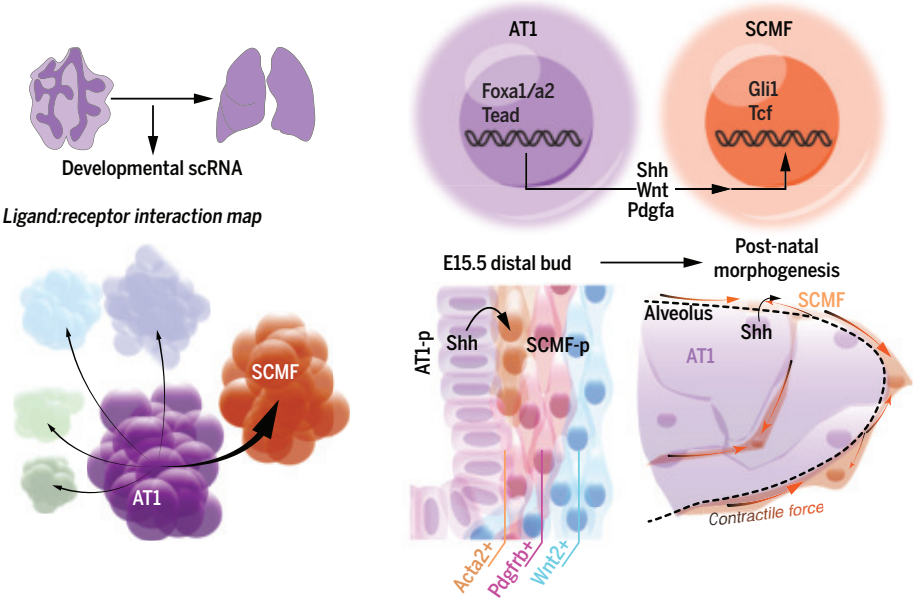


**AT1 cells provide intercellular cues for alveolar development.** A lung single-cell developmental atlas reveals an enriched signature of ligand expression in AT1 epithelial cells. Chromatin accessibility and whole-mount imaging identify the transcriptional and spatial alignment of AT1 and SCMF progenitors in the developing lung. AT1-derived Shh is required for specification and outgrowth of the force-exerting SCMF.

The list of author affiliations is available in the full article online.
*Corresponding author. Email: zeppj@email.chop.edu (J.A.Z.); emorrise@pennmedicine.upenn.edu (E.E.M.)
Cite this article as J. A. Zepp *et al.*, *Science* **371**, eabc3172 (2021). DOI: 10.1126/science.abc3172

READ THE FULL ARTICLE AT
https://doi.org/10.1126/science.abc3172

REPORTS

INORGANIC CHEMISTRY

# Dinitrogen complexation and reduction at low-valent calcium

B. Rösch[1], T. X. Gentner[1], J. Langer[1], C. Färber[1], J. Eyselein[1], L. Zhao[2], C. Ding[2], G. Frenking[2,3]*, S. Harder[1]*

Here we report that attempted preparation of low-valent $Ca^{I}$ complexes in the form of LCa-CaL (where L is a bulky β-diketiminate ligand) under dinitrogen ($N_2$) atmosphere led to isolation of $LCa(N_2)CaL$, which was characterized crystallographically. The $N_2^{2-}$ anion in this complex reacted in most cases as a very potent two-electron donor. Therefore, $LCa(N_2)CaL$ acts as a synthon for the low-valent $Ca^{I}$ complex LCa-CaL, which was the target of our studies. The $N_2^{2-}$ anion could also be protonated to diazene ($N_2H_2$) that disproportionated to hydrazine and $N_2$. The role of Ca d orbitals for $N_2$ activation is discussed.

Earth's atmosphere contains mainly dinitrogen ($N_2$), a diatomic gas with an extremely strong N≡N triple bond. Being unpolarized and having very low proton and electron affinities, $N_2$ is fully chemically inert under a wide range of conditions (*1*). In nature, nitrogenase enzymes convert $N_2$ to ammonia ($NH_3$) under ambient conditions, but this process is slow. The increasing global demand for $NH_3$ is maintained industrially by Haber-Bosch catalysis, a highly energy-consuming bulk process that converts $N_2$ under harsh conditions (400° to 600°C, 200 to 400 bar) (*2*). This process makes use of transition metals for $N_2$ activation. Partially filled d orbitals of suitable energy and symmetry can backdonate electrons into the empty π* orbitals of $N_2$ (Fig. 1A), weakening and in some cases cleaving the triple bond. Although d orbitals are also proposed to play a major role in $N_2$ activation by lanthanide f-block metals (*3*), their contribution is not an absolute requirement. The p-block half-metal boron was recently shown to mimic transition metals in $N_2$ activation (Fig. 1B), and a full cycle to $NH_3$ formation was reported (*4*–*6*). Immediate nitrogen activation in the s-block is limited to lithium. Although the preparative procedure for $Li_3N$ from its elements requires temperatures in the 400° to 800°C range (*7*), it is known that Li is slowly oxidized by $N_2$ under ambient conditions. In contrast, all other alkali metals do not react with $N_2$, even at red heat. Lithium's exceptional reactivity has been explained by its extreme reduction potential, which is the most negative of all s-block metals, and by its small size, resulting in a very high lattice energy for $Li_3N$ (*8*, *9*). Although the heavier alkaline-earth (AE) metals Ca, Sr, and Ba form under $N_2$ loosely bound $AE(N_2)_8$ complexes, which have been detected at 12 K in a neon matrix but cannot be isolated (*10*), they only react with $N_2$ to nitrides at high temperatures (450° to 750°C) (*7*). Here we present the low-temperature reduction of $N_2$ at calcium that was serendipitously discovered during attempts to isolate a low-valent $Ca^{I}$ complex.

Low-valent β-diketiminate $Mg^{I}$ complexes (*11*) have proven to be versatile molecular reducing agents (Fig. 1C) (*12*). Although subvalent $Be^{0}$ and $Be^{I}$ complexes have been reported (*13*, *14*), the claim of a $Ca^{I}$ complex is controversial (Fig. 1D) (*15*, *16*). The theoretical prediction that the AE-AE bond strength rapidly decreases down group 2 (Be–Be > Mg–Mg > Ca–Ca) highlights the difficulty of isolating true $Ca^{I}$ complexes (*17*, *18*). Positing that the challenging stabilization of the Ca–Ca bond might be achieved by our recently reported bulky β-diketiminate ligand (HC{C(Me)N[2,6-(3-pentyl)-phenyl]}$_2$), abbreviated herein as BDI (*19*), we attempted reduction of the corresponding Ca iodide precursor **1** (Fig. 2A). Reaction with $KC_8$ in benzene, however, led to pitch-black crystals of a complex with an antiaromatic, slightly puckered $C_6H_6^{2-}$ anion (**2**); the Mg analog was recently reported (*19*). Density functional theory (DFT) calculations at the BP86-D3BJ/def2-SVP level on **2** show that the triplet state is 2.9 kcal/mol more stable than a singlet state (table S13), which is in line with lack of nuclear magnetic resonance (NMR) signals. Owing to the very negative reduction potential of benzene (–3.42 V versus saturated calomel electrode) (*20*), **2** is highly reducing and decomposes at room temperature to **3** and $H_2$. Repeating the reduction of **1** in toluene, an aromatic solvent that is even more resistant to reduction, gave a similar black product (fig. S74), which could not be isolated and already at –20°C decomposed to the colorless hydride complex **4**. Even electron transfer to *para*-xylene (*p*-xylene) was achieved (**5**). The surprising thermal stability of this black complex featuring a puckered *p*-xylene ring may be due to restricted accessibility of the metal centers on account of steric hindrance imposed by the Me groups. Complexes **1** to **5** have been fully characterized, and crystal structures are shown in figs. S82 to S86.

The highly flexible 3-pentyl substituents in the BDI ligand of **1** confer solubility in aliphatic solvents, which are more inert to reduction than the aromatics. Therefore, the reduction of **1** with several reducing agents in various alkanes was explored. Reacting **1** in methylcyclohexane with K/KI, a highly effective reducing agent (*21*), gave a dark red-brown suspension with one major product (fig. S73). After removal of excess K/KI, the mother liquor reacted with benzophenone to produce a deep-purple ketyl radical, indicative of low-valent species. Although this species could not be crystallized, addition of tetrahydrofuran (THF) or tetrahydropyran (THP) led to immediate formation of red-brown crystals. X-ray analysis revealed that, in the absence of an aromatic solvent, $N_2$, which was used as a protective gas, had been reduced (**6** and **7**; Fig. 2, B and C). Repeating the reduction of **1** under Ar instead of $N_2$ led to formation of multiple species, indicating that the target complex (BDI)Ca-Ca(BDI) is subject to decomposition. All purification attempts culminated in isolation of the homoleptic $(BDI)_2Ca$ complex **8**, which, on account of ligand bulk, crystallized as a distinctive $\eta^2,\eta^1$-complex. This observation suggests that, as predicted by calculation, subvalent $Ca^{I}$ complexes with a Ca–Ca bond are unstable toward $Ca^{II}/Ca^{0}$ disproportionation (*17*).

Crystal structures of the $N_2$ complexes **6** and **7** closely match each other. Both compounds are centrosymmetric dimers with terminal BDI ligands and side-on bridging $N_2$ units (Fig. 3A). The N–N distance [**6**: 1.268(2) Å; **7**: 1.258(3) and 1.268(3) Å] is considerably elongated compared with the bond in $N_2$ (1.098 Å) and consistent with N=N double-bond character in $N_2^{2-}$, an anion isoelectronic to $O_2$. Supporting this interpretation is the observation that the highly charged $N_2^{2-}$ anion is tightly sandwiched between $Ca^{2+}$ cations with a very short mean Ca–N distance of 2.303 Å; note the mean Ca–N(BDI) bond distance is 2.394 Å. Compared with a range of dimeric lanthanide-$N_2$ complexes with side-on bridging $N_2$ ligands [N–N: 1.088 (12) to 1.285(4) Å] (*22*), the extent of $N_2$ activation in **6** and **7** classifies as strong (*23*). Notably, the N–N bond in **6** and **7** is even slightly longer than that in a very similar dimeric BDI Cr-$N_2$ complex with a side-on bridging $N_2$ ligand [N–N: 1.249(5) Å] (*24*). Raman stretching frequencies for **6** (1376 $cm^{-1}$) and **7** (1375 $cm^{-1}$)

[1]Inorganic Chemistry, University Erlangen-Nürnberg, 91058 Erlangen, Germany. [2]Institute of Advanced Synthesis, School of Chemistry and Molecular Engineering, Nanjing Tech University, Nanjing 211816, China. [3]Fachbereich Chemie, Philipps-Universität Marburg, 35043 Marburg, Germany.
*Corresponding author. Email: sjoerd.harder@fau.de (S.H.); frenking@chemie.uni-marburg.de (G.F.)

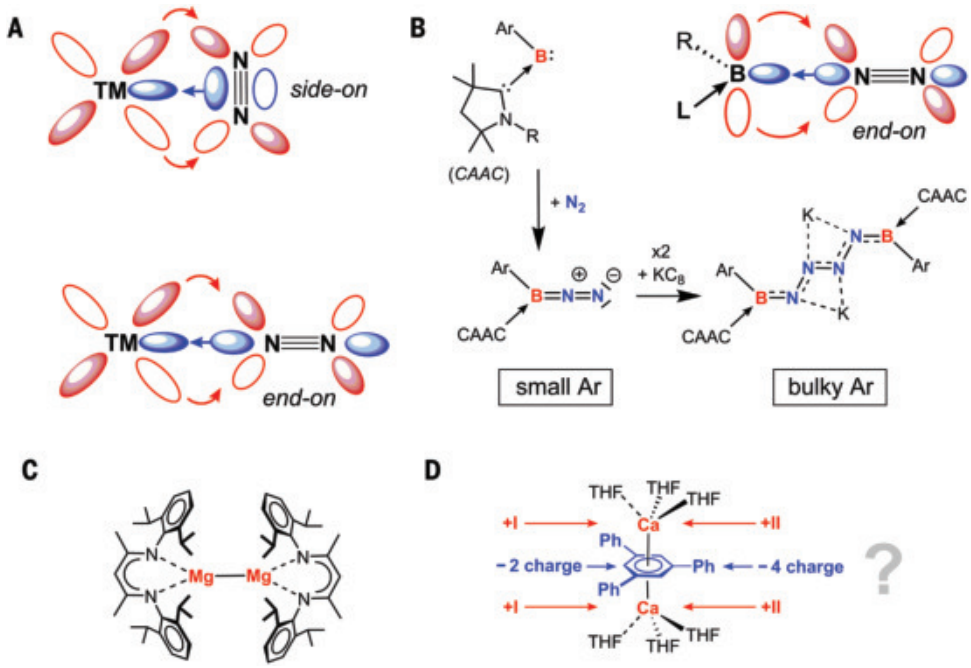


**Fig. 1. Nitrogen activation by transition metals (TM) or boron and examples of low-valent AE metal complexes.** (**A**) Synergistic bonding model for $N_2$ activation by TM (blue is donor bond, red is backdonation). (**B**) $N_2$ activation by a low-valent $B^I$ intermediate. L, neutral ligand; Ar, aryl group; R, organic group. (**C**) A low-valent dimeric β-diketiminate $Mg^I$ complex. (**D**) Ambiguity in the Ca metal oxidation states and arene charges in a reported $Ca^I$ complex. Ph, phenyl.

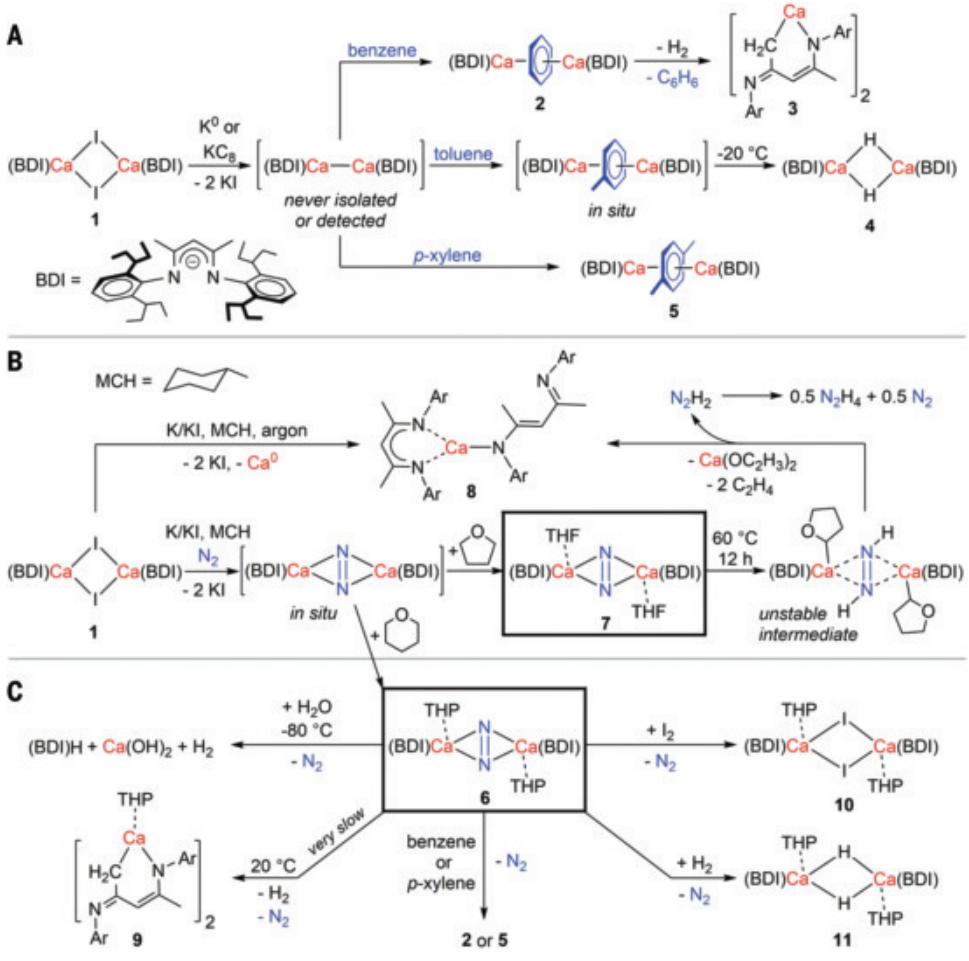


**Fig. 2. Synthesis and reactivities.** (**A**) Reduction of Ca in **1** and subsequent reaction of the $Ca^I$ intermediate with arenes. (**B**) Reduction of Ca in **1** under $N_2$ giving **7**. Under argon, the $Ca^I$ intermediate (BDI)Ca-Ca(BDI) decomposes to $Ca^0$ and **8**. MCH, methylcyclohexane Intramolecular deprotonation of THF in **7** by $N_2^{2-}$ yields hydrazine. (**C**) Reactivity of **6** as a strong two-electron reductant.

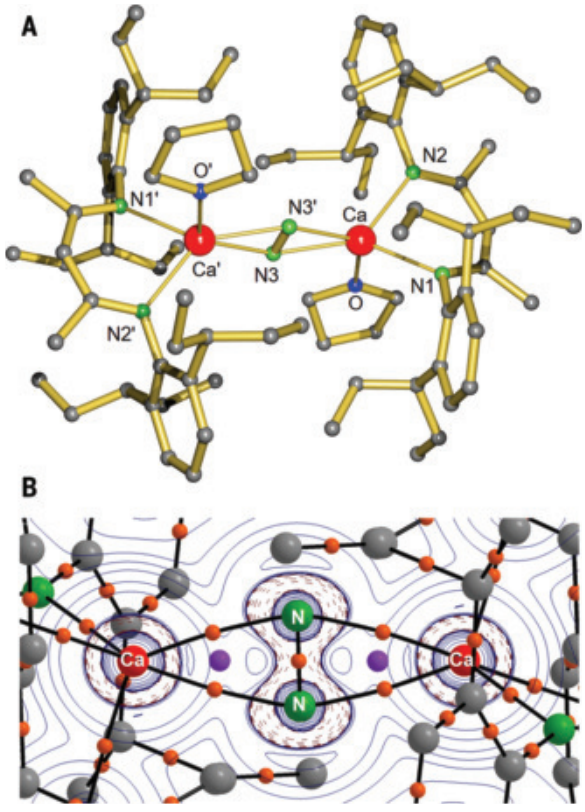


**Fig. 3. Complex 7.** (**A**) Crystal structure of **7** (hydrogen atoms omitted for clarity). The structure of **6** is essentially similar. (**B**) Laplacian distribution for complex **7** in the Ca–$N_2$–Ca plane at the BP86-D3(BJ)/def2-TZVPP//BP86/def2-SVP level. Red dashed lines indicate areas of charge concentration, while blue solid lines show areas of charge depletion. Orange dots are bond critical points, and purple dots are ring critical points.

are almost identical and are strongly red-shifted compared with lanthanide-$N_2$ analogs (1406 to 1473 $cm^{-1}$) (*25*), indicating strong $N_2$ activation.

The $N_2$ complexes **6** and **7** are moderately soluble in cyclohexane-$d_{12}$. Although the THF complex **7** decomposed overnight at room temperature with gas evolution to several unknown species, solutions of the THP complex **6** could be kept for 1 day before slowly decomposing to **9**. $^{1}H$ and $^{13}C$ NMR data for **6** and **7** are in agreement with their centrosymmetric dimeric crystal structures. Samples prepared under $^{15}N_2$ manifested a $^{15}N$ chemical shift at 310 parts per million (compared with $MeNO_2$). Storing a solution of $^{15}N$-labeled **6** under naturally abundant $N_2$ led, overnight, to complete disappearance of the $^{15}N$ signal, while $^{1}H$ and $^{13}C$ NMR spectra remained unchanged. These observations indicate a reversible $N_2$ activation process.

Reaction of complex **6** with benzene or *p*-xylene gave **2** or **5**, respectively, with concomitant release of a gas that is likely $N_2$. This behavior, which also has been reported for β-diketiminate Fe-$N_2$ complexes (*26*), required avoidance of aromatic solvents in further reactivity studies. Reaction of a methylcyclohexane solution of **6** with $I_2$ led to the expected iodide complex **10**. Although the $I_2$-to-$I^-$ reduction is expected, immediate room temperature reaction with $H_2$ to give hydride complex **11** is striking, given that low-valent $Mg^{I}$ complexes do not react with $H_2$ (*11*). In all cases, the reactions are accompanied by considerable gas release, indicating that the bridging $N_2^{2-}$ ion in **6** acts as a strongly reducing electron reservoir. Therefore, the reactivity of **6** is similar to that expected for the low-valent $Ca^{I}$ complex (BDI)Ca-Ca(BDI) that was the original target of our studies.

Attempts to protonate the $N_2^{2-}$ ion by reaction of **6** with water or strong acids led to $H_2$ formation and BDI protonation (fig. S70). Despite recent breakthroughs (*27*), the functionalization of $N_2$ in transition metal–$N_2$ complexes also remains challenging (*28*), and chemical conversion of $N_2^{2-}$ in ionic lanthanide-$N_2$ complexes has not been described. Interestingly, heating a cyclohexane suspension of complex **7** (60°C, 12 hours) led to degradation of THF that is typical for highly basic s-block metal reagents (*29*), i.e., deprotonation of the $OCH_2$ unit in THF followed by ethylene elimination and enolate formation (Fig. 2B); ethylene was detected by $^{1}H$ NMR (fig. S76). Replacing the THF ligands in **7** for THF-$d_8$ ligands gave slower decomposition, indicating that C–H (or C–D) bond cleavage is the rate-determining step, and ethylene-$d_4$ was detected by deuterium ($^{2}H$) NMR spectroscopy (fig. S78). Protonation of $N_2^{2-}$ by THF starts with formation of a nonclassical $N_2\cdots H_2CO$ hydrogen bridge (2.667 Å), the feasibility of which is supported by DFT calculations (fig. S104). The resulting diazene ($N_2H_2$) is unstable above –150°C (*30*) and rapidly disproportionated to $N_2$ and $N_2H_4$. Hydrazine formation was confirmed by trapping with acetone in the form of acetone azine, which could be isolated in 56% of its theoretical yield (figs. S80 and S81), or by detection with the established *p*-dimethylaminobenzaldehyde ultraviolet–visible (UV–VIS) spectroscopy assay (*31*) (fig. S79).

The Ca-$N_2$ complexes **6** and **7** form at temperatures as low as –60°C. Potassium cannot reduce $N_2$, even at high temperature and pressure, and therefore the reduction of $N_2$ by Ca must involve intermediate $Ca^{I}$ species. It can be assumed that the reducing power of true $Ca^{I}$ species is higher than that of established binuclear $Mg^{I}$ complexes that so far did not react with $N_2$. Although $N_2$ activation can be achieved without involvement of metal d orbitals (*4*–*9*), it is tempting to propose that low-lying d orbitals on Ca may play a role in the $N_2$ activation process. Theoretical analysis of $AE(CO)_8$, $AE(N_2)_8$, and $AE(benzene)_3$ complexes, recently detected in a neon matrix at 12 K, demonstrated a high degree of electrostatic character, but residual covalent orbital interactions were dominated by a substantial contribution of AE d orbitals (*10*, *32*, *33*). In light of the current controversial, but stimulating, discussion on π-bond activation by heavier AE metals (*34*, *35*), a comprehensive theoretical analysis on bonding in **7** was undertaken.

The calculated structure of **7** (BP86/def2-SVP), which is in excellent agreement with the experimental geometry (fig. S93), was analyzed with various charge- and energy-decomposition methods. The Laplacian of the electron density in the Ca–$N_2$–Ca plane (Fig. 3B), estimated by the quantum theory of atoms in molecules (QTAIM) (*36*), shows strong electronic charge accumulation at $N_2$ and charge depletion in the valence region of Ca. As is evident from bond paths and bond critical points (orange dots), each N atom binds to both Ca atoms, resulting in two $CaN_2$ metallacycles featuring ring critical points (purple dots). QTAIM gives partial charges of –1.33 for $N_2$ and +1.46 for each Ca. Natural bond orbital analysis (*37*) suggests even larger charges of –1.58 and +1.70, respectively.

The energy decomposition with natural orbitals for chemical valence (EDA-NOCV) analysis (*38*) gave more detailed information on the bonding interactions in **7** by providing a quantitative estimate of the individual orbital interactions. Calculation of interactions between charged fragments, $N_2^{2-}$ and $[(BDI)Ca(THF)]_2^{2+}$, gives information on bonding in **7**, while calculation using neutral fragments, $N_2$ and $[(BDI)Ca(THF)]_2$, reveals interactions during the product formation process. Analyses of interactions between charged fragments show that Ca-$N_2$ bonding in **7** is mainly electrostatic (69%) (Table 1). In contrast, the neutral fragments interact primarily by orbital interactions (79%) and show strong charge donation

**Table 1. EDA-NOCV analysis for complex 7 at the BP86-D3(BJ)/TZ2P//BP86/def2-SVP level of theory using the charged fragments, $N_2^{2-}$ and $[(BDI)Ca(THF)]_2^{2+}$, or neutral moieties, $N_2$ and $[(BDI)Ca(THF)]_2$, as interacting species.** Energies are given in kilocalories per mole. $\Delta E_{int}$, interaction energy; $\Delta E_{Pauli}$, Pauli repulsion; $\Delta E_{disp}$, dispersion contribution; $\Delta E_{elstat}$, electrostatic interaction energy;

| Energy terms | $[(BDI)Ca(THF)]_2^{2+} + N_2^{2-}$ | | $[(BDI)Ca(THF)]_2 + N_2$ | |
|---|---|---|---|---|
| | Energy value | Orbital interaction | Energy value | Orbital interaction |
| $\Delta E_{int}$ | −568.5 | – | −157.7 | – |
| $\Delta E_{Pauli}$ | 188.2 | – | 129.2 | – |
| $\Delta E_{disp}$* | −11.4 (1.5%) | – | −11.4 (4.0%) | – |
| $\Delta E_{elstat}$* | −520.1 (68.7%) | – | −50.0 (17.4%) | – |
| $\Delta E_{orb}$* | −225.2 (29.8%) | – | −225.4 (78.6%) | – |
| $\Delta E_{orb1}$† | −69.3 (30.8%) | $N_2^{2-}\rightarrow[(BDI)Ca(THF)]_2^{2+}$ $\pi_{\|}$* donation | −204.7 (90.8%) | $[(BDI)Ca(THF)]_2 \rightarrow N_2$ π backdonation |
| $\Delta E_{orb2}$† | −16.8 (7.5%) | $N_2^{2-}\rightarrow[(BDI)Ca(THF)]_2^{2+}$ σ(+,+) donation | −9.3 (4.1%) | $N_2\rightarrow[(BDI)Ca(THF)]_2$ π donation‡ |
| $\Delta E_{orb3}$† | −15.1 (6.7%) | $N_2^{2-}\rightarrow[(BDI)Ca(THF)]_2^{2+}$ $\pi_{\|}$ donation | −3.2 (1.4%) | $N_2\rightarrow[(BDI)Ca(THF)]_2$ σ(+,+) donation |
| $\Delta E_{orb4}$† | −11.8 (5.2%) | $N_2^{2-}\rightarrow[(BDI)Ca(THF)]_2^{2+}$ $\pi_{\perp}$ donation | −2.8 (1.2%) | $N_2\rightarrow[(BDI)Ca(THF)]_2$ π' donation‡ |
| $\Delta E_{orb5}$† | −8.8 (3.9%) | $N_2^{2-}\rightarrow[(BDI)Ca(THF)]_2^{2+}$ σ(+,−) donation | −2.6 (1.2%) | $N_2\rightarrow[(BDI)Ca(THF)]_2$ σ(+,−) donation |
| $\Delta E_{rest}$ | −103.4 (45.9%) | Fragment polarization | −2.8 (1.2%) | Fragment polarization |

*The values in parentheses give the percentage contribution to the total attractive interactions $\Delta E_{elstat} + \Delta E_{orb} + \Delta E_{disp}$. †The values in parentheses give the percentage contribution to the total orbital interactions $\Delta E_{orb}$. ‡Both occupied π orbitals ($\pi_{\|}$ and $\pi_{\perp}$) of $N_2$ contribute to the donation, as shown in figs. S100 and S102.

from $[(BDI)Ca(THF)]_2$ to $N_2$. Contributions of dispersion interactions are negligible. Breakdown of total orbital interaction $\Delta E_{orb}$ into individual orbital interactions shows that the major component for interactions between charged fragments $\Delta E_{orb1}$ comes from the donation of the in-plane $\pi_{||}$* orbital of $N_2^{2-}$ to vacant π molecular orbitals of the $[(BDI)Ca(THF)]_2^{2+}$ fragment, providing 31% of the total orbital term. Additionally, there are several smaller donations, $\Delta E_{orb2}$ to $\Delta E_{orb5}$, coming from various occupied $N_2^{2-}$ orbitals into vacant $[(BDI)Ca(THF)]_2^{2+}$ orbitals with individual contributions of 8 to 17% to the total orbital term. The considerable contribution of orbital relaxation ($\Delta E_{rest}$) of 46% originates from large charge migration within the fragments. Orbital interactions between the neutral fragments are clearly dominated by large π backdonation from $[(BDI)Ca(THF)]_2$ to $N_2$ π* orbitals. The nature of each orbital interaction can be identified with the help of the associated deformation densities Δρ and the connected fragment orbitals (figs. S99 to S103). The most important orbital components for fragment $[(BDI)Ca(THF)]_2$ are the d orbitals on Ca interacting with $N_2$ valence orbitals. Albeit highly controversial (*34*, *35*), the EDA-NOCV analysis of **7** supports recent findings that d orbitals on Ca need to be considered (*10*, *32*, *33*). The relevance of d orbitals for covalent bonding of the heavier alkaline-earth metals Ca, Sr, and Ba finds further support in a recent theoretical study (*39*).

Attempts to stabilize a low-valent $Ca^I$ complex with the bulky BDI ligand led to the serendipitous isolation of s-block metal–$N_2$ complexes. These highly ionic complexes contain the $N_2^{2-}$ ion, which reacts as a strong reductant by releasing $N_2$ and two electrons. The complexes could therefore be seen as synthons for $Ca^I$ reagents that feature a considerably higher reducing power than binuclear $Mg^I$ complexes.

## REFERENCES AND NOTES


1. M. J. Chalkley, M. W. Drover, J. C. Peters, *Chem. Rev.* **120**, 5582–5636 (2020).
2. A. J. Martín, T. Shinagawa, J. Pérez-Ramírez, *Chem* **5**, 263–283 (2019).
3. A. J. Ryan, S. G. Balasubramani, J. W. Ziller, F. Furche, W. J. Evans, *J. Am. Chem. Soc.* **142**, 9302–9313 (2020).
4. M. A. Légaré *et al*., *Science* **359**, 896–900 (2018).
5. M. A. Légaré *et al*., *Science* **363**, 1329–1332 (2019).
6. M. A. Légaré *et al*., *Nat. Chem.* **12**, 1076–1080 (2020).
7. G. Brauer, Ed., *Handbook of Preparative Inorganic Chemistry* (Academic Press, ed. 2, 1963).
8. G. J. Moody, J. D. R. Thomas, *J. Chem. Educ.* **43**, 205–206 (1966).
9. D. Roy, A. Navarro-Vazquez, Pv. Schleyer, *J. Am. Chem. Soc.* **131**, 13045–13053 (2009).
10. Q. Wang *et al*., *Nat. Commun.* **10**, 3375 (2019).
11. S. P. Green, C. Jones, A. Stasch, *Science* **318**, 1754–1757 (2007).
12. C. Jones, *Nat. Rev. Chem.* **1**, 0059 (2017).
13. M. Arrowsmith *et al*., *Nat. Chem.* **8**, 638–642 (2016).
14. G. Wang *et al*., *J. Am. Chem. Soc.* **142**, 4560–4564 (2020).
15. S. Krieck, H. Görls, L. Yu, M. Reiher, M. Westerhausen, *J. Am. Chem. Soc.* **131**, 2977–2985 (2009).
16. W. Huang, P. L. Diaconescu, *Dalton Trans.* **44**, 15360–15371 (2015).
17. Y. Xie, H. F. Schaefer III, E. D. Jemmis, *Chem. Phys. Lett.* **402**, 414–421 (2005).
18. S. Krieck, L. Yu, M. Reiher, M. Westerhausen, *Eur. J. Inorg. Chem.* **2010**, 197–216 (2010).
19. T. X. Gentner *et al*., *Angew. Chem. Int. Ed.* **58**, 607–611 (2019).
20. J. Mortensen, J. Heinze, *Angew. Chem. Int. Ed.* **23**, 84–85 (1984).
21. J. Hicks, M. Juckel, A. Paparo, D. Dange, C. Jones, *Organometallics* **37**, 4810–4813 (2018).
22. Y. Tanabe, in *Transition Metal-Dinitrogen Complexes: Preparation and Reactivity*, Y. Nishibayashi, Ed. (Wiley-VCH, 2019), pp. 441–474.
23. M. D. Fryzuk, S. A. Johnson, *Coord. Chem. Rev.* **200–202**, 379–409 (2000).
24. W. H. Monillas, G. P. A. Yap, L. A. MacAdams, K. H. Theopold, *J. Am. Chem. Soc.* **129**, 8090–8091 (2007).
25. M. E. Fieser *et al*., *Dalton Trans.* **45**, 14634–14644 (2016).
26. J. M. Smith *et al*., *J. Am. Chem. Soc.* **128**, 756–769 (2006).
27. S. F. McWilliams *et al*., *Nature* **584**, 221–226 (2020).
28. S. Kim, F. Loose, P. J. Chirik, *Chem. Rev.* **120**, 5637–5681 (2020).
29. R. E. Mulvey *et al*., *Nat. Chem.* **2**, 588–591 (2010).
30. N. Wiberg, H. Bachhuber, G. Fischer, *Angew. Chem. Int. Ed.* **11**, 829–830 (1972).
31. G. W. Watt, J. D. Chrisp, *Anal. Chem.* **24**, 2006–2008 (1952).
32. X. Wu *et al*., *Science* **361**, 912–916 (2018).
33. Q. Wang *et al*., *Angew. Chem. Int. Ed.* **58**, 17365–17374 (2019).
34. C. R. Landis, R. P. Hughes, F. Weinhold, *Science* **365**, eaay2355 (2019).
35. L. Zhao, S. Pan, M. Zhou, G. Frenking, *Science* **365**, eaay5021 (2019).
36. R. F. W. Bader, *Atoms in Molecules: A Quantum Theory* (Clarendon Press, 1990).
37. E. D. Glendening, C. R. Landis, F. Weinhold, *J. Comput. Chem.* **34**, 1429–1437 (2013).
38. M. P. Mitoraj, A. Michalak, T. Ziegler, *J. Chem. Theory Comput.* **5**, 962–975 (2009).
39. I. Fernández, N. Holzmann, G. Frenking, *Chem. Eur. J.* **26**, 14194–14210 (2020).


## ACKNOWLEDGMENTS


We thank S. Grams for the gas chromatography–mass spectrometry measurements, M. Fickert and L. Jurkiewicz for the Raman measurements of **6** and **7**, and A. Roth for elemental analysis. **Funding:** We thank the University of Erlangen-Nürnberg for generous support. L.Z. and G.F. acknowledge financial support from Nanjing Tech University (grants 39837123 and 39837132) and the National Natural Science Foundation of China (grant 21973044). **Author contributions:** B.R.: Conceptualization, Investigation, Validation, Formal analysis, Writing – original draft, and Visualization. T.X.G.: Investigation, Validation, and Formal analysis. J.L., C.F., J.E., and C.D.: Formal analysis. L.Z.: Formal analysis and Visualization. G.F.: Writing – original draft, Writing – review & editing, Visualization, and Supervision. S.H.: Conceptualization, Writing – original draft, Writing – review & editing, Visualization, Supervision, and Project administration. **Competing interests:** The authors declare no competing interests. **Data and materials availability:** X-ray data are available free of charge from the Cambridge Crystallographic Data Centre under reference numbers CCDC 2036237 (**1**), 2036238 (**2**), 2036239 (**3**), 2036240 (**4**), 2036241 (**5**), 2036242 (**6**), 2036243 (**7**), 2036244 (**8**), 2036245 (**9**), 2036246 (**10**), and 2036247 (**11**). All other experimental, spectroscopic, crystallographic, and computational data are included in the supplementary materials.


## SUPPLEMENTARY MATERIALS

science.sciencemag.org/content/371/6534/1125/suppl/DC1
Materials and Methods
Figs. S1 to S104
Tables S1 to S13
References (*40*–*63*)
Data S1

13 October 2020; accepted 2 February 2021
10.1126/science.abf2374

OPTOELECTRONICS

# Chiral-induced spin selectivity enables a room-temperature spin light-emitting diode

Young-Hoon Kim[1]*, Yaxin Zhai[1]*, Haipeng Lu[1]*, Xin Pan[2], Chuanxiao Xiao[1], E. Ashley Gaulding[1], Steven P. Harvey[1], Joseph J. Berry[1], Zeev Valy Vardeny[2], Joseph M. Luther[1]†, Matthew C. Beard[1]†

In traditional optoelectronic approaches, control over spin, charge, and light requires the use of both electrical and magnetic fields. In a spin-polarized light-emitting diode (spin-LED), charges are injected, and circularly polarized light is emitted from spin-polarized carrier pairs. Typically, the injection of carriers occurs with the application of an electric field, whereas spin polarization can be achieved using an applied magnetic field or polarized ferromagnetic contacts. We used chiral-induced spin selectivity (CISS) to produce spin-polarized carriers and demonstrate a spin-LED that operates at room temperature without magnetic fields or ferromagnetic contacts. The CISS layer consists of oriented, self-assembled small chiral molecules within a layered organic-inorganic metal-halide hybrid semiconductor framework. The spin-LED achieves ±2.6% circularly polarized electroluminescence at room temperature.

Typical optoelectronic technologies rely on the manipulation of the charge of current carriers but not their spin. The use of ferromagnetic contacts applied to semiconductors allows for control of spin populations in an applied magnetic field (*1*, *2*); thus, such devices generally include both semiconductors and ferromagnets. We demonstrate control of charge, spin, and light through the use of a chiral metal-halide perovskite (MHP) hybrid semiconductor that exhibits chiral-induced spin selectivity (CISS). When current passes through the chiral-MHP layer, the spin of the transmitting carriers becomes polarized (*3*, *4*). The chiral layer acts as a spin filter, producing a spin-polarized current upon the application of an applied electric field.

We demonstrate this control through the realization of a room-temperature spin-polarized light-emitting diode (spin-LED). Spin-LEDs control the orientation and intensity of circularly polarized electroluminescence (CP-EL), depending on the spin polarization of the injected carriers (*5*, *6*). Circularly polarized organic light-emitting diodes (CP-OLEDs) can also emit CP-EL by incorporating chiral impurities into the emitting layer, but they operate by selective scattering and birefringence rather than by the spin-polarized carriers that govern spin-LEDs (*7*). Our spin-LED emitted CP-EL with 2.6% efficiency at room temperature without applying a magnetic field or using a ferromagnetic contact with a spin-polarized current of >80%. Although spin-LEDs are interesting devices, our demonstration that chiral MHPs can be used to control spin, light, and charge has broader implications for a larger class of opto-spintronic applications, including quantum-based optical computing and information processing, three-dimensional (3D) displays, bioencoding, and tomography (*8*).

MHP semiconductors and their related family of organic-inorganic hybrid semiconductors have a number of notable properties for controlling spins, light, and charges. They have large spin-orbit couplings yet also exhibit long spin-coherence lifetimes (*9*), they exhibit controllable Rashba splitting (*9*–*11*) through the degree and nature of the metal-halide octahedral distortion (*12*), and they exhibit excellent optoelectrical properties (*13*, *14*). As nanocrystals (NCs), MHPs have outstanding optical properties, including narrow spectral emission, ultrahigh color purity, high photoluminescence quantum efficiency (>70%), and wide color tunability (wavelengths, λ, between 400 and 800 nm) (*15*, *16*), which fulfill the requirements for circularly polarized (CP) light technologies. For device applications, MHPs are solution-processable at low temperature (<150°C) and can be fabricated as polycrystalline films, colloidal NCs, and single crystals.

At the band edges, the electronic structure in Pb-halide MHP semiconductors forms a simple two-level system. The valence band consists of Pb 6s and halide 4p orbitals and the conduction band from Pb 6p hybridized orbitals. The large spin-orbit coupling causes the total angular momentum ($J$) to be conserved, yielding a doubly degenerate $J_e = ½$ level for electrons and $J_h = ½$ for holes. Light

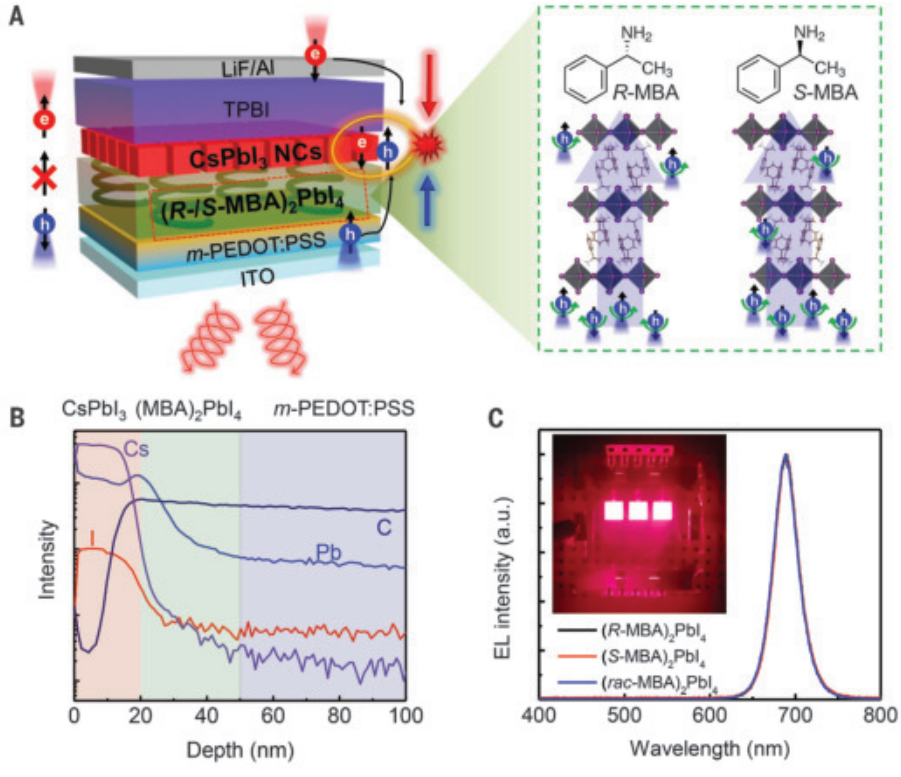


**Fig. 1. Structure and EL characterization of spin-LEDs.** (**A**) Schematic illustration of spin-polarized charge injection and CP-EL emission in spin-LEDs. (**B**) TOF-SIMS depth profile of *m*-PEDOT:PSS/CISS layer/$CsPbI_3$ NC heterostructure. The signal from Cs drops sharply at the interface (purple trace), whereas both I and Pb also drop, but to a lesser extent, because their density in the 2D CISS layer is much lower than that in the NC layer. (**C**) EL spectrum and operating device image (inset) of spin-LEDs based on CISS layer/$CsPbI_3$ NC heterostructure. a.u., arbitrary units.

[1]Chemistry and Nanoscience Center, National Renewable Energy Laboratory, Golden, CO 80401, USA. [2]Department of Physics and Astronomy, University of Utah, Salt Lake City, UT 84112, USA.
*These authors contributed equally to this work.
†Corresponding author. Email: matt.beard@nrel.gov (M.C.B.); joey.luther@nrel.gov (J.M.L.)

emission is governed by optical selection rules with allowed transitions occurring for $\Delta J = 0$ and change in magnetic quantum number, $m_J = \pm\frac{1}{2}$, of $\Delta m_J = \pm 1$. Emission of CP light ($\sigma^+$ or $\sigma^-$) results when the population of carriers, $n$, is spin polarized (i.e., $n_\uparrow > n_\downarrow$, or vice versa). Unpolarized light emission occurs when $n_\uparrow = n_\downarrow$. The CP-EL efficiency is governed by the spin-injection efficiency and spin scattering of the initially polarized carriers before radiative emission.

We demonstrated spin-LEDs based on solution-processed MHP heterostructures in which spin-polarized holes were injected into an adjacent layer of MHP NC emitters (Fig. 1). Chiral organic molecules can be incorporated into the crystal framework of 2D layered hybrid perovskites that incorporate chiral organic molecules into their crystal framework (*17*–*19*), where they induce a chiral-optoelectronic response in the hybrid system (*12*, *20*). The spin-polarized hole injection layer is composed of a 30- to 60-nm-thick chiral 2D layered *R*-/*S*-methylbenzylammonium lead iodide [(*R*-/*S*-MBA)$_2$PbI$_4$] polycrystalline bulk film that resulted in a >80% spin-polarized hole current, with spin orientation determined by the handedness of the MBA cation. The injected spin-polarized holes radiatively recombined with properly aligned injected electrons in the colloidal MHP NC-emitting layer, exhibiting CP-EL.

Spin-polarized charge transport in the CISS layer (fig. S1) and CISS/nonchiral NC heterostructure (Fig. 2, A to C) were studied with magnetic conductive-probe atomic force microscopy (mCP-AFM). Ferromagnetic Co-Cr–coated tips were premagnetized by an external magnet with opposite magnetization directions (up or down relative to the substrate) immediately before the measurement. After charge-carrier injection from the indium tin oxide (ITO)/modified poly(3,4-ethylenedioxythiophene) polystyrene-sulfonate (*m*-PEDOT:PSS) electrode, the carriers drifted perpendicularly through the horizontally oriented organic-inorganic multiple quantum well (MQW)–like chiral structures and then were injected into the NC layer before penetrating into the magnetized AFM tip. ITO/*m*-PEDOT:PSS/(*R*-MBA)$_2$PbI$_4$/CsPbI$_3$ NC film showed much higher current when the tip was magnetized up (13.64 nA at 3 V, which is the operational spin-LED bias) than when the tip was either magnetized down (1.40 nA at 3 V) or nonmagnetized (1.53 nA at 3 V (Fig. 2B). By contrast, current in the ITO/*m*-PEDOT:PSS/(*S*-MBA)$_2$PbI$_4$/CsPbI$_3$ NC film was higher when the tip was magnetized down (6.88 nA at 3 V) compared with when it was magnetized up (0.75 nA at 3 V) or nonmagnetized (1.49 nA at 3V) (Fig. 2C). We calculated the degree of polarized spin current, $P_{spin}$, using

$$P_{spin} = \frac{I_{up} - I_{down}}{I_{up} + I_{down}} \times 100\% \quad (1)$$

where $I_{up}$ and $I_{down}$ were the electrical currents measured when the Co-Cr–coated tips are premagnetized in the up and down directions, respectively. We calculated a $P_{spin}$ in ITO/*m*-PEDOT:PSS/(*R*-MBA)$_2$PbI$_4$/CsPbI$_3$ NC films and ITO/*m*-PEDOT:PSS/(*S*-MBA)$_2$PbI$_4$/CsPbI$_3$ NC films of +81% and −80%, respectively. The ITO/*m*-PEDOT:PSS/CISS films (without

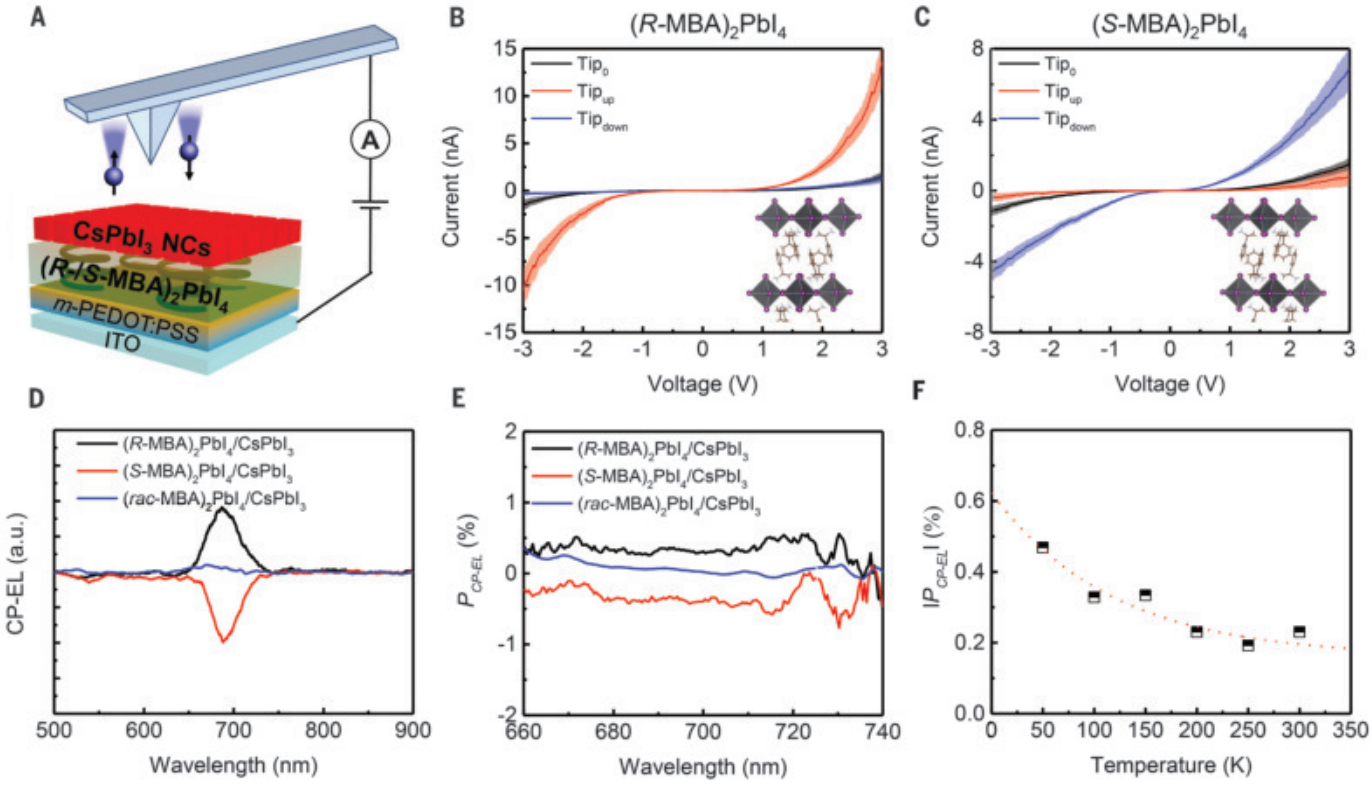


**Fig. 2. Spin-polarized charge injection and CP-EL characteristics in spin-LEDs.** (**A**) Schematic illustration of mCP-AFM measurements of ITO/*m*-PEDOT:PSS/(*R*-/*S*-MBA)$_2$PbI$_4$/CsPbI$_3$ NC films. (**B** and **C**) Current-voltage curves of ITO/*m*-PEDOT:PSS/(*R*-MBA)$_2$PbI$_4$/CsPbI$_3$ NC films (B) and ITO/*m*-PEDOT:PSS/(*S*-MBA)$_2$PbI$_4$/CsPbI$_3$ NC films (C) measured by mCP-AFM at room temperature and crystal structures of (*R*-/*S*-MBA)$_2$PbI$_4$ (insets). The current-voltage curves were measured 80 times from different spots on each sample. The lines are average results, and shaded regions are 95% confidence limits for all average results. Tip$_0$, nonmagnetized AFM tip; Tip$_{up}$, AFM tip magnetized up; Tip$_{down}$, AFM tip magnetized down. (**D** and **E**) The CP-EL spectra (D) and the EL polarization degree, $P_{CP\text{-}EL}$ (E) of spin-LEDs based on CISS layer/CsPbI$_3$ NCs. (**F**) Temperature-dependent absolute average values of $|P_{CP\text{-}EL}|$ in spin-LEDs based on (*S*-MBA)$_2$PbI$_4$/CsPbI$_3$ NCs.

NCs) also exhibited an anisotropic current depending on the MBA chirality (fig. S1 and supplementary text, section 2). The injection barrier decreased without the NC layer, and we could use a lower applied voltage (~1 V) to observe the same $P_{spin}$. The similar $P_{spin}$ values suggested that spin-polarized injection from the CISS layer into the NC layer was high and that the spin-diffusion length in the NC layer was at least one to two NCs. We verified that the mCP-AFM results were not influenced by sampling different regions of the film for up and down magnetization by constructing larger devices that consisted of a magnetized Ni electrode rather than the magnetized AFM tip (figs. S2 and S3 and supplementary text, sections 3 and 4). Van Wees and co-workers have argued that CISS demonstrations using two-terminal device configurations with ferromagnetic contacts can only be observed in a nonlinear regime because of the Onsager reciprocity relationship (*21*). The spin-LEDs presented below detected spin-polarized currents without any ferromagnetic contact and avoided this complication.

Our measurements indicate that chiral MHPs overcame the disadvantages of previous spin-injecting materials and are an attractive system for spin injection in opto-spintronic applications (*5*, *6*). We fabricated spin-LEDs with the following structure (Fig. 1A)—glass/ITO/*m*-PEDOT:PSS (~100 nm)/(*R*-/*S*-/*rac*-MBA)$_2$PbI$_4$ polycrystalline films (~30 nm)/CsPbI$_3$ NCs (~20 nm)/2,2′,2-(1,3,5-benzinetriyl)-tris(1-phenyl-1-H-benzimidazole) (TPBI) (50 nm)/lithium fluoride (LiF) (1 nm)/Al (100 nm). The *m*-PEDOT:PSS consisted of PEDOT:PSS and perfluorinated polymeric ionomer that self-organized to induce a gradual increase in the ionization energy from the bottom (5.20 eV) to the top (5.95 eV) of the film (*14*), which enabled efficient hole injection into the CISS layer. Spin coating the (*R*-/*S*-/*rac*-MBA)$_2$PbI$_4$ CISS layer on *m*-PEDOT:PSS produced polycrystalline films with preferential orientation that had the metal-halide layers parallel to the substrate, whereas the chiral organic molecules were perpendicular (*19*) (fig. S4; x-ray diffraction). The helical axis of the chiral molecule was perpendicular to the NC light-emitting layer and parallel to the charge-conduction direction. The *m*-PEDOT:PSS layer blocked electrons and passed holes, whereas the TPBI layer blocked holes and passed electrons, thereby confining the electron-hole pairs to the NC emitter layer.

We used colloidal CsPbX$_3$ (where X is I or Br) NCs because ligand-mediated solvation enabled processing from octane, which did not redissolve the underlying (*R*-/*S*-/*rac*-MBA)$_2$PbI$_4$ polycrystalline films (*22*). A MHP heterostructure was formed by spin coating colloidal CsPbI$_3$ NCs (sized ~10 to 15 nm) (fig. S5) on top of the CISS layer. To limit transport and spin dephasing losses in the NC layer, we limited its thickness to ~20 to 30 nm (i.e., approximately one to two NCs). The formation of a well-defined CISS/CsPbI$_3$ heterostructure was confirmed by time-of-flight secondary ion mass spectrometry (TOF-SIMS) depth profiling (Fig. 1B).

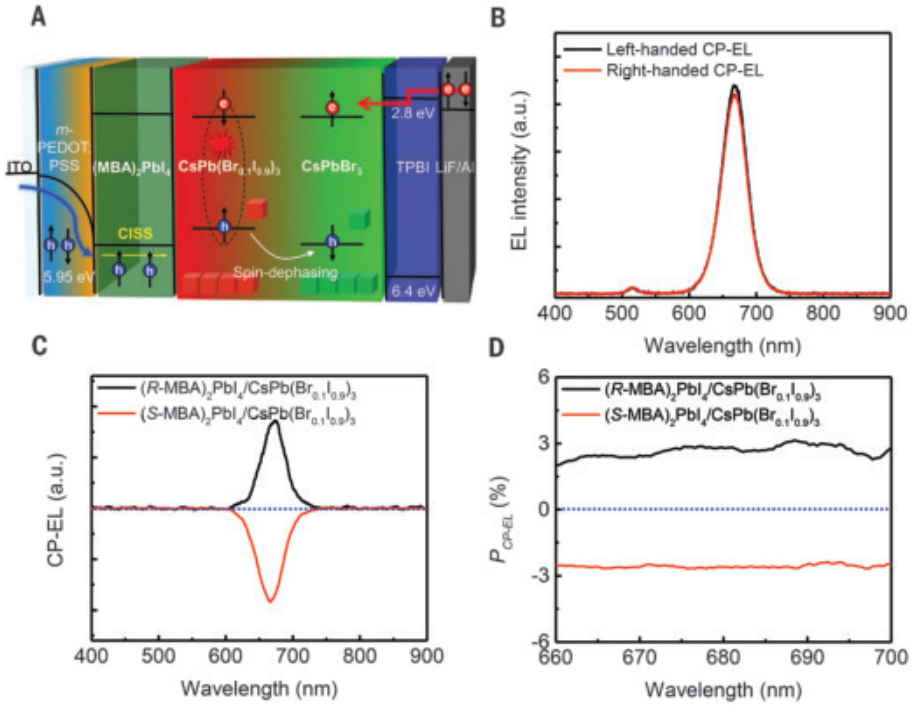


**Fig. 3. CP-EL from mixed halide perovskite NCs.** (**A**) Schematic illustration of hole injection through ITO/*m*-PEDOT:PSS (blue arrow), spin-polarized hole injection through CISS layer (yellow arrow), unpolarized electron injection through TPBI/LiF/Al (red arrow), spin dephasing (white arrow), and formation of mixed halide perovskites under the electric field and generation of CP-EL (dashed circle) in the spin-LEDs. (**B**) Left-handed and right-handed CP-EL spectrum of spin-LEDs based on (*R*-MBA)$_2$PbI$_4$/CsPbBr$_3$ NC heterostructure. (**C** and **D**) CP-EL (C) and $P_{CP\text{-}EL}$ (D) of spin-LEDs based on CISS layer/CsPbBr$_3$ NC heterostructure.

The spin-LEDs showed a turn-on voltage of 2.4 V and external quantum efficiencies (EQEs) [10.05%, 10.53%, and 11.05% for spin-LEDs based on (*R*-MBA)$_2$PbI$_4$, (*S*-MBA)$_2$PbI$_4$, and (*rac*-MBA)$_2$PbI$_4$, respectively] (fig. S6, A to C). These are the highest EQEs among reported MHP LEDs based on pure CsPbI$_3$ NCs without any posttreatment (table S1). Our spin-LEDs displayed bright red emissions with sharp electroluminescence (EL) spectra (688 nm peak, ~32 nm full width at half maximum) that did not change with applied bias up to 8 V, which confirms that the CISS and TPBI layers efficiently confined charge carriers in the NC-emitting layers (Fig. 1C and fig. S6D).

We measured the CP-EL by separating the emitted light into left- and right-CP components using a broadband quarter-wave plate followed by a linear polarizer and a spectrometer (fig. S7 and supplementary text, section 5). We calculated the CP-EL polarization degree, $P_{CP\text{-}EL}$, using

$$P_{CP\text{-}EL} = \frac{I_{left} - I_{right}}{I_{left} + I_{right}} \times 100\% \qquad (2)$$

where $I_{left}$ and $I_{right}$ are the EL intensities of left- and right-CP light, respectively. Spin-LEDs based on CISS/CsPbI$_3$ NC heterostructure showed distinct CP-EL spectra centered at 688 nm with average $P_{CP\text{-}EL}$ = ±0.25% at 660 ≤ λ ≤ 740 nm (Fig. 2, D and E) and showed similar $P_{CP\text{-}EL}$ values with different CISS layer thicknesses (~30 and ~60 nm) (fig. S8). By contrast, the (*rac*-MBA)$_2$PbI$_4$-based devices exhibited no CP-EL emission (Fig. 2, D and E). The thickness independence was consistent with our previous study that found spin polarization saturates at a CISS layer thickness of ~30 nm (*19*). We verified that the NCs themselves do not exhibit a chiral response after processing that could occur if MBA ligands migrated to the NC surfaces (figs. S9 to S11 and supplementary text, section 6). As temperature decreases to 50 K, the spin-LEDs showed a gradual $|P_{CP\text{-}EL}|$ increase up to ~0.47% (Fig. 2F and fig. S12) caused by the longer spin-dephasing time at lower temperatures coupled with concomitant increase in the radiative

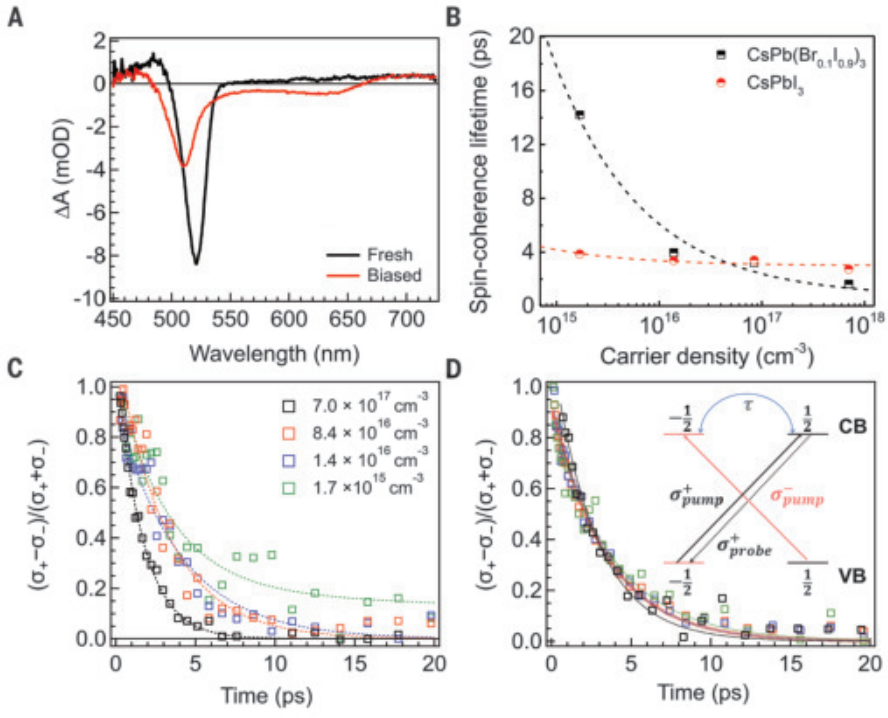


**Fig. 4. Charge and spin dynamics in NCs.** (**A**) TA spectra of spin-LEDs before (fresh) and under applied bias (biased). The pump wavelength was selected at 400 nm. (**B**) Spin-coherence lifetime of $CsPb(Br_{0.1}I_{0.9})_3$ NC and $CsPbI_3$ NC films measured at different excitation carrier densities. The dashed lines are fitted curves of carrier density–dependent spin lifetimes determined using a conventional power law (*33*, *34*). (**C** and **D**) Spin-coherence dynamics in $CsPb(Br_{0.1}I_{0.9})_3$ NC films (C) and $CsPbI_3$ NC films (D) measured at different excitation carrier densities. Inset in (D) is the mechanism of spin-coherence lifetime measurement. Pump $\sigma_+$ (black) has angular momentum of $|+1\rangle$ and generates a $m_J$ polarization, whereas pump $\sigma_-$ (red) does the opposite. The probe $\sigma_+$ pulse selectively detects the change in spin polarization. The flip of a spin will simultaneously lead to a decay of the $\sigma_+$ bleach and a formation of the $\sigma_-$ bleach. CB, conduction band; VB, valence band.

recombination rate (*9*, *23*). These data suggest that $P_{CP\text{-}EL}$ is limited by spin scattering in the NCs.

We achieved a longer spin-coherence time and a concurrent improvement in $P_{CP\text{-}EL}$ by introducing a mixed-halide NC-emitting layer. To accomplish this, we fabricated $CsPbBr_3$ NCs (sized ~10 nm; fig. S13). When a bias was applied, the external electric field drove a partial halide exchange between $(R\text{-}/S\text{-MBA})_2PbI_4$ and $CsPbBr_3$ NC (*24*). The EL spectrum red shifted over time (Fig. 3A and fig. S14). The CP-EL was measured when the partial halide exchange saturated—i.e., when the EL peak no longer red shifted. The EL peak saturated at 678 nm, corresponding to a final composition of $CsPb(Br_{0.1}I_{0.9})_3$ (fig. S15). We also found that a small EL peak at 515 nm remains, resulting from pristine $CsPbBr_3$, which suggests that the halide exchange only occurred near the CISS-NC interface.

These spin-LEDs show a clear intensity difference between left- and right-CP EL emission at 678 nm; however, they did not show CP-EL polarization at 515 nm (Fig. 3B and figs. S16 to S18). We calculated an average $P_{CP\text{-}EL}$ = ±2.6% at $660 \le \lambda \le 700$ nm (Fig. 3, C and D), which was substantially higher than that observed in the pure $CsPbI_3$-based spin-LEDs discussed above. We attributed the absence of a CP-EL signal at 515 nm to two effects. Spin-polarized holes underwent additional spin dephasing upon transferring to the deeper energy level of $CsPbBr_3$ (Fig. 3A), and additional spin scattering occurred as holes transported away from the CISS-NC interface. Both effects indicate that carriers were highly polarized at the CISS-NC interface and our structure promoted CP light emission in the same spatial region. Notably, Van Wees and co-workers have demonstrated that one consequence of the spin-filter action and Onsager reciprocity is that carriers with the wrong spin flip their polarization when reflected from the CISS layer (*25*). In our case, that process should tend to further polarize carriers at the CISS-NC interface. These spin-LEDs operated at room temperature without external magnetic fields or magnetized electrodes and had performances comparable to those of the state-of-the-art GaAs-based spin-LEDs (table S2) (*5*, *6*, *26*).

We measured transient absorption (TA) of the spin-LEDs before and after applying a bias (Fig. 4A and fig. S19) (*27*). Fresh spin-LEDs without bias showed a photobleaching (PB) peak at 510 nm, which corresponded to $CsPbBr_3$ exciton transition. Under an applied bias, a new PB peak forms at 650 nm, and the PB peak at 510 nm substantially decreases (Fig. 4A). The 650-nm PB feature was also observed after exciting the spin-LED devices with a pump photon energy below the bandgap of the $CsPbBr_3$ NCs (fig. S19). The relative intensities of the PB feature at 510 nm versus 650 nm suggested that after the voltage-driven halide exchange, ~80% of the NCs remained as $CsPbBr_3$ and only ~20% were converted to $CsPb(Br_{0.1}I_{0.9})_3$.

By contrast, EL emission was dominated by $CsPb(Br_{0.1}I_{0.9})_3$ (Fig. 3B). We did not observe photocarrier migration from the $CsPbBr_3$ to the $CsPb(Br_{0.1}I_{0.9})_3$ in the TA experiments during the course of ~1 ns. In the EL measurement, polarized holes were injected at the CISS/$CsPb(Br_{0.1}I_{0.9})_3$ interface and needed extra energy to be promoted and transmitted to the $CsPbBr_3$ region. The conduction band was flat and allowed electrons to flow through the $CsPbBr_3$ into the $CsPb(Br_{0.1}I_{0.9})_3$ region (Fig. 3A). Thus, the device promoted CP light emission at the CISS-NC interface, where the carriers were highly polarized both from injection of the polarized holes, as well as spin polarization that occurs from the reflection of electrons at the CISS-NC interface.

To understand the enhanced $P_{CP\text{-}EL}$, we compared the electronic spin dynamics and charge carrier dynamics in $CsPb(Br_{0.1}I_{0.9})_3$ NC and $CsPbI_3$ NC films (*28*, *29*). We studied $CsPb(Br_{0.1}I_{0.9})_3$ NCs that had the same photoluminescence emission wavelength as the CP-EL emission (678 nm) (fig. S15). We determined the spin-coherence lifetime ($\tau_{spin}$) from CP pump-probe TA at various carrier densities ($n_0$) (figs. S20 and S21) compared with the charge carrier lifetime ($\tau_{carrier}$) measured by time-resolved photoluminescence (fig. S22). We previously observed that $\tau_{spin}$ was about three times as long for bulk $MAPbBr_3$ compared with $MAPbI_3$ (*30*). Wang and co-workers have also observed a longer spin-polarized lifetime for $CsPbBr_3$ compared with $CsPbI_3$ (*31*). Deschler and co-workers have reported an intensity-dependent $\tau_{spin}$ in layered Pb-I–based perovskite samples (*32*).

The spin-relaxation time also depended on carrier density. As $n_0$ decreases to $1.7 \times 10^{15}$ $cm^{-3}$ (system limit), $CsPb(Br_{0.1}I_{0.9})_3$ NC films showed gradually increasing $\tau_{spin}$ up to ~14 ps, and $CsPbI_3$ NC films showed a steady $\tau_{spin}$ of ~4 ps (Fig. 4, B to D). In our devices, we estimated that for a 10–mA $cm^{-2}$ current density, the average carrier density in the active area of the device should be ~$10^{14}$ $cm^{-3}$, and for this carrier density, the spin-polarized lifetime estimate

is ~14 ps. We also found a carrier lifetime $\tau_{carrier}$ of ~1.34 ns for the $CsPb(Br_{0.1}I_{0.9})_3$ NC films, whereas $\tau_{carrier}$ was ~1.08 ns for the $CsPbI_3$ NC films. When the current is highly spin polarized, the CP-EL efficiency can be approximated by the ratio of the spin-polarization and photoluminescence lifetimes ($\tau_{spin}/\tau_{carrier}$) (*28*, *29*). We found that $\tau_{spin}/\tau_{carrier} = 1.06 \times 10^{-2}$ in $CsPb(Br_{0.1}I_{0.9})_3$ NC films and $\tau_{spin}/\tau_{carrier} = 3.5 \times 10^{-3}$ in $CsPbI_3$ NC films (table S3), which is in agreement with the measured $P_{CP\text{-}EL}$ values—i.e., ±2.6% for spin-LEDs based on $CsPbBr_3$ NCs and ±0.25% for spin-LEDs based on $CsPbI_3$ NCs. Our device operation relied on injection of spin-polarized holes through the CISS mechanism in the 2D hybrid organic-inorganic perovskite layer, suppression of spin dephasing in the emitting layer, and accumulation of the spin-aligned carriers at the CISS-NC interface.

## REFERENCES AND NOTES


1. S. A. Wolf *et al*., *Science* **294**, 1488–1495 (2001).
2. F. Pulizzi, *Nat. Mater.* **11**, 367 (2012).
3. R. Naaman, Y. Paltiel, D. H. Waldeck, *Nat. Rev. Chem.* **3**, 250–260 (2019).
4. R. Naaman, Y. Paltiel, D. H. Waldeck, *J. Phys. Chem. Lett.* **11**, 3660–3666 (2020).
5. Y. Ohno *et al*., *Nature* **402**, 790–792 (1999).
6. R. Fiederling *et al*., *Nature* **402**, 787–790 (1999).
7. Y. Yang, R. C. da Costa, D. M. Smilgies, A. J. Campbell, M. J. Fuchter, *Adv. Mater.* **25**, 2624–2628 (2013).
8. A. Hirohata, K. Takanashi, *J. Phys. D: Appl. Phys.* **47**, 193001 (2014).
9. P. Odenthal *et al*., *Nat. Phys.* **13**, 894–899 (2017).
10. Y. Zhai *et al*., *Sci. Adv.* **3**, e1700704 (2017).
11. X. Liu *et al*., *Nat. Commun.* **11**, 323 (2020).
12. M. K. Jana *et al*., *Nat. Commun.* **11**, 4699 (2020).
13. S. D. Stranks *et al*., *Science* **342**, 341–344 (2013).
14. H. Cho *et al*., *Science* **350**, 1222–1225 (2015).
15. L. Protesescu *et al*., *Nano Lett.* **15**, 3692–3696 (2015).
16. A. Swarnkar *et al*., *Science* **354**, 92–95 (2016).
17. J. Ahn *et al*., *Mater. Horiz.* **4**, 851–856 (2017).
18. G. Long *et al*., *Nat. Photonics* **12**, 528–533 (2018).
19. H. Lu *et al*., *Sci. Adv.* **5**, eaay0571 (2019).
20. H. Lu *et al*., *J. Am. Chem. Soc.* **142**, 13030–13040 (2020).
21. X. Yang, C. H. van der Wal, B. J. van Wees, *Nano Lett.* **20**, 6148–6154 (2020).
22. Q. Zhao *et al*., *Nat. Commun.* **10**, 2842 (2019).
23. S. De Cesari *et al*., *Phys. Rev. B* **99**, 035202 (2019).
24. L. Zhao *et al*., *Adv. Mater.* **29**, 1605317 (2017).
25. X. Yang, C. H. van der Wal, B. J. van Wees, *Phys. Rev. B* **99**, 024418 (2019).
26. N. Nishizawa, M. Aoyama, R. C. Roca, K. Nishibayashi, H. Munekata, *Appl. Phys. Express* **11**, 053003 (2018).
27. Y. Zhai *et al*., *ACS Energy Lett.* **5**, 47–55 (2020).
28. J. Yu *et al*., *Sci. Rep.* **6**, 35597 (2016).
29. J. Beyer, I. A. Buyanova, S. Suraprapapich, C. W. Tu, W. M. Chen, *Appl. Phys. Lett.* **98**, 203110 (2011).
30. X. Chen, H. Lu, Y. Yang, M. C. Beard, *J. Phys. Chem. Lett.* **9**, 2595–2603 (2018).
31. M. Zhou, J. S. Sarmiento, C. Fei, X. Zhang, H. Wang, *J. Phys. Chem. Lett.* **11**, 1502–1507 (2020).
32. S. A. Bourelle *et al*., *Nano Lett.* **20**, 5678–5685 (2020).
33. J. Bigot, M. T. Portella, R. W. Schoenlein, J. E. Cunningham, C. V. Shank, *Phys. Rev. Lett.* **67**, 636–639 (1991).
34. J. M. Kikkawa, D. D. Awschalom, *Phys. Rev. Lett.* **80**, 4313–4316 (1998).


## ACKNOWLEDGMENTS


The authors acknowledge L. M. Wheeler for help with photoluminescence measurements, C. Zou for help with LED measurements, and X. Chen for help with CP-EL measurements. **Funding:** We gratefully acknowledge funding as part of the Center for Hybrid Organic Inorganic Semiconductors for Energy (CHOISE), an Energy Frontier Research Center funded by the Office of Basic Energy Sciences, Office of Science, within the U.S. Department of Energy through contract no. DE-AC36-08GO28308. The views expressed in the article do not necessarily represent the views of the DOE or the U.S. government. **Author contributions:** Y.-H.K., J.M.L., and M.C.B. conceived of the research idea and designed experiments; Y.-H.K. fabricated NCs and devices; Y.Z. assisted with CP-EL measurements and performed ultrafast measurements; H.L. synthesized CISS layer crystals; X.P. measured temperature-dependent response; C.X. performed mCP-AFM measurements; E.A.G. assisted with transmission electron microscopy characterization; S.P.H. performed TOF-SIMS; J.J.B. assisted with magnetic measurements; and Z.V.V., J.M.L., and M.C.B. supervised the project. Y.-H.K. and M.C.B. wrote the initial draft and all authors contributed to the final manuscript. **Competing interests:** An application has been made for a provisional patent (U.S. patent application no. 63/147,867). The authors declare no other competing interests. **Data and materials availability:** All data are available in the main text or the supplementary materials and are available on request.


## SUPPLEMENTARY MATERIALS

science.sciencemag.org/content/371/6534/1129/suppl/DC1
Materials and Methods
Supplementary Text
Figs. S1 to S22
Tables S1 to S3
References (*35*–*80*)


1 November 2020; accepted 5 February 2021
10.1126/science.abf5291


SUPERCONDUCTIVITY

# Electric field–tunable superconductivity in alternating-twist magic-angle trilayer graphene


**Zeyu Hao[1]*, A. M. Zimmerman[1]*, Patrick Ledwith[1], Eslam Khalaf[1], Danial Haie Najafabadi[1], Kenji Watanabe[2], Takashi Taniguchi[3], Ashvin Vishwanath[1], Philip Kim[1]†**



**Engineering moiré superlattices by twisting layers in van der Waals (vdW) heterostructures has uncovered a wide array of quantum phenomena. We constructed a vdW heterostructure that consists of three graphene layers stacked with alternating twist angles ±θ. At the average twist angle θ ~ 1.56°, a theoretically predicted "magic angle" for the formation of flat electron bands, we observed displacement field–tunable superconductivity with a maximum critical temperature of 2.1 kelvin. By tuning the doping level and displacement field, we found that superconducting regimes occur in conjunction with flavor polarization of moiré bands and are bounded by a van Hove singularity (vHS) at high displacement fields. Our findings display inconsistencies with a weak coupling description, suggesting that the observed moiré superconductivity has an unconventional nature.**


The experimental realization of twisted bilayer graphene (TBG) opened up fresh possibilities for studying interaction effects in moiré engineered electronic bands. According to early theoretical predictions, the hybridization of two twisted graphene sheets could produce nearly flat bands at the so-called "magic angles" (MAs) between the sheets (*1*–*4*). Initial experiments showed a reduction of kinetic energy giving rise to correlated insulating phases and superconductivity upon doping these insulating states (*5*, *6*). In the follow-up experiments, additional interaction-driven phases were discovered in MA-TBG, including isospin symmetry–breaking metals (*7*), orbital ferromagnetism (*8*–*10*), and magnetic field–induced Chern insulators (*11*–*13*). Despite the rapid progress of the field, the question of whether the superconductivity is unconventional, driven by strong electron-electron interactions, or conventional, arising from electron-phonon interaction at weak coupling, remains under debate. Some experiments suggest that the superconducting and insulating phases are independent or maybe even competing, with the superconductivity persisting or strengthening when Coulomb interaction is screened (*14*–*17*). However, others have provided evidence that the superconductivity has unconventional features, such as coexisting nematic order (*18*) and a lack of correlation between large densities of states (DOSs) and higher critical temperatures (*19*).

The creation of moiré engineered van der Waals interfaces has been extended to other two-dimensional (2D) material systems as well, leading to the observation of many interesting interaction-driven phases, such as quantum anomalous Hall states in twisted monolayer-bilayer graphene (*20*, *21*) and generalized Wigner crystal in tungsten diselenide ($WSe_2$)/tungsten disulfide ($WS_2$) moiré superlattices (*22*, *23*). However, MA-TBG remains the only system in which superconductivity is unambiguously established (*6*, *9*, *16*, *24*). By contrast, initial reports of superconductivity in other 2D flat-band systems such as ABC trilayer graphene aligned with boron nitride (BN) (*25*), twisted double-bilayer graphene (*26*, *27*), and twisted $WSe_2$ (*28*) have proven less conclusive (*29*).


[1]Department of Physics, Harvard University, Cambridge, MA 02138, USA. [2]Research Center for Functional Materials, National Institute for Material Science, 1-1 Namiki, Tsukuba 305-0044, Japan. [3]International Center for Materials Nanoarchitectonics, National Institute for Material Science, 1-1 Namiki, Tsukuba 305-0044, Japan.
*These authors contributed equally to this work.
†**Corresponding author. Email: pkim@physics.harvard.edu**

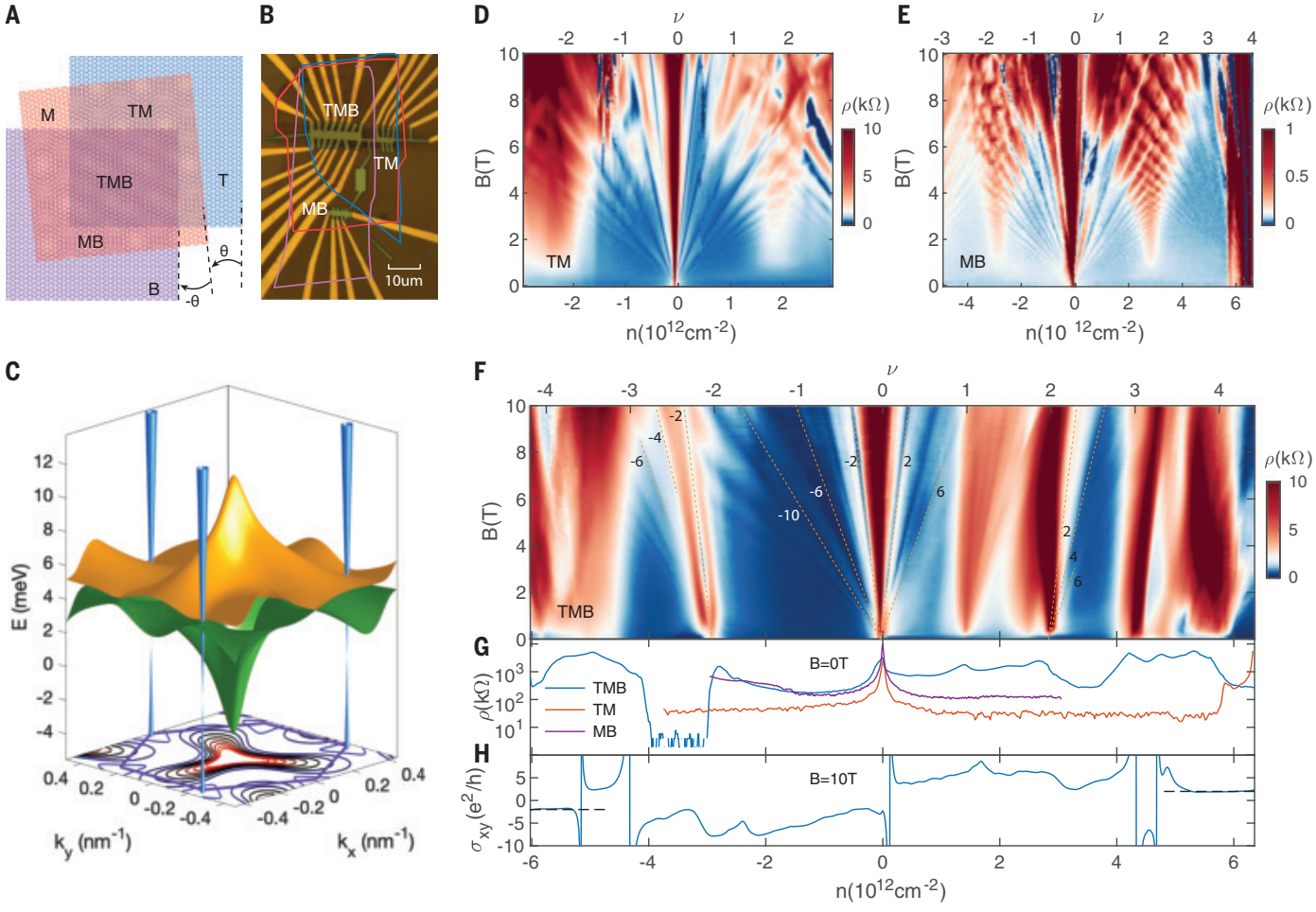


**Fig. 1. Device structure and characterization.** (**A**) Schematic diagram of the three layers of TTG with alternating twist angles θ and −θ. The top and bottom layers are aligned with each other, whereas the middle layer is twisted by θ relative to both layers, preserving the in-plane mirror symmetry. (**B**) Optical microscope image of the TTG device fabricated in the TMB region and two TBG devices fabricated in the TM and MB regions. (**C**) Theoretical band structure for MA-TTG at $D/\varepsilon_0$ = 0 plotted on the mini Brillouin zone (BZ), marked in purple in the bottom face. The blue Dirac cones sit at the mini BZ *K* points, whereas the flat bands, orange (conduction) and green (valence), are the most dispersive at the mini BZ Γ point. A contour plot of the valence band is projected on the *x*-*y* plane. (**D** and **E**) Landau fan diagrams of the two TBG Hall bars TM and MB. In each device, fans are visible emanating from ν = 0 and ν = ±4 as well as an increase in resistance at the vHSs near ν = ±2. (**F**) Landau fan diagram of the TTG Hall bar TMB. Resistive states and fans emerge at ν = 0, ±1, ±2, and +3. The most prominent sequences are traced out with orange dashed lines (fig. S5). (**G**) Zero magnetic field resistivity as a function of filling in TM, MB, and TMB. (**H**) Hall conductivity in TMB at *B* = 10 T.

In this work, we studied a distinct type of moiré engineered graphene multilayer system: MA twisted trilayer graphene (TTG) with vertical mirror symmetry (*30*). We present a clear signature of superconductivity controlled with applied electric field. The continuously tunable band structure of MA-TTG provides an experimental knob for probing the superconducting mechanism.

Our TTG consists of three layers of graphene, with the twist angle between the top layer (T) and middle layer (M) being θ and the twist angle between the middle layer and the bottom layer (B) being −θ, as shown in the schematic in Fig. 1A. The stacking with this alternating sequence of angles with opposite signs preserves the vertical mirror plane symmetry (*31*), differing from the previously studied trilayer systems (*32*). A recent theoretical work predicted that the Hamiltonian for this system can be effectively decoupled into that of a monolayer graphene and a TBG, with the interlayer coupling strength enhanced by a factor of $\sqrt{2}$ (*30*). As a result, the band structure of TTG consists of a Dirac cone from the monolayer graphene coexisting with TBG flat bands. The MA is predicted to be the TBG MA's multiplied by $\sqrt{2}$: $\theta_{TTG} = 1.56°$ (*30*). A band structure of TTG at this angle is shown in Fig. 1C. To experimentally realize such a system, we used the "cut and twist" technique (*15*, *31*). An image of the completed device is shown in Fig. 1B: The colored lines trace the original positions of the three pieces of graphene. In addition to the TTG device fabricated in the three-layer overlapped region (called TMB), we have access to two other TBG devices: one in the region with only the top and middle layers (TM), and the other in the region where there are only the middle and bottom layers (MB). These two devices allow us to measure the TM twist angle, $\theta_{TM}$, and MB twist angle, $\theta_{MB}$, individually to characterize our devices.

Figure 1, D and E, shows the longitudinal resistivity, ρ, as a function of perpendicular magnetic field *B* and carrier density *n*, controlled by both top and bottom gates of the two TBG devices, TM and MB. They exhibit typical magnetotransport features of large-angle TBG (*33*), with no insulating resistivity peaks other than at ν = 0 and 4. Here, ν is the moiré band–filling factor $\nu = 4n/n_s$, where $n_s$ is the carrier density at full filling of the fourfold degenerate moiré bands. From these fan

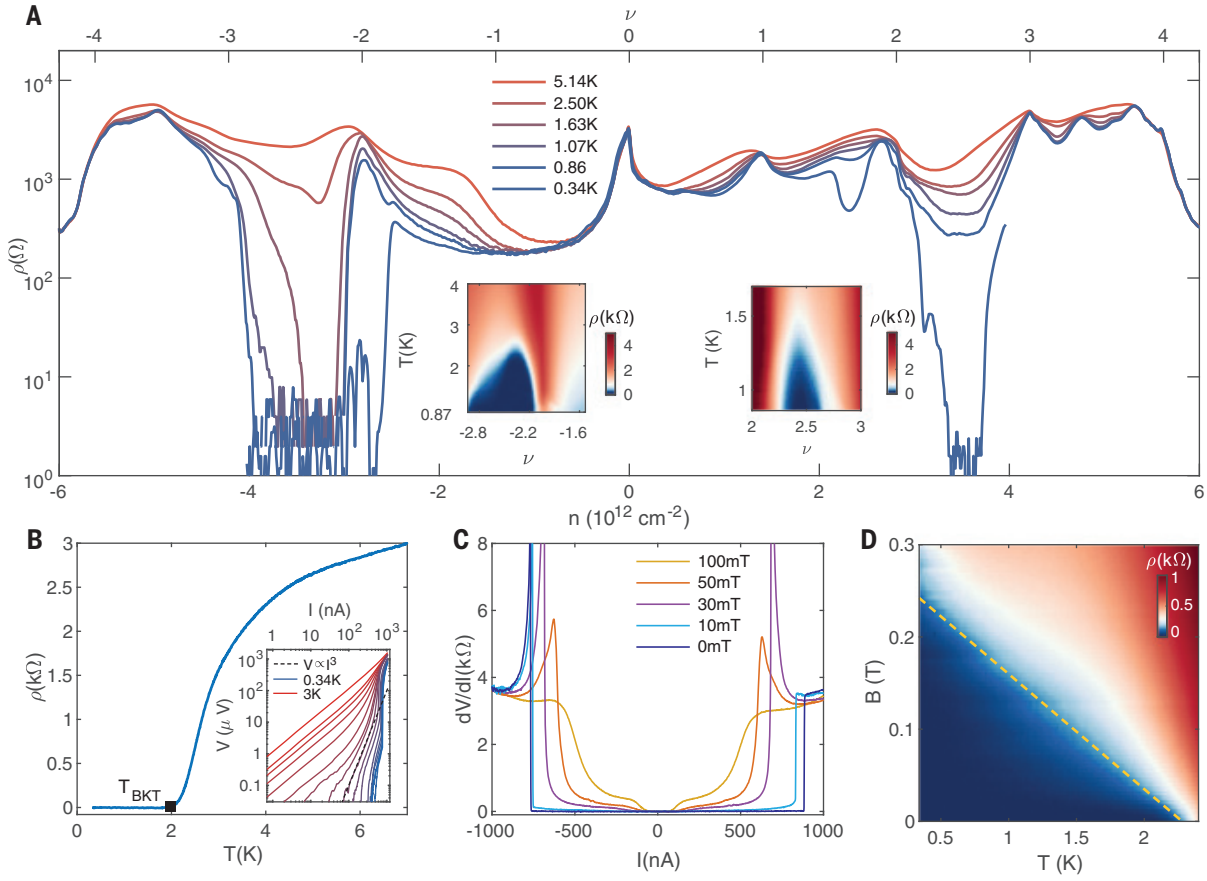


**Fig. 2. Superconductivity in TTG.** (**A**) ρ as a function of ν taken at a fixed back gate voltage $V_{BG}$ = 0 V at several different temperature values. The formation of superconducting regions is visible at ν < −2 and ν > 2. (Insets) The superconducting dome in the *T*-ν plane taken along a cut at (left inset) $V_{BG}$ = 0 V for ν < −2 and (right inset) at $D/\varepsilon_0$ = −0.56 V/nm for ν > 2. (**B**) Superconducting transition in resitivity at ν = −2.3 and $D/\varepsilon_0$ = 0.29 V/nm. The BKT transition temperature $T_{BKT}$ is indicated with the black square. (Inset) *I*-*V* characteristic of the superconductor from 0.34 K (blue) to 3 K (red) on a log-log scale, displaying a crossover from high-power polynomial to linear behavior in the low *V* range. The black dashed line indicates where $V \propto I^3$, defining $T_{BKT}$. (**C**) Differential resistance as a function of dc bias current at different magnetic fields. (**D**) ρ as a function of temperature and perpendicular magnetic field at ν = −2.3 and $D/\varepsilon_0$ = 0.4 V/nm. The dashed line corresponds to a GL theory fit with a coherence length of $\xi_{GL}$ = 34 nm (*31*).

diagrams, we estimate $\theta_{TM} = 1.35°$ and $\theta_{MB} = -1.69°$. The difference in angles is expected because of imperfect angle control in experiments as well as the ubiquitous angle disorder in twisted devices. However, we found that this small angle difference between TM and MB regions yields no appreciable effects in the TTG device formed in the TMB region. The Landau fan diagram of the TTG device at a fixed back gate voltage, $V_{BG}$ = 0, is shown in Fig. 1F. $\rho(B, n)$ exhibits emergent Landau fans at integer fillings ν = 0, ±2, 1, 3, which correspond to a twist angle of 1.55°. In addition, the device is highly uniform across most pairs of contacts, with angle disorder on the order of 0.02° estimated from similar magneto-transport data (*31*). Such high uniformity of twist angle in the TMB region might indicate that the strain relaxation on atomic length scales forces $\theta_{TM} = -\theta_{MB}$ to be the average twist angle, favoring alignment between the top and bottom layers to reduce the structural energy (*34*). An alternative scenario is that the three layers are coupled so strongly that they behave as a single system, with the measured angle the average of $\theta_{TM}$ and $\theta_{MB}$. In either case, the resulting uniform device indicates that TTG is relatively robust against small-angle misalignment and disorder.

We found that, unlike in MA-TBG samples, $\rho(n)$ measured in the TMB device at $B$ = 0 (Fig. 1G) does not exhibit strong insulating behavior at any filling, which is consistent with the additional Dirac cone in the proposed TTG band structure in Fig. 1C. The Landau fan emanating from the charge neutrality has sequence −2, −6, −10, ... on the hole-doped side and 2, 6 on the electron-doped side. This sequence indicates that Landau levels are fourfold degenerate but is different from the typical 4, 8, 12, ... sequence obtained in MA-TBG (*6*). This change is similar to the sequence in ABA trilayer graphene (*35*) and likely results from the presence of the Dirac cone. Figure 1H shows $\sigma_{xy}(n)$ taken at $B$ = 10 T. We see large regions of $\sigma_{xy} = -2e^2/h$ near ν = −4 and $\sigma_{xy} = 2e^2/h$ ($e$ is the electron charge, and $h$ is the Planck constant) near ν = 4 [also, fig. S5, $1/\rho_{xy}(B, n)$]. More direct experimental evidence of the additional Dirac cone is present in the Landau fan diagram taken at zero displacement field, where we observed quantum Hall sequences originating from the Dirac cone at low magnetic fields (fig. S7) (*31*). Flavor symmetry–breaking is evident in the Landau fan coming from ν = −2 with sequence −2, −4, −6, ... and from ν = 2 with sequence 2, 4, 6, ..., showing only twofold degeneracy. Above a perpendicular magnetic field of 1T, the resistive state at ν = −2 shows a resistivity minimum and quantized Hall resistance along the slope of −2, with hysteresis observed near 1 T (fig. S8). This is an indication of a magnetic field–induced Chern insulator with Chern number $C$ = −2 and orbital ferromagnetism associated with it.

At low temperature and magnetic field, we found large regions of robust superconductivity in the TTG sample. Figure 2A shows $\rho(n)$ at different temperatures at $V_{BG}$ = 0 V. At our lowest experimental temperature of $T$ = 0.34 K, zero-resistance regions appear on the hole-doped side of ν = −2 and electron-doped side

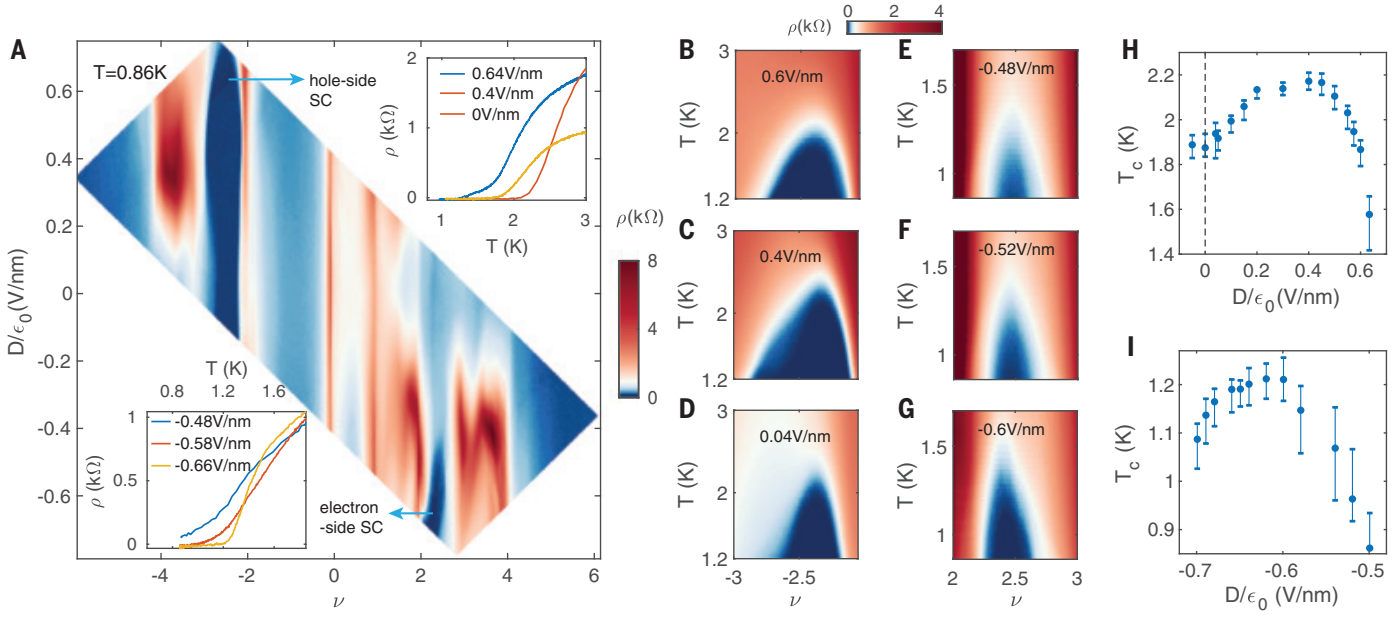


**Fig. 3. Electric field–tuned superconductivity.** (**A**) ρ map as a function of ν and *D* at 0.86 K. Superconducting regions appear for ν < −2 and ν > 2. (Top inset) The ρ at the superconducting transition in the hole region. (Bottom inset) The ρ at the superconducting transition in the electron region. (**B** to **G**) Dome-shaped superconducting regions in the *T*-ν plane at different *D* for [(B) to (D)] ν < −2 and [(E) to (G)] ν > 2. The size and shape of the domes are tuned by *D*. (**H** and **I**) $T_c$ as a function of *D* taken at (H) ν = −2.3 and (I) ν = 2.45. $T_c$ is chosen to be the point at which ρ = 10% $\rho_N$, and error bars correspond to 5% $\rho_N$ and 15% $\rho_N$.

of ν = 2. The Fig. 2A insets show ρ(ν, *T*) near ν = −2 and ν = 2, respectively, both displaying clear superconducting domes. The transition in ρ(*T*) across the dome boundary is sharp, as shown in Fig. 2B at ν = −2.3, the optimal filling for ν < −2. ρ = 0 at *T* ~ 2.1 K, which is higher than most MA-TBG devices in published literature (*6*, *9*, *16*, *24*). At ν = −2.3, we extracted a Berezinskii-Kosterlitz-Thouless (BKT) transition temperature of 2 K from the power law dependence of the current-voltage relation (*I*-*V*) characteristics in the low current and voltage range, as shown in Fig. 2B, inset [analysis details are provided in (*31*)]. Phenomenologically, we define $T_c$ as the temperature at which ρ falls to 10% of the normal state resistance, $\rho_N$, which we found to be consistent with the BKT transition temperature and a better measure for 2D superconductivity (*31*). Additional clear signatures of superconductivity are also visible in the differential resistance, *dV*/*dI*, as a function of dc bias current as shown in Fig. 2C, which shows a sharply defined critical current $I_c$. At *B* = 0 T, the sudden increase of *dV*/*dI* occurs at $I_c$ = 880 nA. At low temperature, there are oscillations of $I_c$ in a Fraunhofer-like pattern, demonstrating phase coherence (fig. S15). As the magnetic field increases, $I_c$ becomes smaller, and the shape of *dV*/*dI* becomes more smooth, which is a characteristic behavior of 2D superconducivity suppressed by a perpendicular magnetic field. The resulting critical field, $B_c$, is evident in ρ(*T*, *B*) in Fig. 2D. We extracted the Ginzburg-Landau (GL) coherence length $\xi_{GL}$ from the theory for a 2D superconductor: $B_c = [\Phi_0/(2\pi\xi_{GL}^2)](1 - T/T_c)$ (*36*), where $\Phi_0$ is the superconducting flux quantum. Using the BKT transition temperature as $T_c$ in the above relation, we estimate $\xi_{GL}$ = 34 nm, which is several times the interparticle distance of 9 nm set by the moiré periodicity. Using the more conventional $T_c$ extracted at ρ = 0.5$\rho_N$, we found $\xi_{GL}$ = 13.4 nm, which is only slightly larger than the interparticle distance. We have also seen superconductivity in an additional TTG device with θ = 1.39° (fig. S17).

Using both the top and bottom gates, we can control both *n* and the displacement field *D* independently, tuning the superconductivity in TTG with the electric field. Figure 3A shows ρ as a function of ν and displacement field *D* at temperature *T* = 0.86 K. We observed at charge neutrality a resistive peak that is not disturbed by *D*. This is expected for the Dirac cone crossings in the flat bands. At ν = ±2, 1, and 3, there are resistivity peaks that are modulated by *D*. At ν = ±4, the system has low ρ, which is expected thanks to the existence of the additional Dirac cone and lack of band insulators at full filling. In Fig. 3A, the superconductivity appears as the dark blue regions both on the hole side between ν = −3 and ν = −2 and on the electron side between ν = 2 and ν = 3. The hole-side superconductivity persists for all *D*, with a width that first increases with *D* and starts to decrease at $D/\varepsilon_0$ ~ 0.4 V/nm. The electron-side superconductivity is weaker and affected more strongly by *D*. At *T* = 0.86 K, it only starts to emerge at $D/\varepsilon_0$ ~ −0.4 V/nm. At a lower temperature, *T* = 0.34 K, superconductivity on both sides extends to larger ranges of ν and *D* (fig. S16A). To better illustrate the evolution of the superconductors with *D*, we have measured ρ(ν, *T*) at several discrete values for *D*, as shown in Fig. 3, B to D, for holes and Fig. 3, E to G, for electrons, showing dome-like superconducting regimes [several representative ρ(*T*) curves are shown in Fig. 3A, insets]. Whereas the optimal doping $\nu_{op}$ at which the maximum $T_c$ occurs is insensitive to *D*, we found the maximum $T_c$ of the dome and the filling range, Δν—the height and width of the dome—to be sensitive to *D*. We measured ρ(*T*) at different *D* at optimal filling to extract the transition temperature $T_c$ at each *D*, providing a quantitative description of the *D* dependence of superconductivity. Figure 3, H and I, shows $T_c$ as a function of *D* for the hole-side and electron-side superconductors, respectively. For the hole-side superconductor, starting from $D/\varepsilon_0$ = 0, $T_c$ first increases, reaches a maximum at around $D/\varepsilon_0$ = 0.4 V/nm, and then decreases quickly. The electron-side superconductor displays a similar trend, with $T_c$ increasing after first appearing at $D/\varepsilon_0$ ~ −0.5 V/nm then decreasing below $D/\varepsilon_0$ ~ −0.62 V/nm.

The electric field–tunable superconductivity in TTG can be ascribed to the tuning of single-particle bands controlled by *D* (*37*). Figure 4A shows renormalized Hall density (measured Hall density divided by $n_s$) $n_H = B/e\rho_{xy}n_s$ at a low magnetic field *B* = 0.5 T, near the region where the hole-side superconductor resides. At $D/\varepsilon_0$ = 0.2 V/nm and away from zero filling, $n_H$(ν) increases linearly with a unity slope and then resets to 0 near ν = −2. This resetting

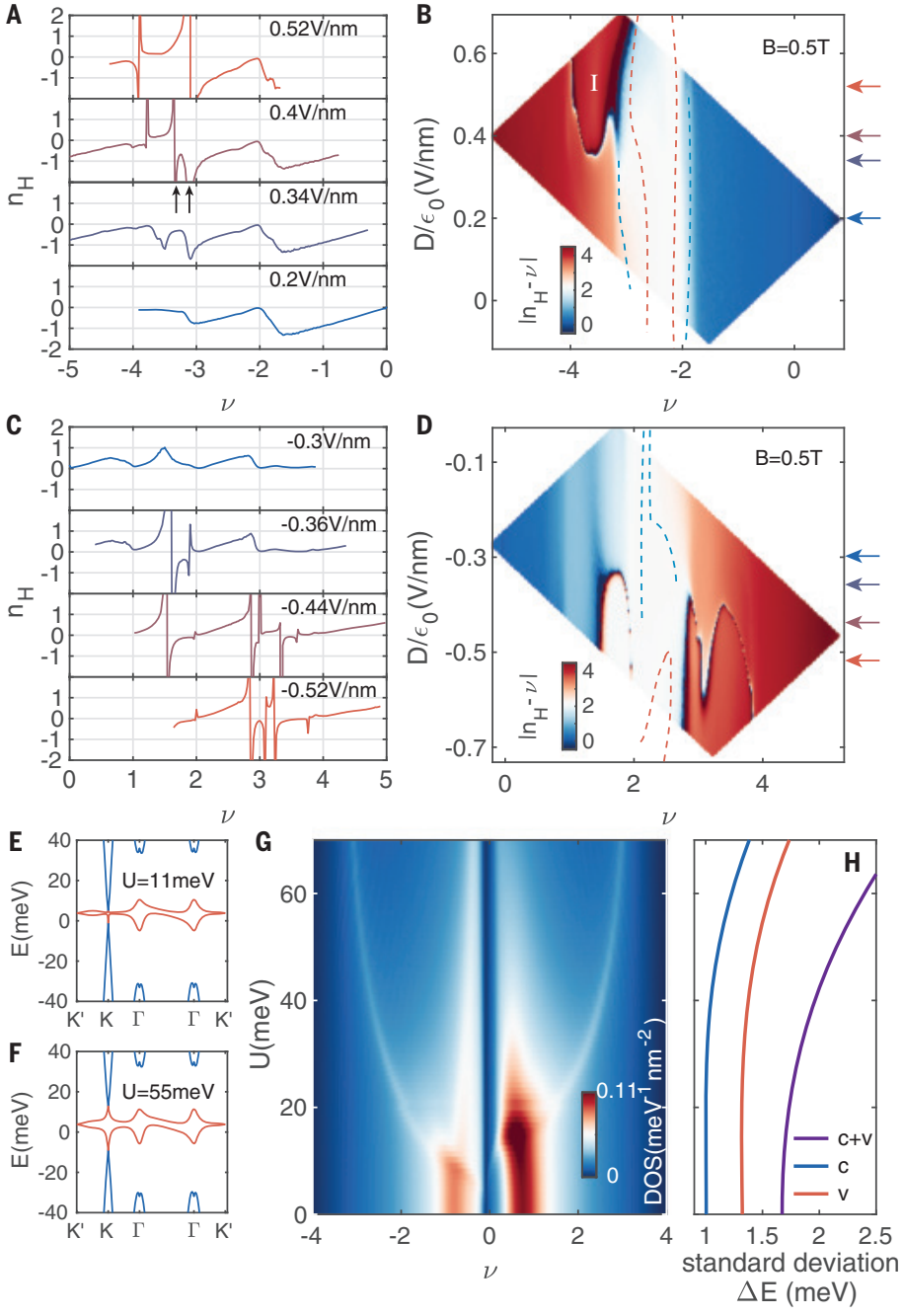


**Fig. 4. Hall data and band structure.** (**A**) Renormalized Hall density $n_H$ at 0.5 T at several $D$ at 0.86 K. Several resets in $n_H$ are visible at flavor symmetry–breaking boundaries. Sign-reversal vHS with flavor symmetry–breaking is indicated with vertical arrows. (**B**) Subtracted Hall density $|n_H - \nu|$ as a function of $\nu$ and $D$ in the same region. The four arrows with different colors indicate the locations of the line cuts in (A). The blue and orange dashed lines trace out the boundaries of the superconducting region at 0.34 K (fig. S16A) and 0.86 K (Fig. 3A), respectively. The $|n_H - \nu| = 4$ region designated "I" crowds out the superconducting region at large $D$. (**C** and **D**) The same as (A) and (B), respectively, but near the $\nu = 2$ superconducting state. (**E** and **F**) Theoretical single-particle band structures at (E) small and (F) large interlayer potential $U$ (*31*). The major change in the band structure is a splitting at the $K$ point. (**G**) Calculated DOS as a function of $\nu$ and $U$. The large flat-band DOS at near $\nu = 0$ at small $U$ diverge into prominent vHSs at large $U$. (**H**) Bandwidth displayed as the standard deviation of the conduction (c), valence (v), and combined (c+v) flat bands as a function of $U$.

behavior has been considered a signature of the spin and valley isospin symmetry–breaking, in which the fourfold degeneracy turns into twofold (*7*). After this flavor symmetry–breaking, the electrons completely fill the two lower-energy bands, and $n_H$ corresponds to the density in the two higher-energy bands. Similar flavor symmetry–breaking in moiré flat bands has been observed and discussed in MA-TBG (*11*, *15*, *38*, *39*). This symmetry breaking can be better illustrated by the quantity $|n_H - \nu|$, which directly gives the degeneracy of the symmetry-breaking phase (*7*). Figure 4B shows $|n_H - \nu|$ as a function of $\nu$ and $D$, showing several symmetry-breaking regions. At $0 > \nu > -2$, the large area of $|n_H - \nu| = 0$ shown in Fig. 4B as dark blue indicates that the holes are filling the four bands equally. At $-2 > \nu > -3$, the system enters the symmetry-breaking phase with two degenerate bands where $|n_H - \nu| = 2$, shown in Fig. 4B in white. At $\nu = -3$ and at small $D$, another reset occurs, and at $\nu < -3$, $|n_H - \nu|$ is not integer-valued, changing gradually from 3 to 4.

This symmetry-breaking behavior is affected as $D$ tunes the single-particle band structure of the MA-TTG. In particular, for the hole-side band ($\nu < 0$), above $D/\varepsilon_0 = 0.35$ V/nm a large region $|n_H - \nu| = 4$ emerges at $\nu < -3$ (Fig. 4B, region I), indicating that the four bands are being filled equally with no symmetry breaking. We found that this region is bounded on the right by a van Hove singularity (vHS) whose existence can be detected from diverging $n_H$ followed by a sign change (*11*). The characteristic sharp divergences of two vHSs can be seen in Fig. 4A at $D/\varepsilon_0 = 0.4$ V/nm near $\nu = -3$ (indicated with vertical arrows), combining into one large divergence at larger $D$. The left boundary of Fig. 4B, region I, also shows a discontinuity. However, the $n_H$ value across this boundary is continuous, indicating that

this is not a vHS. As $D$ increases, the flavor-polarizing vHS moves to the right, expanding the $|n_H - \nu| = 4$ region. This evolution correlates with the reduction of superconductivity. In Fig. 4B, we superimpose the boundaries of the zero–magnetic field superconducting region at 0.34 K (fig. S16A) and 0.86 K (Fig. 3A) onto the $|n_H - \nu|$ plot as blue and orange dashed lines, respectively. The 0.34 K superconducting region boundary aligns well with the $|n_H - \nu| = 2$ symmetry-breaking phase boundary. At 0.86 K, where superconductivity becomes weaker, we can see that the superconducting region is reduced as the vHS and $|n_H - \nu| = 4$ region crowd out the $|n_H - \nu| = 2$ region. For the electron-side superconductor, similar analysis (Fig. 4D) shows that the superconducting region also shrinks when the vHS starts to cross the symmetry-breaking phase boundary.

The region near a vHS has an increased DOS, which promotes superconductivity in conventional Bardeen-Cooper-Schrieffer (BCS) theory in the weak coupling limit (*40*, *41*). Instead, we observed that superconductivity weakens as a vHS approaches, and subsequently, flavor polarization occurs. The prominent role of vHS in the system can also be captured in single-particle band calculations. Figure 4G shows calculated DOS as a function of $\nu$ and interlayer electric potential $U$, which is directly proportional to the experimental $D$. The calculated DOS is symmetric between positive and negative $U$, so only the positive part is shown. We observed that at low $D$, there is high DOS concentrated near charge neutrality, which is a reflection of the flatness of the bands. An example band structure at low $D$ with $U$ = 11 meV is shown in Fig. 4E. As $D$ increases, the bands become more dispersive, and vHSs become prominent, as shown in the DOS calculation in Fig. 4G as the sharp white features at larger $U$. An example band structure in this range is shown in Fig. 4F. The prominence of the vHSs in the theoretical DOS at large $U$ agrees with the vHSs that appear at large $D$ in experiments.

The appearance of these vHSs, and the subsequent flavor ordering that limits the width of the $|n_H - \nu| = 2$ region and consequently the region of superconductivity, accounts for the reduction of the superconducting dome at large $D$. However, the initial enhancement of the superconductivity seems to lie in the region where band flatness dominates the physics. In this regime, the average DOS and bandwidth of the individual conduction and valence band remain roughly constant (Fig. 4, G and H). The major change in the single-particle band structure in this small $D$ range happens at the $K$ point, at which the conduction and valence bands gradually split away from each other, increasing the combined bandwidth at this point. Recent theoretical work has suggested the importance of a second-order process coupling flat bands, reminiscent of super-exchange, as the driving force for pairing (*42*, *43*). This process leads to an energy scale $J \sim t^2/E_c$, where $t$ is related to the overall effective bandwidth and $E_c$ is a measure of the Coulomb repulsion. This pairing mechanism also invokes the presence of the combination of twofold rotation and time-reversal $C_{2z}\mathcal{T}$ symmetry. This symmetry requirement is consistent with MA-TBG and alternating MA-TTG being, at present, the two platforms that exhibit robust superconductivity, and they are also distinct among existing moiré systems in retaining this symmetry. Within this picture, changing the overall effective bandwidth $t$ can enhance superconductivity, which may be related to the observed enhancement of both bandwidth and $T_c$ on increasing the displacement field at small $D$. Further evidence for the strong coupling nature of superconductivity is provided by the rapid increase of $T_c(\nu)$ with doping observed in the superconducting domes for $|\nu| < |\nu_{op}|$. This suggests a picture in which tightly bound Cooper pairs condense, leading to a $T_c$ that is limited by density and therefore grows with doping. We analyzed these results on the basis of a strong coupling theory of skyrmion superconductivity (*43*), in which the $J$ interaction binds charged skyrmions into pairs. We estimate $J$ to be a few milli–electron volts from the experimentally obtained slope of $T_c(\nu)$ in the regime of $|\nu| < |\nu_{op}|$, which is consistent with theoretical expectations (*31*, *43*). We anticipate these results to stimulate further theoretical and experimental investigations into these correlation-driven phenomena.

## REFERENCES AND NOTES


1. R. Bistritzer, A. H. MacDonald, *Proc. Natl. Acad. Sci. U.S.A.* **108**, 12233–12237 (2011).
2. J. M. B. Lopes Dos Santos, N. M. R. Peres, A. H. Castro Neto, *Phys. Rev. Lett.* **99**, 256802 (2007).
3. S. Shallcross, S. Sharma, E. Kandelaki, O. A. Pankratov, *Phys. Rev. B Condens. Matter Mater. Phys.* **81**, 165105 (2010).
4. E. Suárez Morell, J. D. Correa, P. Vargas, M. Pacheco, Z. Barticevic, *Phys. Rev. B Condens. Matter Mater. Phys.* **82**, 121407 (2010).
5. Y. Cao *et al*., *Nature* **556**, 80–84 (2018).
6. Y. Cao *et al*., *Nature* **556**, 43–50 (2018).
7. Y. Saito *et al*., Isospin pomeranchuk effect and the entropy of collective excitations in twisted bilayer graphene. arXiv:2008.10830 [cond-mat.mes-hall] (19 Nov 2020).
8. A. L. Sharpe *et al*., *Science* **365**, 605–608 (2019).
9. X. Lu *et al*., *Nature* **574**, 653–657 (2019).
10. M. Serlin *et al*., *Science* **367**, 900–903 (2020).
11. S. Wu, Z. Zhang, K. Watanabe, T. Taniguchi, E. Y. Andrei, Chern insulators and topological flat-bands in magic-angle twisted bilayer graphene. arXiv:2007.03735 [cond-mat.mes-hall] (11 Dec 2020).
12. K. P. Nuckolls *et al*., *Nature* **588**, 610–615 (2020).
13. Y. Saito *et al*., *Nat. Phys.* (2021).
14. P. Stepanov *et al*., *Nature* **583**, 375–378 (2020).
15. Y. Saito, J. Ge, K. Watanabe, T. Taniguchi, A. F. Young, *Nat. Phys.* **16**, 926–930 (2020).
16. H. S. Arora *et al*., *Nature* **583**, 379–384 (2020).
17. X. Liu *et al*., Tuning electron correlation in magic-angle twisted bilayer graphene using coulomb screening. arXiv:2003.11072 [cond-mat.mes-hall] (8 Jul 2020).
18. Y. Cao *et al*., Nematicity and competing orders in superconducting magic-angle graphene. arXiv:2004.04148 [cond-mat.mes-hall] (8 Apr 2020).
19. J. M. Park, Y. Cao, K. Watanabe, T. Taniguchi, P. Jarillo-Herrero, Flavour hund's coupling, correlated chern gaps, and diffusivity in moiré flat bands. arXiv:2008.12296 [cond-mat.mes-hall] (27 Aug 2020).
20. H. Polshyn *et al*., *Nature* **588**, 66–70 (2020).
21. S. Chen *et al*., *Nat. Phys.* (2020).
22. E. C. Regan *et al*., *Nature* **579**, 359–363 (2020).
23. Y. Xu *et al*., *Nature* **587**, 214–218 (2020).
24. M. Yankowitz *et al*., *Science* **363**, 1059–1064 (2019).
25. G. Chen *et al*., *Nature* **572**, 215–219 (2019).
26. X. Liu *et al*., *Nature* **583**, 221–225 (2020).
27. M. He *et al*., *Nat. Phys.* **17**, 26–30 (2021).
28. L. An *et al*., *Nanoscale Horiz.* **5**, 1309–1316 (2020).
29. L. Balents, C. R. Dean, D. K. Efetov, A. F. Young, *Nat. Phys.* **16**, 725–733 (2020).
30. E. Khalaf, A. J. Kruchkov, G. Tarnopolsky, A. Vishwanath, *Phys. Rev. B* **100**, 085109 (2019).
31. Materials and methods are avialble as supplementary materials.
32. K.-T. Tsai *et al*., Correlated insulating states and transport signature of superconductivity in twisted trilayer graphene moiré of moiré superlattices. arXiv:1912.03375 [cond-mat.mes-hall] (6 Dec 2019).
33. Y. Cao *et al*., *Phys. Rev. Lett.* **117**, 116804 (2016).
34. S. Carr *et al*., *Nano Lett.* **20**, 3030–3038 (2020).
35. E. A. Henriksen, D. Nandi, J. P. Eisenstein, *Phys. Rev. X* **2**, 011004 (2012).
36. M. Tinkham, *Introduction to Superconductivity* (Courier Corporation, 1996).
37. A. Lopez-Bezanilla, J. L. Lado, *Phys. Rev. Res.* **2**, 033357 (2020).
38. D. Wong *et al*., *Nature* **582**, 198–202 (2020).
39. U. Zondiner *et al*., *Nature* **582**, 203–208 (2020).
40. J. Bardeen, L. N. Cooper, J. R. Schrieffer, *Phys. Rev.* **108**, 1175–1204 (1957).
41. Koshino, K. Kuroki, *Phys. Rev. B* **98**, 081102 (2018).
42. N. Bultinck *et al*., *Phys. Rev. X* **10**, 031034 (2020).
43. E. Khalaf, S. Chatterjee, N. Bultinck, M. P. Zaletel, A. Vishwanath, Charged skyrmions and topological origin of superconductivity in magic angle graphene. arXiv:2004.00638 [cond-mat.str-el] (30 Oct 2020).
44. Z. Hao *et al*., Replication Data for: Electric field tunable superconductivity in alternating twist magic-angle trilayer graphene, version 1.0. Harvard Dataverse (2021); doi:10.7910/DVN/OB9CNK.


## ACKNOWLEDGMENTS


We thank P. Jarillo-Herrero, X. Liu, Y. Ronen, O. Gul, and Z. Zhu for fruitful discussions. **Funding:** The major experimental work is supported by NSF (DMR-1922172). P.K. acknowledges support from the U.S. Department of Defense (DOD) Vannevar Bush Faculty Fellowship N00014-18-1-2877. Z.H. is supported by ARO MURI (W911NF-14-1-0247). A.V. and E.K. were supported by a Simons Investigator award (to A.V.) and by the Simons Collaboration on Ultra-Quantum Matter, which is a grant from the Simons Foundation (651440, to A.V.). P.L. was supported by the DOD through the National Defense Science and Engineering Graduate Fellowship (NDSEG) Program. K.W. and T.T. acknowledge support from the Elemental Strategy Initiative conducted by the MEXT, Japan, grant JPMXP0112101001, JSPS KAKENHI grant JP20H00354, and the CREST(JPMJCR15F3), JST. **Author contributions:** Z.H. and D.H.N. fabricated the devices. Z.H. and A.M.Z. performed the measurements and analyzed the data. P.L. and E.K. performed the theoretical calculations. K.W. and T.T. provided the BN crystals. P.K. and A.V. advised on the experiments and theoretical calculations. Z.H., A.M.Z., and P.K. wrote the manuscript, with input from P.L., E.K., and A.V.. **Competing interests:** The authors declare no competing interests. **Data and materials availability:** The data from this study are available at the Harvard Dataverse (*44*).


## SUPPLEMENTARY MATERIALS

science.sciencemag.org/content/371/6534/1133/suppl/DC1
Materials and Methods
Supplementary Text
Figs. S1 to S17
References (*45*–*51*)


7 December 2020; accepted 25 January 2021
10.1126/science.abg0399

CORONAVIRUS

# Recurrent deletions in the SARS-CoV-2 spike glycoprotein drive antibody escape

Kevin R. McCarthy[1,2,3]*, Linda J. Rennick[1,2], Sham Nambulli[1,2], Lindsey R. Robinson-McCarthy[4], William G. Bain[5,6,7], Ghady Haidar[8,9], W. Paul Duprex[1,2]*

Zoonotic pandemics, such as that caused by severe acute respiratory syndrome coronavirus 2 (SARS-CoV-2), can follow the spillover of animal viruses into highly susceptible human populations. The descendants of these viruses have adapted to the human host and evolved to evade immune pressure. Coronaviruses acquire substitutions more slowly than other RNA viruses. In the spike glycoprotein, we found that recurrent deletions overcome this slow substitution rate. Deletion variants arise in diverse genetic and geographic backgrounds, transmit efficiently, and are present in novel lineages, including those of current global concern. They frequently occupy recurrent deletion regions (RDRs), which map to defined antibody epitopes. Deletions in RDRs confer resistance to neutralizing antibodies. By altering stretches of amino acids, deletions appear to accelerate SARS-CoV-2 antigenic evolution and may, more generally, drive adaptive evolution.

Severe acute respiratory syndrome coronavirus 2 (SARS-CoV-2) emerged from a yet-to-be-defined animal reservoir and initiated a pandemic in 2020 (*1*–*5*). It has acquired limited adaptions, most notably the $Asp^{614} \rightarrow Gly$ (D614G) substitution in the spike (S) glycoprotein (*6*–*8*). Humoral immunity to S glycoprotein appears to be the strongest correlate of protection (*9*), and recently approved vaccines deliver this antigen by immunization. Coronaviruses such as SARS-CoV-2 acquire substitutions slowly as the result of a proofreading RNA-dependent RNA polymerase (RdRp) (*10*, *11*). Other emerging respiratory viruses have produced pandemics followed by endemic human-to-human spread. The latter is often contingent upon the introduction of antigenic novelty that enables reinfection of previously immune individuals. Whether SARS-CoV-2 S glycoprotein will evolve altered antigenicity, or specifically how it may change in response to immune pressure, remains unknown. We and others have reported the acquisition of deletions in the N-terminal domain (NTD) of the S glycoprotein during long-term infections of immunocompromised patients (*12*–*15*). We have identified this as an evolutionary pattern defined by recurrent deletions that alter defined antibody epitopes. Unlike substitutions, deletions cannot be corrected by proofreading activity, and this may accelerate adaptive evolution in SARS-CoV-2.

An immunocompromised cancer patient infected with SARS-CoV-2 was unable to clear the virus and succumbed to the infection 74 days after COVID-19 diagnosis (*15*). Treatment included remdesivir, dexamethasone, and two infusions of convalescent serum. We designate this individual as Pittsburgh long-term infection 1 (PLTI1). We consensus-sequenced and cloned S genes directly from clinical material obtained 72 days after COVID-19 diagnosis and identified two variants with deletions in the NTD (Fig. 1A).

These data from PLTI1 and a similar report (*12*) prompted us to interrogate patient metadata sequences deposited in GISAID (*16*). In searching for similar viruses, we identified eight patients with deletions in the S glycoproteins of viruses sampled longitudinally over a period of weeks to months (Fig. 1A and fig. S1A). For each, early time points had intact S sequences and later time points had deletions within the S gene. Six had deletions that were identical to, overlapping with, or adjacent to those in PLTI1. Deletions at a second site were present in viruses isolated from two other patients (Fig. 1B); reports on these patients have since been published (*13*, *14*). Viruses from all but one patient could be distinguished from one another by nucleotide differences present at both early and late time points (fig. S1B). On a tree of representative contemporaneously circulating isolates, they form monophyletic clades, making either a second community-acquired or nosocomially acquired infection unlikely (fig. S1C). The most parsimonious explanation is that these deletions arose independently as the result of a common selective pressure to produce strikingly convergent outcomes.

We searched the GISAID sequence database (*16*) for additional instances of deletions within S glycoproteins. From a dataset of 146,795 sequences (deposited from 1 December 2019 to 24 October 2020) we identified 1108 viruses with deletions in the S gene. When mapped to the S gene, 90% of these deletions occupied four discrete sites within the NTD (Fig. 2A). We term these important sites recurrent deletion regions (RDRs), numbering them 1 to 4 from the 5′ to the 3′ end of the S gene. Deletions identified in patient samples correspond to RDR2 (Fig. 1A) and RDR4 (Fig. 1B). Most deletions appear to have arisen and been retained in replication-competent viruses.

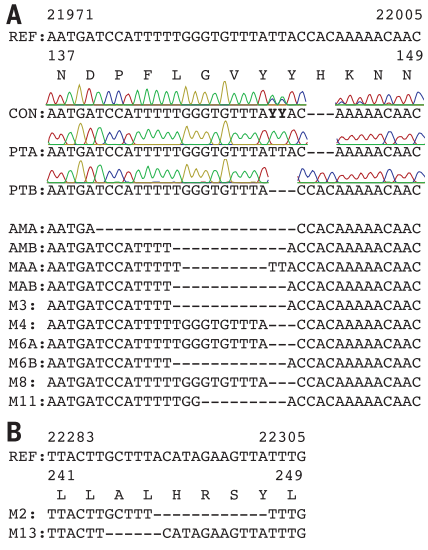


**Fig. 1. Deletions in SARS-CoV-2 spike glycoprotein arise during persistent infections of immunosuppressed patients.** (**A**) Top: Sequences of viruses isolated from PLTI1 (PT) and viruses from patients with deletions in the same NTD region. Chromatograms are shown for sequences from PLTI1, which include sequencing of bulk reverse transcription products (CON) and individual cDNA clones. Bottom: Sequences from other long-term infections from individuals AM (*18*), MA-JL (MA) (*19*), and a MSK cohort (M) with individuals 3, 4, 6, 8, and 11 (*13*). Letters (A and B) designate different variants from the same patient. (**B**) Sequences of viruses from two patients (M2 and M13) with deletions in a different region of the NTD. All sequences are aligned to reference sequence (REF) MN985325 (WA-1). See fig. S1 for genetic analysis of patient isolates. Amino acid abbreviations: A, Ala; D, Asp; F, Phe; G, Gly; H, His; K, Lys; L, Leu; N, Asn; P, Pro; R, Arg; S, Ser; V, Val; Y, Tyr.

[1]Center for Vaccine Research, University of Pittsburgh School of Medicine, Pittsburgh, PA, USA. [2]Department of Microbiology and Molecular Genetics, University of Pittsburgh School of Medicine, Pittsburgh, PA, USA. [3]Laboratory of Molecular Medicine, Boston Children's Hospital, Harvard Medical School, Boston, MA, USA. [4]Department of Genetics, Harvard Medical School, Boston, MA, USA. [5]Division of Pulmonary, Allergy, and Critical Care Medicine, Department of Internal Medicine, UPMC, Pittsburgh, PA, USA. [6]Division of Pulmonary, Allergy, and Critical Care Medicine, Department of Medicine, University of Pittsburgh School of Medicine, Pittsburgh, PA, USA. [7]VA Pittsburgh Healthcare System, Pittsburgh, PA, USA. [8]Division of Infectious Disease, Department of Medicine, University of Pittsburgh School of Medicine, Pittsburgh, PA, USA. [9]Division of Infectious Disease, Department of Internal Medicine, UPMC, Pittsburgh, PA, USA.
*Corresponding author. Email: krm@pitt.edu (K.R.M.); pduprex@pitt.edu (W.P.D.)

Without selective pressure, in-frame deletions should occur one-third of the time. However, we observed a preponderance of in-frame deletions with lengths of 3, 6, 9, and 12 (Fig. 2B). Among all deletions, 93% are in frame and do not produce a stop codon (Fig. 2C). In the NTD, >97% of deletions maintain the open reading frame. Other S glycoprotein domains do not follow this trend; for example, deletions in the receptor binding domain (RBD) and S2 preserve the reading frame 30% and 37% of the time, respectively.

To trace the origins of RDR variants, we produced phylogenies for each with 101 additional genomes that sample much of the genetic diversity within the pandemic (Fig. 2D). The RDR variants interleave with nondeletion sequences and occupy distinct branches, indicating their recurrent generation. This is most pronounced for RDRs 1, 2, and 4 but is also true of RDR3, with conservatively four independent instances. RDR variants form distinct lineages/branches, most prominently in RDR1 (lineage B.1.258), and suggest human-to-human transmission events. Using sequences with sufficient metadata to explicitly differentiate individuals, we verified the transmission of a variant within each RDR between people (fig. S2).

We defined the RDRs on the basis of peaks in the spectrum of S glycoprotein deletions. Deletion lengths and positions vary within RDRs 1, 2, and 4 (Fig. 2E). Variation is greatest in RDRs 2 and 4, with the loss of S glycoprotein residues 144/145 (adjacent tyrosine codons) in RDR2 and residues 243 and 244 in RDR4 appearing to be favored. In contrast, the loss of residues 69 and 70 accounts for the vast majority of RDR1 deletions. On the basis of our phylogenetic analysis and accompanying lineage classifications, this two–amino acid deletion has arisen independently at least 13 times. RDR3 largely consists of three nucleotide deletions in codon 220.

We evaluated the genetic, geographic, and temporal sampling of RDR variants (Fig. 3, A and B). This analysis was limited to sequences deposited in GISAID (*16*) where sequences from specific nations and regions are overrepresented (e.g., United Kingdom and other European countries). We show the distribution of all sequences within the database for reference. For RDR2 and RDR4, the genetic and geographic distributions largely mirror those of reported sequences. Variants of RDR1 and RDR3 are strongly polarized to specific clades and geographies. This is likely the result of successful lineages circulating in regions with strong sequencing initiatives. Our temporal analysis indicates that RDR variants have been present throughout the pandemic (Fig. 3C). Specific variant lineages such as B.1.258 (Fig. 2D) harboring Δ69–70 in RDR1 have rapidly risen to notable abundance (Fig. 3D). Circulation of B.1.36 with RDR3 Δ210 accounts for most of the RDR3 examples (Fig. 2D and Fig. 3, C and D). The abundance of RDR2 Δ144/145 is explained by independent deletion events followed by transmission (Fig. 2D and Fig. 3, C and D).

The recurrence and convergence of RDR deletions, particularly during long-term infections, is indicative of adaptation in response to a common selective pressure. RDRs 2 and 4 and RDRs 1 and 3 occupy two distinct surfaces on the S glycoprotein NTD (Fig. 4A). Both sites contain antibody epitopes (*17*–*19*). The epitope for neutralizing antibody 4A8 is formed entirely by the β sheets and extended connecting loops that harbor RDRs 2 and 4 (*17*). We generated a panel of S glycoprotein mutants representing the four RDRs to assess the impact of deletions on expression and antibody binding; we included an additional double mutant containing the deletions present in the B.1.1.7 variant of concern flagged initially in the United Kingdom. Cells were transfected with plasmids expressing these mutant glycoproteins, and indirect immunofluorescence was used to determine whether RDR deletions modulated 4A8 binding (Fig. 4B). Deletions at RDRs 1 and 3 had no impact on the binding of the monoclonal antibody, confirming that they alter independent sites. The three RDR2 deletions, the one RDR4 deletion, and the double RDR1/2 deletions completely abolished binding of 4A8 while still allowing recognition by a monoclonal antibody

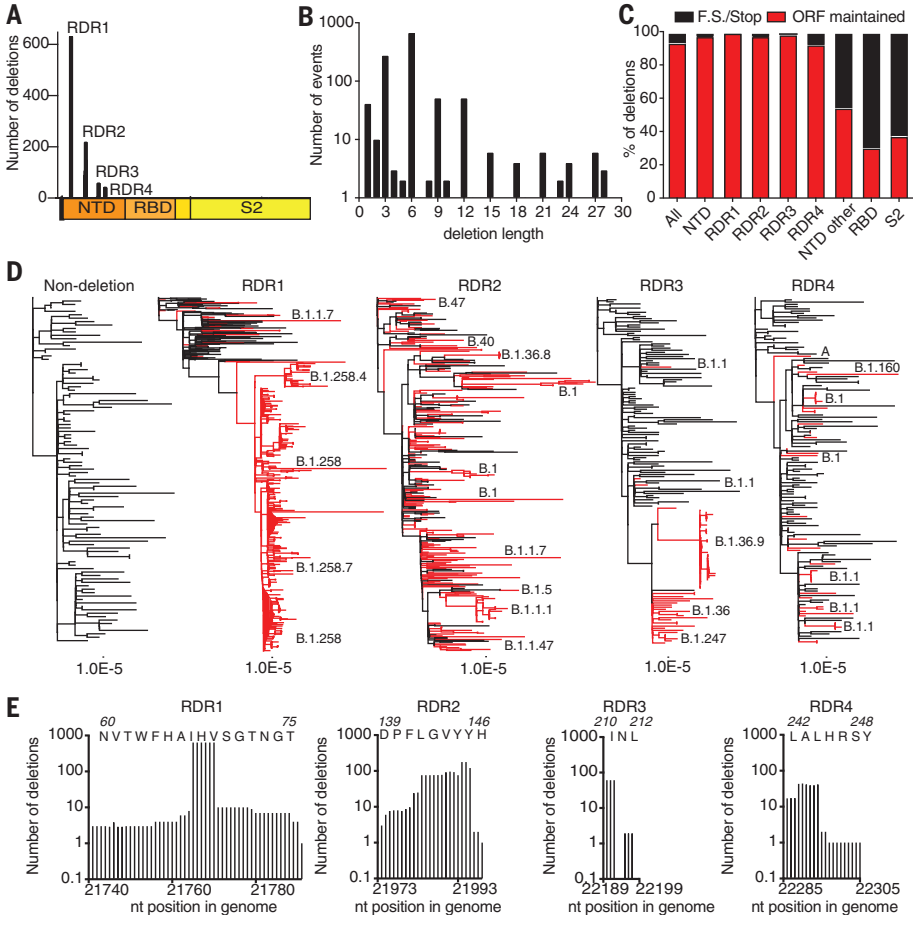


**Fig. 2. Identification and characterization of recurrent deletion regions in SARS-CoV-2 spike protein.** (**A**) Positional quantification of deleted nucleotides in S among GISAID sequences. We designate the four clusters as recurrent deletion regions (RDRs) 1 to 4. (**B**) Length distribution of deletions. (**C**) The percentage of deletion events at the indicated site that either maintain the open reading frame (ORF) or introduce a frameshift or premature stop codon (F.S./Stop). (**D**) Phylogenetic analysis of deletion variants (red branches) and genetically diverse nondeletion variants (black branches). Specific deletion clades/lineages are identified. Maximum likelihood phylogenetic trees, rooted on NC_045512, were calculated with 1000 bootstrap replicates. Trees with branch labels are in fig. S2. (**E**) Abundance of nucleotide (nt) deletions in each RDR. Positions are defined by reference sequence MN985325, by codon (top) and nucleotide (below). Amino acid abbreviations: A, Ala; D, Asp; F, Phe; G, Gly; H, His; I, Ile; L, Leu; N, Asn; P, Pro; R, Arg; S, Ser; T, Thr; V, Val; W, Trp; Y, Tyr.

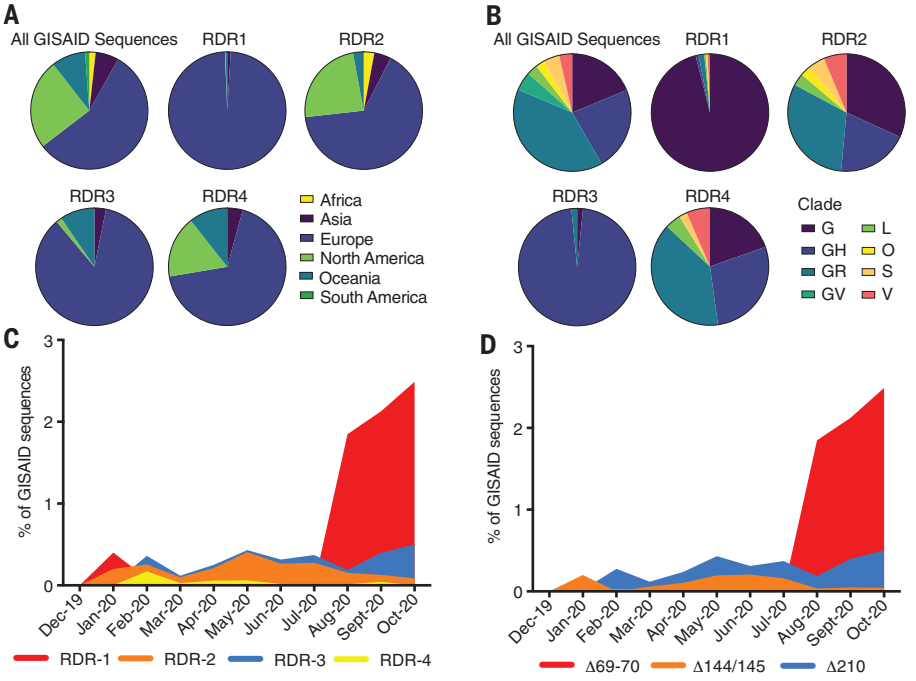


**Fig. 3. Geographic, genetic, and temporal abundance of RDR variants.** (**A** and **B**) Geographic (A) and genetic (B) distributions of RDR variants compared to the GISAID database (sequences from 1 December 2019 to 24 October 2020). GISAID clade classifications are used in (B). (**C**) Frequency of RDR variants among all complete genomes deposited in GISAID. (**D**) Frequency of specific RDR deletion variants (numbered according to spike amino acids) among all GISAID variants. The plot of RDR3/Δ210 has been adjusted by 0.02 units on the *y* axis for visualization in (C) because of its overlap with RDR2, and this adjustment has been retained in (D) to enable direct comparisons between panels.

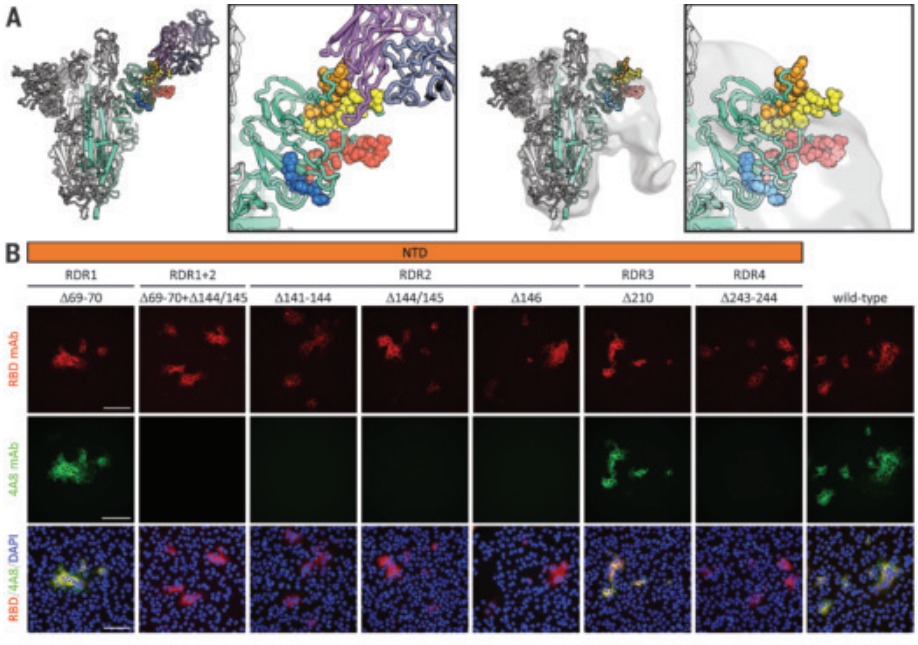


C

| antibody | virus | antibody concentration (μg/ml) | | | | | | | | | |
|---|---|---|---|---|---|---|---|---|---|---|---|
| | | 25 | 12.5 | 6.25 | 3.125 | 1.56 | 0.78 | 0.39 | 0.2 | 0.1 | 0.05 |
| 4A8 (α-S) | PLTI1 | - | - | - | - | - | - | - | - | - | - |
| | Munich: P3 | + | + | + | + | + | + | - | - | - | - |
| H2214 (α-HA) | PLTI1 | - | - | - | - | - | - | ND | ND | ND | ND |
| | Munich: P3 | - | - | - | - | - | - | ND | ND | ND | ND |

| | virus | serum dilution | | | | | |
|---|---|---|---|---|---|---|---|
| | | 1:100 | 1:200 | 1:400 | 1:800 | 1:1600 | 1:3200 |
| human convalescent serum | PLTI1 | + | + | + | + | + | - |
| | Munich: P3 | + | + | + | + | + | - |

+ neutralization (by PRNT 80)
- no neutralization (by PRNT 80)
ND not determined

**Fig. 4. Deletions in the spike NTD alter its antigenicity; RDRs map to defined antigenic sites.** (**A**) Left: A structure of antibody 4A8 (*17*) (PDB ID 7C21) (purple) bound to one protomer (green) of a SARS-CoV-2 spike trimer (gray). RDRs 1 to 4 are colored red, orange, blue, and yellow, respectively, and are shown as spheres. The boxed image is a close-up of the interaction site. Right: The electron microscopy density of COV57 serum Fabs (*18*) (EMDB emd_22125) fit to SARS-CoV-2 S glycoprotein trimer (PDB ID 7C21). The boxed image is a close-up of the interaction site. (**B**) S glycoprotein distribution in Vero E6 cells at 24 hours after transfection with S protein deletion mutants, visualized by indirect immunofluorescence in permeabilized cells. A monoclonal antibody to SARS-CoV-2 S protein receptor-binding domain (RBD mAb; red) detects all mutant forms of the protein (Δ69–70, Δ69–70+Δ141–144, Δ141–144, Δ144/145, Δ146, Δ210, and Δ243–244) and the unmodified protein (wild type), whereas 4A8 mAb (green) does not detect mutants containing deletions in RDR2 or RDR4 (Δ69–70+Δ141–144, Δ141–144, Δ144/145, Δ146, and Δ243–244). Overlay images (RBD/4A8/DAPI) depict colocalization of the antibodies; nuclei were counterstained with 4′,6-diamidino-2-phenylindole (DAPI; blue). Scale bars, 100 μm. (**C**) Virus isolated from PLTI1 resists neutralization by 4A8. A nondeletion variant (Munich) is neutralized by 4A8, both are neutralized by convalescent serum, and neither is neutralized by H2214, an influenza hemagglutinin binding antibody (*29*).

targeting the RBD (Fig. 4B). Thus, convergent evolution operates in individual RDRs and between RDRs, as exemplified by the same phenotype produced by deletions in RDR2 or RDR4.

We used the non–plaque-purified viral population from PLTI1 to determine whether RDR variants escape the activity of a neutralizing antibody. This viral stock was completely resistant to neutralization by 4A8, whereas an isolate with authentic RDRs (*20*) was neutralized (Fig. 4C). We used a high-titer neutralizing human convalescent polyclonal antiserum to demonstrate that both viral stocks could be neutralized efficiently. These data demonstrate that naturally arising and circulating variants of SARS-CoV-2 have altered antigenicity. We used a range of high-, medium-, and low-titer neutralizing human convalescent polyclonal antisera to assess whether there was an appreciable difference in neutralization between the S glycoprotein–deleted and undeleted viruses. No major difference was observed, which suggests that many more changes would be required to generate serologically distinct SARS-CoV-2 variants (table S1).

Coronaviruses, including SARS-CoV-2, have lower substitution rates than other RNA viruses because of an RdRp with proofreading activity (*10*, *11*). However, proofreading cannot correct deletions. We find that adaptive evolution of S glycoprotein is augmented by a tolerance for deletions, particularly within RDRs. The RDRs occupy defined antibody epitopes within the NTD (*17*–*19*), and deletions at multiple sites confer resistance to a neutralizing antibody. Deletions represent a generalizable mechanism through which S glycoprotein rapidly acquires genetic and antigenic novelty of SARS-CoV-2.

The fitness of RDR variants is evident by their representation in the consensus genomes from patients, transmission between individuals, and presence in emergent lineages. Initially documented in the context of long-term infections of immunosuppressed patients, specific variants transmit efficiently between immunocompetent individuals. Characterization of these cases led to the very early identification of RDR variants that are escape mutants. Because deletions are a product of replication, they will occur at a certain rate and variants are likely to emerge in otherwise healthy populations. Indeed, influenza explores variation that approximates future antigenic drift in immunosuppressed patients (*21*).

The RDRs occupy defined antibody epitopes within the S glycoprotein NTD. Selected in vivo, these deletion variants resist neutralization by monoclonal antibodies. Viruses cultured in vitro in the presence of immune serum have also acquired substitutions in RDR2 that confer neutralization resistance (*22*). Potent neutralizing responses and an array of monoclonal antibodies are directed to the RBD (*18*, *19*, *23*). A growing number of NTD-directed antibodies have been identified (*24*, *25*). Why antibody escape in nature is most evident in the NTD highlights a discrepancy, and this requires further study.

Defining recurrent, convergent patterns of adaptation can provide predictive potential. From viral sequences, we have identified a pattern of deletions, contextualized their outcomes in protein structure and antibody epitope(s), and characterized their functional impact on antigenicity. During evaluation of this manuscript, multiple lineages with altered antigenicity and perhaps increased transmissibility have emerged and spread. These variants of global concern are RDR variants and include Mink Cluster 5 Δ69–70 (*26*), B.1.1.7 Δ69–70, and Δ144/145 (*27*), as well as B.1.351 Δ242–244 (*28*). Our analysis preceded the description of these lineages. We had demonstrated that identical or similar recurrent deletions that alter positions 144/145 and 243–244 in the S glycoprotein disrupt binding of antibody 4A8, which defines an immunodominant epitope within the NTD. Our survey for deletion variants captured the first representative of what would become the B.1.1.7 lineage. These real-world outcomes demonstrate the predictive potential of this and like approaches and show the need to monitor viral evolution carefully and continually.

Additional circulating RDR variants have gone virtually unnoticed. Are they intermediates on a pathway of immune evasion? That remains to be determined. However, deletions and substitutions within major NTD and RBD epitopes will likely continue to contribute to that process, as they have already in current variants of concern. The progression of adaptations in both immunocompromised patients and SARS-CoV-2 variants of concern remains to be resolved. Their evolution has thus far converged. The recurrence of adaptations in single patients and on global scales underscores the need to track and monitor deletion variants.

## REFERENCES AND NOTES


1. N. Zhu *et al.*, *N. Engl. J. Med.* **382**, 727–733 (2020).
2. F. Wu *et al.*, *Nature* **579**, 265–269 (2020).
3. H. Zhou *et al.*, *Curr. Biol.* **30**, 3896 (2020).
4. T. T. Lam *et al.*, *Nature* **583**, 282–285 (2020).
5. M. F. Boni *et al.*, *Nat. Microbiol.* **5**, 1408–1417 (2020).
6. B. Korber *et al.*, *Cell* **182**, 812–827.e19 (2020).
7. R. P. McNamara *et al.*, *Cell Rep.* **33**, 108352 (2020).
8. E. Volz *et al.*, *Cell* **184**, 64–75.e11 (2021).
9. K. McMahan *et al.*, *Nature* 10.1038/s41586-020-03041-6 (2020).
10. M. R. Denison, R. L. Graham, E. F. Donaldson, L. D. Eckerle, R. S. Baric, *RNA Biol.* **8**, 270–279 (2011).
11. E. Minskaia *et al.*, *Proc. Natl. Acad. Sci. U.S.A.* **103**, 5108–5113 (2006).
12. V. A. Avanzato *et al.*, *Cell* **183**, 1901–1912.e9 (2020).
13. T. Aydillo *et al.*, *N. Engl. J. Med.* **383**, 2586–2588 (2020).
14. B. Choi *et al.*, *N. Engl. J. Med.* **383**, 2291–2293 (2020).
15. M. K. Hensley *et al.*, *Clin. Infect. Dis.* ciab072 (2021).
16. Y. Shu, J. McCauley, *Euro Surveill.* **22**, 30494 (2017).
17. X. Chi *et al.*, *Science* **369**, 650–655 (2020).
18. C. O. Barnes *et al.*, *Cell* **182**, 828–842.e16 (2020).
19. L. Liu *et al.*, *Nature* **584**, 450–456 (2020).
20. W. B. Klimstra *et al.*, *J. Gen. Virol.* **101**, 1156–1169 (2020).
21. K. S. Xue *et al.*, *eLife* **6**, e26875 (2017).
22. Y. Weisblum *et al.*, *eLife* **9**, e61312 (2020).
23. L. Piccoli *et al.*, *Cell* **183**, 1024–1042.e21 (2020).
24. D. Li *et al.*, bioRxiv 10.1101/2020.12.31.424729 [preprint]. 2 January 2021; https://www.biorxiv.org/content/10.1101/2020.12.31.424729v1.
25. W. N. Voss *et al.*, bioRxiv 10.1101/2020.12.20.423708 [preprint]. 21 December 2020; https://www.biorxiv.org/content/10.1101/2020.12.20.423708v1.
26. World Health Organization, "SARS-CoV-2 mink-associated variant strain – Denmark" (2020); www.who.int/csr/don/06-november-2020-mink-associated-sars-cov2-denmark/en/.
27. S. A. Kemp *et al.*, bioRxiv 10.1101/2020.12.14.422555 [preprint]. 21 December 2020; https://www.biorxiv.org/content/10.1101/2020.12.14.422555v2.
28. H. Tegally *et al.*, medRxiv 10.1101/2020.12.21.20248640 [preprint]. 22 December 2020; https://www.medrxiv.org/content/10.1101/2020.12.21.20248640v1.
29. A. Watanabe *et al.*, *Cell* **177**, 1124–1135.e16 (2019).


## ACKNOWLEDGMENTS

We gratefully acknowledge the authors from the originating laboratories and the submitting laboratories, who generated and shared via GISAID genetic sequence data on which this research is based (table S2). We thank S. C. Harrison for his support. We thank A. Morris, B. McVerry, G. Kitsios, B. Methe, J. S. Lee, P. Ray, H. Michael, M. Busch, J. Ries, and C. Schaefer at the University of Pittsburgh, as well as the physicians, nurses, and respiratory therapists at the University of Pittsburgh Medical Center Shadyside-Presbyterian Hospital intensive care units for assistance with collection and processing of the endotracheal aspirate sample. This work was conducted under University of Pittsburgh Review Board approval CR19050099-099. **Author contributions:** K.R.M., L.J.R., S.N., L.R.R.-M., and W.P.D. designed the experiments; K.R.M., L.J.R., S.N., and L.R.R.M. performed the experiments; K.R.M., L.J.R., S.N., L.R.R.-M., and W.P.D. analyzed data; W.G.B. and G.H. provided reagents and samples; and K.R.M., L.J.R., S.N., L.R.R.-M., and W.P.D. wrote the manuscript. **Competing interests:** The authors declare no competing interests. **Funding:** Supported by the University of Pittsburgh, the Center for Vaccine Research, the Commonwealth of Pennsylvania Department of Community and Economic Development, the Richard King Mellon Foundation, the Henry L. Hillman Foundation (W.P.D.), National Heart, Lung, and Blood Institute award P01HL114453 and U.S. Department of Veterans Affairs Career Development Award IK2 BX004886 (W.G.B.), and UPMC Immune Transplant and Therapy Center (W.G.B., G.H.). **Data availability:** Sequences from PLTI1 were deposited in NCBI GenBank under accession numbers MW269404 and MW269555. All other sequences are available via the GISAID SARS-CoV-2 sequence database (www.gsaid.org; see table S2 for full list of acknowledgments). 

## SUPPLEMENTARY MATERIALS

science.sciencemag.org/content/371/6534/1139/suppl/DC1
Materials and Methods
Figs. S1 to S3
Tables S1 and S2
References (*30*–*34*)
MDAR Reproducibility Checklist

19 November 2020; accepted 30 January 2021
Published online 3 February 2021
10.1126/science.abf6950

NANOMATERIALS

# Synthesis of borophane polymorphs through hydrogenation of borophene

Qiucheng Li[1], Venkata Surya Chaitanya Kolluru[2,3,4], Matthew S. Rahn[1], Eric Schwenker[1,2], Shaowei Li[1]*, Richard G. Hennig[3,4], Pierre Darancet[2,5], Maria K. Y. Chan[2,5], Mark C. Hersam[1,6,7]†

Synthetic two-dimensional polymorphs of boron, or borophene, have attracted attention because of their anisotropic metallicity, correlated-electron phenomena, and diverse superlattice structures. Although borophene heterostructures have been realized, ordered chemical modification of borophene has not yet been reported. Here, we synthesize "borophane" polymorphs by hydrogenating borophene with atomic hydrogen in ultrahigh vacuum. Through atomic-scale imaging, spectroscopy, and first-principles calculations, the most prevalent borophane polymorph is shown to possess a combination of two-center–two-electron boron-hydrogen and three-center–two-electron boron-hydrogen-boron bonds. Borophane polymorphs are metallic with modified local work functions and can be reversibly returned to pristine borophene through thermal desorption of hydrogen. Hydrogenation also provides chemical passivation because borophane reduces oxidation rates by more than two orders of magnitude after ambient exposure.

Since its initial experimental realization (*1*), studies of borophene have focused on its diverse polymorphism and predicted properties, which include two-dimensional (2D) anisotropic metallicity, high mechanical strength and flexibility, and phonon-mediated superconductivity (*2*, *3*). However, borophene rapidly oxidizes in air, which has confined experimental characterization to ultrahigh vacuum (UHV) conditions and also poses challenges to integrating borophene into practical devices (*4*). Chemical passivation can suppress ambient oxidation for electronic materials. For example, monohydride termination of the dangling bonds on silicon surfaces minimizes native oxide formation (*5*, *6*), and covalent modification of 2D black phosphorus improves morphological stability and preserves electronic properties in ambient conditions (*7*). First-principles calculations have suggested that borophene can also be stabilized through surface hydrogenation (*8*).

Beyond passivation, chemical functionalization can modulate the electronic properties of 2D materials. For example, by converting the carbon bonding configuration from $sp^2$ to $sp^3$, hydrogenating graphene to form graphane leads to a tunable bandgap based on the hydrogen surface concentration (*9*). By drawing inspiration from graphane, hydrogenated borophene (borophane) has been explored theoretically. Predicted electronic properties include metallic (*10*), semiconducting (*11*), and Dirac characteristics with ultrahigh Fermi velocity and thermal conductance (*8*, *12*). Although hydrogen boride nanosheets have been reported based on chemical reactions involving inorganic salts (*13*–*15*), atomically well-defined synthesis and characterization of borophane polymorphs have not yet been achieved.

We report hydrogenation of borophene by exposing borophene to atomic hydrogen in UHV conditions. Similar to the high degree of polymorphism in borophene, we observed eight different borophane polymorphs. Of these, we extensively studied the bonding structure and properties of rectangular $v_{1/6}$-30° borophane (abbreviated as rect-$v_{1/6}$-30°) because it has a high surface coverage of hydrogen and a highly ordered structure. In particular, by combining scanning tunneling microscopy and spectroscopy (STM and STS), inelastic electron tunneling spectroscopy (IETS), and density functional theory (DFT), the bonding in rect-$v_{1/6}$-30° borophane was found to consist of two-center–two-electron (2c2e) B–H bonds and three-center–two-electron (3c2e) B–H–B bonds. In situ local work function measurements supported theoretical predictions that rect-$v_{1/6}$-30° borophane has a lower work function than $v_{1/6}$-30° borophene. In addition, unlike pristine borophene that oxidizes almost instantaneously in ambient conditions, borophane showed negligible oxidation according to x-ray photoelectron spectroscopy (XPS) even after 1 week of ambient exposure.

Borophene was grown on atomically clean Ag(111) substrates in UHV by elemental boron evaporation, with the dominant borophene polymorph determined by the substrate temperature (*16*). Subsequent hydrogenation was performed in situ by exposing the borophene sample to atomic hydrogen that was generated by cracking molecular hydrogen with a hot tungsten filament (see supplementary materials for details). After this procedure, STM revealed bright protrusions on the borophene surface that we attributed to hydrogen adatoms (fig. S1). This observation is qualitatively similar to hydrogen adsorption on graphene (*17*), but chemical modification of borophene was more complex than that of graphene because of its multicentered bonding configurations and anisotropic features (*18*). At least eight borophane polymorphs were derived from the four most common borophene phases (i.e., $v_{1/5}$, $v_{1/5}$-30°, $v_{1/6}$, and $v_{1/6}$-30°; see fig. S2 for their schematic structures).

For $v_{1/5}$ borophane, STM images revealed two distinctive structures with square H and honeycomb H patterns (Fig. 1A); a well-ordered square $v_{1/5}$ borophane structure and corresponding inset fast Fourier transform (FFT) pattern are shown in Fig. 1B. The extracted lattice constant (0.43 ± 0.02 nm) agreed well with the interrow distance of $v_{1/5}$ borophene, indicating a commensurate adsorption structure. The honeycomb $v_{1/5}$ borophane structure (Fig. 1C) had a unit cell of 0.60 ± 0.03 nm by 0.80 ± 0.03 nm and an angle of 103° (±1°), which was composed of elongated hexagons that could be broken up into zigzag rows. The edge lengths of the zigzag match those of the square $v_{1/5}$ borophane structure (0.43 ± 0.02 nm).

Unlike $v_{1/5}$ borophene, $v_{1/5}$-30° borophene had stripe-like undulations along its staggered hollow hexagons (*19*). As a result, staggered rectangular H structures intermixed with zigzag H rows were formed along the undulations of $v_{1/5}$-30° borophene (Fig. 1D). The staggered rectangular H structure had a rectangular unit cell of 0.38 ± 0.03 nm by 0.60 nm ± 0.03 nm (Fig. 1E). Intermixed zigzag H rows were also observed in between the staggered rectangular H structures, with a rhombus unit cell with side length of 0.60 ± 0.02 nm (Fig. 1F).

Additional borophane structures were observed after the hydrogenation of $v_{1/6}$ borophene. In this case, $v_{1/6}$ borophane had both hexagonal and rectangular H patterns. The hexagonal H pattern was most prevalent for $v_{1/6}$ borophane with a unit cell of 0.34 ± 0.02 nm by 0.35 ± 0.02 nm (Fig. 1H). Another coexisting $v_{1/6}$ borophane polymorph showed a disordered rectangular H structure (Fig. 1I) composed of a rectangular lattice with vacancies and dislocations. Additional complex patterns on $v_{1/6}$ borophane were imaged as disordered structures with a bare metal tip (fig. S3).

By contrast, $v_{1/6}$-30° borophane had a highly ordered rectangular H structure (Fig. 1J). Compared with the bare-tip STM image that showed an apparent striped structure, rect-$v_{1/6}$-30° borophane was resolved as an ordered rectangular lattice with STM utilizing a CO-functionalized tip (CO-STM) (fig. S4). The unit cell of rect-$v_{1/6}$-30°

[1]Department of Materials Science and Engineering, Northwestern University, 2220 Campus Drive, Evanston, IL 60208, USA. [2]Center for Nanoscale Materials, Argonne National Laboratory, 9700 South Cass Avenue, Lemont, IL 60439, USA. [3]Department of Materials Science and Engineering, University of Florida, 1885 Stadium Road, Gainesville, FL 32611, USA. [4]Quantum Theory Project, University of Florida, 1885 Stadium Road, Gainesville, FL 32611, USA. [5]Northwestern-Argonne Institute of Science and Engineering, 2205 Tech Drive, Evanston, IL 60208, USA. [6]Department of Chemistry, Northwestern University, 2145 Sheridan Road, Evanston, IL 60208, USA. [7]Department of Electrical and Computer Engineering, Northwestern University, 2145 Sheridan Road, Evanston, IL 60208, USA. *Present address: Department of Chemistry and Biochemistry, University of California, San Diego, La Jolla, CA 92093, USA. †Corresponding author. Email: m-hersam@northwestern.edu

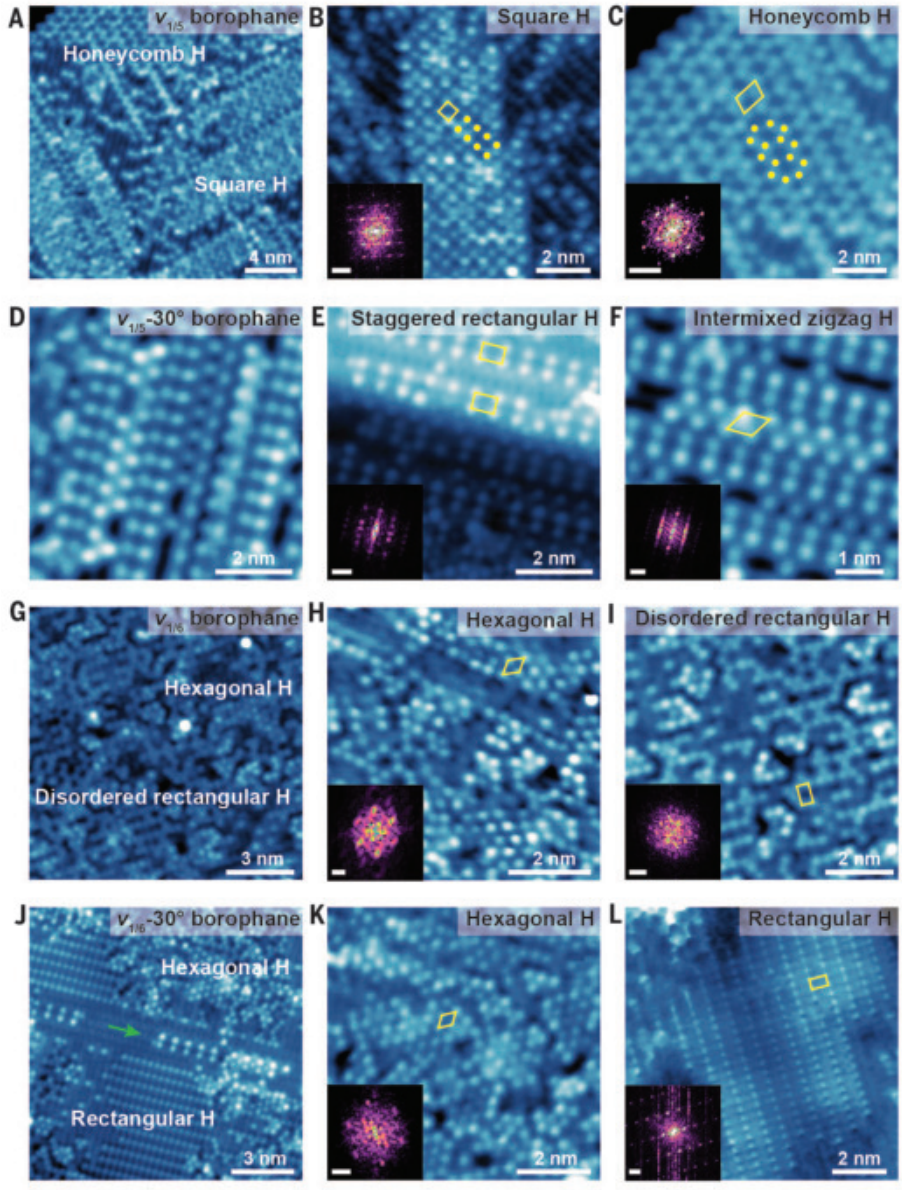


**Fig. 1. Atomic characterization of borophane polymorphs.** (**A**) Representative STM image of $v_{1/5}$ borophane with square H and honeycomb H patterns. (**B**) STM image of square $v_{1/5}$ borophane. (**C**) STM image of honeycomb $v_{1/5}$ borophane. (**D**) Representative STM image of $v_{1/5}$-30° borophane showing intermixing of staggered rectangular H and zigzag H patterns. (**E**) STM image of staggered rectangular $v_{1/5}$-30° borophane. (**F**) STM image of intermixed zigzag $v_{1/5}$-30° borophane. (**G**) Representative STM image of $v_{1/6}$ borophane with hexagonal H and disordered rectangular H patterns. (**H**) STM image of hexagonal $v_{1/6}$ borophane. (**I**) STM image of disordered rectangular $v_{1/6}$ borophane. (**J**) Representative $v_{1/6}$-30° borophane with hexagonal H and rectangular H patterns. A line defect of $v_{1/5}$-30° borophane is also present (marked with a green arrow). (**K**) STM image of hexagonal $v_{1/6}$-30° borophane. (**L**) STM image of rectangular $v_{1/6}$-30° borophane. All STM images are characterized with a CO-functionalized Pt/Ir tip. All insets show FFT images; all scale bars for the FFT images are 2 $nm^{-1}$. Yellow polygons indicate the unit cells of borophane polymorphs; yellow dots indicate the protrusions of H adatoms in STM images. Scanning conditions are as follows: (A) sample bias ($V_S$) = 60 mV, tunneling current ($I_T$) = 200 pA; (B) $V_S$ = 20 mV, $I_T$ = 60 pA; (C) $V_S$ = 60 mV, $I_T$ = 200 pA; (D) $V_S$ = 60 mV, $I_T$ = 300 pA; (E) $V_S$ = 100 mV, $I_T$ = 50 Pa; (F) $V_S$ = 30 mV, $I_T$ = 500 pA; (G) $V_S$ = 8 mV, $I_T$ = 100 pA; (H) $V_S$ = 10 mV, $I_T$ = 100 pA; (I) $V_S$ = 2 mV, $I_T$ = 100 pA; (J) $V_S$ = 100 mV, $I_T$ = 50 pA; (K) $V_S$ = 100 mV, $I_T$ = 50 pA; (L) $V_S$ = 20 mV, $I_T$ = 50 pA. Hydrogen dosing conditions are as follows: [(A) and (C)] $5.0 \times 10^{-7}$ mbar for 20 min; (B) $1.0 \times 10^{-6}$ mbar for 10 min; [(D) and (F)] $5.0 \times 10^{-6}$ mbar for 2 min; (E) $2.5 \times 10^{-6}$ mbar for 10 min; [(G) to (I)] $1.0 \times 10^{-6}$ mbar for 10 min; [(J) to (L)] $2.5 \times 10^{-6}$ mbar for 10 min.

borophane was 0.50 ± 0.02 nm by 0.30 ± 0.02 nm (Fig. 1L), which matched $v_{1/6}$-30° borophene. Although some hexagonal H patterns were observed on $v_{1/6}$-30° borophane (Fig. 1K), rect-$v_{1/6}$-30° borophane has a high surface coverage of hydrogen (fig. S5). As a result of its predominance and highly ordered structure, we selected rect-$v_{1/6}$-30° borophane for in-depth investigation.

High-resolution CO-STM images of rect-$v_{1/6}$-30° borophane acquired at different scanning conditions (Fig. 2, A and B) revealed a bright protrusion within the rectangular unit cell (indicated by the red rectangles) in conjunction with a neighboring dimmer protrusion. These ladder-like patterns were more prominent when acquired at the lower biases (i.e., closer tip-sample spacing) in Fig. 2B. DFT calculations identified three stable hydrogen adsorption structures on $v_{1/6}$-30° borophene that had rectangular unit cells with lattice constants of 0.50 nm by 0.30 nm (see fig. S6 and table S1 for detailed adsorption energy landscapes). The rect-1$H_{top}$ or rect-1$H_{bridge}$ structures had one H atom adsorbed on the top site ($H_{top}$) or on the bridge site ($H_{bridge}$) of $v_{1/6}$-30° borophene, forming a B–H bond or B–H–B "banana" bond, respectively (Fig. 2, C and F, and Fig. 2, D and G, respectively). However, the rect-2H structure was composed of two adsorbed H atoms ($H_{top}$ and $H_{bridge}$) in the rectangular unit cell (Fig. 2, E and H). The elemental ratio of the rect-2H structure is H:B = 2:5, whereas H:B = 1:5 for the rect-1$H_{top}$ and rect-1$H_{bridge}$ structures. The calculated B–H bond lengths in the proposed borophane structures were 133 pm ($H_{bridge}$ site) and 121 pm ($H_{top}$ site), respectively. The values of these bond lengths were comparable with the 3c2e B–H–B bond length of 131 pm in diborane (*20*) and the 2c2e B–H bond length of 119 pm in borane (*21*), indicating the formation of covalent bonds in the borophane structures.

We developed the Ingrained software (*22*) to use DFT calculated partial charge densities and computer vision to simulate and match the STM images. The simulated STM images from rect-1$H_{top}$ (Fig. 2I) and rect-1$H_{bridge}$ (Fig. 2J) revealed the contribution of electron densities from $H_{top}$ and $H_{bridge}$ atoms, respectively, whereas the ladder-like patterns were not apparent in these structures. The rect-2H structure (Fig. 2K) most closely matched the experimentally observed ladder-like patterns. Although the H atoms (on the top and bridge sites) in the rect-2H structure were equidistant in a row, the electron density at the $H_{bridge}$ site slightly shifted toward the $H_{top}$ side in the simulated STM image, resulting in the ladder-like pattern. The uneven brightness in the ladder-like patterns (Fig. 2, A and B) was likely caused by the height difference of ~0.92 Å in the $H_{top}$ and $H_{bridge}$ sites.

Periodic (infinite) and defect-free DFT calculations predicted two different lowest-energy alignments between borophane and Ag ("shifted" alignments) compared with borophene and Ag ("original" alignment) (see fig. S7 and supplementary text for details). This calculation implied that a perfect (i.e., infinite and defect-free) borophene sheet would shift on the Ag substrate upon hydrogen adsorption. However, the simulated STM images from this shifted borophane (fig. S8) did not agree with experimental observations. The presence of borophene edges and defects likely prevented the shifting of borophene with respect to the Ag substrate upon H adsorption.

We also performed STS on rect-$v_{1/6}$-30° borophane to provide additional experimental evidence in support of the rect-2H structure. In particular, the differential tunneling conductance spectrum taken on rect-$v_{1/6}$-30° borophane showed a distinct peak at ~1.2 V (Fig. 2L and fig. S9) that was absent for $v_{1/6}$-30° borophene and other borophane polymorphs (fig. S10). This experimental STS peak agreed well with the calculated projected density of states (pDOS) of boron p-states (averaged per atom) for the rect-2H structure, which also showed a sharp peak at ~1.2 V that was not observed for the rect-1$H_{top}$ and rect-1$H_{bridge}$ structures (Fig. 2M) or the shifted borophane alignments (fig. S11). The electron density from this electronic state was mainly contributed from the $H_{top}$ sites in the rect-2H structure, as plotted in the partial charge density map in fig. S12. Moreover, STS revealed the metallic characteristics of borophane polymorphs (fig. S10), which resemble those of borophene as 2D metals.

The bonding geometry of rect-$v_{1/6}$-30° borophane was further investigated by IETS measurements. Given the sensitivity of vibrational spectra to isotopic identity, hydrogenated and deuterated rect-$v_{1/6}$-30° borophane samples were prepared for IETS characterization. The IETS spectra of rect-$v_{1/6}$-30° borophane with hydrogen (red) and deuterium (orange) in addition to pristine $v_{1/6}$-30° borophene (purple) are shown in Fig. 2N. Figure 2N also shows the eigenvectors of the vibrational modes of hydrogen at both the $H_{bridge}$ and $H_{top}$ sites. The peak at ~310 (230) meV in the IETS spectra for rect-$v_{1/6}$-30° borophane with H (D) closely matched the DFT calculated stretch mode of the B–H(D) bonds (top site) in the rect-2H(D) structures at 311 (229) meV. The same stretch mode [i.e., B–H(D) bond] was expected in the rect-1H(D)$_{top}$ structures, with these vibrations calculated to be 308 (227) meV.

In comparison, the B–H(D)–B bonds (bridge site) vibrations were not observed experimentally, which were calculated to be 240 (177) meV (rect-2H) or 231 (172) meV (rect-1$H_{bridge}$). The experimental absence of the stretch mode of the B–H(D)–B bonds could be explained

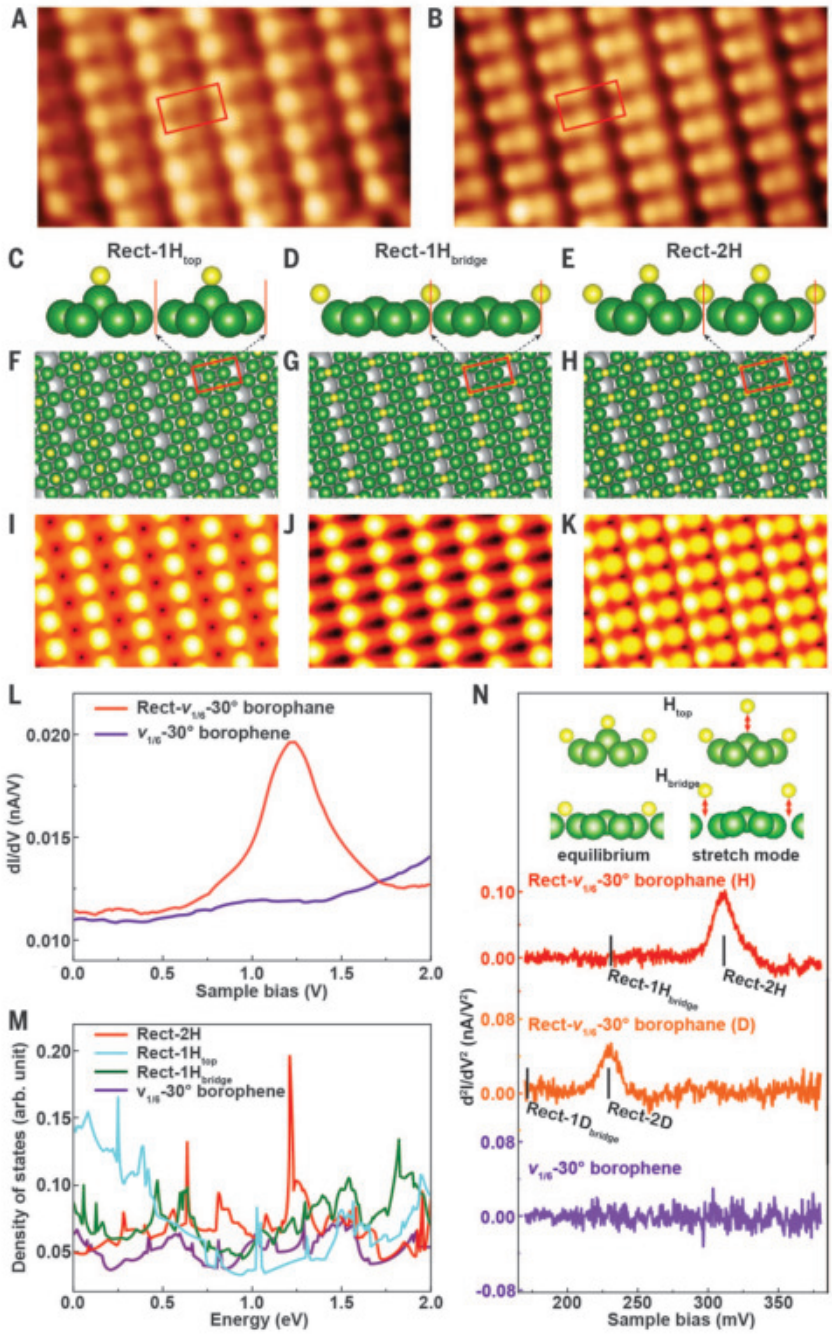


**Fig. 2. Rect-$v_{1/6}$-30° borophane structure and electronic properties.** (**A** and **B**) CO-STM images of rect-$v_{1/6}$-30° borophane with overlaid unit cell of 0.50 nm by 0.30 nm (indicated by the red rectangles) at different biases. Scanning conditions are as follows: (A) $V_S$ = 100 mV, $I_T$ = 100 pA; (B) $V_S$ = 24 mV, $I_T$ = 80 pA. (**C** and **F**) Side (C) and top (F) views of the rect-1$H_{top}$ structure with one $H_{top}$ atom in the rectangular unit cell. (**D** and **G**) Side (D) and top (G) views of the rect-1$H_{bridge}$ structure with one $H_{bridge}$ atom in the rectangular unit cell. (**E** and **H**) Side (E) and top (H) views of the rect-2H structure with one $H_{top}$ atom and one $H_{bridge}$ atom in the rectangular unit cell. (**I** to **K**) Simulated constant-current STM images with the energy range of 100 meV above the Fermi level of rect-1$H_{top}$ (I), rect-1$H_{bridge}$ (J), and rect-2H (K) structures. (**L**) STS spectra taken on rect-$v_{1/6}$-30° borophane (red) and $v_{1/6}$-30° borophene (purple). (**M**) Simulated pDOS of B p-states for rect-1$H_{top}$ (blue), rect-1$H_{bridge}$ (green), rect-2H (red), and $v_{1/6}$-30° borophene (purple). (**N**) IETS spectra taken on rect-$v_{1/6}$-30° borophane with hydrogen (red) and deuterium (orange) in addition to $v_{1/6}$-30° borophene (purple). The stretch modes of rect-1$H_{bridge}$ and rect-2H structures are shown on top. Simulated vibrational energies of rect-1H(D)$_{bridge}$ and rect-2H(D) structures are labeled with black lines on the IETS spectra.

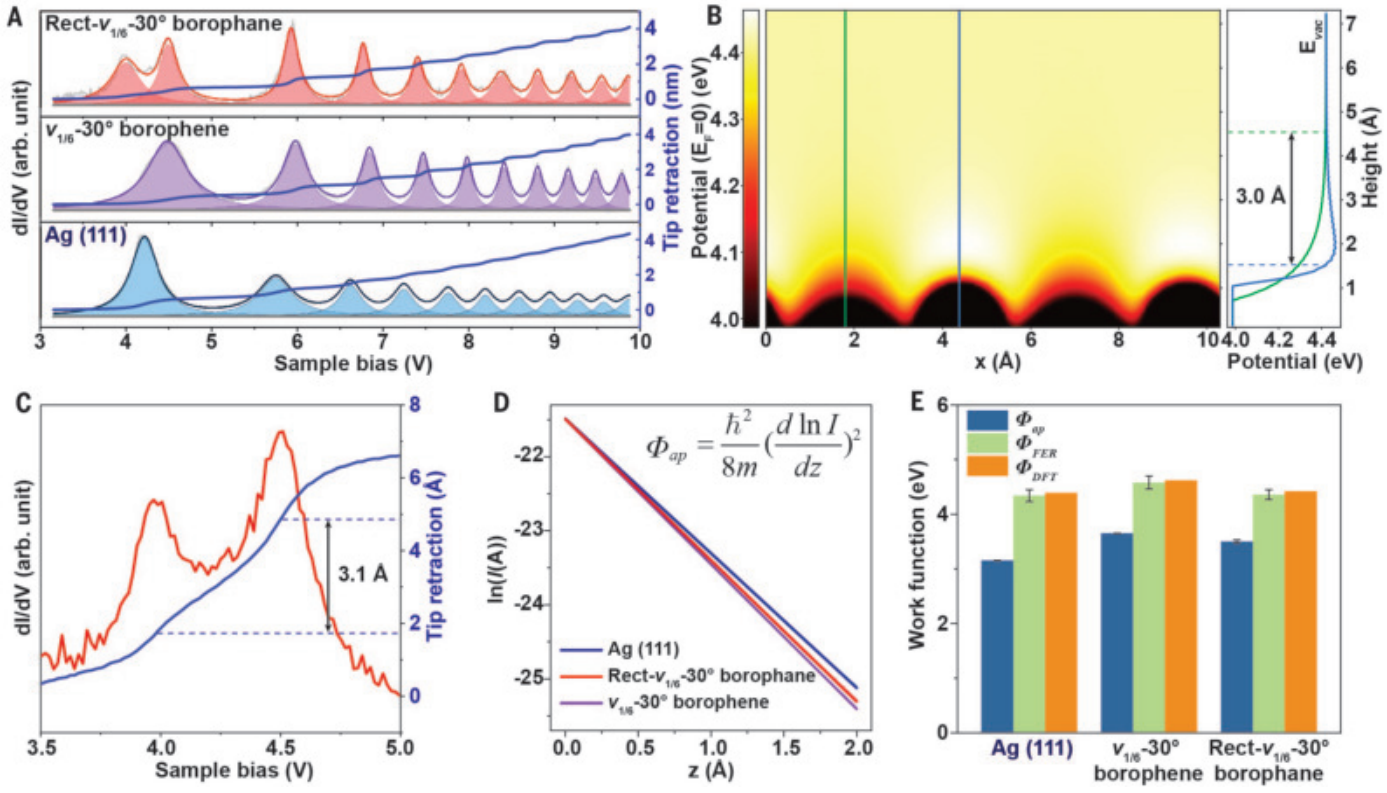


**Fig. 3. Rect-$v_{1/6}$-30° borophane work function characterization.** (**A**) FER spectra taken on rect-$v_{1/6}$-30° borophane (red), $v_{1/6}$-30° borophene (purple), and Ag(111) (blue). The tunneling current was held constant (100 pA) under feedback control while allowing the tip-sample distance to change during the FER measurement. The $\Delta z$-$V_{bias}$ curves were simultaneously measured and are shown as navy blue lines. (**B**) Side view of the calculated local potential distribution above the surface of the rect-2H structure. The potentials are reported relative to the Fermi energy $E_F$. The vertical green and blue lines represent the locations of the H atoms in the B–$H_{bridge}$–B and B–$H_{top}$ bonds in the rect-2H structure, respectively. Corresponding line profiles of the potential distribution versus height are shown on the right, indicating that the difference in height is ~3.0 Å between the points when the two line profiles reach above the vacuum level ($E_{vac}$). (**C**) Magnified plots of FER spectra (red) and corresponding $\Delta z$-$V_{bias}$ curves (blue) of rectangular $v_{1/6}$-30° borophane, showing a change in tip distance of ~3.1 Å between the split FER peaks. (**D**) ln|$I$|-$z$ curves measured on Ag(111) (blue), rectangular $v_{1/6}$-30° borophane (red), and $v_{1/6}$-30° borophene (purple). The slopes of these plots are proportional to the apparent tunneling barrier height ($\Phi_{ap}$), as shown in the inset, where $\hbar$ is the reduced Planck constant and $m$ is electron mass. (**E**) Comparison of the work functions of Ag(111), $v_{1/6}$-30° borophene, and rect-$v_{1/6}$-30° borophane extracted from the apparent tunneling barrier height (blue), FER (green), and DFT (orange).

by its small IETS cross section (fig. S13). Unlike the stretch mode of B–H(D) bonds, the stretch mode of B–H(D)–B bonds induced a net out-of-plane dipole with respect to displacement, resulting in negligible changes in tunneling rates with respect to displacement amplitude. Overall, the combination of STM, STS, and IETS provides strong evidence that rect-$v_{1/6}$-30° borophane possesses the rect-2H structure.

The local work function (LWF) of rect-$v_{1/6}$-30° borophane was probed with STM by measuring field-emission resonances (FERs), also known as Gundlach oscillations, which arose in the Fowler-Nordheim regime through standing-wave states in the tip-sample gap (*23*, *24*). The FER measurements taken on Ag (blue), $v_{1/6}$-30° borophene (purple), and rect-$v_{1/6}$-30° borophane (red) were performed at a constant tunneling current of 100 pA with the resulting tip retraction curves being simultaneously recorded and plotted (Fig. 3A). The first FER peak appeared at ~4.2 eV on Ag(111), consistent with previously reported results (*25*). By contrast, $v_{1/6}$-30° borophene showed its first FER peak at ~4.5 eV, indicating an increased work function compared with that of pristine Ag(111). For rect-$v_{1/6}$-30° borophane, the first FER peak split into two subpeaks located at ~4.0 and ~4.5 eV. The energy splitting of the image states was previously reported on InAs(111) and attributed to surface potential corrugation (*26*).

To better understand the surface potential for rect-$v_{1/6}$-30° borophane, DFT calculations with dipole corrections were performed to obtain electrostatic potential profiles. In the side view of the local potential distribution along the plane of adsorbed H atoms above the surface of the rect-2H structure (Fig. 3B), the green and blue vertical lines indicate the lateral position of the H atoms at the $H_{bridge}$ and $H_{top}$ sites, respectively. The potential profiles versus height along the green and blue lines are shown on the right side of Fig. 3B. Because of the large in-plane inhomogeneities across the rect-$v_{1/6}$-30° borophane unit cell, the potential rose sharply above $H_{top}$ (blue line) and exceeded the far-field potential, whereas the potential increased gradually toward (but never exceeded) the far-field level above $H_{bridge}$ (green line). The vertical extent of the region where the potential was above the vacuum level was 3.0 Å, which was consistent with the tip retraction height of 3.1 Å between the split initial peaks in the rect-$v_{1/6}$-30° borophane FER spectrum (Fig. 3C). The potential profile of the rect-1$H_{top}$ structure is shown in fig. S14 for comparison, where the potential above the $H_{top}$ site decreased gradually instead of the sharp rise above the $H_{top}$ site in the rect-2H structure. This result suggested that the energy splitting of the first FER peak for rect-$v_{1/6}$-30° borophane originated from the potential corrugation of the different local environments above the $H_{bridge}$ and $H_{top}$ sites.

The LWFs for Ag(111), $v_{1/6}$-30° borophene, and rect-$v_{1/6}$-30° borophane were extracted from the FER spectra as 4.34 ± 0.11, 4.58 ± 0.12, and 4.36 ± 0.09 eV, respectively (see fig. S15 and supplementary text for details). These values agreed well with DFT calculations that yielded LWFs of 4.39, 4.62, and 4.42 eV, respectively. Rect-$v_{1/6}$-30° borophane exhibited a slightly lower work function than $v_{1/6}$-30° borophene, indicating a change in areal dipole caused by hydrogen adsorption. By contrast, hex-$v_{1/6}$-30° borophane showed a higher work function than $v_{1/6}$-30° borophene, which was extracted from the FER measurement in fig. S16.

The work function differences between these borophane polymorphs were a consequence of the different B–H bonding types and resulting areal dipoles as confirmed by Bader charge analysis (fig. S17). The LWF differences were also supported by apparent barrier height measurements using $I(z)$ spectroscopy. The $\ln I(z)$ plots of Ag(111), $v_{1/6}$-30° borophene, and rect-$v_{1/6}$-30° borophane (Fig. 3D) resulted in extracted apparent barrier heights of 3.15 ± 0.004, 3.65 ± 0.004, and 3.48 ± 0.03 eV, respectively (see supplementary text for details). Despite the quantitative discrepancy between these extracted apparent barrier heights and the FER and DFT results that arose from the oversimplified approximation of the tunnel gap as a trapezoidal barrier, the apparent barrier height results still yielded the correct qualitative trend in LWF, thus allowing apparent barrier height imaging to be used for spatial mapping of the LWF. For example, we visualized the spatial variations in LWF between borophane polymorphs and Ag(111) using $|\mathrm{d} \ln I/\mathrm{d}z|$ imaging in fig. S18.

The ambient stability of borophane was evaluated using XPS and atomic force microscopy (AFM) measurements after different periods of ambient exposure. Unencapsulated borophene sheets chemically degrade in ambient conditions (*4*). We confirmed this result by performing XPS on unencapsulated mixed-phase $v_{1/5}$ and $v_{1/6}$-30° borophene after 1 hour of ambient exposure (20°C, relative humidity between 20 and 50%) (Fig. 4A; see fig. S19 for details). The resulting XPS spectrum was fit with three peaks centered at 187.8, 189.1, and 192.3 eV, with the two low–binding energy peaks (green and blue) corresponding to the B–B bonds in borophene and the higher–binding energy peak (yellow) corresponding to B–O bonds formed during ambient oxidation (*27*). Furthermore, the ex situ AFM image (Fig. 4B) showed a rough surface decorated with particles that was consistent with the decomposition of borophene into boron oxides.

By contrast, the borophane sample exhibited markedly improved chemical and morphological stability in ambient conditions. This sample contains multiple borophane polymorphs (e.g., rect-$v_{1/6}$-30° borophane, hex-$v_{1/6}$-30° borophane,

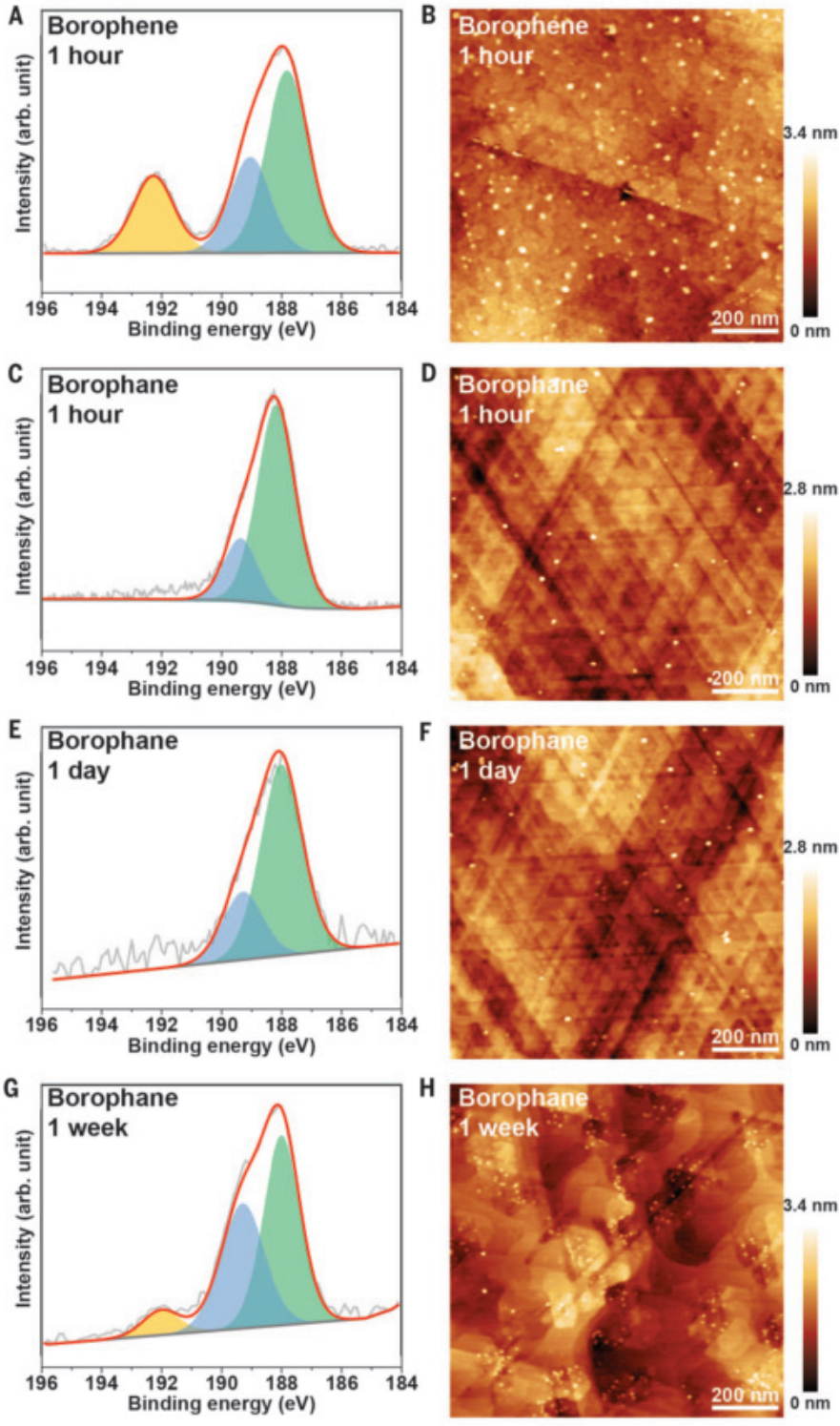


**Fig. 4. Stability of borophane in ambient conditions.** (**A** and **B**) XPS spectrum and AFM image of mixed-phase $v_{1/5}$ and $v_{1/6}$-30° borophene after ambient exposure for 1 hour. (**C** to **H**) XPS spectra and AFM images of mixed-phase $v_{1/5}$ and $v_{1/6}$-30° borophane (hydrogen dosing condition: $2.5 \times 10^{-6}$ mbar for 10 min) after ambient exposure for 1 hour [(C) and (D)], 1 day [(E) and (F)], and 1 week [(G) and (H)]. In (A), (C), (E), and (G), the yellow-, blue-, and green-shaded peaks correspond to the fitted peaks of B–O and B–B bonds, and the gray and red lines represent the original spectrum and the sum of the fitted peaks, respectively.

square-$v_{1/5}$ borophane, and honeycomb-$v_{1/5}$ borophane), thus showing that diverse hydrogen-bonding motifs on borophene impart ambient stability. This borophane sample showed no detectable B–O peak in the XPS spectrum after 1 hour of ambient exposure (Fig. 1C; see fig. S20 for the wide-scan XPS spectra). Similarly, Fig. 4D reveals the smooth morphology of the borophane sample with no discernible evidence of degradation as measured by AFM after 1 hour in ambient conditions.

The chemical and morphological invariance of the borophane sample persisted after 1 day of ambient exposure (Fig. 4, E and F). Only after 1 week of ambient exposure is degradation detected in the borophane sample, with the XPS spectrum showing a small B–O peak (Fig. 4G). This oxidation peak is clearly smaller than that of the borophene sample after 1 hour of ambient exposure, indicating that the oxidation rate is reduced by more than two orders of magnitude. AFM imaging of this sample revealed that the oxidation initiated at the borophane flake edges, as evidenced by the location of the emerging oxide particles (Fig. 4H). With ambient stability on the order of days, borophane provides a sufficient time window for most ambient characterization and processing methods.

Moreover, similar to the case of hydrogenated graphene (*28*), the hydrogenation of borophene was reversible upon thermal annealing. Specifically, borophane samples could be recovered to pristine borophene without apparent degradation after annealing the sample to ~300°C (fig. S21). Consequently, hydrogenation of borophene can be viewed as a reversible passivation scheme in which the hydrogenation can be removed to regain pristine borophene once ambient processing is complete and/or robust encapsulation layers are applied.

## REFERENCES AND NOTES


1. A. J. Mannix *et al.*, *Science* **350**, 1513–1516 (2015).
2. A. J. Mannix, Z. Zhang, N. P. Guisinger, B. I. Yakobson, M. C. Hersam, *Nat. Nanotechnol.* **13**, 444–450 (2018).
3. E. S. Penev, A. Kutana, B. I. Yakobson, *Nano Lett.* **16**, 2522–2526 (2016).
4. B. Feng *et al.*, *Nat. Chem.* **8**, 563–568 (2016).
5. J. A. Dagata *et al.*, *Appl. Phys. Lett.* **56**, 2001–2003 (1990).
6. J. W. Lyding, T. C. Shen, J. S. Hubacek, J. R. Tucker, G. C. Abeln, *Appl. Phys. Lett.* **64**, 2010–2012 (1994).
7. C. R. Ryder *et al.*, *Nat. Chem.* **8**, 597–602 (2016).
8. L.-C. Xu, A. Du, L. Kou, *Phys. Chem. Chem. Phys.* **18**, 27284–27289 (2016).
9. R. Balog *et al.*, *Nat. Mater.* **9**, 315–319 (2010).
10. A. A. Kistanov *et al.*, *Nanoscale* **10**, 1403–1410 (2018).
11. Z.-Q. Wang, T.-Y. Lü, H.-Q. Wang, Y. P. Feng, J.-C. Zheng, *ACS Appl. Electron. Mater.* **1**, 667–674 (2019).
12. D. Li *et al.*, *Adv. Funct. Mater.* **28**, 1801685 (2018).
13. H. Nishino *et al.*, *J. Am. Chem. Soc.* **139**, 13761–13769 (2017).
14. C. Hou *et al.*, *Angew. Chem. Int. Ed.* **59**, 10819–10825 (2020).
15. S. Tominaka *et al.*, *Chem* **6**, 406–418 (2020).
16. X. Liu *et al.*, *Nat. Commun.* **10**, 1642 (2019).
17. R. Balog *et al.*, *J. Am. Chem. Soc.* **131**, 8744–8745 (2009).
18. X. Liu, Z. Zhang, L. Wang, B. I. Yakobson, M. C. Hersam, *Nat. Mater.* **17**, 783–788 (2018).
19. Z. Zhang *et al.*, *Nano Lett.* **16**, 6622–6627 (2016).
20. P. Laszlo, *Angew. Chem. Int. Ed.* **39**, 2071–2072 (2000).
21. W. N. Lipscomb, *Science* **196**, 1047–1055 (1977).
22. E. Schwenker *et al.*, Ingrained: An automated framework for fusing materials imaging simulations into experiments (2021); https://github.com/MaterialEyes/ingrained-lite.
23. G. Binnig *et al.*, *Phys. Rev. Lett.* **55**, 991–994 (1985).
24. R. S. Becker, J. A. Golovchenko, B. S. Swartzentruber, *Phys. Rev. Lett.* **55**, 987–990 (1985).
25. J. Martínez-Blanco, S. Fölsch, *J. Phys. Condens. Matter* **27**, 255008 (2015).
26. J. Martínez-Blanco, S. C. Erwin, K. Kanisawa, S. Fölsch, *Phys. Rev. B* **92**, 115444 (2015).
27. C. W. Ong *et al.*, *J. Appl. Phys.* **95**, 3527–3534 (2004).
28. D. C. Elias *et al.*, *Science* **323**, 610–613 (2009).


## ACKNOWLEDGMENTS


**Funding:** This work was supported by the Office of Naval Research (ONR N00014-17-1-2993) and the National Science Foundation Materials Research Science and Engineering Center (NSF DMR-1720139). The computational work was supported, in part, by the Center for Electrochemical Energy Science (an Energy Frontier Research Center), Laboratory Directed Research and Development (LDRD) funding from Argonne National Laboratory, and the Center for Nanoscale Materials, funded by the U.S. Department of Energy Office of Science under contract no. DE-AC02-06CH11357. M.K.Y.C. acknowledges support from the BES SUFD Early Career award. **Author contributions:** Q.L. and M.C.H. conceived the experiments. Q.L. performed sample preparation, characterization, and data analysis with assistance from M.S.R. and S.L. and guidance from M.C.H. Density functional theory calculations were performed by V.S.C.K. and E.S. with guidance from R.G.H., P.D., and M.K.Y.C. M.K.Y.C, V.S.C.K., and E.S. conceived, developed, and applied the STM simulation code ingrained. All authors contributed to data interpretation and manuscript writing. **Competing interests:** A patent application is being prepared based on the borophane synthesis reported in this work. The authors declare no competing financial interests. **Data and materials availability:** All data are available in the main text or the supplementary materials. The Ingrained software containing STM simulation and matching modules, created to help solve the structure of borophane from STM images, is available via https://github.com/MaterialEyes/ingrained-lite (*22*).


## SUPPLEMENTARY MATERIALS

science.sciencemag.org/content/371/6534/1143/suppl/DC1
Materials and Methods
Supplementary Text
Figs. S1 to S21
Table S1
References (*29*–*38*)

16 December 2020; accepted 29 January 2021
10.1126/science.abg1874

CARBON CYCLE

# Temperature controls carbon cycling and biological evolution in the ocean twilight zone

**Flavia Boscolo-Galazzo[1]*†‡, Katherine A. Crichton[1]†§, Andy Ridgwell[2], Elaine M. Mawbey[3]¶, Bridget S. Wade[3], Paul N. Pearson[1]**

**Theory suggests that the ocean's biological carbon pump, the process by which organic matter is produced at the surface and transferred to the deep ocean, is sensitive to temperature because temperature controls photosynthesis and respiration rates. We applied a combined data-modeling approach to investigate carbon and nutrient recycling rates across the world ocean over the past 15 million years of global cooling. We found that the efficiency of the biological carbon pump increased with ocean cooling as the result of a temperature-dependent reduction in the rate of remineralization (degradation) of sinking organic matter. Increased food delivery at depth prompted the development of new deep-water niches, triggering deep plankton evolution and the expansion of the mesopelagic "twilight zone" ecosystem.**

Metabolic temperature dependency is a physiological response wherein biochemical reaction rates roughly double in response to an ambient temperature increase of 10°C (*1*–*5*). On an organismal level, the link between temperature and biochemistry predicts the scaling of metabolism with temperature (*3*). The same relationship has the potential for shaping communities and ecosystems by altering the flux of elements between organisms and the environment (*1*, *2*). A direct implication of this metabolic theory of ecology is that biological fluxes of carbon also should scale with temperature as the planet warms or cools. Crucially, because respiration has faster temperature response rates than photosynthesis (*1*–*5*), more organic

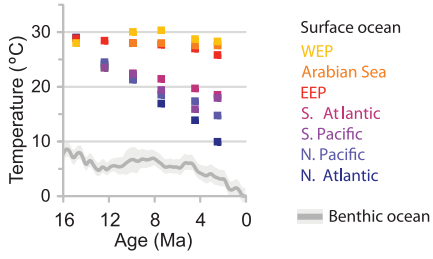


**Fig. 1. Global compilation of surface and bottom water temperatures for the past 15 million years.** Bottom water temperatures are from (*24*). Surface temperature is presented as a mean value for ocean regions and is compiled from (*19*, *20*, *22*, *43*, *44*). WEP, West Equatorial Pacific; EEP, East Equatorial Pacific.

[1]School of Earth and Environmental Sciences, Cardiff University, Cardiff, UK. [2]Department of Earth and Planetary Sciences, University of California, Riverside, CA, USA. [3]Department of Earth Sciences, University College London, London, UK.
***Corresponding author. Email: flavia.boscologalazzo@uib.no**
†These authors contributed equally to this work. ‡Present address: Department of Earth Science, Bergen University and Bjerknes Centre for Climate Research, Bergen, Norway. §Present address: Department of Geography, Exeter University, Exeter, UK. ¶Present address: British Antarctic Survey, Cambridge, UK.

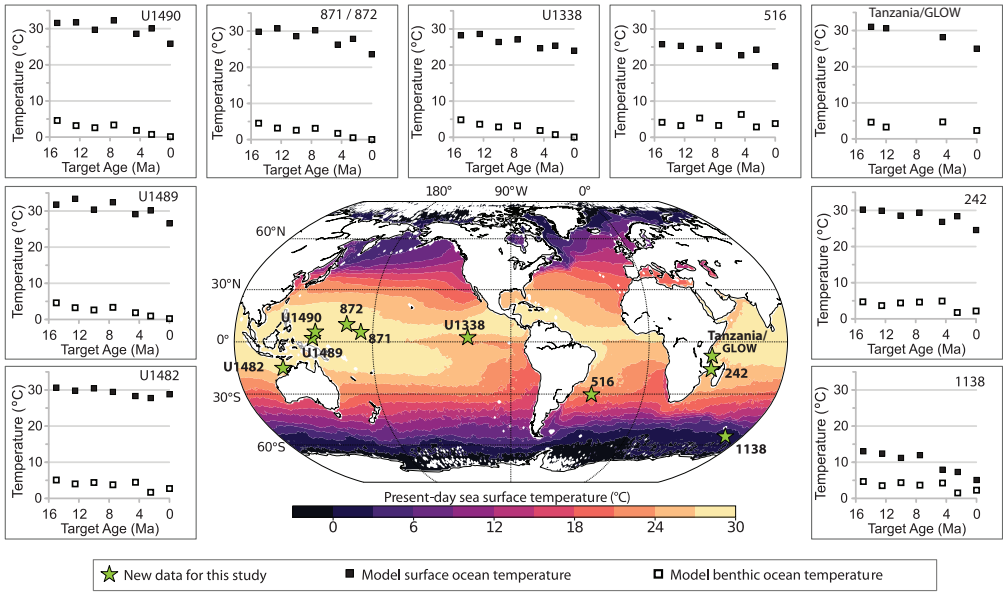


**Fig. 2. Modern location of study sites and modeled temperatures.** Map shows modern mean annual sea surface temperatures from *World Ocean Atlas 2013* (*45*). Square boxes show surface (solid squares) and bottom (open squares) ocean temperatures as modeled in this study for each location and target age. Sediment core locations: Deep Sea Drilling Project Sites 242 (western Indian Ocean) and 516 (southwest Atlantic Ocean); Ocean Drilling Program Sites 871 and 872 (western tropical Pacific Ocean) and 1138 (Southern Ocean, Indian Ocean sector); Integrated Ocean Drilling Program Site U1338 (eastern tropical Pacific Ocean); International Ocean Discovery Program Sites U1482 (eastern Indian Ocean), U1489, and U1490 (west Pacific Warm Pool); and hemipelagic sediments collected onshore and offshore (GLOW) Tanzania.

carbon should be converted to $CO_2$ at warmer mean global temperatures, potentially creating a positive feedback to global climate change (*1*–*6*).

An important component of the global carbon cycle is the ocean's biological carbon pump (BCP) (*7*), in which carbon is fixed at the surface by photosynthesis and is then transferred down the water column by sinking of particulate organic carbon (POC). Bacterial-driven respiration returns carbon and nutrients to seawater ("remineralization") with the residual organic matter buried in marine sediments (*7*–*9*). The strength of the BCP is defined as the magnitude of POC settling flux out of the euphotic zone; the transfer efficiency is defined as the fraction of that POC which is transported to greater depths (*10*). Together they determine the efficiency of the BCP in delivering carbon to the deep ocean (*10*). A key controller of the BCP efficiency is the POC remineralization rate: When remineralization is fast, less carbon is transported from the surface to the mesopelagic "twilight zone" (200 to 1000 m) and deep ocean (*9*, *11*).

According to the metabolic theory of ecology (*1*, *2*), photosynthesis and POC remineralization rates should be sensitive to secular changes in ocean temperature, modulating the efficiency of the BCP on geological time scales. We tested this inference using the rich fossil record of planktonic foraminifera, a group of calcifying heterotrophic protists that live stratified over a range of depth habitats from the surface mixed layer to thermocline and subthermocline intermediate waters (*12*). Foraminiferal shells accumulate on the sea floor where they retain a geochemical imprint of the water column conditions in which they grew, but which can also be affected by postdepositional alteration (*13*). Previous studies have used foraminiferal shell carbon isotope ratios ($\delta^{13}C$) as a means of estimating BCP efficiency, and their results suggest that it may have been far weaker when the climate was much warmer than at present, such as in the early Eocene [56 to 48 million years ago (Ma)] (*14*, *15*). Modeling has shown that the BCP may have been stronger during glacial maxima (*16*) and could decline as a result of ocean warming by the end of this century (*17*). BCP efficiency could have influenced habitability and biological evolution in subsurface marine environments by affecting food supply and levels of oxygen depletion at depth (*18*). However, exploring the sensitivity of the BCP to metabolic temperature dependency and the implications for ocean ecosystems requires extensive datasets across large spatial and temporal scales, which are currently lacking.

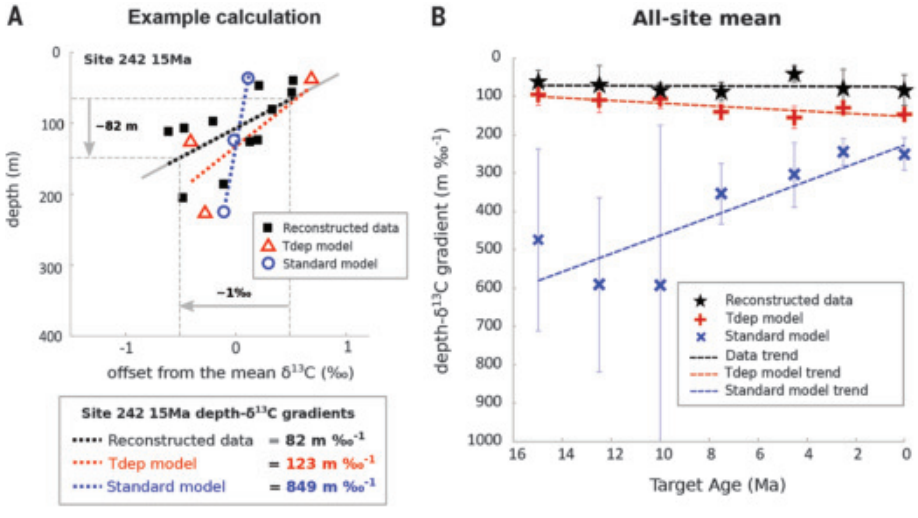


**Fig. 3. Comparison of reconstructed and modeled $\delta^{13}C$ DIC gradients.** The depth-$\delta^{13}C$ gradient is calculated for planktonic foraminiferal $\delta^{13}C$ data, the Tdep model, and the Standard model for each target age and site. (**A**) Depth-$\delta^{13}C$ gradients are obtained by calculating the rate of change in $\delta^{13}C$ with depth in the upper 228 m of the water column (*25*). An example calculation of the data and model $\delta^{13}C$ depth gradients for Site 242 at 15 Ma is shown (see figs. S2 and S3 for all data and model points). In the example, planktonic foraminiferal $\delta^{13}C$ changes by 1‰ in 82 m (indicated by gray dashed lines and gray arrows); the Tdep and Standard model $\delta^{13}C$ decrease by an equivalent amount in 123 and 849 m, respectively. (**B**) Reconstructed and modeled depth-$\delta^{13}C$ gradients are summarized as their mean value and one standard deviation of all sites per target age expressed as m $‰^{-1}$ (depth change in meters for 1‰ change in $\delta^{13}C$).

Here, we focused on the period since the middle Miocene (15 Ma); over this time span, there has been a global average temperature decline of 4° to 6°C in the surface ocean (*19*–*22*) as well as the deep ocean (*23*, *24*) (Fig. 1). Unlike earlier intervals of warming or cooling, it is possible to obtain relevant data from all the ocean basins and across a wide range of latitudes (Fig. 2). We obtained foraminiferal samples with good to excellent preservation, focusing on seven target ages between 15 and 0 Ma (Fig. 2 and data S1). From these samples we obtained abundance counts of the different planktonic foraminiferal species and measured the oxygen ($\delta^{18}O$) and carbon ($\delta^{13}C$) stable isotope ratios and Mg:Ca ratios of the shells (data S2 to S4).

With appropriate adjustments for factors such as global ice volume and the local oxygen isotope composition of seawater, planktonic foraminiferal shell $\delta^{18}O$ can be used as a proxy for relative temperature (*13*), which declines with depth and hence is useful as an indicator of paleodepth ecology (*14*). The $\delta^{13}C$ of near-surface dissolved inorganic carbon (DIC) in the ocean is largely controlled by the ratio between organic matter production by photosynthesis and its destruction by microbial respiration, setting up a $\delta^{13}C$ DIC gradient in the water column (*7*, *26*). The $\delta^{13}C$ of planktonic foraminiferal shells is in turn controlled by a combination of the isotopic composition of DIC in seawater and the physiology of biomineralization (*26*–*29*). With the use of constrained shell size fractions, physiological disequilibrium effects can be minimized and the $\delta^{13}C$ of DIC can be estimated from the shells (*29*). From this, the seawater $\delta^{13}C$ profile can be reconstructed, provided that the depth habitats of planktonic foraminifera are also known (*14*, *25*) (Fig. 3).

We implemented a series of configurations of the cGENIE Earth system model with appropriate paleogeography and optimized ocean circulation patterns for each target age (table S1) (*25*, *30*, *31*). We further made use of a new version of the model biogeochemistry module that includes temperature-dependent nutrient uptake rates at the surface and respiration in the ocean interior (*32*). This temperature-dependent model configuration ("Tdep") gave rise to profound differences in the physical and biogeochemical properties of the global ocean relative to the model that omitted these processes ("Standard") (*32*). For example, the oldest and warmest middle Miocene (15 Ma) target age is characterized by a much less efficient BCP in the Tdep configuration, with less POC reaching the twilight zone than in the colder Holocene (0 Ma), in accordance with the metabolic theory of ecology (*1*, *2*) (fig. S1). The Tdep configuration also exhibits higher surface nutrient concentrations (due to more vigorous near-surface nutrient recycling across a steeper nutricline) and a shallower oxygen minimum zone in warmer climates (fig. S1). Combined, this produces a decline in POC export from 15 Ma to the Holocene in the model but a tripling in transfer efficiency, such that there is a net increase in the BCP efficiency upon cooling.

To investigate the impact of changes in metabolic rates on the ocean carbon cycle, we first identified the average depth habitats of each planktonic foraminiferal species and reconstructed planktonic foraminiferal upper ocean depth-$\delta^{13}C$ gradients as outlined in (*25*) (Fig. 3A). We then contrasted our reconstructed depth-$\delta^{13}C$ gradients with the results of the standard and Tdep versions of the cGENIE model (Fig. 3B). At each site, the measured planktonic foraminiferal $\delta^{13}C$ through the upper 228 m (*25*) tends to decrease less with depth from 15 Ma to the present (figs. S2 and S3). As a result, the data-reconstructed global mean depth-$\delta^{13}C$ gradient (expressed in Fig. 3B as m $‰^{-1}$, i.e., depth change in meters for 1‰ change in $\delta^{13}C$) shows a slight trend toward greater depths with cooling (Fig. 3B, black dashed line). In contrast, the standard model (Fig. 3B, blue dashed line) exhibits a strongly opposite trend. Lacking temperature-dependent biological processes in the ocean, the shallowing trend shown by the depth-$\delta^{13}C$ gradient in the Standard model (Fig. 3B) is driven by physical climate and ocean circulation changes that result in increasing POC export upon cooling. In the Tdep model, the rate of nutrient and carbon cycling in near-surface waters reduces upon cooling and counters the "abiotic" trend which results in the nearly muted net projected gradient response. The relatively flat data-reconstructed depth-$\delta^{13}C$ gradient trend is therefore consistent with the hypothesis that carbon remineralization rates in the upper ocean have declined in parallel with global cooling, as characterized in the Tdep model. We note that even the Tdep model configuration underestimates the reconstructed $\delta^{13}C$ gradient in most cases (Fig. 3B and figs. S2 and S3), which may be attributable to the method used to reconstruct $\delta^{13}C$ profiles from the data (*25*) or to the various simplifications inherent in the model (*33*).

Most planktonic foraminiferal species in the modern ocean live in the surface mixed layer or upper thermocline around the deep chlorophyll maximum where light is available for photosymbionts and food supply is most abundant (*34*), but some live deeper in the water column, either grazing on sinking phytodetritus

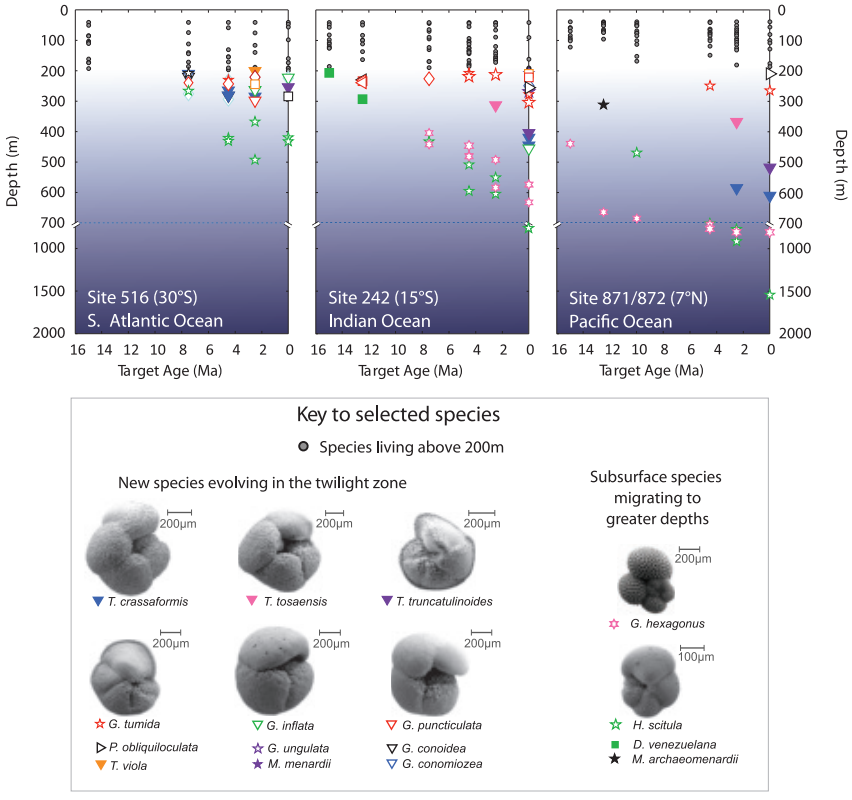


**Fig. 4. Expansion of planktonic foraminiferal depth habitat over the past 15 million years.** Species in the top 200 m are shown as gray symbols. Deep-dwellers (>200 m reconstructed depth habitat) are highlighted with colored symbols (see fig. S10 for a complete symbol key). Scanning electron microscopy images of some mesopelagic planktonic foraminifera from the study sites are also shown. Similar plots for all the study sites are available in fig. S10.

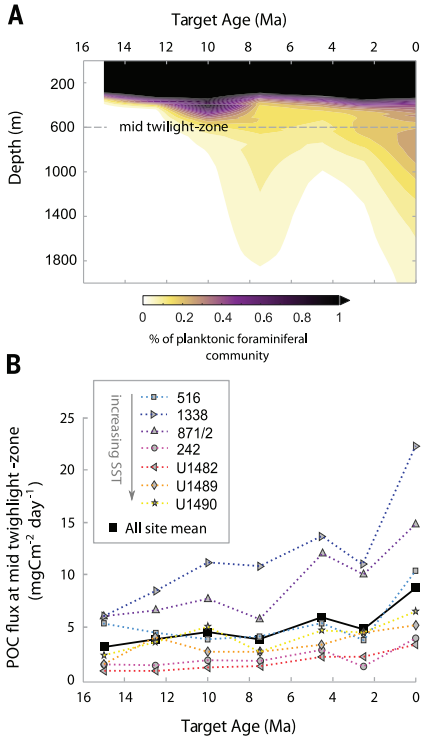


**Fig. 5. Abundance depth distributions of planktonic foraminifera over the past 15 million years.** (**A**) Global mean planktonic foraminiferal community distribution versus time [subpolar Site 1138 not included (*25*)]. (**B**) Modeled POC flux for the Tdep model configuration versus time (plotted data are from 600 m depth, the mid-twilight zone). Note that not all sites have abundance data for each target age; this explains some of the variability, particularly from 10 to 4.5 Ma.

or predating on mesopelagic organisms such as copepods (*34*). Among this deeper group (Fig. 4, colored symbols), we observe a major deepening of species-specific depth habitats through time, which is also reflected by the larger spread in $\delta^{18}O$ and Mg/Ca values in younger target ages (figs. S4 to S9 and data S3 and S4) (*25*). This deepening of habitats coincides with the surface and deep-water cooling shown in global temperature records (Fig. 1). In the older, warmer target ages (15 to 10 Ma), most species lived in the upper 200 m of the water column (Fig. 4 and fig. S10). As cooling progressed, subsurface-dwelling species moved to greater depths and new lineages of deep-water species evolved. In the most recent target age (0.0 Ma or Holocene), reconstructed depth habitats extend to >1000 m depth (Fig. 4 and fig. S10), consistent with observations in the modern ocean (*34*). The deepening pattern is evident in most of the sites, although it is affected by local factors: At the two equatorial sites (Sites U1338 and U1489, fig. S10) it is complicated by the evolution of the modern zonal temperature gradient between the eastern and western equatorial Pacific Ocean (*19*); at Site U1338 it is also affected by equatorial upwelling (*35*); and at Site 1138 in the Southern Ocean it is obscured by the dominating influence of the subpolar front on the $\delta^{18}O$ of seawater (*36*). Our data emphasize that planktonic foraminiferal species and assemblages have responded in a dynamic way to global climate change and did not occupy constant habitats through time, as is sometimes assumed in paleoceanographic reconstructions.

The global decrease in the POC remineralization rate since 15 Ma implies increasing food availability for deep-water organisms that feed directly on POC settling through the water column, and for their associated food chain. Slower remineralization rates of sinking organic matter in the mesopelagic ocean over time would be expected to lead to deeper and less intense oxygen minimum zones (fig. S1), also favoring organisms that require oxygen for respiration. To investigate whether planktonic foraminiferal biomass reflects increased habitability at depth, we reconstructed the abundance depth distribution of planktonic foraminiferal assemblages at each site and time slice (*25*) (figs. S11 to S14 and data S2). Although planktonic foraminifera are always less abundant in deep water than in the euphotic zone, our data show a doubling of biomass in the twilight zone from the middle Miocene to the present (Fig. 5A), paralleled by a factor of >2 increase in POC delivery to this region in the Tdep model (Fig. 5B). These coupled data-modeling results suggest that enhanced food availability was critical for the development of deep plankton niches as the oceans cooled.

Food supply and subsurface oxygen levels are of fundamental importance to all heterotrophs, so we suggest that the mesoplankton and associated nekton as a whole increased in biomass and diversity since 15 Ma. More broadly, the past 15 million years represent the most recent phase in a global cooling trend since the mid-Cretaceous super-greenhouse of ~100 Ma (*37*). Although most of the twilight zone ecosystem leaves no fossil record, the temperature dependency of the BCP may have left a mark on the genetics and phylogenetics of deep-dwelling groups. For instance, the ctenophores (comb jellies), which are common at mesopelagic depths, appear to have a history of recent diversification despite their very ancient (~500 Ma) split from other metazoans (*38*). In addition, various deep-water bony fish clades have diversified rapidly since the Miocene (*39*–*41*), including the extremely abundant lanternfish, which are a dominant proportion of the modern mesopelagic biomass (*41*). Our model results also suggest that since the middle Miocene, a higher proportion of organic carbon fixed at the surface would have reached the sea floor. This fits with previous observations of a marked increase, over the past 15 million years, in the abundance of benthic organisms that bloom in response to the deposition of phytodetritus aggregates (*42*).

Our study provides a global test of the effects of temperature changes on metabolic rates in the ocean ecosystem over geological time scales. We found that DIC $\delta^{13}C$ gradients in the upper open ocean changed over the past 15 million years of global cooling in a way that is consistent with reducing remineralization rates and a greater transfer efficiency of the BCP. Increasing abundance of deep-dwelling zooplankton through the same interval suggests that a more efficient BCP enhanced the flux of particulate organic carbon to the twilight zone. New ecological niches opened up in response, promoting evolutionary radiation and the establishment of the modern mesopelagic ecosystem. This evolutionary history raises the possibility that the twilight zone ecosystem may now be vulnerable to a reduction in carbon pump transfer efficiency associated with anthropogenic warming.

## REFERENCES AND NOTES


1. J. H. Brown, J. F. Gillooly, A. P. Allen, V. M. Savage, G. B. West, *Ecology* **85**, 1771–1789 (2004).
2. A. P. Allen, J. F. Gillooly, J. H. Brown, *Funct. Ecol.* **19**, 202–213 (2005).
3. J. F. Gillooly, J. H. Brown, G. B. West, V. M. Savage, E. L. Charnov, *Science* **293**, 2248–2251 (2001).
4. B. Chen, M. R. Landry, B. Huang, H. Liu, *Limnol. Oceanogr.* **57**, 519–526 (2012).
5. F. Boscolo-Galazzo, K. A. Crichton, S. Barker, P. N. Pearson, *Global Planet. Change* **170**, 201–212 (2018).
6. A. Olivarez-Lyle, M. W. Lyle, *Paleoceanography* **21**, PA2007 (2006).
7. M. P. Hain, D. M. Sigman, G. H. Haug, in *Treatise on Geochemistry, Volume 8: The Oceans and Marine Geochemistry*, H. D. Holland, K. K. Turekian, Eds. (Elsevier, ed. 2, 2014), pp. 485–517.
8. P. W. Boyd, H. Claustre, M. Levy, D. A. Siegel, T. Weber, *Nature* **568**, 327–335 (2019).
9. E. Y. Kwon, F. Primeau, J. L. Sarmiento, *Nat. Geosci.* **2**, 630–635 (2009).
10. K. O. Buesseler, P. W. Boyd, E. E. Black, D. A. Siegel, *Proc. Natl. Acad. Sci. U.S.A.* **117**, 9679–9687 (2020).
11. A. Martin *et al.*, *Nature* **580**, 26–28 (2020).
12. A. Rebotim *et al.*, *Biogeosciences* **14**, 827–859 (2017).
13. P. N. Pearson, in *Reconstructing Earth's Deep-Time Climate, Paleontological Society Papers Volume 18*, L. Ivany, B. Huber, Eds. (2012), pp. 1–38.
14. E. H. John *et al.*, *Philos. Trans. R. Soc. A* **371**, 20130099 (2013).
15. E. H. John, J. D. Wilson, P. N. Pearson, A. Ridgwell, *Palaeogeogr. Palaeoclimatol. Palaeoecol.* **413**, 158–166 (2014).
16. K. Matsumoto, T. Hashioka, Y. Yamanaka, *J. Geophys. Res.* **112**, G02007 (2007).
17. M. Barange *et al.*, *Front. Mar. Sci.* **3**, 290 (2017).
18. P. N. Pearson, H. K. Coxall, *Palaeontology* **57**, 243–267 (2014).
19. Y. G. Zhang, M. Pagani, Z. Liu, *Science* **344**, 84–87 (2014).
20. T. D. Herbert *et al.*, *Nat. Geosci.* **9**, 843–847 (2016).
21. S. M. Sosdian *et al.*, *Earth Planet. Sci. Lett.* **498**, 362–376 (2018).
22. J. R. Super *et al.*, *Geology* **46**, 519–522 (2018).
23. B. S. Cramer, K. G. Miller, P. J. Barrett, J. D. Wright, *J. Geophys. Res.* **116**, C12023 (2011).
24. C. H. Lear *et al.*, *Paleoceanography* **30**, 1437–1454 (2015).
25. See supplementary materials.
26. A. Mackensen, G. Schmiedl, *Earth Sci. Rev.* **197**, 102893 (2019).
27. H. J. Spero, D. F. Williams, *Nature* **335**, 717–719 (1988).

28. O. Friedrich *et al*., *Earth Planet. Sci. Lett.* **319–320**, 133–145 (2012).
29. H. Birch, H. K. Coxall, P. N. Pearson, D. Kroon, M. O'Regan, *Mar. Micropaleontol.* **101**, 127–145 (2013).
30. A. Ridgwell *et al*., *Biogeosciences* **4**, 87–104 (2007).
31. K. A. Crichton, A. Ridgwell, D. J. Lunt, A. Farnsworth, P. N. Pearson, *Clim. Past* 10.5194/cp-2019-151 (2020).
32. K. A. Crichton, J. D. Wilson, A. Ridgwell, P. N. Pearson, *Geosci. Model Dev.* **14**, 125–149 (2021).
33. D. E. Gaskell, P. M. Hull, *Geology* **47**, 1156–1160 (2019).
34. R. Schiebel, C. Hemleben, *Planktic Foraminifers in the Modern Ocean* (Springer, 2017).
35. L. R. Fox, B. S. Wade, *J. Foraminiferal Res.* **44**, 374–405 (2014).
36. M. Verducci *et al*., *Palaeogeogr. Palaeoclimatol. Palaeoecol.* **280**, 371–386 (2009).
37. M. Pagani, M. Huber, B. Sageman, in *Treatise on Geochemistry, Volume 6: The Atmosphere—History*, H. D. Holland, K. K. Turekian, Eds. (Elsevier, ed. 2, 2014), pp. 281–297.
38. M. Podar, S. H. D. Haddock, M. L. Sogin, G. R. Harbison, *Mol. Phylogenet. Evol.* **21**, 218–230 (2001).
39. I. G. Priede, R. Froese, *J. Fish Biol.* **83**, 1528–1550 (2013).
40. T. J. Near *et al*., *Proc. Natl. Acad. Sci. U.S.A.* **109**, 13698–13703 (2012).
41. X. Irigoien *et al*., *Nat. Commun.* **5**, 3271 (2014).
42. E. Thomas, A. J. Gooday, *Geology* **24**, 355–358 (1996).
43. A. Holbourn *et al*., *Geology* **38**, 783–786 (2010).
44. A. E. Shevenell, J. P. Kennett, D. W. Lea, *Science* **305**, 1766–1770 (2004).
45. R. A. Locarnini *et al*., *World Ocean Atlas 2013, Volume 1: Temperature*, S. Levitus, A. Mishonov, Eds. (NOAA, 2013).
46. Zenodo DOI: 10.5281/zenodo.4469673.
47. Zenodo DOI: 10.5281/zenodo.4469678.

### ACKNOWLEDGMENTS

We thank L. Cotton and C. Nicholas for collecting the Tanzania surface samples, the Tanzania Commission for Science and Technology for research permission, M. Latas for assisting with sample preparation, the International Ocean Discovery Program (IODP) for supplying samples for this study, and J. Farmer and two anonymous reviewers for constructive reviews that greatly benefited the manuscript. This research used samples provided by the IODP, JOIDES Resolution, Expedition 363, West Pacific Warm Pool. This research also used samples provided by Netherlands Organisation for Scientific Research (NWO), RV Pelagia, Paleogene Global Warming (GLOW) expedition. **Funding:** Supported by Natural Environment Research Council (NERC) grant NE/N001621/1 to P.N.P. (F.B.G. and K.A.C.); NERC grants NE/P016375/1 and NE/F523293/1 to participate in IODP Expedition 363 and the GLOW expedition, respectively (P.N.P.); NSF grants 1702913 and 1736771 and the Heising Simons Foundation (A.R.); and NERC grant NE/N002598/1 to B.S.W. (E.M.M.). **Author contributions:** Conceptualization, P.N.P.; software, K.A.C.; formal analysis, K.A.C.; investigation, F.B.G. and E.M.M.; resources, F.B.G.; writing–original draft, F.B.G.; writing–review and editing, F.B.G., K.A.C., P.N.P., A.R., B.S.W., E.M.M.; visualization, F.B.G., K.A.C., E.M.M.; supervision, P.N.P., A.R., B.S.W.; project administration and funding acquisition, P.N.P. and B.S.W. **Competing interests:** Authors declare no competing interests. **Data and materials availability:** All data are available in the supplementary materials. The code for the version of the "muffin" release of the cGENIE Earth system model used in this paper is tagged as v0.9.18 and is assigned a DOI: 10.5281/zenodo.4469673 (*46*). Configuration files for the specific experiments presented in the paper can be found in the directory genie-userconfigs/MS/boscologalazzoetal.2021. Details of the experiments, plus the command line needed to run each one, are given in the readme.txt file in that directory. All other configuration files and boundary conditions are provided as part of the code release. A manual detailing code installation, basic model configuration, tutorials covering various aspects of model configuration and experimental design, plus results output and processing, is assigned a DOI: 10.5281/zenodo.4469678 (*47*).

### SUPPLEMENTARY MATERIALS

science.sciencemag.org/content/371/6534/1148/suppl/DC1
Materials and Methods
Figs. S1 to S16
Table S1
Data S1 to S5
References (*48*–*67*)

20 April 2020; accepted 28 January 2021
10.1126/science.abb6643

CORONAVIRUS

# Neutralization of SARS-CoV-2 lineage B.1.1.7 pseudovirus by BNT162b2 vaccine–elicited human sera

**Alexander Muik[1], Ann-Kathrin Wallisch[1], Bianca Sänger[1], Kena A. Swanson[2], Julia Mühl[1], Wei Chen[2], Hui Cai[2], Daniel Maurus[1], Ritu Sarkar[2], Özlem Türeci[1], Philip R. Dormitzer[2], Uğur Şahin[1,3]***

**Recently, a new severe acute respiratory syndrome coronavirus 2 (SARS-CoV-2) lineage called B.1.1.7 (variant of concern: VOC 202012/01), which is reported to spread more efficiently and faster than other strains, emerged in the United Kingdom. This variant has an unusually large number of mutations, with 10 amino acid changes in the spike (S) protein, raising concerns that its recognition by neutralizing antibodies may be affected. In this study, we tested SARS-CoV-2-S pseudoviruses bearing either the Wuhan reference strain or the B.1.1.7 lineage spike protein with sera of 40 participants who were vaccinated in a previously reported trial with the messenger RNA–based COVID-19 vaccine BNT162b2. The immune sera had slightly reduced but overall largely preserved neutralizing titers against the B.1.1.7 lineage pseudovirus. These data indicate that the B.1.1.7 lineage will not escape BNT162b2-mediated protection.**

In a phase 3 trial conducted in the United States, Argentina, Brazil, South Africa, Germany, and Turkey, the BioNTech-Pfizer mRNA vaccine BNT162b2 was 95% effective in preventing COVID-19 through the data cutoff date of 14 November 2020 (*1*). The severe acute respiratory syndrome coronavirus 2 (SARS-CoV-2) lineage B.1.1.7 (variant of concern: VOC 202012/01) was discovered to have emerged in the United Kingdom in September 2020 (*2*), and it subsequently increased in prevalence, showed enhanced transmissibility, and spread to other countries and continents (*3*). B.1.1.7 has a series of mutations in its spike (S) protein: ΔH69/V70, ΔY144, N501Y, A570D, D614G, P681H, T716I, S982A, and D1118H (H, His; V, Val; Y, Tyr; N, Asn; A, Ala; D, Asp; G, Gly; P, Pro; T, Thr; I, Ile; S, Ser). One of these mutations, N501Y, was of particular concern because it is located in the

[1]BioNTech, An der Goldgrube 12, 55131 Mainz, Germany. [2]Pfizer, 401 N. Middletown Rd., Pearl River, NY 10960, USA. [3]TRON gGmbH – Translational Oncology at the University Medical Center of the Johannes Gutenberg University, Freiligrathstraße 12, 55131 Mainz, Germany.
***Corresponding author. Email: ugur.sahin@biontech.de**

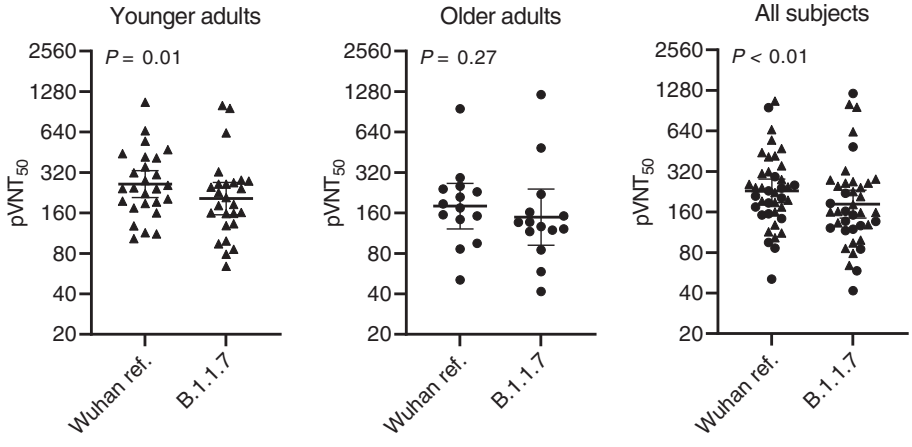


**Fig. 1. 50% pseudovirus neutralization titers ($pVNT_{50}$) of 40 sera from BNT162b2 vaccine recipients against VSV-SARS-CoV-2-S pseudovirus bearing the Wuhan reference strain or lineage B.1.1.7 spike protein.** Sera from $n$ = 26 younger adults (aged 23 to 55 years; indicated by triangles) and $n$ = 14 older adults (aged 57 to 73 years; indicated by circles) drawn at either day 29 or day 43 (7 or 21 days after vaccine dose two) were tested. Statistical significance of the difference between the neutralization of the VSV-SARS-CoV-2-S pseudovirus bearing the Wuhan or lineage B.1.1.7 spike protein was calculated by a Wilcoxon matched-pairs signed rank test. Two-tailed $P$ values are reported. GMTs and 95% CIs are indicated.

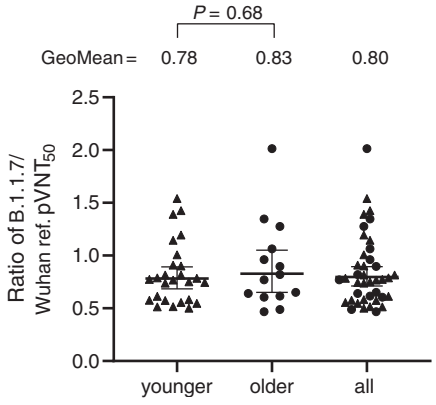


**Fig. 2. $pVNT_{50}$ ratio of SARS-CoV-2 lineage B.1.1.7 to Wuhan reference strain spike–pseudotyped VSV.** Triangles represent sera from younger adults (aged 23 to 55 years), and circles represent sera from older adults (aged 57 to 73 years). Sera were drawn on either day 29 or day 43 (7 or 21 days after vaccine dose two). Geometric means of the $pVNT_{50}$ ratios of SARS-CoV-2 lineage B.1.1.7 to Wuhan spike–pseudotyped VSV and 95% CIs are indicated. The difference in distribution of titer ratios between younger and older adults was tested for statistical significance with a two-tailed Mann-Whitney *U* test.

receptor binding site. The spike with this mutation binds more tightly to its cellular receptor, ACE-2 (*4*), and virus with this mutation has an increased host range that includes mice (*5*). BNT162b2-immune sera neutralized SARS-CoV-2 (USA/WA-1/2020 background strain) with an introduced N501Y mutation as efficiently as they neutralized SARS-CoV-2 without the mutation (*6*). Further, 19 pseudoviruses, each bearing a SARS-CoV-2 S with a different mutation found in circulating virus strains, were also neutralized as efficiently as nonmutant SARS-CoV-2 S–bearing pseudoviruses by BNT162b2-immune sera (*7*). However, it was still unclear whether a virus with the full set of mutations in the lineage B.1.1.7 spike, each of which may potentially interfere with antibody binding, would be neutralized efficiently by BNT162b2-immune sera.

To answer this question, we generated vesicular stomatitis virus (VSV)–SARS-CoV-2-S pseudoviruses bearing the Wuhan reference strain or the lineage B.1.1.7 spike protein (fig. S1). An unbiased set of sera of 40 participants in the previously reported German phase 1/2 trial (*7*)—drawn from 26 younger (aged 23 to 55 years) and 14 older adults (aged 57 to 73 years) at 7 or 21 days after the booster immunization with 30 μg of BNT162b2 (fig. S2)—was tested for neutralization of SARS-CoV-2 Wuhan and lineage B.1.1.7 spike–pseudotyped VSV by a 50% neutralization assay [50% pseudovirus neutralization titer ($pVNT_{50}$)]. The 50% neutralization geometric mean titers (GMTs) of the sera against the SARS-CoV-2 lineage B.1.1.7 spike–pseudotyped VSV for the younger adult group and the full analysis set were slightly but statistically significantly reduced compared with the GMTs against the Wuhan reference spike–pseudotyped VSV (Fig. 1 and table S1). GMTs were not significantly different for the older adult group. The calculated geometric mean ratio with 95% confidence interval (CI) of the B.1.1.7 pseudotype and the Wuhan pseudotype GMTs was 0.78 (95% CI: 0.68 to 0.89) for the younger group and 0.83 (95% CI: 0.65 to 1.1) for the older adults [0.80 (95% CI: 0.71 to 0.89) in aggregate] (Fig. 2). No statistical difference in the ratio was observed between the younger and the older vaccinated participants.

On the basis of experience from studying antibody correlates of disease protection for influenza virus vaccines, a 20% reduced titer does not indicate a biologically relevant change in neutralization activity (*8*, *9*). The largely preserved neutralization of pseudoviruses bearing the B.1.1.7 spike by BNT162b2-immune sera makes it unlikely that the U.K. variant virus will escape BNT162b2-mediated protection.

A potential limitation of the work may be the use of a nonreplicating pseudovirus system. However, previous reports have shown good concordance between pseudotype neutralization and SARS-CoV-2 neutralization assays (*10*, *11*). Still, concordance may vary between different SARS-CoV-2 strains and remains to be demonstrated for the SARS-CoV-2 B.1.1.7 lineage. Additional experiments will be needed to confirm efficient neutralization of B.1.1.7 lineage clinical isolates. This study has evaluated sera elicited by the recommended regimen of two doses administered 21 days apart and does not provide insight into neutralization if the recommended dosing regimen is not followed. The ongoing evolution of SARS-CoV-2 necessitates continuous monitoring of the biological relevance of changes for maintained protection by the currently authorized vaccines. Unlike the protocol for influenza vaccines, the degree of reduction in neutralization that might indicate a need for a strain change has not yet been established for COVID-19 vaccines. A previous study demonstrated that BNT162b2 elicits both a polyepitopic CD8+ T cell response to the encoded spike protein and virus-neutralizing antibodies (*7*). Given the multiple potential mediators of protection elicited by BNT162b2, it is possible that vaccine efficacy could be preserved in the longer term, even with substantial losses of neutralization by vaccine-elicited sera. This view is further supported by the rapid onset of disease protection ~12 days after the first dose of BNT162b2, at a time when neutralizing antibody titers are still very low (*1*). Without an established correlate of protection, clinical effectiveness data will be needed to provide definitive assessment of vaccine-mediated protection against viral variants.

Although sustained neutralization of the current B.1.1.7 variant is reassuring, preparation for potential COVID-19 vaccine strain change is prudent. Adaptation of the vaccine to a new virus strain would be facilitated by the flexibility of mRNA-based vaccine technology.

## REFERENCES AND NOTES

1. F. P. Polack *et al*., *N. Engl. J. Med.* **383**, 2603–2615 (2020).
2. Preliminary genomic characterisation of an emergent SARS-CoV-2 lineage in the UK defined by a novel set of spike mutations. virological.org (2020); https://virological.org/t/preliminary-genomic-characterisation-of-an-emergent-sars-cov-2-lineage-in-the-uk-defined-by-a-novel-set-of-spike-mutations/563.
3. medRxiv 2020.12.30.20249034 [Preprint]. 4 January 2021. https://doi.org/10.1101/2020.12.30.20249034.
4. T. N. Starr *et al*., *Cell* **182**, 1295–1310.e20 (2020).
5. H. Gu *et al*., *Science* **369**, 1603–1607 (2020).
6. bioRxiv 2021.01.07.425740 [Preprint]. 7 January 2021.
7. medRxiv 2020.12.09.20245175 [Preprint]. 11 December 2020. https://doi.org/10.1101/2020.12.09.20245175.
8. D. J. Smith *et al*., *Science* **305**, 371–376 (2004).
9. S. Black *et al*., *Pediatr. Infect. Dis. J.* **30**, 1081–1085 (2011).
10. J. B. Case *et al*., *Cell Host Microbe* **28**, 475–485.e5 (2020).
11. A. B. Vogel *et al*., *Nature* 10.1038/s41586-021-03275-y (2021).

## ACKNOWLEDGMENTS

We thank the BioNTech German clinical trial (NCT04380701, EudraCT: 2020-001038-36) participants, from whom the postimmunization human sera were obtained. We thank the many colleagues at BioNTech and Pfizer who developed and produced the BNT162b2 vaccine candidate. We thank S. Jägle and N. Beckmann for logistical support. **Funding:** This work was supported by BioNTech and Pfizer. **Author contributions:** U.Ş., Ö.T., A.M., and P.R.D. conceived and conceptualized the work. K.A.S. and A.M. planned and supervised experiments. A.M., A.-K.W., J.M., B.S., H.C., W.C., and R.S. performed experiments. A.M., D.M., H.C., and K.A.S. analyzed data. U.Ş., Ö.T., A.M., P.R.D., and K.A.S. interpreted data and wrote the manuscript. All authors supported the review of the manuscript. **Competing interests:** U.Ş. and Ö.T. are management board members and employees at BioNTech SE. A.M., A.-K.W., J.M., B.S., and D.M. are employees at BioNTech SE. U.Ş., Ö.T., and A.M. are inventors on patents and patent applications related to RNA technology and COVID-19 vaccine. U.Ş., Ö.T., A.M., J.M., and B.S. have securities from BioNTech SE. K.A.S., W.C., H.C., R.S., and P.R.D. are employees at Pfizer and may have securities from Pfizer. **Data and materials availability:** A table of the neutralization titers is provided in table S1. Materials are available from the authors under a material transfer agreement with BioNTech. 

## SUPPLEMENTARY MATERIALS

science.sciencemag.org/content/371/6534/1152/suppl/DC1
Materials and Methods
Figs. S1 to S3
Tables S1 and S2
Reference (*12*)
MDAR Reproducibility Checklist

16 January 2021; accepted 27 January 2021
Published online 29 January 2021
10.1126/science.abg6105

MICROBIOTA

# *Debaryomyces* is enriched in Crohn's disease intestinal tissue and impairs healing in mice

Umang Jain[1], Aaron M. Ver Heul[1,2], Shanshan Xiong[1]*, Martin H. Gregory[2], Elora G. Demers[3], Justin T. Kern[1], Chin-Wen Lai[1,4], Brian D. Muegge[1,2,5], Derek A. G. Barisas[1], J. Steven Leal-Ekman[1], Parakkal Deepak[2], Matthew A. Ciorba[2], Ta-Chiang Liu[1], Deborah A. Hogan[3], Philip Debbas[6], Jonathan Braun[6], Dermot P. B. McGovern[6,7], David M. Underhill[6,7], Thaddeus S. Stappenbeck[1,8]†

Alterations of the mycobiota composition associated with Crohn's disease (CD) are challenging to link to defining elements of pathophysiology, such as poor injury repair. Using culture-dependent and -independent methods, we discovered that *Debaryomyces hansenii* preferentially localized to and was abundant within incompletely healed intestinal wounds of mice and inflamed mucosal tissues of CD human subjects. *D. hansenii* cultures from injured mice and inflamed CD tissues impaired colonic healing when introduced into injured conventionally raised or gnotobiotic mice. We reisolated *D. hansenii* from injured areas of these mice, fulfilling Koch's postulates. Mechanistically, *D. hansenii* impaired mucosal healing through the myeloid cell–specific type 1 interferon–CCL5 axis. Taken together, we have identified a fungus that inhabits inflamed CD tissue and can lead to dysregulated mucosal healing.

When a tissue is injured, appropriate wound healing is necessary to regain function. Wounds can remain chronically nonhealed or inflamed owing to a persistent injury stimulus and/or failure of repair. This occurs in inflammatory bowel disease (IBD), including Crohn's disease (CD) and ulcerative colitis (UC) (*1*), and is associated with shifts in luminal microbial populations (*2*–*6*). The potential link between specific microbes and inflammation in IBD has been of long-standing interest.

To test the role of microbes in intestinal mucosal repair, we and others have used a biopsy injury model where the timing and site of injuries are known (*7*–*9*). Mucosal healing in this model occurs in distinct phases in which, immediately upon injury, neutrophils are recruited to the injured site, followed by the restoration of an epithelial barrier (*7*, *10*). The second phase of healing is characterized by an expansion of fibroblasts and macrophages in the wound bed that is concomitant with enhanced epithelial proliferation in the crypts immediately adjacent to the area of injury, eventually leading to formation of new crypts (*7*, *8*). Arrest of the healing process at any phase typically leads to chronic inflammation characterized by a large area lacking crypts and infiltration by immune cells (*9*). We found that the broad-spectrum antibiotics vancomycin, neomycin, ampicillin, and metronidazole (VNAM) impair healing in wild-type (WT) mice obtained from two different vendors (Fig. 1, A and B, and fig. S1A). Despite a known role for bacterial metabolites (i.e., deoxycholate) to promote crypt regeneration by modulating host prostaglandin $E_2$ ($PGE_2$) (*9*), the phenotype in VNAM-pretreated mice was not dependent on excess $PGE_2$ (Fig. 1, C and D, and fig. S1, B to D), suggesting that additional mechanisms contribute to impaired healing. We found multiple lines of evidence suggesting that fungi, which can expand in the luminal microbiota after antibiotic treatment (*11*), contributed to defective repair after injury in VNAM-pretreated mice. First, quantitative polymerase chain reaction (qPCR) of the internal transcribed spacer (ITS) region at day 8 after injury indicated enhanced abundance of fungi within intestinal wounds of VNAM-pretreated mice (fig. S2A). Second, antifungal stains at day 8 after injury showed abundant fungal antigen within all wound sections examined from VNAM-pretreated mice (*12*) and none in vehicle-treated controls (fig. S2B). Third, the broad-spectrum antifungal agent amphotericin B (*13*) reduced fungal antigen detection in the wounds of VNAM-treated mice and reversed the crypt regeneration defects (Fig. 1, E and F, and fig. S2C). Taken together, these data suggest that fungi in the wound bed can inhibit crypt regeneration after injury.

To determine which fungi were enriched after VNAM treatment, we first characterized the luminal mycobiota by isolating DNA from the stool of VNAM-pretreated mice and controls. High-throughput sequencing of ITS amplicons showed considerable interindividual variation and no significant difference in the relative abundance of any detectable fungal genera in the mycobiota composition when we compared control and VNAM-treated mice (fig. S3). However, similar analysis of ITS amplicons from mucosal wounds showed a single dominant genus, *Debaryomyces*, in the VNAM-pretreated mice but not controls (Fig. 2, A and B). These data from wounds are in contrast to the luminal data, where *Debaryomyces* was low to nondetectable in all mice (fig. S3). To determine if the sequencing represented live or dead fungi, we cultured wound beds using fungus-selective Sabouraud dextrose agar (SDA) plates (Fig. 2A) (*14*). We found that only wound homogenates from VNAM-pretreated mice contained viable fungal colonies (Fig. 2, C and D). *Debaryomyces* was confirmed by ITS sequencing of pooled colonies (Fig. 2E). Additional sequencing of the *ACT1* locus was performed to identify species and showed these microbes were *Debaryomyces hansenii* (also known as *Candida famata*) (fig. S4 and table S1).

*D. hansenii*, when introduced by gavage into non–antibiotic-treated, conventionally raised WT mice was sufficient to impair healing (Fig. 2, F to H, and fig. S5A). Viable *D. hansenii* was recovered from wound homogenates of WT mice gavaged with *D. hansenii*, whereas no growth was observed in wound homogenates from controls (fig. S5, B and C). Notably, colonization of wounds with *D. hansenii*, but not *Saccharomyces cerevisiae*, a yeast commonly found in human gut microbiota (*15*), impaired crypt regeneration (Fig. 2, G and H, and fig. S5D). We also studied the effects of *D. hansenii* on mucosal healing after dextran sodium sulfate (DSS)–induced colonic mucosal damage (Fig. 2I). Mice gavaged with *D. hansenii* showed more extensive mucosal ulceration and increased crypt loss (Fig. 2, J and K, and fig. S5E) compared with controls or mice gavaged with *Candida tropicalis*, a fungus enriched in the lumen of CD subjects (*16*). These experiments showed that *D. hansenii* requires intestinal damage to exert effects on pathology, whereas opportunistic pathogens such as *C. tropicalis* or *C. albicans* additionally require disruption of the microbiome and/or host immunodeficiency (*12*).

As the role of bacterial factors in the above experiments is unknown, we also used gnotobiotic mice in the DSS injury and recovery model. Germ-free (GF) mice were colonized with altered Schaedler flora (ASF), a defined bacterial consortium, and then treated with DSS in the presence or absence of *D. hansenii* (fig. S6, A to C). *D. hansenii* colonization did not alter the levels of any of the eight ASF bacteria (fig. S6D). Furthermore, *D. hansenii* impaired healing after DSS injury in ASF-colonized gnotobiotic mice that was characterized by extensive crypt loss (fig. S7, A and B). Finally,

[1]Department of Pathology and Immunology, Washington University School of Medicine, St. Louis, MO 63110, USA. [2]Department of Medicine, Washington University School of Medicine, St. Louis, MO 63110, USA. [3]Department of Microbiology and Immunology, Geisel School of Medicine at Dartmouth, Hanover, NH 03755, USA. [4]Department of Inflammation and Oncology, Amgen Research, Amgen Inc., South San Francisco, CA 94080, USA. [5]Department of Medicine, VA Medical Center, St. Louis, MO 63106, USA. [6]F. Widjaja Inflammatory Bowel and Immunobiology Research Institute, Cedars-Sinai Medical Center, Los Angeles, CA 90048, USA. [7]Department of Biomedical Sciences, Cedars-Sinai Medical Center, Los Angeles, CA 90048, USA. [8]Department of Inflammation and Immunity, Cleveland Clinic, Cleveland, OH 44195, USA.
*Present address: Department of Gastroenterology, The First Affiliated Hospital, Sun Yat-Sen University, Guangzhou 510080, China.
†Corresponding author. Email: stappet@ccf.org

oral inoculation of GF mice with *D. hansenii*, in the absence of ASF bacteria, also impaired wound healing after DSS injury (fig. S7, C and D). This latter experiment suggests that bacterial factors are not required for *D. hansenii* to affect wound repair, though we cannot rule out their role in conventionally raised mice (*17*, *18*). These studies demonstrate, with multiple models of intestinal injury and repair, that *D. hansenii* can fulfill Koch's postulates and is sufficient to impair wound healing in the intestine.

To determine the mechanism by which *D. hansenii* impairs healing, we first established the cell type that *D. hansenii* preferentially localizes with in vivo. Immunofluorescence analysis of VNAM-treated colonic wounds, where *Debaryomyces* is the dominant fungus detected (Fig. 2, B and E), indicated that the majority of intracellular fungi were located within F4/80$^+$ macrophages (fig. S8A). We also found that prelabeled *D. hansenii*, when administered to biopsy injured WT mice, preferentially colocalized with F4/80$^+$ macrophages (fig. S8B). Finally, analysis of sorted wound bed cells of *D. hansenii*–infected WT mice also showed that F4/80$^+$ macrophages predominantly contained *D. hansenii*, as shown by sequencing and culture of the intracellular contents of these cells (Fig. 3, A and B, and fig. S8C). These findings are consistent with a preferential infiltration of macrophages within wounds colonized by *D. hansenii* (fig. S8, D and E). To identify the most prominent immune responses induced by *D. hansenii* introduction, we compared the expression of 111 cytokines in parallel from wound tissue and macrophage lysates. *D. hansenii* was not broadly proinflammatory and instead induced a robust production of CCL5 both in vitro and in vivo, which we further validated by enzyme-linked immunosorbent assay (ELISA) and in situ hybridization in multiple models (Fig. 3C and fig. S9). Notably, expression of CCL5 was preferentially induced in F4/80$^+$ macrophages in the wound bed in vivo (fig. S10).

We thus hypothesized that *D. hansenii* colonization impairs wound healing through CCL5 up-regulation. Accordingly, in contrast to WT littermate controls, *D. hansenii* gavage did not impede mucosal healing in *Ccl5*$^{-/-}$ mice despite similar colonization within wounds as in WT mice (Fig. 3, D to F, and fig. S11). We tested if this phenotype in *Ccl5*$^{-/-}$ mice was potentially due to developmental defects. In the DSS recovery model, we found that WT mice infected with *D. hansenii* and treated with a CCL5-neutralizing antibody rescued the wound repair defect (fig. S12). We found that the receptor for CCL5, CCR5 (*19*), was required for the detrimental effects of *D. hansenii* (fig. S13). On the basis of our findings and considering that CCL5 is increased in CD (*20*), we propose that CCL5 is a potential therapeutic target in CD.

To determine how *D. hansenii* induces CCL5, we performed an RNA sequencing (RNA-seq) analysis of bone marrow–derived macrophages (BMDMs) in the presence or absence of *D. hansenii* and found a marked increase in genes associated with the type 1 interferon (IFN) pathway (fig. S14). Fungal induction can induce type 1 IFNs (*21*). To validate RNA-seq findings in vivo, we determined that the expression of type I IFN pathway genes, including *Irf7*, *Isg15*, and *Mx2* (*22*), were significantly increased in the wounds of *D. hansenii*–colonized mice compared with controls (fig. S15). Furthermore, in concordance with CCL5 expression data, IFN-β mRNA was also preferentially induced in the wound bed F4/80$^+$ macrophages in vivo (fig. S16). We then measured CCL5 in the supernatants of *D. hansenii*–infected macrophages isolated from WT and *Ifnar*$^{-/-}$ mice. The absence of *Ifnar* completely abolished the production of CCL5, suggesting that type 1 IFN activity is upstream of CCL5

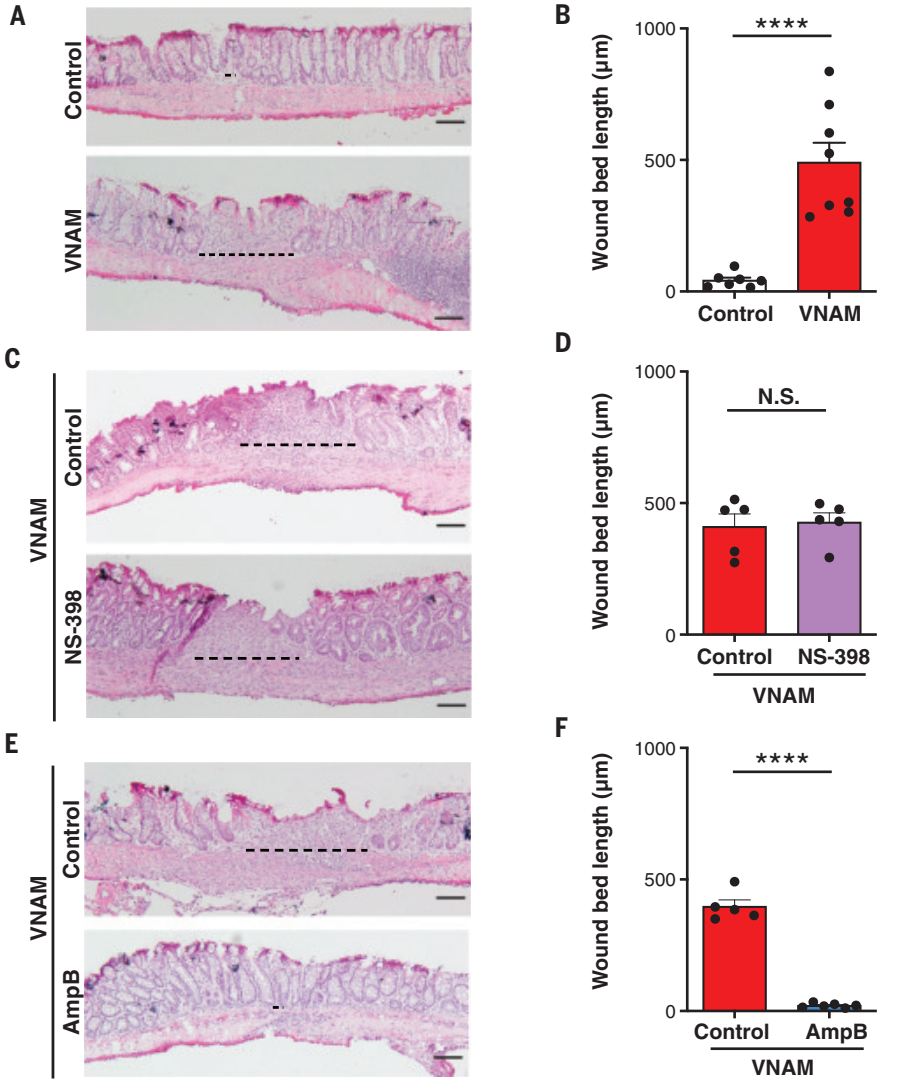


**Fig. 1. Broad-spectrum antibiotic–mediated inhibition of colonic crypt regeneration was reversed by treatment with amphotericin B.** (**A** and **B**) WT mice were pretreated for 4 weeks with antibiotics (VNAM) or vehicle, biopsy injured, and analyzed at day 12 after injury. Representative hematoxylin and eosin (H&E) images (A) and wound bed lengths (B) are shown ($n$ = 11 to 17 wounds per group; seven or eight mice per group). (**C** and **D**) VNAM-pretreated mice were biopsy injured and treated with NS-398 ($PGE_2$ synthesis inhibitor) or vehicle (control) twice daily from days 4 to 10 after injury. Representative H&E images (C) and wound bed lengths (D) are shown ($n$ = 11 to 12 wounds per group; five mice per group) at day 12 after injury. (**E** and **F**) VNAM-pretreated mice were administered amphotericin B (AmpB) or vehicle (control) and then biopsy injured. Representative H&E images (E) and wound bed lengths ($n$ = 12 or 13 wounds per group; five to seven mice per group) at day 12 after injury are shown. Significance (unpaired Student's $t$ test): ****$P$ < 0.0001; N.S., not significant. All values in (B), (D), and (F) are means ± SEM. Dashed black lines in (A), (C), and (E) represent wound bed lengths (largest distance between the crypts). Scale bars, 100 μm.

induction (Fig. 3G). In further support of this result, the pathogenic effects of *D. hansenii* were abolished in biopsy-injured *Ifnar*$^{-/-}$ mice (Fig. 3, H and I). We also found that *Stat1*, a key transcription factor downstream of IFNAR (*23*), was required for *D. hansenii*–induced CCL5 production; mice lacking *Stat1* in myeloid cells were protected from *D. hansenii*–induced healing defects compared with littermate controls (Fig. 3, J to L). We tested candidate pathways upstream of CCL5 and found the effects of *D. hansenii* were Dectin-1 independent but partially dependent on Toll-like receptor 3 (fig. S17). Collectively, these findings suggest that *D. hansenii* requires type 1 IFN and CCL5 in myeloid cells to impair mucosal healing after injury.

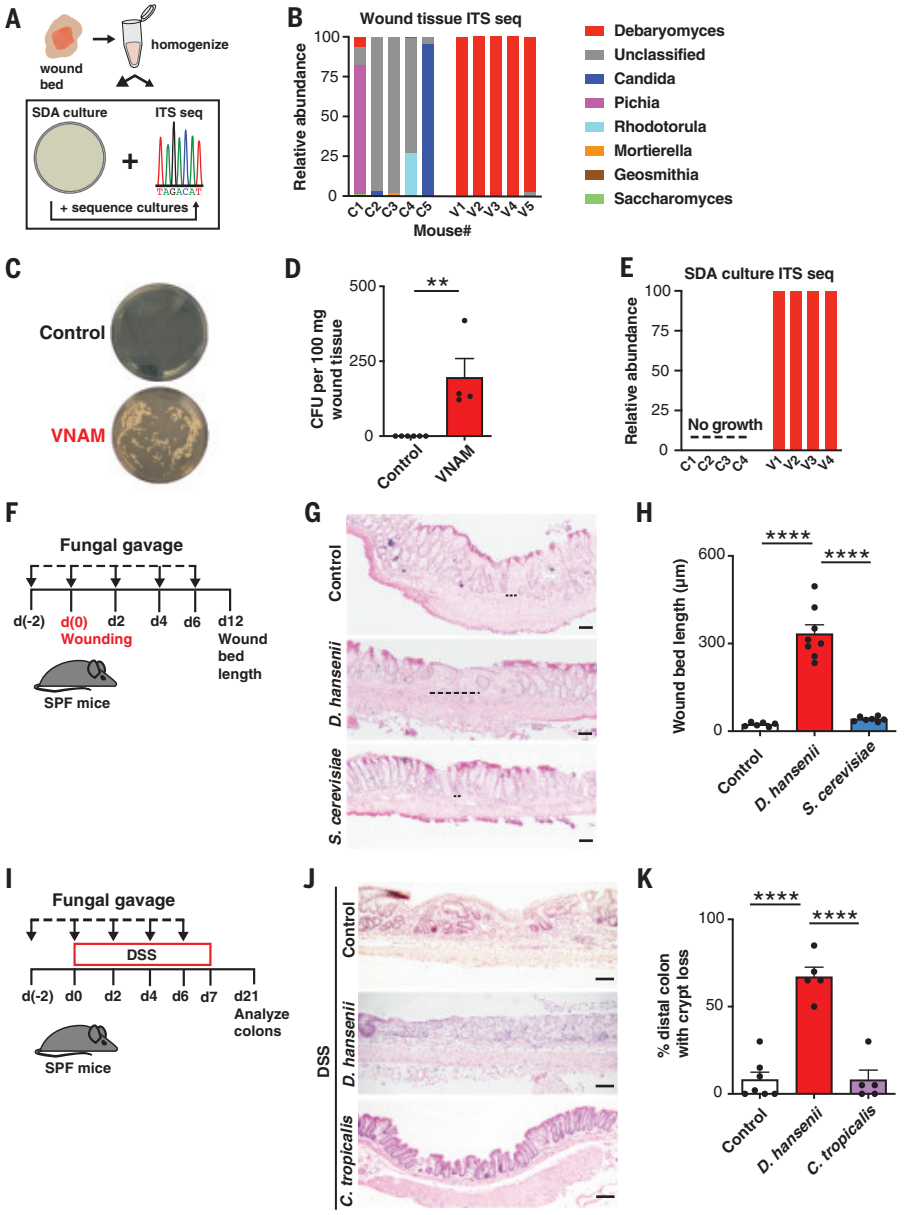


**Fig. 2. *Debaryomyces* was enriched in wounds of VNAM-pretreated mice; its administration to conventionally raised or gnotobiotic mice led to impaired crypt regeneration.** (**A** to **E**) WT mice, pretreated for 4 weeks with VNAM or Kool-Aid (control), were biopsy injured and wounds were analyzed at day 8 after injury. A schematic representation (A) and relative abundance of fungi in the wounds (B) are shown. C, control; V, VNAM treated. The representative cultures (C) and counts of viable colonies (D) are for 14 to 16 wounds per group with four to six mice per group. Significance (unpaired Student's *t* test): $^{**}P < 0.01$. In (E), we show the identification of fungi by ITS sequencing of the pooled colonies per mouse in (C). (**F** to **H**) WT mice gavaged with phosphate-buffered saline (PBS; controls), *D. hansenii* (B6A1), or *S. cerevisiae* were biopsy injured and wounds were analyzed at day (d) 12 after injury. The experimental scheme (F), representative H&E images (G), and wound bed lengths are shown for 13 to 19 wounds per group with six to eight mice per group. (**I** to **K**) WT mice were gavaged with PBS (control), *D. hansenii*, or *C. tropicalis* and analyzed after DSS recovery. The experimental setup (I), representative H&E images (J), and percent colonic crypt loss (*n* = five to seven mice per group) are shown. Significance [one-way analysis of variance (ANOVA) and Tukey's post hoc test]: $^{****}P < 0.0001$. All values in (D), (H), and (K) are means ± SEM. Dashed black line in (G) represents wound bed length. Scale bars, 100 μm.

Because CD is characterized by impaired mucosal healing and is closely associated with fungal dysbiosis (*24*, *25*), we hypothesized that *Debaryomyces* is present in the tissues obtained from individuals with CD. In the first cohort (WashU), we obtained ileal biopsy tissue from CD patients ($n$ = 7) and healthy controls ($n$ = 10) undergoing routine endoscopy (table S2). These tissues were homogenized and streaked on SDA (Fig. 4A). Fungi were present in all the homogenates from CD biopsy tissues, but only 1 of 10 healthy biopsy tissues (Fig. 4B). *Debaryomyces* was detected in all CD patient tissue samples as determined by ITS sequencing of pooled colonies (Fig. 4B). In the WashU cohort, we then used an alternative approach. We performed ITS sequencing on genomic DNA isolated directly from ileal resection samples of CD patients ($n$ = 6) and found that *Debaryomyces* was significantly enriched in inflamed regions compared with uninflamed regions from the same patient (Fig. 4, C and D, and fig. S18). Notably, inflamed regions of CD tissue samples from surgical resections were highly enriched for culturable *Debaryomyces* (Fig. 4E). Despite detectable *Debaryomyces* sequencing reads in noninflamed regions (Fig. 4D), we were unable to recover viable fungi in five of six tissue samples. Having confirmed the presence of *Debaryomyces* using two independent approaches, we expanded the analysis of CD samples from our WashU cohort using *D. hansenii* species-specific primers (*26*). We found that *D. hansenii* was significantly enriched in inflamed areas of both the ileum ($n$ = 7) and colon ($n$ = 8) compared with respective uninflamed counterparts (Fig. 4F). We used this approach to validate the presence of *D. hansenii* in ileal CD samples ($n$ = 10) from another clinical center, Cedars-Sinai. In this second cohort, *D. hansenii* demonstrated increased abundance in inflamed ileal tissue compared with uninflamed ileal tissue from the same patient (Fig. 4F).

As serum antibodies directed against fungi have been associated with severe CD (*27*), we tested if antibodies in CD serum could recognize *D. hansenii*. Using a clinical isolate of *D. hansenii* (CDA1) (table S3), we found that immunoglobulin A (IgA) that recognized this strain was increased in the serum of CD patients compared with healthy controls (fig. S19A). In addition, the level of IgA showed a significant correlation with serum CCL5 levels (fig. S19, B and C).

To ascertain whether human clinical isolates of *D. hansenii* were capable of inducing repair

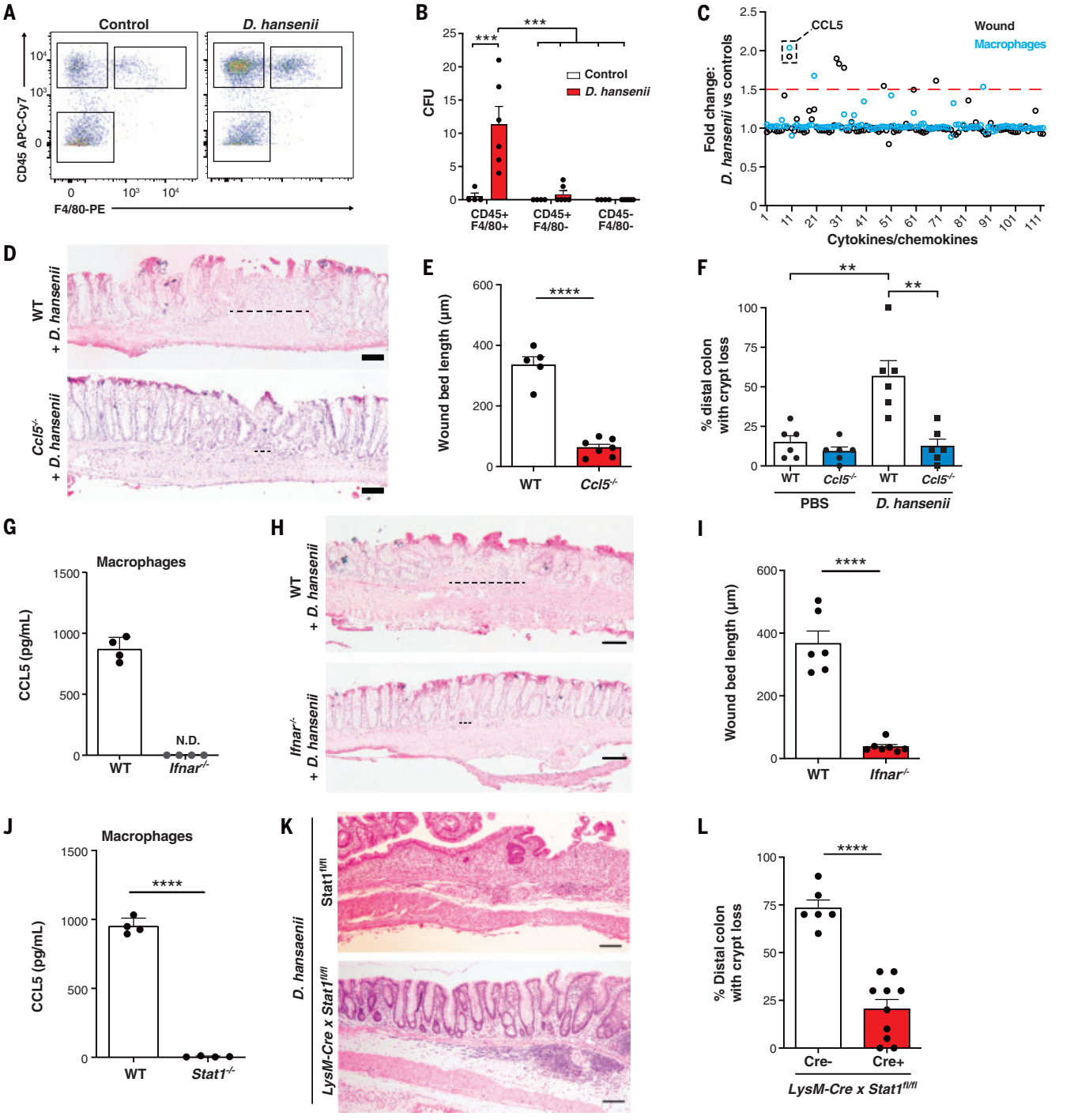


**Fig. 3. *D. hansenii* impairs crypt regeneration through type I IFN and CCL5.** (**A**) Representative plots of live cells isolated from mouse colons after DSS recovery. (**B**) Cells from (A) were lysed and cultured on SDA ($n$ = 4 to 6 mice per group). Significance (two-way ANOVA with Tukey's post hoc test): ***$P$ < 0.001. (**C**) Fold change in *D. hansenii*–infected wounds (black circles) or macrophages (blue circles) compared with respective controls. (**D** and **E**) Representative H&E images (D) and wound bed lengths (E) at day 12 after injury ($n$ = 12 to 17 wounds per group; five to seven mice per group) in *Ccl5*$^{-/-}$ and WT mice gavaged with *D. hansenii* (B6A1). Significance (unpaired Student's $t$ test): ****$P$ < 0.0001. (**F**) Percent colonic crypt loss in mice after DSS recovery in the absence or presence of *D. hansenii* ($n$ = 6 mice per group). Significance (two-way ANOVA and Tukey's post hoc test): **$P$ < 0.01. (**G**) CCL5 in BMDM supernatant 24 hours after *D. hansenii* stimulation ($n$ = four experiments). N.D., not detected. (**H** and **I**) Representative H&E images (H) and wound bed lengths (I) at day 12 after injury ($n$ = 16 wounds; six to seven mice per group) in mice gavaged or not with *D. hansenii* as indicated. Significance (unpaired Student's $t$ test): ****$P$ < 0.0001. (**J**) CCL5 in BMDM supernatant 24 hours after *D. hansenii* stimulation ($n$ = 4 experiments). Significance (unpaired Student's $t$ test): ****$P$ < 0.0001. (**K** and **L**) Representative H&E images (K) and percent colonic crypt loss (L) in *LysMCre Stat1*$^{fl/fl}$ and *Stat1*$^{fl/fl}$ mice after DSS recovery in the presence of *D. hansenii* ($n$ = 6 to 10 mice per group). Significance (unpaired Student's $t$ test): ****$P$ < 0.0001. All values in (B), (E), (F), (G), (I), (J), and (L) are means ± SEM. Dashed black lines in (D) and (H) represent wound bed lengths. Scale bars, 100 µm.

defects, we gavaged WT mice with *D. hansenii* CDA1; as anticipated, this isolate resulted in impaired crypt regeneration in the biopsy injury model, an effect reversed by amphotericin B treatment (Fig. 4, G to I). Notably, administration of amphotericin B, in the absence of *D. hansenii* gavage, did not demonstrate any obvious defects in repair of WT mice (fig. S20). Collectively, these findings suggest that *D. hansenii* is enriched in inflamed tissues of individuals with CD and isolates impair colonic repair in mouse models of colonic damage,

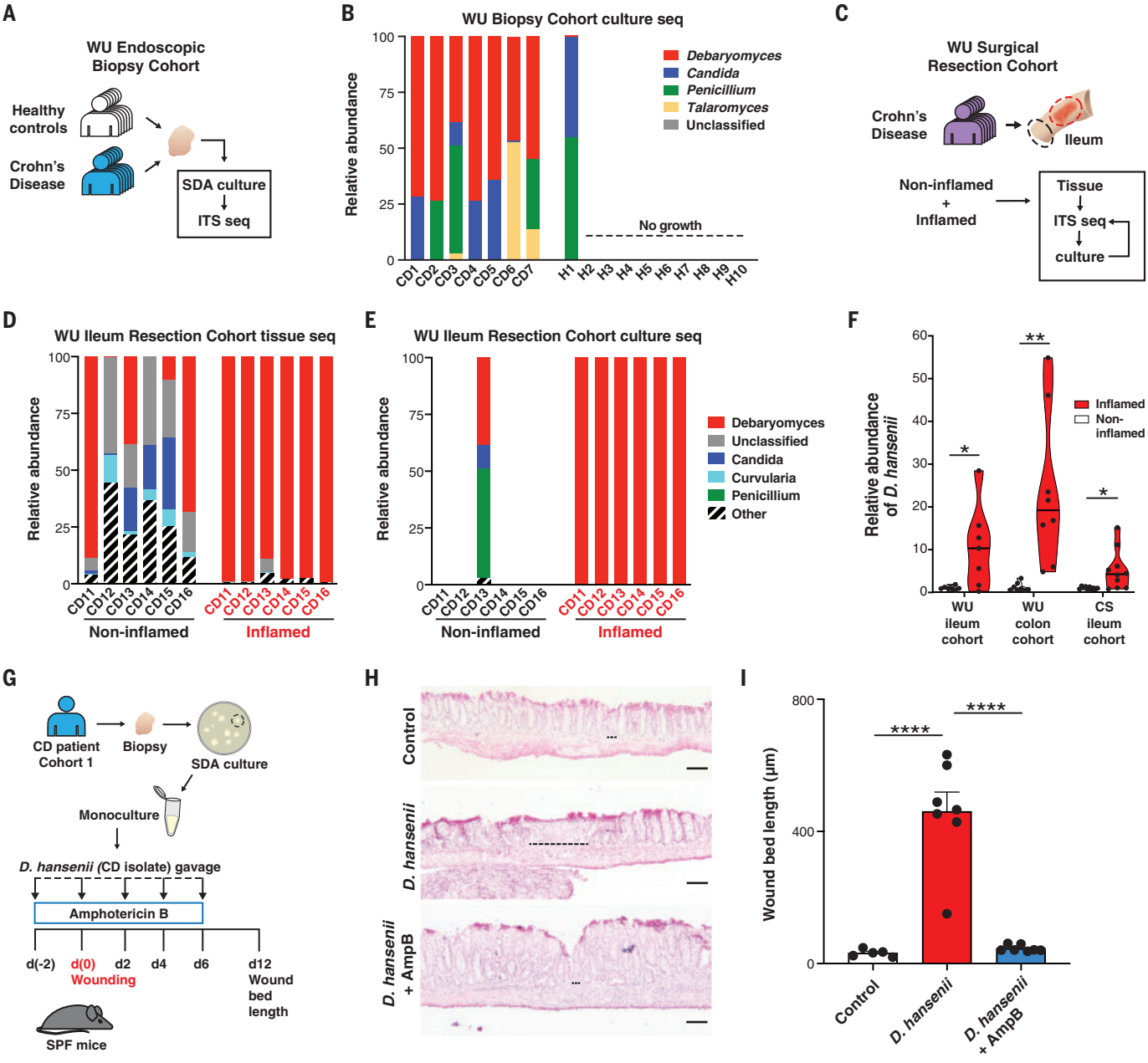


**Fig. 4. *D. hansenii* was enriched in inflamed intestinal tissue of patients with CD, and the human isolate impaired crypt regeneration in vivo.** (**A** and **B**) Ileal biopsy tissue from healthy individuals and CD patients, cultured on SDA, shown in a schematic representation (A) and as the relative abundance of fungi assessed by ITS sequencing of the pooled colonies for each individual (B). (**C** and **D**) ITS sequencing of DNA isolated from inflamed and noninflamed ileal regions of CD surgical resections, as shown in a schematic representation (C) and as the relative abundance of fungi (D). Only genera with a combined mean across both groups of >1.5% relative abundance are plotted. All other genera are combined into "Other." (**E**) Relative fungal abundance of colonies cultured from the surgical resections in (C). (**F**) *D. hansenii* abundance was analyzed by qPCR and normalized to human *Gapdh* DNA. Significance (paired Student's *t* test): $*P < 0.05$; $**P < 0.01$. WU, Washington University; CS, Cedars-Sinai. (**G** to **I**) WT mice were gavaged with *D. hansenii* (CDA1) in the presence or absence of amphotericin B (AmpB) and biopsy injured. A schematic representation (G), representative H&E images (H), and wound bed lengths (I) at day 12 after injury are shown ($n = 14$ to 17 wounds per group; five to seven mice per group). Significance (one-way ANOVA and Tukey's post hoc test): $****P < 0.0001$. All values in (I) are means ± SEM. The dashed black line in (H) represents the wound bed. Scale bars, 100 μm.

suggesting that targeting this microbe could be a therapy for CD.

*D. hansenii* is commonly found in a variety of dairy products, in particular, different varieties of cheese and processed meats, and is considered to be a rare human fungal pathogen (*28*). For technical and experimental reasons, it is unclear if *D. hansenii* is an intestinal symbiont. Two independent reports recently showed *D. hansenii* in association with UC and colorectal cancer (*29*, *30*); however, the functional role of *D. hansenii* in the context of human diseases has not yet been characterized. Here, we confirmed that both mouse and human isolates of *D. hansenii* impede repair, providing a previously uncharacterized host microbial axis that can be targeted to improve mucosal healing in IBD. We provide direct evidence that the mycobiota ecosystem in the tissue is not well reflected in the fecal material, and it was only profiling of intestinal tissue that allowed us to isolate *D. hansenii* and test functionality. Thus, our findings support the use of a combination of culture-dependent and -independent approaches from affected organs to identify pathogenic microbiota members in human diseases.

## REFERENCES AND NOTES


1. M. F. Neurath, *Mucosal Immunol.* **7**, 6–19 (2014).
2. M. Schirmer, A. Garner, H. Vlamakis, R. J. Xavier, *Nat. Rev. Microbiol.* **17**, 497–511 (2019).
3. A. Lavelle, H. Sokol, *Nat. Rev. Gastroenterol. Hepatol.* **17**, 223–237 (2020).
4. J. Lloyd-Price *et al*., *Nature* **569**, 655–662 (2019).
5. L. Sun, G. M. Nava, T. S. Stappenbeck, *Curr. Opin. Gastroenterol.* **27**, 321–327 (2011).
6. J. J. Limon, J. H. Skalski, D. M. Underhill, *Cell Host Microbe* **22**, 156–165 (2017).
7. H. Seno *et al*., *Proc. Natl. Acad. Sci. U.S.A.* **106**, 256–261 (2009).
8. H. Miyoshi, R. Ajima, C. T. Luo, T. P. Yamaguchi, T. S. Stappenbeck, *Science* **338**, 108–113 (2012).
9. U. Jain *et al*., *Cell Host Microbe* **24**, 353–363.e5 (2018).
10. H. Miyoshi *et al*., *EMBO J.* **36**, 5–24 (2017).
11. S. Dollive *et al*., *PLOS ONE* **8**, e71806 (2013).
12. I. D. Iliev *et al*., *Science* **336**, 1314–1317 (2012).
13. D. Ellis, *J. Antimicrob. Chemother.* **49** (suppl. 1), 7–10 (2002).
14. P. Sandven, J. Lassen, *J. Clin. Microbiol.* **37**, 3731–3732 (1999).
15. A. K. Nash *et al*., *Microbiome* **5**, 153 (2017).
16. G. Hoarau *et al*., *mBio* **7**, e0125016 (2016).
17. A. Y. Peleg, D. A. Hogan, E. Mylonakis, *Nat. Rev. Microbiol.* **8**, 340–349 (2010).
18. Q. H. Sam, M. W. Chang, L. Y. Chai, *Int. J. Mol. Sci.* **18**, 330 (2017).
19. A. P. Moreira *et al*., *J. Immunol.* **180**, 3049–3056 (2008).
20. J. C. Nieto *et al*., *Sci. Rep.* **7**, 92 (2017).
21. S. Ali *et al*., *Front. Immunol.* **10**, 778 (2019).
22. W. M. Schneider, M. D. Chevillotte, C. M. Rice, *Annu. Rev. Immunol.* **32**, 513–545 (2014).
23. K. Honda, A. Takaoka, T. Taniguchi, *Immunity* **25**, 349–360 (2006).
24. J. D. Lewis *et al*., *Cell Host Microbe* **22**, 247 (2017).
25. G. Liguori *et al*., *J. Crohns Colitis* **10**, 296–305 (2016).
26. P. Wrent, E. M. Rivas, E. Gil de Prado, J. M. Peinado, M. I. de Silóniz, *Int. J. Food Microbiol.* **193**, 109–113 (2015).
27. J. J. Limon, K. M. Kershaw, D. M. Underhill, *Curr. Opin. Gastroenterol.* **34**, 398–403 (2018).
28. U. Breuer, H. Harms, *Yeast* **23**, 415–437 (2006).
29. J. S. Mar *et al*., *mBio* **7**, e0107216 (2016).
30. O. O. Coker *et al*., *Gut* **68**, 654–662 (2019).


## ACKNOWLEDGMENTS


We thank the Washington University gnotobiotic core, M. Baldridge, and M. Diamond. **Funding:** Crohn's & Colitis Foundation (T.S.S.), Lawrence C. Pakula, MD IBD Innovation (U.J.), NIH/VA: AT009741 (T.S.S.), AI127548 (D.A.H.), DK125296 (T.-C.L.), IK2BX004909-01(B.D.M.), and American College of Gastroenterology (P.Dee.). B.D.M. was supported by Career Development Award IK2 BX004909-01 from the U.S. Department of Veterans Affairs Biomedical Laboratory Research and Development Service. The views expressed in this article are those of the authors and do not necessarily reflect the position or policy of the Department of Veterans Affairs or the U.S. government. J.B. was supported by NIH grant NIH DK46763. **Author contributions:** U.J. and T.S.S. conceived the study and designed experiments; U.J., A.M.V.H., D.A.G.B., S.X., C.-W.L., E.G.D., J.S.L.-E., T.-C.L., B.D.M., D.M.U., and D.A.H. performed experiments and analyzed data; M.H.G., P.Dee., P.Deb., J.B., D.P.B.M., and M.C. provided human samples; and U.J. and T.S.S. wrote the manuscript. **Competing interests:** U.J. and T.S.S. are co-inventors on the patent application (PCT/US2020/064376). P.Dee. has served as a consultant or advisory board member for Janssen, Pfizer, Celgene, Arena, and Prometheus and has received research grants from Takeda. All other authors declare no conflict of interest. **Data and materials availability:** ITS, Sequence Read Archive SRA:PRJNA634694; RNA:Array Express, E-MTAB-9806. Cultured fungi are available from Washington University, St. Louis, with a completed materials transfer agreement.


## SUPPLEMENTARY MATERIALS

science.sciencemag.org/content/371/6534/1154/suppl/DC1
Materials and Methods
Supplementary Text
Figs. S1 to S21
Tables S1 to S3
References (*31*–*46*)
MDAR Reproducibility Checklist


31 May 2020; resubmitted 15 November 2020
Accepted 15 January 2021
10.1126/science.abd0919


HYDROLOGY

# Globally observed trends in mean and extreme river flow attributed to climate change


**Lukas Gudmundsson[1]*, Julien Boulange[2], Hong X. Do[3,4,5], Simon N. Gosling[6], Manolis G. Grillakis[7], Aristeidis G. Koutroulis[8], Michael Leonard[3], Junguo Liu[9], Hannes Müller Schmied[10,11], Lamprini Papadimitriou[12,13], Yadu Pokhrel[14], Sonia I. Seneviratne[1], Yusuke Satoh[2,15], Wim Thiery[1,16], Seth Westra[3], Xuebin Zhang[17], Fang Zhao[18,19]**



**Anthropogenic climate change is expected to affect global river flow. Here, we analyze time series of low, mean, and high river flows from 7250 observatories around the world covering the years 1971 to 2010. We identify spatially complex trend patterns, where some regions are drying and others are wetting consistently across low, mean, and high flows. Trends computed from state-of-the-art model simulations are consistent with the observations only if radiative forcing that accounts for anthropogenic climate change is considered. Simulated effects of water and land management do not suffice to reproduce the observed trend pattern. Thus, the analysis provides clear evidence for the role of externally forced climate change as a causal driver of recent trends in mean and extreme river flow at the global scale.**


Among key concerns with respect to anthropogenic climate change (ACC) are impacts on the terrestrial water cycle. Earth system models (ESMs) indicate that projected ACC can influence water availability on land (*1*) and may trigger more floods (*2*) and droughts (*3*). Although detection and attribution studies have shown that observed changes in atmospheric variables such as precipitation (*4*, *5*) and water vapor (*6*) are consistent with model simulations that account for historical ACC, evidence for a human fingerprint on past changes in river flow and hydrological extremes is still lacking at the global scale.

Two factors have complicated the detection and attribution of changes in terrestrial water systems at the global scale. First, although river flow time series are the most abundant observations of water resources and hydrological extremes, the slow mobilization of in situ observations has confined past assessments to regional and continental case studies (*7*–*12*) or to small collections of large river basins, with most of the records ending in the 20th century (*13*–*15*). To circumvent this lack of global in situ observations, researchers have used reconstructions of essential hydrological variables such as soil moisture (*16*–*18*) or evapotranspiration (*19*) and indicators of water availability (*20*) as the basis for climate change detection and attribution studies. Although these efforts have revealed that ACC is detectable in terrestrial water systems, they lack a direct connection to in situ observations of quantities relevant for water management.

Second, besides ACC, on-ground human activities such as historical water and land management (HWLM) are also altering water resources and hydrological extremes, e.g., directly through flow regulation and water abstractions or indirectly through effects of land-cover change (*13*). For example, large-scale water withdrawal for irrigation might induce declining trends in river flow. Likewise, reservoir expansion may lead to changes in stream flow. Several studies have shown that effects of HWLM on water resources could

be equally large or might even exceed climate change impacts in some regions (*13*, *21*, *22*). However, ESMs, which are an important tool for attributing observed changes to human influences on the climate system, typically do not account for HWLM as a possible confounding factor (*7*).

Recent advances in mobilizing in situ river flow observations (*23*, *24*) and an unprecedented multimodel ensemble that combines the ESMs' ability to account for ACC with the capacity of high-resolution global hydrology models (GHMs) to incorporate HWLM (*25*) allow us to tackle the challenge of attributing observed changes in river flow at the global scale. Here, we consider in situ observations of daily average river flow from 7250 gauging stations (fig. S1) that have at least 28 years with almost complete daily data from 1971 to 2010 (*26*). To balance the uneven spatial distribution of in situ observations, the analysis is constrained to predefined subcontinental regions (*27*) with at least 80 stations. Yearly time series of low (annual 10th percentile), mean (annual mean), and high (annual 90th percentile) river flows are considered, respectively representing very dry, average, and very wet conditions. For each time series, trends are estimated and expressed in terms of percentage change per decade. Subsequently, the median trend is computed for each region to reduce the effects of local-scale natural variability, observational errors, and spatial autocorrelation for further statistical analyses (*28*).

Figure 1 reveals spatially complex trend patterns in observed low, mean, and high river flow. Some regions such as northeast Brazil, southern Australia, and the Mediterranean show a drying tendency. Other regions such as northern Europe tend toward wetter conditions. We also note that the level of spatial aggregation may mask subregional differences. The analysis also confirms previous results (*29*) indicating that the direction of change is often consistent throughout the entire flow distribution, i.e., trends in low, mean, and high flows share the same sign. Reconstructions of global river flow from the Inter-Sectoral Impact Model Intercomparison Project phase 2a (ISIMIP2a) that are based on GHMs driven with observational atmospheric data (*30*) are highly correlated with the observed trend pattern (Fig. 1), although the reconstructions have a tendency to underestimate the magnitude of the observed trends. Accounting for HWLM does not improve the skill of the reconstruction in reproducing the spatial patterns of observed regional median trends, even though it can improve overall model performance (*31*).

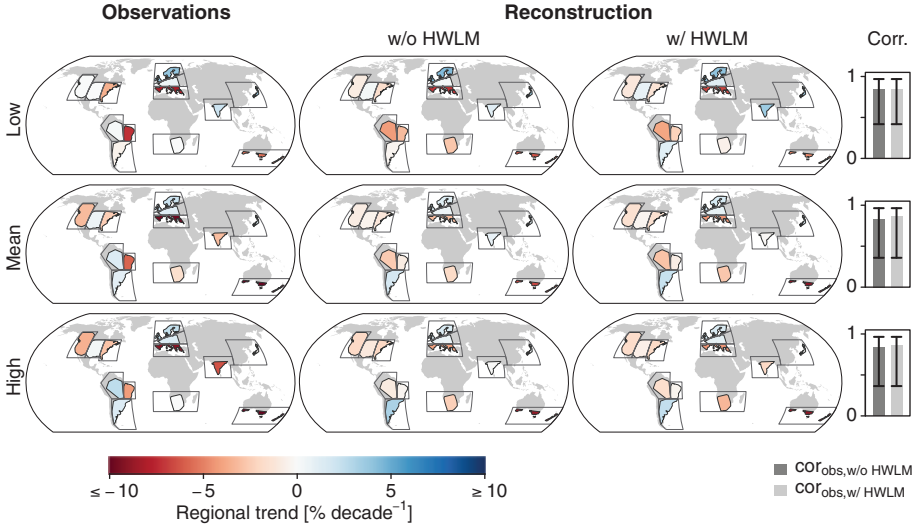


**Fig. 1. Comparison of observed and reconstructed regional median river flow trends (1971–2010).** "Observations" represent trends computed from in situ observations. "Reconstruction" represents multimodel mean trend of global hydrology model simulations driven by observational atmospheric forcing, with (w/) and without (w/o) the effects of HWLM. Hollow polygons indicate predefined regions used for grouping stations. Colored polygons are defined by the convex hull around the station coordinates in the respective regions. Colors indicate the regional median trend. The color scale for the trends has been truncated to enhance the readability of the maps. Figure S9 displays the full range of all data presented here. The plots labeled "Corr." show Pearson correlation coefficients between the spatial patterns of observed and reconstructed regional median trends, alongside 99% confidence intervals that are based on Fisher's *z* transform.

Although the above assessment shows that changes in the atmospheric conditions are driving observed trends in low, mean, and high river flow, it remains unclear if these changes can be attributed to ACC. To tackle this question, we used the climate change detection and attribution approach (*32*), which ingests both observations and simulation experiments that include or exclude the drivers of ACC. If (i) simulations that include the drivers of ACC are consistent with the observations and (ii) simulations that do not include them fail to be consistent with the observations, then it is possible to claim attribution. Here, we consider two simulation experiments from the Inter-Sectoral Impact Model Intercomparison Project phase 2b (ISIMIP2b) (*25*), where GHMs that account for HWLM are driven with output from ESMs that ingest different radiative forcing. The first experiment considers preindustrial radiative forcing and is referred to as PIC&HWLM from here onward. Because preindustrial radiative forcing does not impose systematic trends in the simulations, the PIC&HWLM experiment allows us to test the hypothesis of whether the observed trend patterns can be explained by the simulated effects of HWLM alone. The second experiment considers historical radiative forcing, which includes both anthropogenic (e.g., human greenhouse gas or aerosol emissions) as well as natural (e.g., influence of large volcanic eruptions) factors throughout the past century. This experiment is referred to as HIST&HWLM and allows us to test the hypothesis of whether the addition of historical radiative forcing contributes to explaining the observed trend pattern.

Figure 2 compares observed river flow trends to trends from both the PIC&HWLM and the HIST&HWLM simulations. The consistency of the observed trend pattern with

[1]Institute for Atmospheric and Climate Science, Department of Environmental Systems Science, ETH Zurich, Zürich, Switzerland. [2]National Institute for Environmental Studies (NIES), Tsukuba, Japan. [3]School of Civil, Environmental and Mining Engineering, University of Adelaide, Adelaide, SA, Australia. [4]Faculty of Environment and Natural Resources, Nong Lam University, Ho Chi Minh City, Vietnam. [5]School for Environment and Sustainability, University of Michigan, Ann Arbor, MI, USA. [6]School of Geography, University of Nottingham, Nottingham NG7 2RD, UK. [7]Institute for Mediterranean Studies, Foundation for Research and Technology Hellas, Rethymno 74100, Greece. [8]School of Environmental Engineering, Technical University of Crete, Chania, Greece. [9]School of Environmental Science and Engineering, Southern University of Science and Technology (SUSTech), Shenzhen 518055, China. [10]Institute of Physical Geography, Goethe University Frankfurt, Frankfurt am Main, Germany. [11]Senckenberg Leibniz Biodiversity and Climate Research Centre (SBiK-F), Frankfurt am Main, Germany. [12]Cranfield Water Science Institute, Cranfield University, Cranfield, UK. [13]Mott MacDonald Ltd, Cambridge, UK. [14]Department of Civil and Environmental Engineering, Michigan State University, East Lansing, MI, USA. [15]International Institute for Applied Systems Analysis, Laxenburg, Austria. [16]Department of Hydrology and Hydraulic Engineering, Vrije Universiteit Brussel, Brussels, Belgium. [17]Environment Canada, Toronto, ON, Canada. [18]Key Laboratory of Geographic Information Science (Ministry of Education), School of Geographic Sciences, East China Normal University, Shanghai, China. [19]Potsdam Institute for Climate Impact Research (PIK), Potsdam, Germany.
***Corresponding author. Email: lukas.gudmundsson@env.ethz.ch**

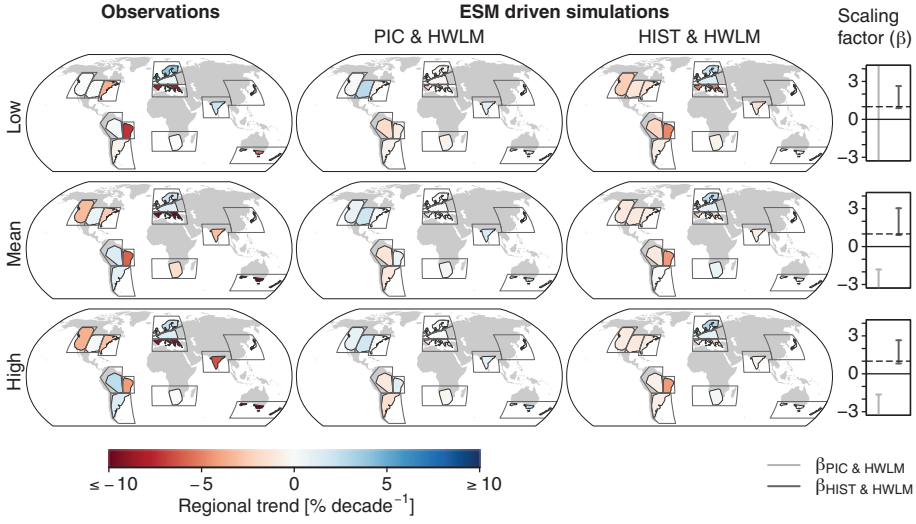


**Fig. 2. Comparison of observed and simulated river flow trends (1971–2010).** "Observations" are the same as in Fig. 1 and included here to facilitate comparison. "ESM-driven simulations" represent trends computed from model experiments that account for HWLM but consider simulated atmospheric data with either preindustrial (PIC) or historical (HIST) radiative forcing. The color scale for the trends has been truncated to enhance the readability of the maps. Figures S9 and S10 display the full range of all data presented here. The scaling factor plots show 10 to 90% confidence intervals of the scaling factors from the detection analysis. The simulated patterns are consistent with the observations if the lower bound of the confidence interval is larger than zero (solid horizontal line). The magnitude of observed and simulated change is consistent if the confidence intervals include one (dashed horizontal line). Confidence intervals exceeding the range of the ordinate are truncated to enhance readability of the plot.

either of the simulation results is tested using optimal fingerprinting (*28*, *33*). To this end, the multimodel mean of the simulations ($x$) is regressed on the observations ($y$) while accounting for natural variability ($\epsilon$) as well as model and sampling errors ($\nu$), such that $y = \beta \times (x - \nu) + \epsilon$ (*33*). Testing the significance of the association between the observed and simulated patterns is based on the magnitude of the scaling factor $\beta$. The simulated pattern is said to be detected in the observations if $\beta$ is significantly larger than zero, i.e., if the lower ends of the associated confidence intervals are above zero. Scaling factors derived from simulations with PIC&HWLM are never significantly larger than zero (Fig. 2). This shows that simulated effects of HWLM without accounting for historical radiative forcing cannot explain the observed trend pattern. This is in agreement with the above assessment, where accounting for HWLM did not improve the consistency of observed and reconstructed trends (Fig. 1). The situation differs for the analysis of HIST&HWLM, i.e., the simulations that account for historical radiative forcing. Here, the scaling factors of all indices are significantly larger than zero ($p < 0.1$).

The results show that the combined effect of historical radiative forcing and HWLM is detected in observed trend patterns of low, mean, and high river flow. The analysis also suggests that the magnitude of the simulated trend patterns under historical radiative forcing is consistent with the observations ($\beta \approx 1$). This, in combination with the finding that accounting for HWLM does not improve reconstructions (Fig. 1), implies that simulated impacts of HWLM only have a minor effect on regional median river flow trends. Consequently, the results suggest that the simulated effects of historical radiative forcing on the climate system are essential for explaining the observed patterns of regional median low, mean, and high river flows.

To investigate effects of the mismatch between point-scale observatories and model grid cells and to assess impacts of regional sampling biases of the observations, the analysis was repeated using GHM-based river flow reconstructions that allow for full spatial coverage (figs. S2 to S7). Despite additional uncertainties induced by model-based reconstructions, the results are widely consistent with the observational assessment (fig. S8). Furthermore, a detailed inspection of observed, reconstructed, and simulated trends shows that the internal variability implied by HIST&HWLM simulations is comparable to observed variability (figs. S9 to S12), indicating the validity of the assumption that natural climate variability can be approximated through chaotic model trajectories.

We note that as in any climate change detection and attribution exercise, we cannot fully rule out that processes not captured by the models might contribute to the observed trend pattern (*32*). For example, there remain uncertainties regarding the response of transpiration to dryness stress or in the representation of HWLM. Furthermore, although the ISIMIP2b ensemble allows HWLM to be accounted for in a climate change detection and attribution setup for the first time, the fact that no separate simulations with either anthropogenic or historical natural forcing are available hinders an unambiguous attribution of the observed trend pattern to ACC. In particular, natural changes in the radiative forcing triggered by large volcanic eruptions have been shown to affect the global hydrological cycle. However, recent research has demonstrated that the effects of such eruptions on river flow are typically confined to a few years after the eruption (*34*) and are therefore expected to only have a small influence on long-term trends.

Overall, the presented analysis lines up with the existing body of literature documenting that ACC is influencing the world's water cycle (*4*–*6*, *16*–*20*). Possible mechanisms that drive trends in low, mean, and high river flow include large-scale shifts in precipitation (*4*, *5*, *17*), changes in factors that influence evapotranspiration (*6*, *19*, *20*), and alterations of the timing of snow accumulation and melt driven by rising temperatures (*8*, *12*). Combining the evidence of these findings with the results of the presented analysis (Figs. 1 and 2) supports the conclusion that it is likely that ACC is contributing to the global pattern of trends in low, mean, and high river flow.

We demonstrate for the first time that the global pattern of observed changes in river flow are only captured by model simulations that account for historical radiative forcing and that simulated effects of HWLM do not substantially contribute to explaining global trend patterns of low, mean, and high flows. Thus, we have provided clear evidence for the role of historical radiative forcing as a causal driver of trends in mean and extreme river flow at the global scale.

## REFERENCES AND NOTES


1. P. Greve, L. Gudmundsson, S. I. Seneviratne, *Earth Syst. Dyn.* **9**, 227–240 (2018).
2. Y. Hirabayashi *et al.*, *Nat. Clim. Chang.* **3**, 816–821 (2013).
3. C. Prudhomme *et al.*, *Proc. Natl. Acad. Sci. U.S.A.* **111**, 3262–3267 (2014).
4. X. Zhang *et al.*, *Nature* **448**, 461–465 (2007).
5. K. Marvel, C. Bonfils, *Proc. Natl. Acad. Sci. U.S.A.* **110**, 19301–19306 (2013).
6. K. M. Willett, N. P. Gillett, P. D. Jones, P. W. Thorne, *Nature* **449**, 710–712 (2007).
7. L. Gudmundsson, S. I. Seneviratne, X. Zhang, *Nat. Clim. Chang.* **7**, 813–816 (2017).
8. T. P. Barnett *et al.*, *Science* **319**, 1080–1083 (2008).
9. G. Blöschl *et al.*, *Nature* **573**, 108–111 (2019).
10. G. Blöschl *et al.*, *Science* **357**, 588–590 (2017).
11. C. Rosenzweig *et al.*, *Nature* **453**, 353–357 (2008).
12. H. G. Hidalgo *et al.*, *J. Clim.* **22**, 3838–3855 (2009).
13. F. Jaramillo, G. Destouni, *Science* **350**, 1248–1251 (2015).
14. P. C. D. Milly, K. A. Dunne, A. V. Vecchia, *Nature* **438**, 347–350 (2005).
15. P. Wu, R. Wood, P. Stott, *Geophys. Res. Lett.* **32**, L02703 (2005).
16. X. Gu *et al.*, *Geophys. Res. Lett.* **46**, 2573–2582 (2019).
17. K. Marvel *et al.*, *Nature* **569**, 59–65 (2019).

18. B. Mueller, X. Zhang, *Clim. Change* **134**, 255–267 (2016).
19. H. Douville, A. Ribes, B. Decharme, R. Alkama, J. Sheffield, *Nat. Clim. Chang.* **3**, 59–62 (2012).
20. R. S. Padrón *et al.*, *Nat. Geosci.* **13**, 477–481 (2020).
21. C. J. Vörösmarty, P. Green, J. Salisbury, R. B. Lammers, *Science* **289**, 284–288 (2000).
22. I. Haddeland *et al.*, *Proc. Natl. Acad. Sci. U.S.A.* **111**, 3251–3256 (2014).
23. H. X. Do, L. Gudmundsson, M. Leonard, S. Westra, *Earth Syst. Sci. Data* **10**, 765–785 (2018).
24. L. Gudmundsson, H. X. Do, M. Leonard, S. Westra, *Earth Syst. Sci. Data* **10**, 787–804 (2018).
25. K. Frieler *et al.*, *Geosci. Model Dev.* **10**, 4321–4345 (2017).
26. Materials and methods are available as supplementary materials.
27. S. I. Seneviratne *et al.*, in *Managing the Risks of Extreme Events and Disasters to Advance Climate Change Adaptation: Special Report of the Intergovernmental Panel on Climate Change*, C. B. Field *et al.*, Eds. (Cambridge Univ. Press, 2012), pp. 109-230.
28. M. R. Allen, P. A. Stott, *Clim. Dyn.* **21**, 477–491 (2003).
29. L. Gudmundsson, M. Leonard, H. X. Do, S. Westra, S. I. Seneviratne, *Geophys. Res. Lett.* **46**, 756–766 (2019).
30. S. Gosling *et al.*, ISIMIP2a Simulation Data from Water (global) Sector (V. 1.1). GFZ Data Services (2019); https://doi.org/10.5880/PIK.2019.003.
31. T. I. E. Veldkamp *et al.*, *Environ. Res. Lett.* **13**, 055008 (2018).
32. N. L. Bindoff *et al.*, in *Climate Change 2013: The Physical Science Basis. Working Group I Contribution to the Fifth Assessment Report of the Intergovernmental Panel on Climate Change*, T. F. Stocker *et al.*, Eds. (Cambridge Univ. Press, 2013), pp. 867–952.
33. A. Hannart, A. Ribes, P. Naveau, *Geophys. Res. Lett.* **41**, 1261–1268 (2014).
34. C. E. Iles, G. C. Hegerl, *Nat. Geosci.* **8**, 838–842 (2015).
35. L. Gudmundsson, H. X. Do, M. Leonard, S. Westra, The Global Streamflow Indices and Metadata Archive (GSIM) – Part 2: Time series indices and homogeneity assessment. PANGAEA (2018); https://doi.org/10.1594/PANGAEA.887470.



## ACKNOWLEDGMENTS

**Funding:** We acknowledge financial support as follows: L.G. and S.I.S. were supported through the H2020 projects CRESCENDO (grant no. 641816) and 4C (grant no. 821003). S.I.S. acknowledges support from the European Research Council through the ERC DROUGHT-HEAT project (grant no. FP7-IDEAS-ERC-617518). H.M.S. is supported in part by the German Federal Ministry of Education and Research (BMBF, grant no. 01LS1711F). H.X.D. is supported by the University of Michigan (grant no. U064474). W.T. acknowledges support from the Uniscientia Foundation and the ETH Zurich Foundation (grant no. Fel-45 15-1). J.L. is supported by the National Natural Science Foundation of China (grant nos. 41625001 and 41571022) and the Strategic Priority Research Program of Chinese Academy of Sciences (grant no. XDA20060402). J.B. acknowledges support from MEXT/JSPS KAKENHI (grant no. 16H06291) and the Environmental Research and Technology Development Fund (grant no. 2RF-1802). Y.P. acknowledges support from the National Science Foundation (grant no. 1752729). Y.S. was supported by the Ministry of Education, Culture, Sports, Science and Technology of Japan (Integrated Research Program for Advancing Climate Models) (grant no. JPMXD0717935715). M.G.G. received support from the Greek State Scholarship Foundation (IKY) (grant no. MIS5033021). **Author contributions**: L.G. conceptualized the study, conducted the data analysis, and drafted the paper with contributions from all co-authors. H.M.S., J.B., W.T., and Y.S. conducted model simulations contributing to the ISIMIP ensembles. S.N.G. and H.M.S. coordinated the ISIMIP model simulations. **Competing interests:** The authors declare no competing interests. **Data and materials availability**: Observed river flow indices can be downloaded from PANGAEA (*35*). The model-based data are freely available through the ISIMIP project [ISIMIP2a: available through GFZ Data Services (*30*); ISIMIP2b: available at https://esgf-data.dkrz.de/projects/esgf-dkrz/].

## SUPPLEMENTARY MATERIALS

science.sciencemag.org/content/371/6534/1159/suppl/DC1
Materials and Methods
Figs. S1 to S12
Tables S1 to S7
References (*36*–*44*)

29 November 2019; accepted 25 January 2021
10.1126/science.aba3996


QUANTUM GASES

# Evidence of superfluidity in a dipolar supersolid from nonclassical rotational inertia


**L. Tanzi[1,2], J. G. Maloberti[1,2], G. Biagioni[1,2], A. Fioretti[1], C. Gabbanini[1], G. Modugno[1,2]***



**A key manifestation of superfluidity in liquids and gases is a reduction of the moment of inertia under slow rotations. Nonclassical rotational effects have also been considered in the context of the elusive supersolid phase of matter, in which superfluidity coexists with a lattice structure. Here, we show that the recently discovered supersolid phase in dipolar quantum gases features a reduced moment of inertia. Using a dipolar gas of dysprosium atoms, we studied a peculiar rotational oscillation mode in a harmonic potential, the scissors mode, previously investigated in ordinary superfluids. From the measured moment of inertia, we deduced a superfluid fraction that is different from zero and of order of unity, providing direct evidence of the superfluid nature of the dipolar supersolid.**


Superfluids exhibit their most spectacular properties during rotation. This is because the superfluid state is described by a macroscopic wave function, the phase of which can change only by integer multiples of $2\pi$ upon completing a closed path. For a cylindrical superfluid rotating at low angular velocities, $\omega \to 0$, this condition leads to the vanishing of both angular momentum $L$ and moment of inertia $I = \langle L \rangle / \omega$. An angular momentum can appear only for sufficiently large $\omega$ at integer multiples of the reduced Planck's constant $\hbar$, through the appearance of quantized vortices. These nonclassical rotational effects have been verified for most known superfluids: nuclear matter (*1*), $^4$He (*2*), $^3$He (*3*), gaseous Bose-Einstein condensates (*4*), degenerate Fermi gases (*5*), and exciton-polariton condensates (*6*). A related phenomenon is the Meissner effect in superconductors (*7*).

At the end of the 1960's, another type of bosonic phase of matter described by a macroscopic wave function, the supersolid, was predicted to exist. In a supersolid, superfluidity coexists with a crystal-type structure (*8*–*10*). A. J. Leggett suggested that a rotating supersolid should show a moment of inertia intermediate between that of a superfluid and that of a classical system, $I = (1 - f_s)\, I_c$. Here, $I_c$ is the classical moment of inertia and $0 \le f_s \le 1$ is the so-called superfluid fraction (*10*). This phenomenon is called nonclassical rotational inertia (NCRI). Standard superfluids can have $f_s < 1$, but only at finite temperature, $T > 0$, because of the presence of a thermal component. In a supersolid at $T = 0$, the reduction of the superfluid fraction is instead caused by the spatially modulated density, which tends to increase the inertia toward the classical limit (*10*, *11*).

At the time it was proposed, the primary candidate for observing supersolidity was solid helium. Torsion oscillators were used extensively to attempt detecting NCRI (*12*). The original announcement of the possible presence of a large superfluid fraction, $f_s \approx 10^{-1}$ (*13*, *14*), later received a different interpretation based on a change of the elastic properties of the solid (*15*) and has not been confirmed by more recent studies (*16*). Superfluidity in bulk solid helium has now been excluded down to the level of $10^{-4}$ (*17*), and the search goes on in two-dimensional (2D) films (*18*).

We studied a different supersolid candidate, a gaseous Bose-Einstein condensate (BEC) of strongly dipolar atoms in which a density-modulated regime coexisting with the phase coherence necessary for supersolidity has been recently discovered (*19*–*21*). So far, its superfluid nature has been tested through nonrotational excitation modes that can be described in terms of the hydrodynamic equations for superfluids (*22*–*24*). Here, we aimed instead at characterizing the NCRI of such a system, searching for direct evidence of superfluidity under rotation, in the spirit of the helium experiments.

Achieving dipolar supersolids large enough to realize a cylindrical geometry has so far not been possible, so we used a specific rotation technique that fits the asymmetric, small-sized systems available in the laboratory. We excited the so-called scissors mode, a small-angle rotational oscillation of the harmonic potential that naturally holds the system. This technique, inspired by an excitation mode of nuclei (*25*), has been proposed (*26*, *27*) and used (*28*) to demonstrate the superfluidity of ordinary BECs. A recent theoretical study has shown that the scissors mode can also be used to characterize the NCRI of a dipolar supersolid (*29*). We studied the change of the scissors mode frequency across the transition from BEC to the supersolid regime to directly compare the supersolid with a fully superfluid system.


[1]CNR-INO, Sede Secondaria di Pisa, 56124 Pisa, Italy. [2]LENS and Dipartimento di Fisica e Astronomia, Università di Firenze, 50019 Sesto Fiorentino, Italy.
***Corresponding author. Email: modugno@lens.unifi.it**

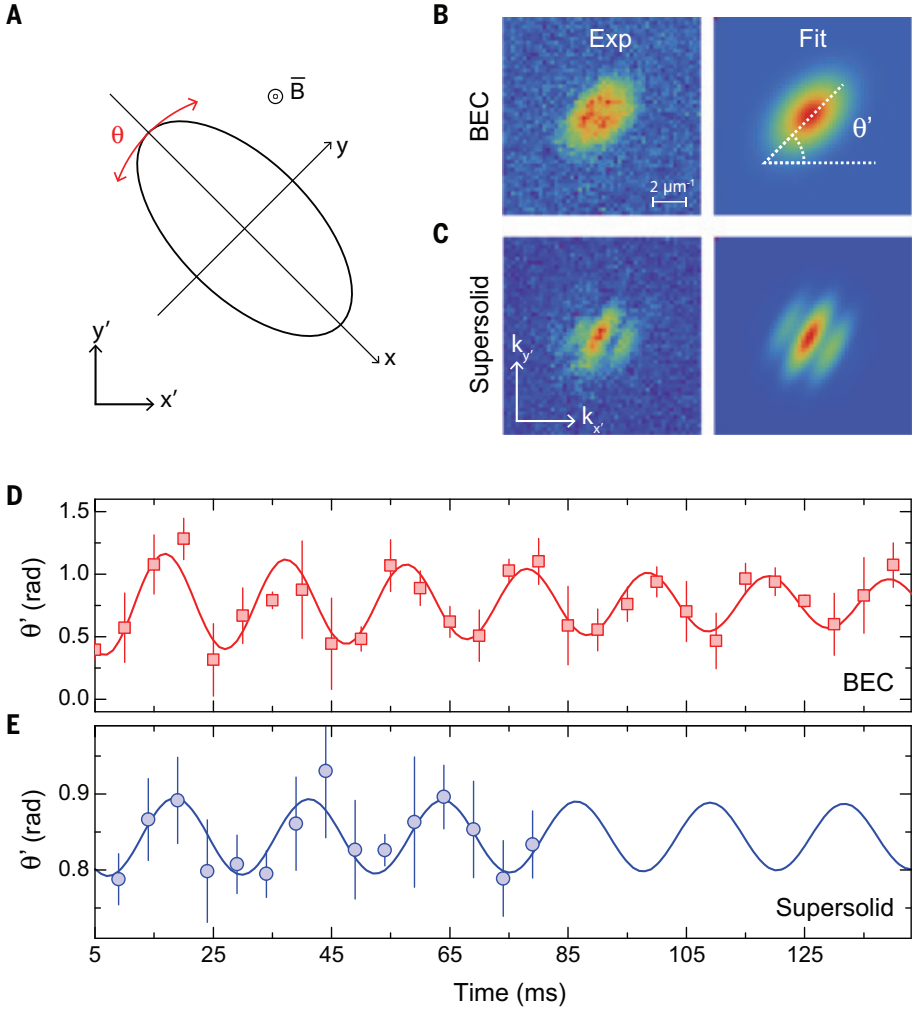


**Fig. 1. Scissors mode measurements.** (**A**) Sketch of the experimental geometry. The atomic system (ellipse) is trapped in an anisotropic potential with eigenaxes *x* and *y*. A sudden rotation of the trapping potential excites an angular oscillation $\theta(t)$ (red arrows). (**B** and **C**) Examples of the experimental distributions after free expansion and of the corresponding 2D fits used for extracting the oscillation angle $\theta'$ after the free expansion in the BEC regime [$\varepsilon_{dd}$ = 1.14 (B)] and the supersolid regime [$\varepsilon_{dd}$ =1.45 (C)]. (**D** and **E**) Time evolution of the angle $\theta'(t)$ in the BEC regime (D) and the supersolid regime (E). Error bars represent the SD of four to eight measurements.

In this experiment, a BEC of strongly magnetic Dy atoms is held in an anisotropic harmonic trap, with frequencies $\omega_{x,y,z} = 2\pi$ (23,46,90) $s^{-1}$, with the dipoles oriented in the *z* direction by a magnetic field *B* (Fig. 1). The temperature is sufficiently low to have a negligible thermal component (*30*). We induced the transition from BEC to supersolid by tuning through a magnetic Feshbach resonance the interaction parameter $\varepsilon_{dd}$, which parametrizes the ratio of the dipolar and van der Waals interaction energies (*19*). In the supersolid regime, a density modulation develops along the weak *x* axis, leading to the appearance of interference peaks in the momentum distribution. We know our lattice to be composed of two principal density maxima, or "droplets," each containing ~$10^4$ atoms (*22*). This realizes a so-called cluster supersolid (*31*), very different from the hypothesized helium supersolid with one particle per lattice site. In principle, further tuning of $\varepsilon_{dd}$ would bring the system into the so-called droplet crystal regime, with no coherence between the droplets (*19*–*21*).

The scissors mode is excited by changing suddenly the direction of the eigenaxes of the harmonic trap (*30*). This results in a sinusoidal oscillation with frequency $\omega_{sc}$ of the angle $\theta$ between the long axis of the system and the corresponding trap axis. We chose to rotate the system in the (*x*,*y*) plane, perpendicular to the direction of the dipoles, so that the dipolar interaction potential would be independent of $\theta$ (*32*, *33*).

The oscillation frequency can be directly related to the moment of inertia of the superfluid through the following equation:

$$I = I_c\, \alpha\, \beta\, (\omega_x^2 + \omega_y^2)/\omega_{sc}^2 \qquad (1)$$

Where $\alpha = (\omega_y^2 - \omega_x^2)/(\omega_y^2 + \omega_x^2)$ and $\beta = \langle x^2 - y^2\rangle/\langle x^2 + y^2\rangle$ are geometrical factors measuring the deviation from cylindrical symmetry of the trap and of the density distribution, respectively (*26*, *29*). Whereas $\alpha$ can be measured experimentally, $\beta$ needs to be calculated theoretically (*30*). For nondipolar BECs in the Thomas-Fermi regime, one has the simplification $\beta = \alpha$ (*27*). For dipolar systems, the density deformation changes instead with the interaction parameter because of magnetostriction, $\beta = \beta(\varepsilon_{dd}) \neq \alpha$ (*32*). If the oscillation amplitude is much smaller than $\beta$, then the density deformation stays constant during the motion (*26*).

We can now connect the moment of inertia to a superfluid fraction, which we define specifically for our system in analogy with Leggett's definition, taking into account our noncylindrical geometry as follows:

$$I = (1 - f_s)\, I_c + f_s\, \beta^2\, I_c \qquad (2)$$

It is easy to see that this definition coincides with Leggett's one in the cylindrical case, $\beta = 0$. It also coincides with the known results for a superfluid with elliptical geometry, $I = \beta^2 I_c$ (*1*, *26*, *34*). The presence of a residual moment of inertia in the BEC, despite $f_s = 1$ at $T = 0$, derives from a peculiar velocity distribution, which is very different from the one in a cylindrical geometry (*26*, *27*). Finally, by combining Eqs. 1 and 2, one can directly relate the superfluid fraction to the trap and scissors frequencies and to the deformation as follows:

$$f_s = [1 - \alpha\beta(\omega_x^2 + \omega_y^2)/\omega_{sc}^2]/(1 - \beta^2) \qquad (3)$$

We note that the scissors mode is analogous to the helium torsion oscillators because both detect NCRI through the oscillation frequency (*13*–*16*), although there are some differences. In the scissors mode, all atoms experience the restoring force from the trap, so there are no elastic effects to consider (*15*). A finite deformation $\beta$ is clearly necessary for the scissors mode, whereas torsion oscillators are normally symmetric, although macroscopic deformations can be taken into account with the same formalism (*34*, *35*) and a related tortuosity effect is present for superfluids in porous media (*13*).

Let us now turn to the experimental results. Figure 1, B to E, summarizes the scissors measurements in the BEC and supersolid regimes. The 2D density distributions are imaged after a free expansion of the system, representing

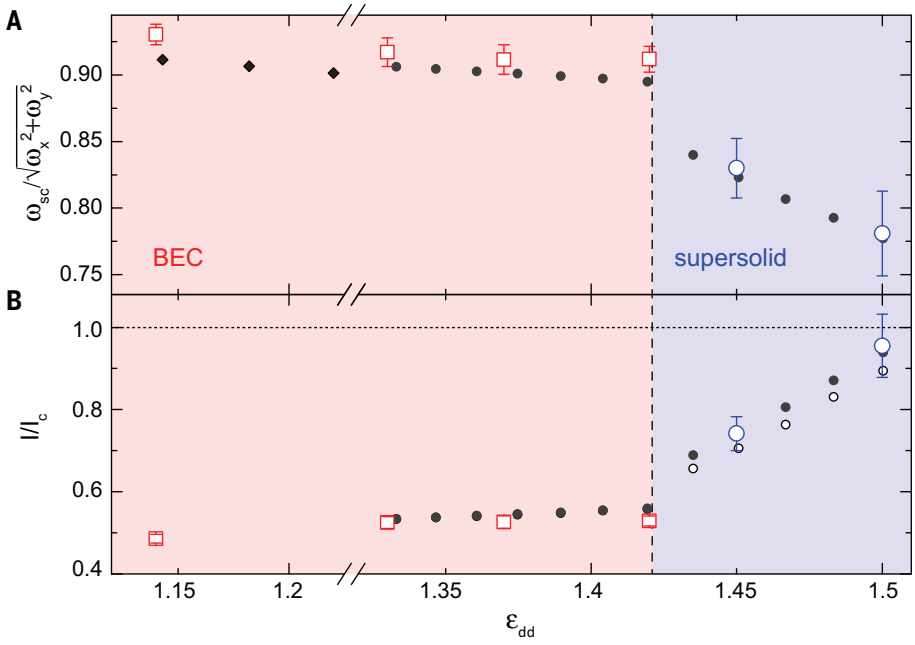


**Fig. 2. Scissors mode frequency and moment of inertia versus the interaction parameter.** (**A**) Scissors mode frequencies. Large circles and squares are the experimental measurements. Black diamonds and dots are the mean-field and beyond-mean-field theoretical predictions, respectively (*29, 32*). (**B**) Moment of inertia. Large squares and circles are derived from Eq. 1 using the experimental measurements of the scissors frequencies and the theoretical β (*29*). Black dots are the numerical simulation (*29*). Small open dots are the theoretical prediction for $\beta^2$ (*29*). Error bars indicate 1 SD (*30*). In the experiment, $\varepsilon_{dd}$ has a calibration uncertainty of 3%. The dashed line separating the BEC and supersolid regimes was determined numerically (*29*).

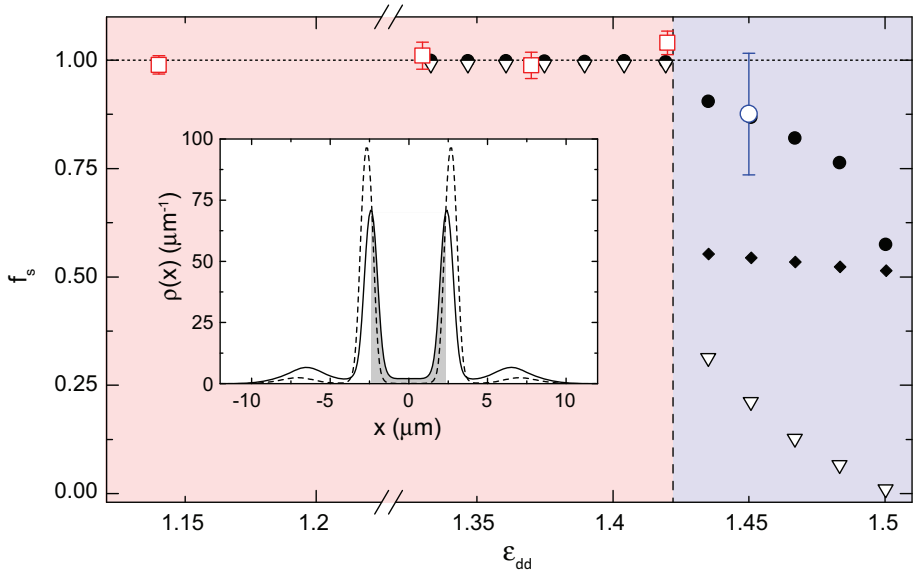


**Fig. 3. Superfluid fraction from BEC to supersolid.** Red squares and blue circle are the superfluid fraction from the experimentally measured scissors frequency and the theoretical β using Eq. 3, respectively. Black dots are the superfluid fraction from the theoretical frequency (*29*). Open triangles are the upper limit for the 1D superfluid fraction from Eq. 4. Diamonds are the estimated superfluid fraction of independent droplets. Inset shows the calculated mean density distribution (30) for $\varepsilon_{dd}$ = 1.45 (continuous line) and $\varepsilon_{dd}$ = 1. 5 (dashed line). Gray indicates the region of integration for Eq. 4.

effective momentum distributions. They are fitted to extract the angle θ′ in the laboratory frame for various observation times *t*. The resulting data for θ′(*t*) are fitted with a sinusoid to measure $\omega_{sc}$ (*30*). Both the BEC and supersolid regimes feature single-frequency oscillations, as expected for weakly interacting superfluids (*26*). We ensured that a thermal sample featured instead a two-frequency oscillation, as expected for a weakly interacting system [fig. S1 (*30*)].

To avoid perturbations caused by other collective modes (*30*), we used two different excitation techniques for the BEC and the supersolid regimes, which result in a lower amplitude of the scissors mode for the supersolid (Fig. 1, D and E). The accuracy in the determination of the scissors frequency in that regime is limited also by the finite lifetime of the supersolid (*19*).

A summary of the experimental results for the scissors frequency and the related moment of inertia is shown in Fig. 2. The results are compared with the theoretical predictions of (*29*), calculated for trap parameters and atom numbers close to the experimental ones. For the BEC, we measure a frequency that depends only weakly on the interaction parameter $\varepsilon_{dd}$, consistent with the prediction of a weak change of the deformation β ($\varepsilon_{dd}$) (*32*). By contrast, when the system enters the supersolid regime, we observed a clear reduction of the frequency, in agreement with the theory. From the measured frequency, we can determine the moment of inertia $I/I_c$ through Eq. 1, where the deformation β is determined from the numerically calculated density distributions (*29*). These results are shown in Fig. 2B. In the BEC regime, the moment of inertia differs by a factor of two from the classical value and the ratio $I/I_c$ is consistent with $\beta^2$, as expected for a fully superfluid system. In the supersolid regime, at $\varepsilon_{dd}$ = 1.45, the moment of inertia increases toward the classical value but does not reach it. This provides evidence of NCRI for the dipolar supersolid.

The data point in Fig. 2B further in the supersolid regime, at $\varepsilon_{dd}$ = 1.5, has larger error bars because of the shorter lifetime of the system. We were unable to study the droplet crystal regime, which is predicted to appear for $\varepsilon_{dd} \approx 1.52$ (*29*) because of the loss of the interference pattern (*19*–*21*).

The change of $I/I_c$ is in principle caused by both the change of shape, β ($\varepsilon_{dd}$), when the supersolid modulation forms and the related change of the superfluid fraction. The experiment-theory agreement for $I/I_c$ both in the BEC regime, where $f_s$ = 1, and at $\varepsilon_{dd}$ =1.45, where *I* is expected to be close to $I_c$, supports the validity of the calculated β for our system. Equation 2 shows that if the superfluid fraction of the supersolid varies between 0 and 1, then $I/I_c$ shown in Fig. 2B should vary between

1 and $\beta^2$. More directly, we calculate the superfluid fraction from Eq. 3, using the experimental frequencies and the theoretical β. The results are shown in Fig. 3, together with the corresponding points calculated from the theoretical predictions of (*29*).

In the BEC regime, the data confirm that the system is fully superfluid, $f_s = 1$, as already found for nondipolar BECs (*28*). In the supersolid regime, we can reliably calculate the superfluid fraction only for the experimental data point at $\varepsilon_{dd} = 1.45$. Unexpectedly, the superfluid fraction of the supersolid is very large, $f_s \approx 0.9$, in agreement with the numerical calculations. Given the measurement uncertainty, $f_s$ is consistent with unity and inconsistent with zero. This result demonstrates the superfluid nature of the dipolar supersolid under rotation.

The theory predicts a reduction of the superfluid fraction moving further into the supersolid regime, although $f_s$ remains finite even in the droplet crystal regime because of the superfluidity of the individual droplets under rotation (*29*). In the experiment, we cannot check whether $f_s$ decreases moving to $\varepsilon_{dd} = 1.5$ because the lower measurement accuracy and the increase of $\beta^2$ shown in Fig. 2B prevent us from measuring $f_s$ reliably (*30*).

It is interesting to compare our results with the original prediction by Leggett for the superfluid fraction of a supersolid rotating in a 1D annulus,

$$f_s \leq \left[\int dx/\rho(x)\right]^{-1} \qquad (4)$$

where $\rho(x)$ is the normalized density along the annulus and the integral is performed on a lattice cell (*10*, *11*). Equation 4 shows that the reduction of the superfluid fraction is a consequence of the breaking of translational invariance, because $f_s$ is determined by the minimum density between lattice sites. Intuitively, in a homogeneous superfluid, $\rho(x)$ = constant implies that each atom is equally delocalized so no rotation happens. In a system where $\rho(x) \rightarrow 0$ between neighboring lattice sites, the sites are distinguishable, so the system rotates classically. The supersolid is the intermediate case in which the atoms are still delocalized, but the density modulation allows a partial rotation, increasing the moment of inertia compared with a homogeneous superfluid.

In 1970, Leggett used Eq. 4 and the known information on the helium lattice to estimate $f_s < 10^{-4}$ for solid helium (*10*), a result compatible with current measurements (*17*). Our dipolar supersolid does not move in a 1D configuration as in the Leggett model but has a more complex dynamics in the whole $(x,y)$ plane, with both motion along the $x$ axis, where the density modulation forms, and rotation of the individual droplets. Therefore, we expect Eq. 4 to account only for the superfluid fraction related to the dynamics along $x$, because it does not consider the superfluidity of the individual droplets.

Because we cannot measure $\rho(x)$ experimentally, we used numerical calculations (*30*). The right side of Eq. 4 is shown in Fig. 3 as triangles. It drops from unity for the BEC to ~0.3 for the supersolid, a relatively large value set by the large overlap between the two central droplets (Fig. 3, inset). It then decreases for increasing $\varepsilon_{dd}$, reaching almost zero at $\varepsilon_{dd} = 1.5$, where the droplets overlap almost vanishes. In that regime, one can recover the finite superfluid fraction of the numerical calculations by considering the droplets' superfluidity. Indeed, applying Eq. 2 to the case of independent droplets and considering that each droplet's moment of inertia about its axis is zero because of the cylindrical symmetry (*30*), one obtains the estimate $f_s^{drop} \approx (1 - \beta)/(1 - \beta^2)$. Using the theoretical distributions, we get $f_s^{drop} \approx 0.5$ for all the data points in the supersolid regime (black diamonds in Fig. 3). This estimate is quite close to the numerical data point for $f_s$ at $\varepsilon_{dd} = 1.5$, and >2 SDs below the experimental data point at $\varepsilon_{dd} = 1.45$. Together with the qualitatively similar reduction of the two theoretical datasets for increasing $\varepsilon_{dd}$, this suggests that the mechanism identified by Leggett might have a relevant role in our small dipolar supersolid. To obtain a quantitative assessment, one will need further measurements and a theoretical analysis based on a 2D analog of the Leggett result (*36*, *37*).

We have established the superfluid nature of the dipolar supersolid by characterizing its nonclassical rotational inertia. The supersolid is different from standard superfluids because of the reduced superfluid fraction caused by the spontaneous breaking of translational invariance. The techniques that we have demonstrated, with an improvement of the measurement precision and of the resolution on $\varepsilon_{dd}$, will allow testing whether the superfluid fraction of the supersolid is indeed smaller than unity. Achieving larger systems might also allow studying the supersolid behavior in an annular geometry or in a 2D configuration, as well as studying the dynamics of quantized vortices in the supersolid phase (*29*).

## REFERENCES AND NOTES


1. A. B. Migdal, *Sov. Phys. JETP* **10**, 176–185 (1960); http://www.jetp.ac.ru/cgi-bin/dn/e_010_01_0176.pdf.
2. G. B. Hess, W. M. Fairbank, *Phys. Rev. Lett.* **19**, 216–218 (1967).
3. P. J. Hakonen *et al.*, *Phys. Rev. Lett.* **48**, 1838–1841 (1982).
4. F. Chevy, K. W. Madison, J. Dalibard, *Phys. Rev. Lett.* **85**, 2223–2227 (2000).
5. M. W. Zwierlein, J. R. Abo-Shaeer, A. Schirotzek, C. H. Schunck, W. Ketterle, *Nature* **435**, 1047–1051 (2005).
6. K. G. Lagoudakis *et al.*, *Nat. Phys.* **4**, 706–710 (2008).
7. A. J. Leggett, in *Quantum Liquids: Bose Condensation and Cooper Pairing in Condensed-Matter Systems*, (Oxford Univ. Press, ed. 1, 2006), pp. 20–26.
8. A. F. Andreev, I. M. Lifshitz, *Sov. Phys. JETP* **29**, 1107–1113 (1969).
9. G. V. Chester, *Phys. Rev. A* **2**, 256–258 (1970).
10. A. J. Leggett, *Phys. Rev. Lett.* **25**, 1543–1546 (1970).
11. A. J. Leggett, *J. Stat. Phys.* **93**, 927–941 (1998).
12. M. H. W. Chan, R. B. Hallock, L. Reatto, *J. Low Temp. Phys.* **172**, 317–363 (2013).
13. E. Kim, M. H. W. Chan, *Nature* **427**, 225–227 (2004).
14. E. Kim, M. H. W. Chan, *Science* **305**, 1941–1944 (2004).
15. J. Day, J. Beamish, *Nature* **450**, 853–856 (2007).
16. D. Y. Kim, M. H. W. Chan, *Phys. Rev. Lett.* **109**, 155301 (2012).
17. A. Eyal, X. Mi, A. V. Talanov, J. D. Reppy, *Proc. Natl. Acad. Sci. U.S.A.* **113**, E3203–E3212 (2016).
18. J. Nyéki *et al.*, *Nat. Phys.* **13**, 455–459 (2017).
19. L. Tanzi *et al.*, *Phys. Rev. Lett.* **122**, 130405 (2019).
20. F. Böttcher *et al.*, *Phys. Rev. X* **9**, 011051 (2019).
21. L. Chomaz *et al.*, *Phys. Rev. X* **9**, 021012 (2019).
22. L. Tanzi *et al.*, *Nature* **574**, 382–385 (2019).
23. M. Guo *et al.*, *Nature* **574**, 386–389 (2019).
24. G. Natale *et al.*, *Phys. Rev. Lett.* **123**, 050402 (2019).
25. N. L. Iudice, F. Palumbo, *Phys. Rev. Lett.* **41**, 1532–1534 (1978).
26. D. Guéry-Odelin, S. Stringari, *Phys. Rev. Lett.* **83**, 4452–4455 (1999).
27. F. Zambelli, S. Stringari, *Phys. Rev. A* **63**, 033602 (2001).
28. O. M. Maragò *et al.*, *Phys. Rev. Lett.* **84**, 2056–2059 (2000).
29. S. M. Roccuzzo, A. Gallemí, A. Recati, S. Stringari, *Phys. Rev. Lett.* **124**, 045702 (2020).
30. Materials and methods are available as supplementary materials.
31. Y. Pomeau, S. Rica, *Phys. Rev. Lett.* **72**, 2426–2429 (1994).
32. R. M. W. van Bijnen, N. G. Parker, S. J. J. M. F. Kokkelmans, A. M. Martin, D. H. J. O'Dell, *Phys. Rev. A* **82**, 033612 (2010).
33. I. Ferrier-Barbut *et al.*, *Phys. Rev. Lett.* **120**, 160402 (2018).
34. A. L. Fetter, *J. Low Temp. Phys.* **16**, 533–555 (1974).
35. A. S. C. Rittner, J. D. Reppy, *Phys. Rev. Lett.* **97**, 165301 (2006).
36. C. Josserand, Y. Pomeau, S. Rica, *Phys. Rev. Lett.* **98**, 195301 (2007).
37. A. Aftalion, X. Blanc, R. L. Jerrard, *Phys. Rev. Lett.* **99**, 135301 (2007).
38. L. Tanzi *et al.*, Data for: Evidence of superfluidity in a dipolar supersolid from nonclassical rotational inertia. Zenodo (2020); https://doi.org/10.5281/zenodo.4288848.


## ACKNOWLEDGMENTS


We thank E. Lucioni for contributions to the early stages of the experiment; A. Gallemi, A. Recati, S. Roccuzzo, and S. Stringari for discussions and for providing the theoretical data; D. E. Galli for discussions; and A. Barbini, F. Pardini, M. Tagliaferri, and M. Voliani for technical assistance. **Funding:** This work was supported by the EC-H2020 research and innovation program (grant no. 641122 - QUIC). **Author contributions:** L.T., A.F., C.G., and G.M. developed the experimental methods. L.T., J.G.M., G.B., and C.G. acquired the experimental data. L.T., J.G.M., G.B., C.G., and G.M. analyzed the data. G.B. performed the comparison with Leggett's theory. All authors contributed to the discussion and to manuscript preparation. **Competing interests:** The authors declare no competing interests. **Data and materials availability:** All data needed to evaluate the conclusions in the paper are present in the main text or the supplementary materials. All data have been uploaded to Zenodo (*38*).


## SUPPLEMENTARY MATERIALS

science.sciencemag.org/content/371/6534/1162/suppl/DC1
Materials and Methods
Fig. S1
Table S1
References (*39*–*47*)


4 December 2019; accepted 2 February 2021
Published online 18 February 2021
10.1126/science.aba4309

SYNTHETIC BIOLOGY

# T cell circuits that sense antigen density with an ultrasensitive threshold

Rogelio A. Hernandez-Lopez[1,2], Wei Yu[1], Katelyn A. Cabral[2,3,4]*, Olivia A. Creasey[2,3,4]*, Maria del Pilar Lopez Pazmino[1,2], Yurie Tonai[1], Arsenia De Guzman[1], Anna Mäkelä[5], Kalle Saksela[5], Zev J. Gartner[2,3], Wendell A. Lim[1,2]†

Overexpressed tumor-associated antigens [for example, epidermal growth factor receptor (EGFR) and human epidermal growth factor receptor 2 (HER2)] are attractive targets for therapeutic T cells, but toxic "off-tumor" cross-reaction with normal tissues that express low levels of target antigen can occur with chimeric antigen receptor (CAR)–T cells. Inspired by natural ultrasensitive response circuits, we engineered a two-step positive-feedback circuit that allows human cytotoxic T cells to discriminate targets on the basis of a sigmoidal antigen-density threshold. In this circuit, a low-affinity synthetic Notch receptor for HER2 controls the expression of a high-affinity CAR for HER2. Increasing HER2 density thus has cooperative effects on T cells—it increases both CAR expression and activation—leading to a sigmoidal response. T cells with this circuit show sharp discrimination between target cells expressing normal amounts of HER2 and cancer cells expressing 100 times as much HER2, both in vitro and in vivo.

The specificity with which chimeric antigen receptor (CAR)–T cells can recognize and kill tumor cells and discriminate against normal cells remains limited (*1*–*3*). A major challenge is finding surface proteins that are absolutely tumor specific (*4*). CAR-T cells are effective in treating hematologic cancers (*5*–*7*), but they indiscriminately kill both cancerous and normal B cells because they target the lineage-specific protein CD19. The loss of B cells is tolerable, but the killing of normal tissue when treating solid cancers with CAR-T cells remains a major challenge that can lead to toxicity and, in some cases, has proven lethal (*8*–*10*). Antigen receptors such as epidermal growth factor receptor (EGFR) and human epidermal growth factor receptor 2 (HER2) are overexpressed in cancers, but they are also expressed at lower densities in normal epithelial tissues (*11*, *12*). Thus, anti-HER2 CAR-T cells have shown, in some cases, toxic cross-reaction with normal organs (*8*). Such on-target, off-tumor toxicity has been observed for CARs directed at several other overexpressed tumor-associated antigens (*13*, *14*). Although some toxicity cases can be managed clinically (*9*), ideally, engineered T cells should reliably discriminate cancer cells from normal cells on the basis of antigen density (Fig. 1A, top).

To widen their therapeutic window, engineered T cells must sense target antigen density with a sigmoidal response and a sharper killing threshold (Fig. 1A, bottom). Dose-response behaviors in which small changes in input can generate large, nonlinear changes in output activity are referred to as "ultrasensitive" responses (*15*, *16*).

Ultrasensitive behavior is observed in many critical regulatory systems and can be achieved through various mechanisms, ranging from allosteric molecules (for example, hemoglobin) to more complex regulatory cascades or circuits (*17*–*19*). Ultrasensitive circuits shift linear responses toward switch-like "all-or-none" responses in many biological systems (*15*, *18*, *20*). In T cells, binding of the cytokine interleukin-2 (IL-2) to basally expressed low-affinity receptors results in induced expression of the high-affinity alpha subunit of the IL-2 receptor (CD25) (*21*). Thus, IL-2 acts on T cells in two ways: It both directly activates the cells and makes the cells more sensitive to IL-2, thereby

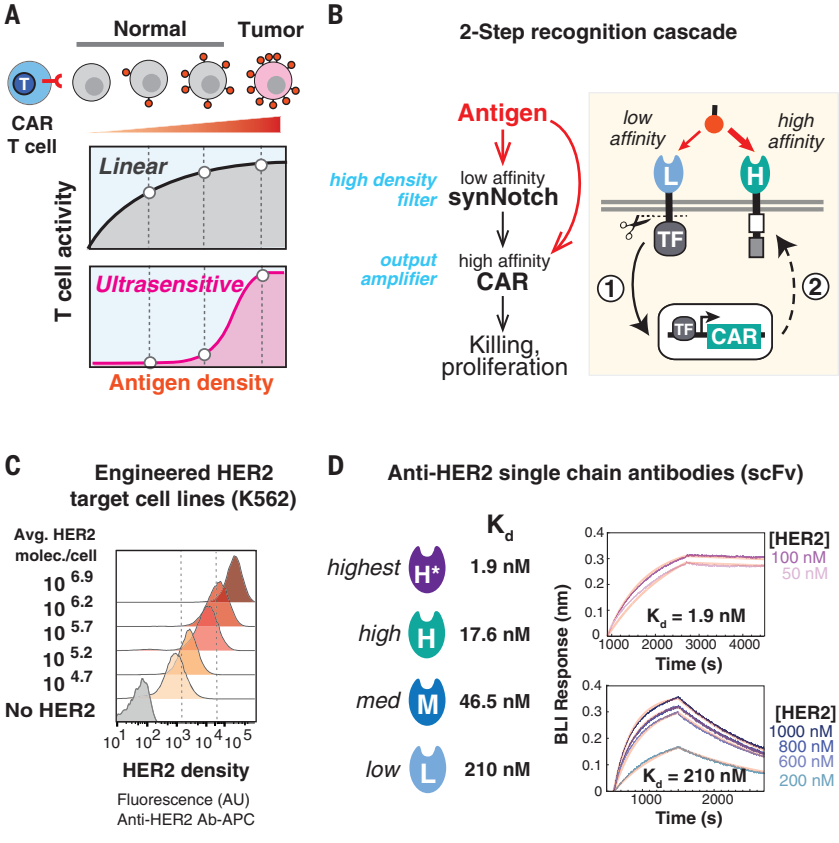


**Fig. 1. Design of T cells with ultrasensitive antigen-density sensing.** (**A**) Ideal therapeutic T cells will distinguish between tumor cells that express high antigen density and normal cells that express low antigen amounts. A CAR-T cell with a standard linear response curve distinguishes poorly between high- and low-density cells. Effective discrimination requires a sigmoidal ultrasensitive dose-response curve. (**B**) Design of two-step recognition circuit. A synNotch receptor detects an antigen (HER2) with low affinity. This synNotch receptor, when fully activated, induces expression of a high-affinity CAR. The low-affinity synNotch acts as a high–antigen-density filter, and the high-affinity CAR activates T cell killing and proliferation, acting as an amplifier. TF, transcription factor. (**C**) Densities of the tumor-associated antigen HER2 on engineered stable cell lines of human leukemia K562. Representative flow cytometry plots ($n$ = 3) are shown. These cell lines can be compared to tumor cell lines (fig. S1A). The average HER2 molecules per cell was measured ($n$ = 3) as shown in fig. S1A. To construct different HER2 sensing systems, we used a series of anti-HER2 scFvs with affinities spanning a 100-fold range. Ab, antibody; APC, allophycocyanin; AU, arbitrary units. (**D**) Binding affinities for anti-HER2 scFvs used in this study (for details of sequences and binding affinity measurements, see fig. S2). Biolayer interferometry sensograms show the binding kinetics for human HER2 and immobilized anti-HER2 scFvs. Data are shown as colored lines, and the best fit for data to a 1:1 binding model is shown in pink. HER2 concentrations used for binding affinity measurements are indicated. BLI, biolayer interferometry.

resulting in a form of positive feedback and cooperativity.

We used a modular approach to engineer ultrasensitive T cells (*22*–*24*). Our strategy recognizes the cognate antigen with a low-affinity synthetic notch (synNotch) receptor, which would, in turn, induce the expression of a high-affinity CAR for the same antigen (synNotch receptors activate transcription of a genetically encoded payload when they engage input ligand) (Fig. 1B) (*23*–*25*). In this circuit design, the low-affinity synNotch receptor acts as a filter and constrains transcription induction to occur only when the T cell encounters target cells with high antigen expression. Once past this initial filter, the induced high-affinity CAR permits strong T cell killing and proliferation. Together, the circuit could yield an all-or-none, ultrasensitive response.

To evaluate T cell circuits engineered to achieve density-dependent recognition of the HER2 antigen, we constructed a series of stable human leukemia (K562) tumor cell lines that differ only in their amount of HER2 expression over a 100-fold range (Fig. 1C). The HER2 densities correspond to those of several cancer cell lines (fig. S1A). A clinically relevant goal is to be able to reliably discriminate between cells expressing >$10^{6.5}$ [HER2 pathology score of 3+, as defined by American Society of Clinical Oncology–College of American Pathologists (ASCO-CAP) scoring guidelines] versus $10^{4.5}$ molecules per cell (HER2 score of 0 or 1+, termed "HER2 negative"), as these are the expression amounts found in several HER2-amplified cancers and several normal HER2-expressing human tissue samples (*26*), respectively. To build the synNotch receptors and CARs, we made a series of anti-HER2 single-chain antibodies (scFvs; Fv denotes a heterodimer of the variable region of the light and heavy chains) with affinities that span a 100-fold range (dissociation constants between 2.0 and 200 nM) (Fig. 1D and fig. S2).

We constructed and tested several versions of the anti-HER2 synNotch → anti-HER2 CAR circuit in human primary CD8+ T cells in vitro (fig. S3A). To assay density-sensing behavior, we measured target cell killing by quantitative flow cytometry. Several circuit T cells showed antigen density ultrasensitivity [Hill coefficients ($n_H$) of 1.7 to 4.4] (Fig. 2A, bottom). By contrast, T cells with constitutive expression of either high- or low-affinity CARs showed little density discrimination (Fig. 2A, top). In circuit T cells in which a low-affinity synNotch receptor [scFv dissociation constant ($K_d$) = 210 nM] was used to control the expression of a high-affinity CAR (scFv $K_d$ = 17.6 nM) (Fig. 2A, red line), their ultrasensitive threshold clearly discriminated between the target densities of $10^{4.5}$ and $10^{6.5}$ [Fig. 2B; $n_H$ = 4.4, antigen density that produces a 50% maximal response ($den_{50}$) = $10^{5.5}$] (for circuit activity in T cells from multiple donors, see fig. S4B).

The observed ultrasensitivity appears to originate from the designed transcriptional cascade. The steady-state amounts of CAR expression (monitored by tagging CARs with an mCherry protein) (fig. S3A) depended strongly on target antigen density (Fig. 2B, left, and fig. S4C, red line). T cell proliferation, a critical component of an antitumor response, also showed

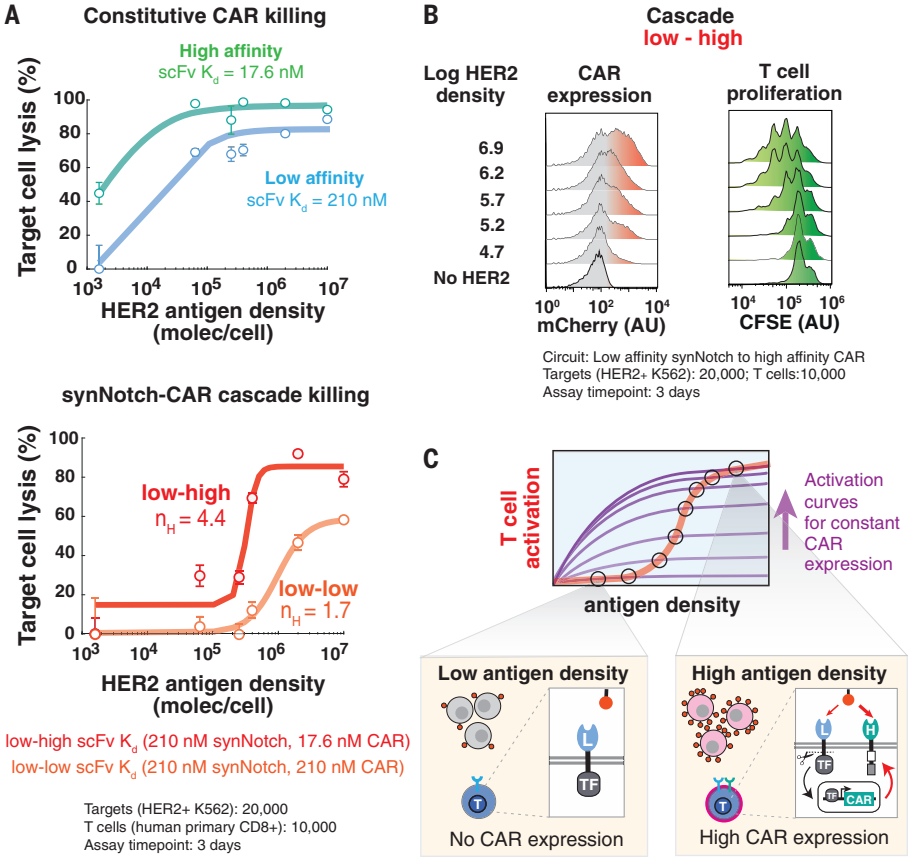


**Fig. 2. A two-step low- to high-affinity recognition circuit yields ultrasensitive antigen-density sensing.** (**A**) In vitro cell killing curves as a function of target cell antigen density, using human primary CD8+ T cells expressing a constitutive CAR of high (scFv $K_d$ = 17.6 nM) or low affinity (scFv $K_d$ = 210 nM) (top) or a two-step circuit in which the low-affinity synNotch receptor induces expression of either a low- or a high-affinity CAR (scFv $K_d$ = 210 nM synNotch, 17.6 nM CAR) (bottom). For the circuits, lines are fitted to a Hill equation (Hill coefficient for each curve is indicated) (fig. S4A). For constitutive CARs, the lines are drawn on the basis of inspection. The percentage of specific lysis was determined by using flow cytometry to count the number of target cells after 3 days relative to a coculture of targets in the presence of untransduced T cells (see fig. S3C for gating details). Data points denote means, and error bars represent SEM ($n$ = 3). (**B**) Representative fluorescence-activated cell sorting (FACS) distributions ($n$ = 3) for CAR expression and T cell proliferation measured as a function of target cell HER2 density (at 3 days) for T cells expressing a low- to high-affinity recognition circuit. T cell proliferation was only observed at HER2 densities of >$10^5$ (fig. S4C). CFSE, carboxyfluorescein diacetate succinimidyl ester. (**C**) Model for the mechanism of a two-step circuit expressing a low-affinity synNotch to a high-affinity CAR. In principle, cells with this circuit display two very different responses; in the presence of a low–antigen-density target (left), the T cell activity is dominated by the low-affinity synNotch and low amounts of a CAR. In the presence of a high–antigen-density target (right), the expression of a CAR is increased, and the T cell activity is dominated by the high-affinity CAR response that activates proliferation and killing. T cell activity is predicted to show a sigmoidal response curve (shown in red) because as antigen density increases, CAR expression also gradually increases, transiting between the series of linear response curves shown in purple.

[1]Cell Design Institute, Department of Cellular and Molecular Pharmacology, University of California San Francisco, San Francisco, CA, USA. [2]Center for Cellular Construction, University of California San Francisco, San Francisco, CA, USA. [3]Department of Pharmaceutical Chemistry, Chan Zuckerberg BioHub, University of California San Francisco, San Francisco, CA, USA. [4]Graduate Program in Bioengineering, University of California Berkeley and University of California San Francisco, San Francisco, CA, USA. [5]Department of Virology, Haartman Institute, University of Helsinki, Helsinki, Finland.
*These authors contributed equally to this work
†Corresponding author. Email: wendell.lim@ucsf.edu

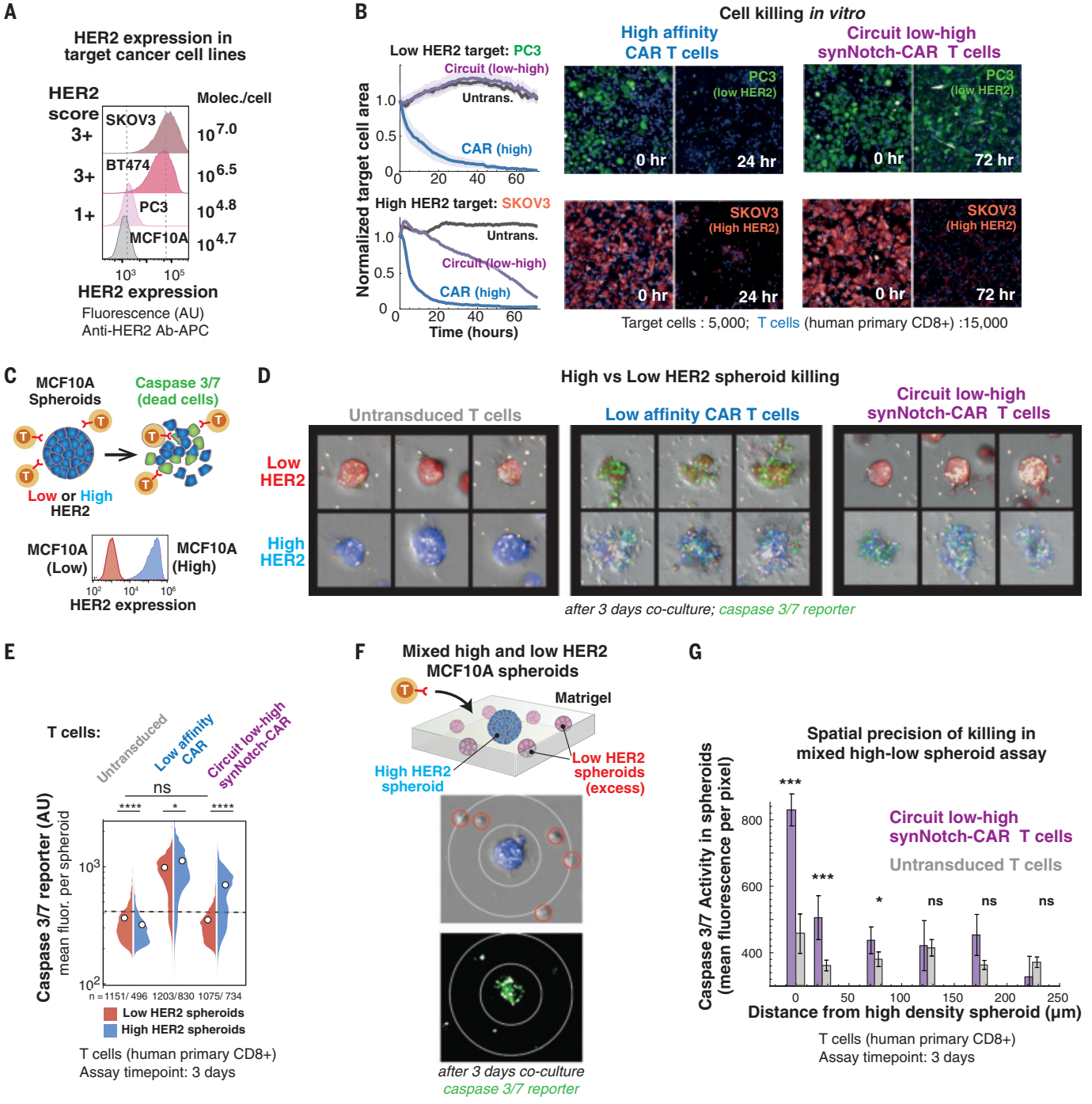


**Fig. 3. Low-to-high synNotch-to-CAR circuit: Discrimination between high- and low-density tumor cancer cell lines and 3D spheroids.** (**A**) Representative FACS distributions ($n$ = 3) showing the HER2 expression of low- and high-HER2 cell lines. The HER2 score (as defined by ASCO-CAP scoring guidelines) is shown to the left, and the average HER2 density is shown to the right. (**B**) Area occupied by target cells as a function of time, normalized by the area occupied by target cells at time 0 (left). Low–HER2-density cancer cells (top plot), PC3 (1+ tumor line), or high–HER2-density cancer cells (bottom plot), SKOV3 (3+ tumor line), were cultured with human primary CD8+ T cells expressing either a two-step circuit low-affinity to high-affinity CAR (scFv $K_d$ = 210 nM synNotch, 17.6 nM CAR) (purple lines) or a high-affinity CAR (scFv $K_d$ = 17.6 nM) (blue lines). Gray lines correspond to the target area in the presence of untransduced T cells. Solid lines show the average normalized target area, and the shaded areas depict the SEM ($n$ = 3 wells, three fields of view per well). To the right, representative images of the in vitro cell killing experiment are shown. T cells are shown in blue, the low–HER2-density cells in green, and the high–HER2-density cells in red (for data from additional cell lines, see fig. S6; see also movies S1 and S2). (**C**) Schematics of T cell killing assay of spheroids made of MCF10A cells expressing high or low HER2. A caspase dye (shown in green) was used to track cell death. The FACS distributions show the HER2 expression on MCF10A lines used to make the 3D spheroids. The MCF10A line engineered to express high HER2 is shown in blue, and wild-type MCF10As that express low levels of HER2 are shown in red. (**D**) Representative images of spheroids expressing low (shown in red) or high (shown in blue) HER2 in the presence of untransduced T cells (left) or T cell expressing either a low-affinity CAR (middle) or a two-step low-to-high

recognition circuit (right). The caspase 3/7 signal is in green, and the T cells are labeled in yellow. (**E**) Violin plots showing the distributions of mean caspase 3/7 signal per spheroid. The distributions for the low–HER2-density spheroids are shown to the left in red and the ones for the high–HER2-density spheroids to the right in blue. The mean of the distribution is shown as a white circle, and the number of analyzed spheroids in each case is shown at the bottom. The statistical significance of differences in mean caspase 3/7 signal in each coculture condition was determined by a Kruskal-Wallis test with Bonferroni's post hoc for multiple comparisons [not significant (ns) > 0.05, *$P$ < 0.05, ****$P$ < 0.0001]. (**F**) Schematics of experiment to study the distance dependence of killing activity of low-to-high–circuit T cells in a 3D culture system. High–HER2-density spheroids were mixed with a large excess of low–HER2-density cells and engineered low-to-high–circuit T cells. A caspase 3/7 dye was used as a reporter for cell killing. The spheroids and cells were embedded in a thin slab of cell-laden Matrigel to constrain their position along the $z$ axis. A representative image of a high-HER2 spheroid is shown in blue surrounded by low-HER2 spheroids, highlighted in red circles, after 3 days of coculture. The corresponding image for the caspase 3/7 activity is shown below. (**G**) Caspase 3/7 activity (fluorescence per pixel within spheroids) is plotted as a function of distance from a high-HER2 spheroid, located at the origin. The distances for each low-density spheroid to the closest high-density spheroid were binned in 50-μm bins, and the means of the caspase signal of all spheroids within the bin were computed (on a per-pixel basis to account for differences in spheroid size). The gray bars show the mean values of caspase signal for spheroids cocultured with untransduced T cells; the purple bars show the mean values of caspase signal for spheroids cocultured with low-to-high–circuit T cells. The error bars indicate the SEM. A two-sample Kolmogorov-Smirnov test was used to determine the significance of distributions differences (ns > 0.05, *$P$ < 0.05, ***$P$ < 0.001). For representative images for each channel showing high-density spheroids (blue) surrounded by low-HER2 spheroids, see fig. S7. T cells were labeled with a yellow cell trace dye.

an ultrasensitive dependence on target antigen density (Fig. 2B, right, and fig. S4C, green line).

The response of the T cell circuit could be tuned by altering the receptor affinities within the circuit. For example, lowering the CAR affinity (scFv $K_d$ = 210 nM) while maintaining a low-affinity synNotch increased the density threshold ($den_{50} = 10^{6.0}$) (fig. S4D) but also reduced the maximal killing activity and lowered the overall ultrasensitivity ($n_H$ = 1.7). The ultrasensitivity began to break down when we used a medium-affinity synNotch (scFv $K_d$ = 46.5 nM) receptor as the circuit filter (fig. S4D, brown line). Thus, a robust ultrasensitive response is generated by linking low- and high-affinity recognition into a two-step cascade (Fig. 2C). Low-affinity synNotch receptors that encounter low densities of HER2 antigen produce low amounts of CAR expressed at the T cell surface (Fig. 2C, left). By contrast, when low-affinity synNotch receptors encounter high HER2 densities (Fig. 2C, right), they express higher steady-state amounts of CARs. Thus, high target antigen density both increases CAR expression level and activates T cell proliferation and killing, leading to a nonlinear all-or-none response (Fig. 2C).

By contrast, we found that constitutively expressed CARs, even with reduced CAR expression or affinity (fig. S3B), triggered T cell killing of low-density antigen cells (fig. S5, A and B). CARs and synNotch receptors showed different sensitivities, even when using the same antigen binding domain. CARs are more sensitive, triggering killing activity with relatively low antigen density (Fig. 2A and fig. S5), whereas synNotch-mediated gene expression requires higher antigen densities. Thus, the low-affinity synNotch receptor does not induce a sufficient amount of CAR expression to trigger a killing response with low-density targets and only initiates strong killing with high-density targets [Fig. 2, A (bottom) and B, and fig. S4C].

We further tested the $synNotch_{low\ affinity} \rightarrow CAR_{high\ affinity}$ (scFv $K_d$ = 210 nM synNotch, 17.6 nM CAR) HER2 antigen density–sensing circuit against a number of different human cancer cell lines with low and high HER2 expression (Fig. 3, A and B, and fig. S6). In in vitro killing assays, engineered T cells were mixed with target cancer cells that expressed either low-density HER2 [human prostate adenocarcinoma (PC3), $10^{4.8}$ HER2 molecules per cell, HER2 score 1+] or high-density HER2 [human ovary adenocarcinoma (SKOV3), $10^{7.0}$ HER2 molecules per cell, HER2 score 3+]. With the low–HER2-density cells, neither the untransduced T cells nor the $synNotch_{low\ affinity} \rightarrow CAR_{high\ affinity}$ circuit T cells showed cytotoxicity over 72 hours (Fig. 3B and movie S2). For the high–HER2-density cells, the $synNotch_{low\ affinity} \rightarrow CAR_{high\ affinity}$ circuit T cells effectively killed the high-HER2 cells (movie S2). However, we observed delayed activation onset and a lag in the time required for complete killing compared with the conditions observed for T cells with constitutive CAR expression (72 hours versus 24 hours) (movie S1). This delay is consistent with a model in which CAR expression mediated by synNotch recognition requires additional time to accumulate sufficient CAR for effective killing (Fig. 3B). Similar discriminatory behavior was observed against other human cancer lines of varying HER2 densities (fig. S6, A and B). By contrast, the constitutive CAR-T cells (both high- and low-affinity CARs) rapidly eliminated both the low- and high-HER2 target cells in this assay (figs. S5D and S6, A and B, and movie S1). In the circuit T cells, CAR expression and T cell proliferation also showed a clear dependence on the input HER2 antigen density (fig. S6C, top row). The $synNotch_{low\ affinity} \rightarrow CAR_{high\ affinity}$ T cells notably improve discrimination between multiple high- and low-density cancer cells, but the timing of circuit activation results in the delayed onset of tumor killing.

To evaluate how these ultrasensitive density-sensing T cells behave in a more complex multicellular context, we used a three-dimensional (3D) target spheroid culture model (*27*, *28*). We engineered a human breast epithelial MCF10A line, which normally expresses low amounts of HER2 ($10^{4.7}$ HER2 molecules per cell, HER2 score 0), to express high HER2 (equivalent to HER2 score 3+) (Fig. 3C). We assembled 3D spheroids (*29*) using either low- or high-HER2 MCF10A cells and embedded them in Matrigel with engineered T cells. Using 3D confocal microscopy and a caspase activity dye, we quantified the caspase fluorescence per spheroid over 3 days as an assay for target cell killing (Fig. 3C). The two-step circuit $synNotch_{low\ affinity} \rightarrow CAR_{high\ affinity}$ (scFv $K_d$ = 210 nM synNotch, 17.6 nM CAR) T cells effectively invaded, killed, and disassembled the high–HER2-density spheroids but discriminated against the low-HER2 spheroids (Fig. 3, D and E, right). By contrast, a low-affinity anti-HER2 CAR killed and disassembled the low– and high–HER2-density spheroids indiscriminately (Fig. 3, D and E, middle).

We also used this spheroid assay to evaluate the degree of spatial discrimination. If a circuit T cell was activated by a high-density spheroid, could it then migrate to a low-density spheroid and kill those cells? We mixed a low number of high-HER2 spheroids with an excess of low-HER2 spheroids and T cells, all embedded in Matrigel. T cells were observed to migrate freely among the spheroids (Fig. 3F and fig. S7, B and C). We then measured the caspase signal within the low-HER2 spheroids as a function of radial distance from the closest high-HER2 spheroid (Fig. 3F). We found a very sharp decay of killing activity as a function of distance from the high-HER2 spheroid and estimated a radius of off-target killing to be <100 μm (Fig. 3G). The circuit T cells only infiltrated, expanded, and launched a killing response in high–antigen-density spheroids (fig. S7, B and C). Many aspects of T cell activation, including increased adhesion and production of local cytokine gradients, may contribute to this high level of spatial discrimination.

Finally, we evaluated the density discrimination of $synNotch_{low\ affinity} \rightarrow CAR_{high\ affinity}$ (scFv $K_d$ 210 nM synNotch, 17.6 nM CAR) circuit T cells in multiple mouse tumor models (Fig. 4A). We first implanted immunocompromised NOD scid gamma (NSG) mice

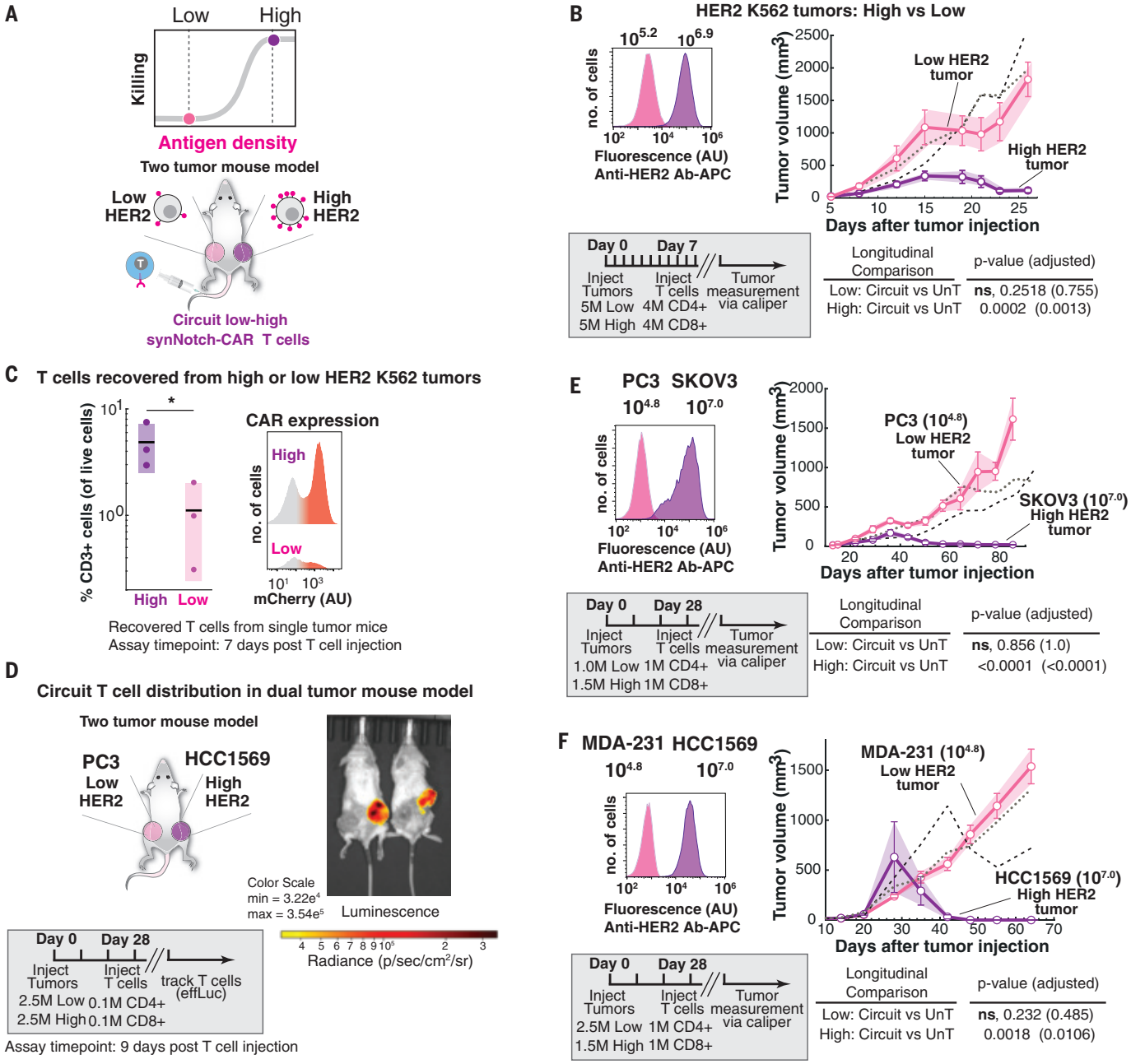


**Fig. 4. Low-o-high synNotch-to-CAR circuit: Antigen density discrimination in mouse models.** (**A**) Schematics of a two-tumor mouse model experiment to test the efficacy and safety of ultrasensitive antigen density–sensing T cells: low-affinity synNotch to high-affinity CAR circuit (scFv $K_d$ = 210 nM synNotch, 17.6 nM CAR). Low- and high-HER2 tumor cells were injected subcutaneously in the flanks of NSG mice. Engineered primary human CD4+ and CD8+ T cells were injected intravenously at the indicated times after tumor injection. Tumor volume was monitored through caliper measurement over several days after tumor injection. (**B**) FACS distributions showing the HER2 expression of cell lines used in the experiment. The doses and injection times for tumors and T cells are indicated in the gray box. Tumor volumes of cells with high and low K562 HER2 density after treatment with T cells expressing a two-step circuit (low-affinity synNotch to high-affinity CAR) are shown. The high-density tumor is shown in dark purple and the low-density tumor in pink. The solid lines connect the means, and the error bars indicate the SEM ($n$ = 7). The gray and black dotted lines show the low-density and high-density tumor volumes after treatment with untransduced T cells, respectively (for details of control experiment, see fig. S10A). UnT, untransduced. (**C**) Fraction of CD3+ T cells infiltrated in high or low K562 tumors 7 days after T cell injection. Representative FACS distributions ($n$ = 3) showing the CAR expression (mCherry tagged) in CD3+ engineered T cells are given. (**D**) Schematics of a dual-tumor mouse model to test the circuit T cell distribution. The doses and injection times for tumors and T cells are indicated in the gray box. A representative image of luciferase activity in dual-tumor mice treated with low-to-high–circuit T cells 9 days after T cell injection is shown. Luciferase signal was only detected in the high-HER2 tumor, indicating localized expansion ($n$ = 2). effLuc, firefly luciferase. (**E**) Tumor volumes of cancer lines PC3 (low) and SKOV3 (high) after treatment with T cells expressing a two-step circuit (low-affinity synNotch to high-affinity CAR) ($n$ = 5). The doses and injection times for tumors and T cells are indicated in the gray box. (**F**) Tumor volumes of cancer lines MDA-231 (low) and HCC1569 (high) after treatment with T cells expressing a two-step circuit (low-affinity synNotch to high-affinity CAR) ($n$ = 6). The doses and injection times for tumors and T cells are indicated in the gray box. For more details and individual mouse tumor volume plots, see fig. S9. Statistical longitudinal analyses were performed over entire segments of the tumor growth curves by using TumGrowth (*32*). See materials and methods for more details.

with a high–HER2-density K562 tumor on one side and a low–HER2-density K562 tumor on the opposite side. After establishing the tumors, we injected the tail vein with a mix of equal numbers of CD4+ and CD8+ primary human T cells transduced with the synNotch$_{\text{low affinity}} \rightarrow$ CAR$_{\text{high affinity}}$ circuit. The circuit T cells showed strong density discrimination (Fig. 4B and fig. S9A); the high-density tumors were cleared rapidly, but the low-density tumors grew at similar rates to those observed for untransduced T cells. This tumor discrimination was also observed at a fivefold higher effector-to-target ratio (fig. S12). The circuit T cells show significant expansion and induced CAR expression only within the high-density tumors (Fig. 4, C and D, and fig. S11). Consistent discrimination was observed with other pairs of human cancer cell lines that expressed high (~$10^{7.0}$ molecules per cell) or low (~$10^{5}$ molecules per cell) amounts of HER2 (Fig. 4, E and F, and fig. S9, B and C). We performed control experiments with untransduced T cells (fig. S10) or T cells constitutively expressing either a low- or a high-affinity anti-HER2 CAR (fig. S8). The constitutive low- or high-affinity CAR-T cells showed poor density discrimination, clearing both the low- and high-density tumors (fig. S8).

This work demonstrates that a general design principle, the use of a two-step regulatory circuit to generate an ultrasensitive dose-response behavior, can be used to engineer T cells that discriminate between target cells with high– and low–antigen-density expression. These two-step synNotch-to-CAR circuits function well both in vitro and in vivo, and the threshold can be tuned by altering the affinities of the synNotch and CAR receptors. This approach should enable expansion of the repertoire of target antigens to include other examples that are overexpressed in cancer cells compared with normal cells. Indeed, we were able to show that engineered T cells with a low-affinity synNotch receptor to a high-affinity CAR circuit, built from anti-EGFR binding domains (*30*, *31*), resulted in ultrasensitive EGFR density–sensing T cells (fig. S13).

The effective deployment of therapeutic T cells to treat solid tumors will require overcoming several other challenges, including tumor heterogeneity and suppressive tumor microenvironments, as well as improving trafficking of cells to the tumors. However, the ability to achieve ultrasensitive antigen-density discrimination provides a critical tool for widening the therapeutic window of engineered T cells against solid cancers, in which many tumor-associated antigens are overexpressed but not absolutely tumor specific.

## REFERENCES AND NOTES


1. W. A. Lim, C. H. June, *Cell* **168**, 724–740 (2017).
2. L. M. Whilding, J. Maher, *Mol. Oncol.* **9**, 1994–2018 (2015).
3. J. N. Brudno, J. N. Kochenderfer, *Nat. Rev. Clin. Oncol.* **15**, 31–46 (2018).
4. M. M. D'Aloia, I. G. Zizzari, B. Sacchetti, L. Pierelli, M. Alimandi, *Cell Death Dis.* **9**, 282 (2018).
5. S. L. Maude *et al.*, *N. Engl. J. Med.* **378**, 439–448 (2018).
6. S. S. Neelapu *et al.*, *N. Engl. J. Med.* **377**, 2531–2544 (2017).
7. S. J. Schuster *et al.*, *N. Engl. J. Med.* **380**, 45–56 (2019).
8. R. A. Morgan *et al.*, *Mol. Ther.* **18**, 843–851 (2010).
9. C. H. Lamers *et al.*, *Mol. Ther.* **21**, 904–912 (2013).
10. F. C. Thistlethwaite *et al.*, *Cancer Immunol. Immunother.* **66**, 1425–1436 (2017).
11. A. McCabe, M. Dolled-Filhart, R. L. Camp, D. L. Rimm, *J. Natl. Cancer Inst.* **97**, 1808–1815 (2005).
12. W. Yasui *et al.*, *Cancer Res.* **48**, 137–141 (1988).
13. M. R. Parkhurst *et al.*, *Mol. Ther.* **19**, 620–626 (2011).
14. Y. Guo *et al.*, *Clin. Cancer Res.* **24**, 1277–1286 (2018).
15. Q. Zhang, S. Bhattacharya, M. E. Andersen, *Open Biol.* **3**, 130031 (2013).
16. S. A. Frank, *Biol. Direct* **8**, 31 (2013).
17. S. Hooshangi, S. Thiberge, R. Weiss, *Proc. Natl. Acad. Sci. U.S.A.* **102**, 3581–3586 (2005).
18. J. E. Ferrell Jr., S. H. Ha, *Trends Biochem. Sci.* **39**, 612–618 (2014).
19. X. Wan *et al.*, *Nat. Chem. Biol.* **15**, 540–548 (2019).
20. C. Y. Huang, J. E. Ferrell Jr., *Proc. Natl. Acad. Sci. U.S.A.* **93**, 10078–10083 (1996).
21. D. Busse *et al.*, *Proc. Natl. Acad. Sci. U.S.A.* **107**, 3058–3063 (2010).
22. C. Y. Wu, L. J. Rupp, K. T. Roybal, W. A. Lim, *Curr. Opin. Immunol.* **35**, 123–130 (2015).
23. K. T. Roybal *et al.*, *Cell* **167**, 419–432.e16 (2016).
24. K. T. Roybal *et al.*, *Cell* **164**, 770–779 (2016).
25. L. Morsut *et al.*, *Cell* **164**, 780–791 (2016).
26. M. Klichinsky *et al.*, *Nat. Biotechnol.* **38**, 947–953 (2020).
27. V. Dangles-Marie *et al.*, *Cancer Res.* **63**, 3682–3687 (2003).
28. M. Pickl, C. H. Ries, *Oncogene* **28**, 461–468 (2009).
29. A. E. Cerchiari *et al.*, *Proc. Natl. Acad. Sci. U.S.A.* **112**, 2287–2292 (2015).
30. A. Lehmann *et al.*, *mAbs* **7**, 1058–1071 (2015).
31. R. C. Roovers *et al.*, *Int. J. Cancer* **129**, 2013–2024 (2011).
32. D. P. Enot, E. Vacchelli, N. Jacquelot, L. Zitvogel, G. Kroemer, *OncoImmunology* **7**, e1462431 (2018).


## ACKNOWLEDGMENTS


We thank K. T. Roybal, A. Ng, and G. Allen for sharing DNA plasmids; M. Moasser for sharing tumor cell lines for in vivo experiments; W. McKeithan for assistance with microscopy data collection; I. Eigl for assistance with biolayer interferometry data collection; A. Li, J. Choe, and members of the Lim Lab for advice and helpful discussions; and V. Nguyen and G. Allen for critical reading of this manuscript. **Funding:** This work was supported by NIH grants (P50GM081879, U54CA244438, and R01 CA196277 to W.A.L.), Howard Hughes Medical Institute (W.A.L.), and the UCSF Center for Cellular Construction (DBI-1548297), an NSF Science and Technology Center. R.A.H.-L. is a Cancer Research Institute Irvington Fellow supported by the Cancer Research Institute. R.A.H.-L. was a postdoctoral fellow of UC-MEXUS. **Author contributions:** R.A.H.-L. and W.A.L. conceived the project. The experimental plan was implemented by R.A.H.-L., W.Y., K.A.C., O.A.C., M.d.P.L.P., Y.T., and A.D.G.; R.A.H.-L., K.A.C., and O.A.C. designed and carried out 3D culture experiments supervised by Z.J.G. and W.A.L.; R.A.H.-L., W.Y., Y.T., and A.D.G. designed and carried out in vivo experiments supervised by W.A.L.; and A.M. and K.S. designed protein expression vectors and provided scFv-GST purified protein constructs. R.A.H.-L. analyzed all data. R.A.H.-L. and W.A.L. prepared the figures and wrote the manuscript with suggestions from all authors. W.A.L. supervised all aspects of the work. **Competing interests:** A provisional patent application has been filed by the University of California related to this work (U.S. application number 62738995). Z.J.G. is an equity holder in Scribe Biosciences and Provenance Bio. **Data and materials availability:** All data are available in the manuscript or supplementary materials. Reagents are available from the corresponding author upon reasonable request. Plasmids from this paper will be made available on Addgene (deposit 79031).


## SUPPLEMENTARY MATERIALS

science.sciencemag.org/content/371/6534/1166/suppl/DC1
Materials and Methods
Figs. S1 to S13
References
MDAR Reproducibility Checklist
Movies S1 and S2


10 April 2020; accepted 11 February 2021
Published online 25 February 2021
10.1126/science.abc1855


# *Science* Careers helps you advance your career. Learn how!

- Register for a free online account on **ScienceCareers.org**.
- Search hundreds of job postings and find your perfect job.
- Sign up to receive e-mail alerts about job postings that match your criteria.
- Upload your resume into our database and connect with employers.
- Watch one of our many webinars on different career topics such as job searching, networking, and more.
- Download our career booklets, including Career Basics, Careers Beyond the Bench, and Developing Your Skills.
- Complete an interactive, personalized career plan at "my IDP."
- Visit our Employer Profiles to learn more about prospective employers.
- Read relevant career advice articles from our library of thousands.

Visit **ScienceCareers.org** today — all resources are free

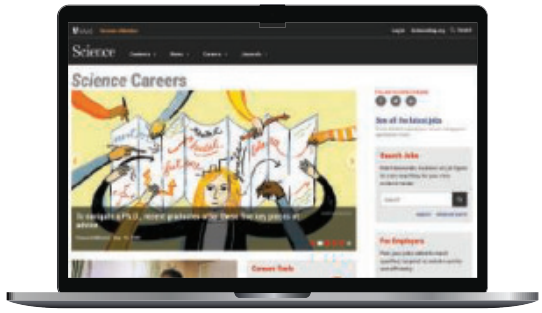


SCIENCECAREERS.ORG

ScienceCareers
FROM THE JOURNAL SCIENCE AAAS

University of Pittsburgh | UPMC HILLMAN CANCER CENTER

Three NIH-funded post-doctoral positions are available for enthusiastic, hard-working individuals to conduct research into the mechanisms that impact T cell function in mouse models of cancer and autoimmunity in Dr. Dario Vignali' s laboratory at the University of Pittsburgh.

**Position #1; ID# 21000729:** The successful applicant will investigate the role of regulatory T cells (Tregs) within the tumor microenvironment with the goal of understanding novel mechanisms that control their function and survival, and identifying and developing Treg-specific targets for therapeutic intervention. This project will emphasize use of complex mouse models, system biology approaches and other sophisticated immunological techniques.

**Position #2; ID# 21000901:** The successful applicant will be a part of a multi-institutional team funded by a research program grant examining the role of inhibitory receptors, PD1 and LAG3, on T cells in the tumor microenvironment. This project will emphasize use of complex mouse models, system biology approaches and other sophisticated immunological techniques.

**Position #3; ID# 21000742:** The successful applicant will investigate the regulatory mechanisms that collapse and lead to autoimmunity with an emphasis on Tregs and inhibitory receptors with the goal of identifying novel therapeutic strategies. This project will involve the NOD mouse model of Type 1 Diabetes, system biology approaches and other sophisticated immunological techniques.

These positions will focus on gaining a mechanistic understanding and therapeutic development of pathways and processes under investigation. Candidates should have a PhD or MD/PhD (no more than 2 years post second degree), a solid understanding of basic immunology, and practical experience with mouse models of disease. Training grant eligible candidates (US citizens and green card holders) are strongly encouraged to apply. Candidates will also develop skills in mouse models of cancer, immune function assays, flow cytometry, microscopy, biochemistry and molecular biology techniques. The candidate will also gain considerable experience writing manuscripts, reviews and grants along with oral presentations. Additional duties will include mouse colony management, training of undergraduate and graduate students, participation in department activities, presentations at lab, local and national meetings and any other assignments that the PI may request.

Additional information about the Vignali Lab can be found at:
Twitter: **@Vignali_Lab**
Websites: **https://www.vignali-lab.com**
**http://www.immunology.pitt.edu/person/dario-vignali-phd**

Interested candidates should go to **https://www.join.pitt.edu** and apply for the position by searching for the ID# associated with the position. Attach **(a)** a cover letter noting the position of interest listed above, a brief description of research interests and future career goals, **(b)** CV, and **(c)** contact information for three references to your application.

*By* **Megan J. Shen**

# A mother's plea

"Please don't wake up," I plead silently to my 10-month-old son as I log into another Zoom meeting from my tiny New York City apartment. I use a virtual background—a picture of my university office—to hide the fact that I'm in my kitchen, where it's easier to avoid the loud calls for "Mama!" from my 3-year-old daughter and the hunger cries of my infant son. Such meetings—a byproduct of the COVID-19 pandemic—add to the stress I feel as a working mom, trying to hide the messy reality of my life as a parent. It has led to a unique type of Zoom burnout, one I fear is specific to working mothers.

I've always tried to hide my motherhood duties from plain view. I don't have photos of my children on display in my university office, even though some of my male colleagues clearly feel comfortable doing so. I'm keenly aware of the bias mothers experience in the workplace, and I haven't wanted my colleagues to view me as less committed to my work because I have children. But now, working from home, I feel unable to control whether my children are visible.

My workdays are filled with meetings to discuss research projects with collaborators and mentees. When the pandemic started and the meetings switched to Zoom, I felt an unspoken pressure to turn my camera on. Almost everyone else had their camera on, and I feared that if I kept mine off, I wouldn't be viewed as "present."

**"The anxiety I experience during Zoom meetings compounds other stressors in my life."**

As a result, I spent most meetings fretting my daughter would waltz in, sit on my lap, and ask, "Mama, are those your co-workers?" It happened more than once, nullifying my futile attempts to hide my home life with a virtual background. Meanwhile, my husband—a motion graphic designer at an advertising agency—never sweats it when the children intrude. He has even voluntarily taken our son on camera to let his co-workers swoon over him.

I've encountered difficulties even when my children have stayed off camera. For instance, I was taken aback recently when a colleague brought our meeting to an abrupt end. As my son screamed in the background, he told me, "It sounds like someone needs mommy; I'd better let you go." Later, I ran the story by my husband, who was shocked. He has never once received comments indicating a child of ours might need him—their father—as they scream in the background.

My husband's more positive experiences could be due to his personality or his different profession. But I think a major contributing factor is gender inequities in how parents are perceived: I'm the distracted and much-needed mother, whereas he's the professional who also happens to be the father of two cute little kids.

The anxiety I experience during Zoom meetings compounds other stressors in my life. We haven't had child care for much of the pandemic. My husband has been a wonderful partner—splitting child care duties—but the reality is that he simply can't perform some tasks, such as nursing our infant son. I am in demand by my family and my job, and that makes my daily life as a working mother incredibly challenging.

One strategy that makes it all easier to juggle is to take work calls and even join Zoom meetings by phone. I started to do this a few months into the pandemic, when it was clear I was burning out and needed a different strategy. I realize colleagues might perceive me as less engaged when I'm not on camera, but the payoff—reduced anxiety and a chance to take care of household duties while still contributing to the meeting—is worth it to me.

I offer this advice to colleagues of working mothers: Understand that many of us are burnt out. Allow flexibility in how we call into meetings, outlining the policy with explicit language. Avoid making us feel uninvolved or not committed to our work when our cameras are turned off. And think carefully about whether you are treating us differently, perhaps by asking yourself, "Would I say the same thing to a father?" ■

Megan J. Shen is an assistant professor at Weill Cornell Medicine.
Send your career story to SciCareerEditor@aaas.org.

ILLUSTRATION: ROBERT NEUBECKER

# Science Webinars

AAAS

*Science* Webinars help you keep pace with emerging scientific fields!

Stay informed about scientific breakthroughs and discoveries.

Gain insights into current research from top scientists.

Take the opportunity to ask questions during live broadcasts.

Get alerts about upcoming free webinars.

**Sign up at: webinar.sciencemag.org/stayinformed**

# The heart of the matter.

The NEBNext® Ultra™ II workflow lies at the heart of NEB's portfolio for next gen sequencing library preparation. With specially formulated master mixes and simplified workflows, high quality libraries can be generated with low inputs and reduced hands-on time.

As sequencing technologies improve and applications expand, the need for compatibility with ever-decreasing input amounts and sub-optimal sample quality grows. Scientists must balance reliability and performance with faster turnaround, higher throughput and automation compatibility.

NEBNext Ultra II modules and kits for Illumina® are the perfect combination of reagents, optimized formulations and simplified workflows, enabling you to create DNA or RNA libraries of highest quality and yield, even when starting from extremely low input amounts.

The Ultra II workflow is central to many of our NEBNext products, including:

- Ultra II DNA & FS DNA Library Prep
- Enzymatic Methyl-seq
- Ultra II RNA & Directional RNA Library Prep
- Single Cell/Low Input RNA Library Prep
- Module products for each step in the workflow

The Ultra II workflow is available in convenient kit formats or as separate modules – it is easily scalable and automated on a range of liquid handling instruments.

| End Repair/ dA-Tailing | Adaptor Ligation | Clean Up/ Size Selection | PCR Enrichment | Clean Up |
|---|---|---|---|---|
| Module NEB #E7546 | Module NEB #E7595 | Component of NEB #E7103 | Module NEB #M0544 | Component of NEB #E7103 |
| NEBNext Ultra II DNA Library Prep Kit for Illumina (NEB #E7645) | | | | |
| NEBNext Ultra II Library Prep with Sample Purification Beads (NEB #E7103) | | | | |

The NEBNext Ultra II workflow has been cited in thousands of publications, as well as a growing number of preprints and protocols related to COVID-19. Citation information and extensive performance data for each product is available on neb.com.

To learn more about why NEBNext is the choice for you, visit **NEBNext.com**.



NEW ENGLAND BioLabs® Inc.

*be* INSPIRED
*drive* DISCOVERY
*stay* GENUINE